Experimental Study of the Decay $K_L^0 \to \pi^0 \nu \bar{\nu}$

Hideki Morii

Department of Physics, Graduate School of Science,
Kyoto University

April, 2010

Abstract

The world-first dedicated search for the rare neutral-kaon decay $K_L^0 \to \pi^0\nu\bar{\nu}$ has been carried out in the E391a experiment at the KEK 12-GeV proton synchrotron. A new upper limit of 2.6 $\times 10^{-8}$ at the 90% confidence level was set on the branching ratio for the decay by using the entire data set collected during the experiment.

Acknowledgements

This thesis could not be achieved without any supports from many people. First of all, I would like to express my appreciation to my supervisor Prof. Noboru Sasao. He involved me with the exciting kaon physics experiment, and gave me chances to take important role in it. His insight and instinct for physics has always impressed and excited me. I would like to make an appreciation to Prof. Tadashi Nomura. He has taught me physics and experimental methods throughout my graduate course. I learned a lot of things from basic knowledge to technical issues. This analysis is strongly supported by many effective guidances given by him. I am also grateful to Prof. Hajime Nanjo for the help and instructions. He gave me a number of thoughtful comments which greatly supported this work.

I wish to express my appreciation to Prof. Takao Inagaki, the spokesperson of the E391a experiment. The E391a experiment could not be carried out without his strong leadership. I also learned many things about the accelerator and detectors by him. I would like to extend my great appreciation to Prof. Takeshi Komatsubara. I learned a lot of things, including attitudes to physics and analysis, through the discussion with him. This study strongly depends on the hard works of the E391a collaborators. I present my appreciation to Prof. Hideki Okuno, Prof. Takahiro Sato, Prof. Gei Youb Lim, for their perfect work in the operation of the experiment and for their supports in the analysis. I really thank Prof. Mitsuhiro Yamaga, Prof. Hiroaki Watanabe, Dr. Mikhail Doroshenko, for developing the electronics and software platform, which perfectly performed in E391a.

I would like to appreciate Prof. Taku Yamanaka, Prof. Yee Bob Hsiung, and Prof. Yau W. Wah, for their advice in this work. I was helped by a number of thought-provoking advices from them.

I must thank Prof. Ken Sakashita and Dr. Toshi Sumida for teaching me everything about E391a. I leaned so many things from them, sometimes directly and sometimes through their beautiful analysis code. I would like to present my special thank to Run-2 persons, Dr. Toshi Sumida and Dr. Gabriel N. Perdue, for their splendid work in the Run-2 analysis. This work could not be completed without their achievement.

I would like to show my special thank to Dr. Jiasen Ma for his great efforts in this analysis. Throughout the Run-3 work, we have worked closely to get the job done. My special thank should be extended to Mr. Hiroyasu Ishii for his perfect work in the preparation and operation of Run-3. In the preparation of Run-3, we worked together around the clock, from early in the morning to late at night. He also prevented me to fall into a habit to take energy drinks, caring for my health. I wish to present my thanks Mr. Tetsushi Shimogawa and Ms. Risa Ogata for the preparation of Run-3 and for the calibration of its data. I have enjoyed discussions, and sometimes chats, with them.

I would like to express my thanks to all the fellows and the graduate students who worked together with me for the E391a experiment, Dr. K. F. “Jack” Chen, Dr. J. Ma, Dr. S. Podolsky,

Mr. H. Ishii, Mr. H. Sato, Mr. S. Ishibashi, Mr. T. Sasaki, Ms. S. Takita, Mr. E. Iwai, Mr. T. Nomura, Mr. T. Shimogawa, Ms. R. Ogata, Mr. M. L. Wu, Ms. I. Kato, Mr. Y. C. Tung, for giving me the help and pleasant time.

I thank all the members of the High Energy Physics Group in Kyoto University, Prof. N. Sasao, Prof. K. Nishikawa, Prof. T. Nakaya, Prof. A. K. Ichikawa, Prof. T.Nomura, Prof. M. Yokoyama, Prof. H. Nanjo, Prof. T. Nakadaira, Dr. K. Nitta, Dr. H. Tanaka, Prof. A. Minamino, Mr. M. Suehiro, Mr. T. Fujiwara, Prof. S. Nishida, Mr. H. Yokoyama, Dr. I. Kato, Prof. H. Maesaka, Dr. K. Mizouchi, Dr. M. Hasegawa, Dr. S. Yamamoto, Mr. K. Maeda, Mr. S. Ueda, Mr. K. Hayashi, Mr. T. Morita, Mr. T. Sasaki, Mr. J. Kubota, Mr. T. Shirai, Ms. K. Takezawa, Dr. N. Taniguchi, Dr. K. Hiraide, Dr. Y. Kurimoto, Mr. Y. Nakajima, Mr. T. Nobuhara, Mr. K. Ezawa, Mr. K. Matsuoka, Mr. M. Taguchi, Mr. H. Kawamuko, Mr. S. Gomi, Mr. Y. Kurosawa, Mr. H. Kubo, Mr. K. Shiomi, Mr. T. Usuki, Mr. N. Kawasaki, Mr. T. Masuda, Mr. N. Nagai, Mr. M. Otani, Mr. K. Asada, Mr. K. Ieki, Mr. Y. Maeda, Mr. A. Murakami, Mr. D. Naito, Mr. T. Kikawa, Mr. D. Orme, Mr. K. Suzuki, Mr. G. Takahashi, Mr. S. Takahashi, Mr. T. Hiraki, Mr. T. Yamauchi. My life in the university have been always happy with them. My special thank goes to the "coffee club" members in the laboratory. I have always enjoyed tasty coffee as well as interesting conversation with the members.

I hope to express my appreciation to the members of the $K^{O}TO$ experiment. The discussion with them enriched my understandings to the experiment. Also, even though I am the second to last person to analyze the E391a, I was free from loneliness because I have been surrounded by many active members of the $K^{O}TO$ experiment.

Finally, I would like to express my special appreciation to my family, especially my parents Hideo and Tomoko Morii, for the infinite supports throughout my life.

Hideki Morii
Kyoto, Japan.
April 2010

Contents

Contents . . . iv
List of Figures . . . viii
List of Tables . . . ix
Glossary . . . xii

1 Introduction **1**
1.1 Symmetries . . . 1
1.2 Kaon phenomenology . . . 2
1.2.1 Neutral kaon system . . . 2
1.2.2 Indirect CP violation . . . 3
1.2.3 Direct CP violation . . . 4
1.3 CP violation in the Standard Model . . . 5
1.3.1 CKM matrix . . . 5
1.3.2 Unitarity triangle . . . 6
1.3.3 Current status of CKM parameters . . . 6
1.4 $K_L^0 \to \pi^0\nu\bar{\nu}$ decay in the SM . . . 7
1.5 $K_L^0 \to \pi^0\nu\bar{\nu}$ decay beyond the SM . . . 9
1.5.1 Grossman-Nir limit . . . 9
1.5.2 Several examples of theories beyond the Standard Model . . . 10
1.6 History of $K_L^0 \to \pi^0\nu\bar{\nu}$ search . . . 11
1.7 Outline of the thesis . . . 12

2 Experimental Method **14**
2.1 Signature of the $K_L^0 \to \pi^0\nu\bar{\nu}$ decay . . . 14
2.2 Background sources . . . 15
2.3 Features of the E391a experiment . . . 15
2.3.1 Hermetic high-sensitivity veto system . . . 15
2.3.2 Pencil beamline . . . 16
2.3.3 Methods to reduce the neutron interactions . . . 17

3 Experimental Apparatus and Runs **18**
3.1 Beamline . . . 18
3.1.1 Primary proton beamline and K_L^0 production target . . . 18
3.1.2 Neutral beamline . . . 19
3.2 Detectors . . . 23
3.2.1 Overview . . . 23
3.2.2 CsI calorimeter . . . 23
3.2.3 Charged veto counter . . . 27

3.2.4 Barrel counters . . . 28
3.2.5 Counters along the beam . . . 32
3.2.6 Beam counters . . . 36
3.3 Vacuum . . . 39
3.4 Data acquisition . . . 40
3.4.1 Electronics . . . 40
3.4.2 Triggers . . . 44
3.5 Calibration . . . 46
3.6 Data taking . . . 48
3.6.1 Run periods . . . 48
3.6.2 Physics run . . . 48
3.6.3 Calibration runs . . . 48
3.6.4 Al-plate run . . . 49

4 Analysis Overview **51**
4.1 Analysis-2008 . . . 51
4.2 Key points of the current analysis . . . 52

5 Event Reconstruction **54**
5.1 Photon reconstruction . . . 54
5.1.1 Cluster finding . . . 54
5.1.2 A criterion to reject non-isolated clusters . . . 55
5.1.3 Energy and position calculation . . . 57
5.1.4 Sorting of events . . . 57
5.2 π^0 reconstruction . . . 57
5.3 Energy and position corrections . . . 58

6 Monte Carlo Simulations **62**
6.1 Beamline simulation . . . 63
6.2 K_L^0 simulation . . . 63
6.2.1 Parameterization for K_L^0 beam . . . 64
6.2.2 K_L^0 decay . . . 64
6.3 Neutron simulation . . . 65
6.3.1 Halo neutron generation . . . 66
6.3.2 Simulation of neutron interaction in the detector . . . 66
6.4 Detector Response . . . 67
6.4.1 Energy smearing for CsI . . . 67
6.4.2 Other detectors . . . 69
6.5 Accidental activity . . . 70
6.6 Reproducibility of the MC simulations . . . 70
6.6.1 K_L^0 simulation . . . 71
6.6.2 Neutron simulation . . . 73
6.6.3 Photo-nuclear interaction . . . 73

7 Event Selection **76**
7.1 Characteristics of the signal and background events . . . 76
7.1.1 The $K_L^0 \to \pi^0\nu\bar{\nu}$ signal . . . 76
7.1.2 Kaon backgrounds . . . 78
7.1.3 Halo neutron backgrounds . . . 78
7.2 Optimization principle for the event selections . . . 79
7.3 Veto cuts . . . 81
7.3.1 CsI veto cut . . . 81
7.3.2 Other photon veto cuts . . . 81
7.3.3 Charged particle veto cuts . . . 83
7.4 Kinematic selections . . . 83
7.4.1 Photon-cluster quality selections: . . . 83
7.4.2 Two photons selections . . . 90
7.4.3 π^0 selections . . . 90
7.5 Signal region . . . 92

8 Background Estimation **94**
8.1 Halo neutron background . . . 94
8.1.1 CC02-π^0 background . . . 95
8.1.2 CV-π^0 background . . . 95
8.1.3 CV-η background . . . 95
8.2 K_L^0 background . . . 95
8.2.1 $K_L^0 \to \pi^0\pi^0$ background . . . 99
8.2.2 $K_L^0 \to \gamma\gamma$ background . . . 99
8.2.3 Charged decay backgrounds . . . 99
8.3 Other background sources . . . 100
8.3.1 Backward-going π^0 background . . . 100
8.3.2 Residual gas background . . . 101
8.4 Total number of estimated backgrounds . . . 101

9 Normalization **104**
9.1 Principle of normalization . . . 104
9.1.1 Acceptance . . . 104
9.1.2 Single Event Sensitivity . . . 105
9.2 Analysis of normalization modes . . . 105
9.2.1 K_L^0 reconstruction . . . 105
9.2.2 Event selection . . . 106
9.2.3 Accidental loss . . . 107
9.3 Number of K_L^0 decays . . . 109

10 Results **114**
10.1 Acceptance and single event sensitivity . . . 114
10.1.1 Signal acceptance . . . 114
10.1.2 Single event sensitivity . . . 117
10.2 Results . . . 117

11 Systematic Uncertainties **119**
11.1 Uncertainty of the single event sensitivity . . . 119
11.2 Uncertainty of the halo neutron backgrounds . . . 121

12 Conclusion and Discussion **124**
12.1 Conclusion of the present analysis . . . 124
12.2 KOTO experiment : $K_L^0 \to \pi^0\nu\bar{\nu}$ search in near future . . . 126
12.2.1 Improvements in sensitivity . . . 126
12.2.2 Improvements in background suppression . . . 126
12.3 Other possible improvements in the $K_L^0 \to \pi^0\nu\bar{\nu}$ search . . . 131
12.3.1 Angle measurement . . . 131
12.3.2 K_L^0 momentum measurement . . . 131
12.4 Prospects of the kaon physics . . . 132

A CsI Calibration **133**
A.1 Cosmic ray calibration . . . 133
A.2 $K_L^0 \to \pi^0\pi^0\pi^0$ calibration . . . 133

B Neural Network Selection **137**
B.1 Introduction to neural network . . . 137
B.1.1 Number of hidden layers and neurons . . . 137
B.1.2 Functional models for synapses . . . 138
B.2 Selections with neural network technique . . . 139

C Statistical Methods on the Upper Limit **140**
C.1 Considering the uncertainty in the number of K_L^0 decay . . . 140
C.1.1 Upper limit with the Poisson statistics . . . 140
C.1.2 Incorporating the errors in the number of K_L^0 decays . . . 141
C.2 Feldman-Cousins method . . . 141
C.2.1 Upper limit with Feldman-Cousins method . . . 141
C.2.2 FC method with the effect of uncertainties . . . 142
C.2.3 Effective sensitivity of the experiment . . . 142

List of Figures

1.1 Recent results by CKM fitter . . . 7
1.2 Feynman diagrams of the $K_L^0 \to \pi^0\nu\bar{\nu}$ decay . . . 8
1.3 Unitary triangle related to the Kaon rare decays . . . 8
1.4 Schematic (ρ, η) determination from the B system and K system . . . 10
1.5 Correlation between BR($K_L^0 \to \pi^0\nu\bar{\nu}$) and BR($K^+ \to \pi^+\nu\bar{\nu}$) in several new physics models . . . 11
1.6 History of $K_L^0 \to \pi^0\nu\bar{\nu}$ search . . . 12

2.1 Concept of hermetic veto detector system in E391a . . . 16
2.2 Concept of π^0 reconstruction in E391a . . . 17
2.3 P_T distributions of two photons for the signal mode and other K_L^0 decay modes . 17

3.1 Layout of the East Counter Hall and the location of the E391a area . . . 19
3.2 Schematic view of the neutral beamline . . . 21
3.3 Momentum spectrum of K_L^0 by MC . . . 22
3.4 Beam profiles of neutrons and photons by MC . . . 22
3.5 Beam profiles of K_L^0 by MC . . . 22
3.6 E391a detection system. . . . 23
3.7 Assembly of detector subsystems in the downstream end-cap . . . 24
3.8 Schematic drawing of the CsI module . . . 25
3.9 Cross-sectional shapes of Edge CsI . . . 25
3.10 Cross-sectional drawings of the Sandwich module . . . 26
3.11 Schematic view of the Xenon gain monitoring system . . . 26
3.12 Gain stability of CsI's PMT . . . 26
3.13 Energy resolution as a function of the incident energy . . . 27
3.14 Schematic drawings of CV . . . 28
3.15 Position dependence of the CV light yield . . . 28
3.16 Cross-sectional end view of MB and FB . . . 29
3.17 Schematic drawing of MB . . . 30
3.18 Structure of MB module . . . 30
3.19 Schematic drawings of Prism-shape photo-cathode (EGP-PMT) . . . 30
3.20 Light yield of MB module as a function of the distance from the PMT . . . 31
3.21 Linearity and timing resolution of a MB module . . . 31
3.22 Schematic drawing of a BCV module . . . 31
3.23 Overview of the FB and CC02 . . . 33
3.24 The location of downstream counters . . . 33
3.25 Cross-sectional drawing of CC00 . . . 34

3.26 Schematic drawings of CC02 . . . 35
3.27 Schematic drawings of CC04 and CC05 . . . 36
3.28 Front view of CC06 and CC07 . . . 37
3.29 Side view of BA used in Run-2 and Run-3 . . . 38
3.30 Schematic front view of BHCV . . . 38
3.31 Schematic drawing of APC . . . 39
3.32 E391a vacuum system . . . 41
3.33 Membrane used for the vacuum separation . . . 42
3.34 The discharge voltage of a PMT as a function of the vacuum pressure . . . 42
3.35 Schematic view of the E391a DAQ system . . . 42
3.36 Segments of CsI blocks for the hardware clustering . . . 45
3.37 Distribution of the number of the hardware clusters in data . . . 45
3.38 Cosmic ray track used for calibration . . . 47
3.39 Stability of the kinematic variables over the Run-3 period . . . 47
3.40 Time difference between two photons from the $K_L^0 \to \pi^0\pi^0\pi^0$ decay . . . 48

5.1 An example of six photon events of the $K_L^0 \to \pi^0\pi^0\pi^0$ decay in the CsI calorimeter 55
5.2 An example of cluster finding algorithm . . . 56
5.3 Distribution of the number of crystals having the energy deposit greater than 5 MeV in a photon cluster, comparing the data and $K_L^0 \to \pi^0\pi^0\pi^0$ MC. The top portion shows a comparison between the number of events in the data and MC, and the bottom portion shows the ratio between them. All analysis cuts for the $K_L^0 \to \pi^0\pi^0\pi^0$ mode, as will be described in Sec. 9.2.2 , are imposed. . . . 56
5.4 Schematic diagram of isolated and non-isolated clusters . . . 56
5.5 Schematic view of parameters used to reconstruct the π^0 vertex . . . 58
5.6 Correlation between the incident angle and the fraction of leaked energy . . . 59
5.7 Schematic illustration of the position correction . . . 59
5.8 Correlations between the true hit position and x_{COE} in MC . . . 60
5.9 Scheme of the energy and position correction for the photon cluster . . . 60
5.10 The result of the energy and position corrections . . . 61

6.1 Flowchart of MC simulation . . . 62
6.2 Characteristics of the core and halo neutrons . . . 63
6.3 Functions used to determine the initial state of K_L^0's . . . 65
6.4 Definition of the parameters used in the halo neutron generation . . . 66
6.5 Distribution of visible ratio of the photon energy with and without the photo-nuclear effects . . . 69
6.6 Probability to lose the visible ratio of photon energy by the photo-nuclear effects 69
6.7 Reconstructed radial position distribution with and without the position correction 71
6.8 Reconstructed kinematic variables of six-photon events for the data and $K_L^0 \to \pi^0\pi^0\pi^0$ MC . . . 72
6.9 Reconstructed invariant-mass distribution of four-photon events by data and MC 73
6.10 Schematic layout of the Al plate run . . . 74
6.11 Reconstructed invariant mass distribution of two photons in the Al-plate run . . 74
6.12 Reconstructed Z_{VTX} distribution of two photons in the Al plate run . . . 75

7.1 P_T vs. Z_{VTX}distributions for the signal mode and background modes by MC . . 77
7.2 An example of the optimization for the event selection . . . 80

7.3 Position-depended veto for the CsI . . . 82
7.4 Example of the photon cluster . . . 85
7.5 An illustration of normal and fusion cluster . . . 87
7.6 Distributions of output values of fusion neural network by the signal and CV-π^0 BG MC . . . 87
7.7 Schematic drawing of geometrical characteristics of the CV-η background . . . 88
7.8 Incident angle distribution of photons for the $K_L^0 \to \pi^0\nu\bar{\nu}$ signal and the CV-η background events . . . 89
7.9 Distribution of RMS along the radial direction for the $K_L^0 \to \pi^0\nu\bar{\nu}$ signal and the CV-η background . . . 89
7.10 Distributions of output values of CV-η neural network by the signal and CV-η BG MC . . . 89
7.11 Distributions of the P_{min} parameters by the signal and CC02-π^0 MC . . . 91
7.12 Schematic view of the projected opening angle . . . 92
7.13 Distributions of the θ_{proj} for the signal and $K_L^0 \to \gamma\gamma$ BG by MC . . . 92
7.14 Performance of the angle neural network . . . 93
7.15 Distributions of the $\Delta\theta$ parameters for the signal and CV-π^0 BG by MC . . . 93

8.1 Z_{VTX}-P_T distribution of the background MC and the real data . . . 96
8.2 Z_{VTX} distribution of the CC02-π^0 events for the data and MC . . . 97
8.3 Z_{VTX}-P_T distribution of the CC02-π^0 BG by MC . . . 97
8.4 Z_{VTX}-P_T distribution of the CV-π^0 BG by MC . . . 97
8.5 Z_{VTX}-P_T distribution of the CV-η BG by MC . . . 98
8.6 Z_{VTX}-P_T distribution of the $K_L^0 \to \pi^0\pi^0$ BG by MC . . . 99
8.7 Z_{VTX}-P_T distribution of the $K_L^0 \to \gamma\gamma$ BG by MC . . . 100
8.8 Z_{VTX}-P_T distribution of the $K_L^0 \to \pi^- e^+ \nu$ BG without CV veto by MC . . . 100
8.9 Mechanism of backward-going π^0 background . . . 101
8.10 Z_{VTX}-P_T distribution of the backward-going π^0 BG by MC . . . 101
8.11 Acceptance and rejection power of each kinematic selection . . . 103

9.1 Momentum distributions of K_L^0 for $K_L^0 \to \pi^0\nu\bar{\nu}$, $K_L^0 \to \pi^0\pi^0\pi^0$, $K_L^0 \to \pi^0\pi^0$, and $K_L^0 \to \gamma\gamma$ by MC . . . 106
9.2 Accepted regions for the reconstructed mass and vertex position for six-photon samples . . . 107
9.3 Accepted regions for the reconstructed mass and vertex position for four-photon samples . . . 108
9.4 Accepted regions for the reconstructed vertex position for two-photon samples . . . 108

10.1 Z_{VTX}-P_T distribution of the $K_L^0 \to \pi^0\nu\bar{\nu}$ signal by MC . . . 115
10.2 "Final plot": showing the Z_{VTX}-P_T distribution for the combined sample of Run-2 and Run-3 . . . 118

11.1 Fractional difference of veto and kinematic cuts for the normalization mode . . . 120
11.2 Acceptance of veto and kinematic cuts for the $K_L^0 \to \pi^0\pi^0$mode . . . 120
11.3 Fractional difference of kinematic selection for the halo neutron BG . . . 122

12.1 History of the $K_L^0 \to \pi^0\nu\bar{\nu}$ search with the result reported in this thesis . . . 125
12.2 The momentum distribution of K_L^0 for the E391a and K$^{\mathrm{O}}$TO experiment . . . 127

12.3 Estimated profiles of the neutral beamline 128
12.4 Front view of the upgraded CsI calorimeter in the K^{O}TO experiment 129
12.5 CV upgrade in the K^{O}TO experiment 130

A.1 Distribution of raw chage, path length, and normalized charge in the cosmic calibration of CsI 134
A.2 Invariant mass distributions of the K_L^0 before and after the $K_L^0 \to \pi^0\pi^0\pi^0$ calibration 136

B.1 Schematic drawing of neural network 138
B.2 Sigmoid function used as the model of synapse connections 138

C.1 Distribution of the number of background 143
C.2 Probability density function of the observed number of events 143

List of Tables

3.1 Basic parameters of detectors along the beam 34
3.2 Characteristics of vacuum regions 40
3.3 Online veto thresholds for veto counters 45
3.4 Summary of three physics runs 49
3.5 Run conditions of Al-plate run 50

4.1 Estimated number of BG in the Analysis-2008. 52

6.1 Parameters for the crystal-by-crystal smearing 68
6.2 Parameters for the attenuation in the barrel detectors 69

7.1 Summary of loose and tight veto energy threshold for each detector 84
7.2 Kinematic selections for the $K_L^0 \to \pi^0\nu\bar{\nu}$ events 93

8.1 Numbers of events outside the signal box for the BG simulation and data 97
8.2 Summary of MC samples for K_L^0 BG estimations 98
8.3 Estimated number of BG 102

9.1 Kinematic selections for $K_L^0 \to \pi^0\pi^0\pi^0$ mode 111
9.2 Kinematic selections for $K_L^0 \to \pi^0\pi^0$ mode 111
9.3 Kinematic selections for $K_L^0 \to \gamma\gamma$ mode 111
9.4 Accidental losses of Run-3 data for the normalization modes 112
9.5 Accidental losses of each detector 112
9.6 Estimated numbers of K_L^0 decays for Run-3 data 112
9.7 Estimated numbers of K_L^0 decays for the Run-2, Run-3, and combined sample of Run-2 and Run-3 113
9.8 Estimated numbers of K_L^0 decays from three decay modes 113

10.1 Acceptance to the $K_L^0 \to \pi^0\nu\bar{\nu}$ signal events. 116
10.2 Breakdown lists of the signal acceptance for the veto cuts and kinematic selections. 116

11.1 Systematic uncertainties in the number of K_L^0 decay 121
11.2 Systematic uncertainties in the halo neutron BG estimation 123

12.1 Comparison between the E391a and K$^{\mathrm{O}}$TO beamline 127
12.2 Comparison between the E391a and K$^{\mathrm{O}}$TO experiment. 127

C.1 Upper limits calculated by different methods 142
C.2 Effective sensitivity of the Analysis-2008 and the present Run-2+3 analysis . . . 144

Glossary

AD	amplifier-discriminator module, (pp.40)
APC	aerogel photon counter — a photon tagging counter located in front of the BA, (pp.37)
BA	back anti — a photon veto counter located inside the neutral beamline at the downstream end of the detector system, (pp.36)
BCV	barrel charged veto — a barrel-shaped charged particle veto counter located inside the MB, (pp.29)
BHCV	beam hole charged veto — a charged particle veto counter located inside the neutral beamline at the downstream end of the detector system, (pp.37)
CC00	collar counter #0 — a composite of tungsten collimator and veto counter located upstream of the detector system, (pp.32)
CC02	collar counter #2 — a collar-shaped veto counter located upstream of the decay region, (pp.32)
CC03	collar counter #3 — a collar-shaped veto counter located inside the CsI calorimeter, (pp.35)
CC04	collar counter #4 — a collar-shaped veto counter located downstream of the decay region, (pp.35)
CC05	collar counter #5 — a collar-shaped veto counter located downstream of the decay region, (pp.35)
CC06	collar counter #6 — a collar-shaped veto counter located downstream of the decay region, (pp.36)
CC07	collar counter #7 — a collar-shaped veto counter located downstream of the decay region, (pp.36)

CV	charged veto counter — a charged particle veto counter located in front of the CsI, (pp.27)
EGP PMT	a newly developed photo-multiplier tube having prism-shape photo cathode and high quantum efficiency for green light, (pp.29)
FB	front barrel — a barrel-shaped photon veto counter located upstream of the decay region, (pp.28)
FLUKA	a simulation package for hadronic interactions, (pp.52)
HCC	hardware cluster counter — number of hits in the CsI counted by hardware segments shown in Fig. 3.36, (pp.44)
MB	main barrel — a barrel-shaped photon veto counter located at the middle of detector system, (pp.28)
NN	neural network, (pp.86)
POT	protons on target — number of protons hitting the production target, (pp.18)
SEC	secondary emission chamber — an intensity monitor of the primary beam, (pp.18)
TDI	timing dispersion selection — a selection on the timing dispersion in a photon cluster, (pp.85)
TMON	target monitor — a counter monitoring the secondary particles at the production target), (pp.19)

Chapter 1

Introduction

Brief summary

In this thesis, we report the final results of the search for the rare kaon decay $K_L^0 \to \pi^0\nu\bar{\nu}$ in the E391a experiment. First, we discuss the importance of the search for the decay by explaining the theoretical backgrounds. The $K_L^0 \to \pi^0\nu\bar{\nu}$ decay occurs via a loop diagram accompanied by the flavor changing neutral current (FCNC). Since the $K_L^0 \to \pi^0\nu\bar{\nu}$ decay is a process violating the CP symmetry, studying the decay gives us the information of CP asymmetry in the weak interaction. Also, the decay mode is a good testing field for probing new physics beyond the Standard Model because the amplitude of the decay can vary when unknown particles appear in the loop diagram.

Next, the current status of experimental searches for the decay mode is described. Several experimental searches for the $K_L^0 \to \pi^0\nu\bar{\nu}$ decay were made with improving the sensitivity. The previous searches for the $K_L^0 \to \pi^0\nu\bar{\nu}$ decay was made as a by-product of other physics themes. E391a was the world first experiment dedicated to the search for $K_L^0 \to \pi^0\nu\bar{\nu}$, and had a role to confirm the experimental concepts to search the decay. Also, we briefly summarize the overview of this thesis in the last part of this chapter.

1.1 Symmetries

Symmetries and corresponding invariances have been taking the important role in the development of physics. As described in Noether's theorems, any continuous symmetry has corresponding invariance, e.g. the transitional and rotational symmetries lead to the momentum and angular momentum invariances, respectively. In addition to these continuous symmetries, discrete symmetries also have importance in physics. There are three fundamental discrete symmetries:

- Charge conjugation (C) : transforming particle to anti-particle
- Parity (P) : reflecting the space coordinate from $\vec{x}$ to $-\vec{x}$
- Time reversal (T) : inverting the time coordinate from t to $-t$.

A combined symmetry of CPT, which is obtained by a successive transformation of C, P, and T, is one of the most important symmetry in quantum field theories. Because only minimal

assumptions, like the locality and Lorentz invariance, are needed to conserve the CPT, the symmetry is naturally considered to be conserved.

In the early time, C, P, and T symmetries were considered to be held in electrodynamics, and in the strong and weak interactions as well. P violation in the weak interaction was suggested by Lee and Yang [1], and it was experimentally confirmed in 1957 [2]. This observation was shortly followed by the discovery of C violation in pion decay [3, 4]. Lev Landau suggested that CP instead of C should be the proper symmetry for inverting particle to anti-particle. With C conversion, neutrino changes like $\nu_L \to \overline{\nu}_L$. Since the weak interaction only sees left-handed neutrinos (and right-handed anti-neutrinos), the situation becomes different under C conversion. When P is also invoked, the conversion becomes like $\nu_L \to \overline{\nu}_R$, and this results in the conversion from particle to anti-particle. In 1957 and 1958, the V–A theory were build to describe the weak interaction that have good symmetries to CP and T.

However, CP symmetry was found to be broken by observing the $K_L \to \pi\pi$ decay in 1964 [5]. Considering the CPT conservation, the CP violation implies the T violation. The T violation is a kind of 'surprise': the nature makes a difference between past and future, even in the microscopic level. Another important point of the CP violation is that it has potential to answer the matter-antimatter asymmetries in the universe [6], which is one of the most fundamental questions to our universe.

In this Chapter, we describe the kaon rare decay $K_L^0 \to \pi^0\nu\bar{\nu}$, which is deeply related to CP violation. Section 1.2 explains the phenomenology of CP violation in neutral kaon system. The CKM matrix and the relation between the complex phase in the CKM matrix and the CP voilation is explained in Sec. 1.3. Section 1.4 describes how the $K_L^0 \to \pi^0\nu\bar{\nu}$ decay plays a role in the Standard Model, and Sec. 1.5 shows several theories beyound the Standard Model, which may include new sources of the CP violation. The history of experimental search for the $K_L^0 \to \pi^0\nu\bar{\nu}$ is mentioned in Sec. 1.6. An outline of this thesis is given in Section 1.7.

1.2 Kaon phenomenology

1.2.1 Neutral kaon system

The neural kaon was first observed by Rochester and Butler in 1947 [7]. They used a cloud chamber and the neutral kaon was detected as a "V-particle" in the chamber. Now, the kaons are described as a meson formed by a strange quark and a first generation (up and down) quark. For the neutral kaons, there can be two possible combinations, and these two states are presented as strangeness eigenstates like,

$$K^0 = \begin{pmatrix} d \\ \overline{s} \end{pmatrix} \quad (S = +1) \tag{1.1}$$

and

$$\overline{K^0} = \begin{pmatrix} \overline{d} \\ s \end{pmatrix} \quad (S = -1), \tag{1.2}$$

where S denotes the strangeness quantum number. K^0 and $\overline{K^0}$ are not eigenstates of CP, because

$$CP|K^0\rangle = |\overline{K^0}\rangle, \tag{1.3}$$

$$CP|\overline{K^0}\rangle = |K^0\rangle. \tag{1.4}$$

We can represent them in *CP* eigenstates by taking linear combinations of the two states like

$$|K_1\rangle = \frac{1}{\sqrt{2}}(|K^0\rangle + |\overline{K^0}\rangle), \tag{1.5}$$

$$|K_2\rangle = \frac{1}{\sqrt{2}}(|K^0\rangle - |\overline{K^0}\rangle). \tag{1.6}$$

Applying *CP* transformation, K_1 and K_2 changes like

$$CP|K_1\rangle = \frac{1}{\sqrt{2}}(|\overline{K^0}\rangle + |K^0\rangle) = +|K_1\rangle \ \ (CP = +1), \tag{1.7}$$

$$CP|K_2\rangle = \frac{1}{\sqrt{2}}(|\overline{K^0}\rangle - |K^0\rangle) = -|K_2\rangle \ \ (CP = -1), \tag{1.8}$$

where K_1 is a *CP* even state and K_2 is a *CP* odd state.

The *CP* even state mostly decays into two-pion final state (*CP*-even). On the other hand, the *CP*-odd state cannot decay into two pions, and then should have longer lifetime than the *CP* even state. The existence of the neutral kaon having longer lifetime was predicted by Gell-Mann and Pais [8], and the long-lived neutral kaon was observed by Lederman *et al.* in 1956 [9].

Owing to the large difference in the lifetime between two neutral kaon states, it is easy to produce "pure" long-lived neutral kaon beam by using the long beamline between the production target and the detector system; the short-lived kaon decays away in passing through the long beamline. A famous experiment using such kind of concept was made by Christenson, Cronin, Fitch, and Turlay in 1963 [5]. In their experiment, they tried to set an upper limit on the $K_2 \to \pi^+\pi^-$, but they observed 45 events of that decay, establishing the *CP* violation. This process was explained from the mixing between K_1 and K_2, and called as "indirect *CP* violation". Afterwards, another source of *CP* violation, which is not caused by the mixing of two states, was observed, and called "direct *CP* violation". In the following sections, we briefly introduce the mechanism of indirect and direct *CP* violations.

1.2.2 Indirect CP violation

The indirect *CP* violation is caused by the mixing of K_1 and K_2. Considering the mixing of K_1 and K_2, the short-lived kaon K_S and long-lived kaon K_L can be written by the superposition of K_1 and K_2 as,

$$|K_S\rangle = \frac{1}{\sqrt{1+|\varepsilon|^2}}(|K_1\rangle + \varepsilon|K_2\rangle) \tag{1.9}$$

$$= \frac{1}{\sqrt{1+|\varepsilon|^2}}((1+\varepsilon)|K^0\rangle + (1-\varepsilon)|\overline{K^0}\rangle), \tag{1.10}$$

$$|K_L\rangle = \frac{1}{\sqrt{1+|\varepsilon|^2}}(|K_2\rangle + \varepsilon|K_1\rangle) \tag{1.11}$$

$$= \frac{1}{\sqrt{1+|\varepsilon|^2}}((1+\varepsilon)|K^0\rangle - (1-\varepsilon)|\overline{K^0}\rangle). \tag{1.12}$$

where ε represents the contribution of K_1 and K_2 to K_L and K_S, respectively. With this equation, K_L can decay into *CP* even states via the component of K_1; the process is referred as the "indirect" *CP* violation.

The measurement on the indirect *CP* violation was done by using the decay of neutral kaon to two-pion state. We define the ratios for these decay as

$$\eta_{00} = \frac{\langle \pi^0\pi^0|\mathcal{H}|K_L\rangle}{\langle \pi^0\pi^0|\mathcal{H}|K_S\rangle}, \quad \eta_{+-} = \frac{\langle \pi^+\pi^-|\mathcal{H}|K_L\rangle}{\langle \pi^+\pi^-|\mathcal{H}|K_S\rangle}. \tag{1.13}$$

If the *CP* is conserved, $\eta_{00} = \eta_{+-} = 0$, and the latest measurements on these parameters give,

$$|\eta_{00}| = (2.221 \pm 0.011) \times 10^{-3} \ [10, 11] \ , \tag{1.14}$$
$$|\eta_{+-}| = (2.232 \pm 0.011) \times 10^{-3} \ [10, 12] \ . \tag{1.15}$$

1.2.3 Direct CP violation

The direct *CP* violation appears through the direct transition of a *CP* even to odd state (and not through the mixing of K^0 and $\overline{K^0}$). In the example of the kaon decays into the pions, direct *CP* violation means K_2 (K_1) decays into two (three) pion final state.

The difficulty in measuring the direct *CP* violation is that we can only access K_L instead of K_2 itself. The amplitude of $K_L \to \pi\pi$ decay is expressed as

$$\langle \pi\pi|\mathcal{H}|K_L\rangle \sim \langle \pi\pi|\mathcal{H}|K_2\rangle + \varepsilon\langle \pi\pi|\mathcal{H}|K_1\rangle \ , \tag{1.16}$$

where the component of indirect *CP* violation, $\varepsilon\langle \pi\pi|\mathcal{H}|K_1\rangle$, dominates over the component of direct *CP* violation, $\langle \pi\pi|\mathcal{H}|K_2\rangle$.

The access to the direct *CP* violation can be obtained by using a small difference between $\pi^+\pi^-$ and $\pi^0\pi^0$, which caused by their isospin dependence. With a historical reason, we introduce parameters ϵ and ϵ', which have been used to describe the *CP* violation in neutral kaon decays. Parameters ϵ and ϵ' are related to the observables, η_{00} and η_{+-} as

$$\eta_{00} = \epsilon - 2\epsilon' \ , \tag{1.17}$$
$$\eta_{+-} = \epsilon + \epsilon' \ . \tag{1.18}$$

An evidence of the direct *CP* violation was found by measuring the double ratio of the decay widths of $K_{L/S} \to \pi^+\pi^-$ and $K_{L/S} \to \pi^0\pi^0$:

$$\frac{\Gamma(K_L \to \pi^+\pi^-)/\Gamma(K_S \to \pi^+\pi^-)}{\Gamma(K_L \to \pi^0\pi^0)/\Gamma(K_S \to \pi^0\pi^0)} \approx 1 + 6\mathrm{Re}(\epsilon'/\epsilon) \ . \tag{1.19}$$

The current experimental value of the parameter $\mathrm{Re}(\epsilon'/\epsilon)$ [10] is

$$\mathrm{Re}(\epsilon'/\epsilon) = (1.65 \pm 0.26) \times 10^{-3}. \tag{1.20}$$

The non-zero value of $\mathrm{Re}(\epsilon'/\epsilon)$ shows the existence of direct *CP* violation [13].

In the $K_L^0 \to \pi^0\nu\bar{\nu}$ decay, the origin of *CP* violation is direct one, as described in later sections. In the following sections, the interpretations of the *CP* violation are described by the Standard Model (SM) and beyond the SM.

1.3 CP violation in the Standard Model

In the Standard model [14], the Lagrangian of the charged current in the weak interaction is given by:

$$\mathcal{L}_{CC} = \frac{g}{\sqrt{2}}[\overline{u_i} V_{ij} d_j W^- + \overline{d_j} V_{ij}^* u_i W^+] \tag{1.21}$$

where $u_i = (u, c, t)$ are left-handed up-type quarks and $d_i = (d, s, b)$ are left-handed down-type quarks, and $W^\pm$ denote the weak bosons. V_{ij} is the 3×3 unitary matrix (Cabibbo-Kobayashi-Maskawa or CKM matrix) which connects the up-type quarks with the down type quarks:

$$V_{CKM} = \begin{pmatrix} V_{ud} & V_{us} & V_{ub} \\ V_{cd} & V_{cs} & V_{cb} \\ V_{td} & V_{ts} & V_{tb} \end{pmatrix} \tag{1.22}$$

When *CP* transformation is applied to the Lagrangian, it changes as:

$$L_{CC} \to \frac{g}{\sqrt{2}}[\overline{d}_j V_{ij} u_i W^+ + \overline{u}_i V_{ij}^* d_j W^-]. \tag{1.23}$$

Thus, if the $V_{ij} = V_{ij}^*$, the interaction is invariant under *CP*.

1.3.1 CKM matrix

Even though the matrix elements of V_{CKM} contain complex phases, it doesn't result in *CP* asymmetries, because there are freedom of degrees to re-choose the phases of the quark fields. Kobayashi and Maskawa pointed out that the complex phase cannot be removed away in the case of 3×3 complex matrix with the condition of unitarity.

A general $n \times n$ complex matrix has $2n^2$ real parameters. They are reduced by the unitarity conditions:

$$\sum_j V_{ij} V_{jk}^* = \delta_{ik}, \tag{1.24}$$

having n constraints for $i = k$ and $n(n-1)$ for $i \neq k$. Thus $n \times n$ unitary matrix have n^2 independent parameters. Next, the phases of the quark fields can be rotated like:

$$U_i^m \to e^{i\phi_i^U} U_i^m, \;\; D_j^m \to e^{i\phi_j^D} D_j^m. \tag{1.25}$$

This results in reduction of $2n-1$ relative phases, and V have $(n-1)^2$ independent parameters. When we write down the matrix by using the rotation angles, we have $\frac{1}{2}n(n-1)$ angles in $n \times n$ orthogonal matrix. Subtracting the number of rotation angles from the number of independent parameters, we obtain

$$N_{\mathrm{p}hase} = (n-1)^2 - \frac{1}{2}n(n-1) = \frac{1}{2}(n-1)(n-2). \tag{1.26}$$

Thus, for the case of two generation, 2×2 unitary matrix have 1 rotation angle and no phases. For the case of three generation, 3×3 unitary matrix have 3 rotation angles and 1 phases, which represents the source of *CP* violation.

A representation of V_{CKM} using three angles and one phase is

$$V_{CKM} = \begin{pmatrix} c_{12}c_{13} & s_{12}c_{13} & s_{13}e^{-i\delta_{13}} \\ -s_{12}c_{23} - c_{12}s_{23}s_{13}e^{i\delta_{13}} & c_{12}c_{23} - s_{12}s_{23}s_{13}e^{i\delta_{13}} & s_{23}c_{13} \\ s_{12}s_{23} - c_{12}c_{23}s_{13}e^{i\delta_{13}} & -c_{12}s_{23} - s_{12}c_{23}s_{13}e^{i\delta_{13}} & c_{23}c_{13} \end{pmatrix}, \tag{1.27}$$

where $c_{ij} = \cos\theta_{ij}$ and $s_{ij} = \sin\theta_{ij}$ for the Eular angles θ_{ij} with i and j being family labels.

A more 'visual' way to represent V_{CKM} is known as the Wolfenstein parametrization [15]. In the Wolfenstein parametrization, matrix elements are expanded in powers of $\lambda = |V_{us}| = 0.22$, like:

$$V_{CKM} = \begin{pmatrix} 1-\lambda^2/2 & \lambda & A\lambda^3(\rho - i\eta) \\ -\lambda & 1-\lambda^2/2 & A\lambda^2 \\ A\lambda^3(1-\rho-i\eta) & -A\lambda^2 & 1 \end{pmatrix} + \mathcal{O}(\lambda^4), \tag{1.28}$$

where η represents the complex phase causing the *CP* violation.

1.3.2 Unitarity triangle

The unitarity of V_{CKM} leads to the following relations:

$$\sum_{i=u,c,t} |V_{id}|^2 = \sum_{i=u,c,t} |V_{is}|^2 = \sum_{i=u,c,t} |V_{ib}|^2 = 1 \ , \tag{1.29}$$

$$\sum_{i=u,c,t} V_{ji}V_{ki}^* = 0 = \sum V_{ij}V_{ik}^* \ \ (j,k = d,s,b \ ; \ j \neq k). \tag{1.30}$$

Since the matrix elements of V_{CKM} is complex, Eq. 1.30 can be represented as closed triangles in a complex plane, and the triangle is called unitarity triangle. Taking $j = d$ and $k = b$in Eq. 1.30, we obtain

$$V_{ub}^* V_{ud} + V_{cb}^* V_{cd} + V_{tb}^* V_{td} = 0. \tag{1.31}$$

All the *CP* violating observables are proportional to a quantity called Jarlskog invariant [16], J, defined as

$$J = \mathrm{I}m[V_{ij}V_{kl}V_{kj}^*V_{il}^*] \ \ (i \neq l, j \neq k) \ . \tag{1.32}$$

The parameter J means the area size of the unitarity triangle. In the Wolfenstein parametrization, J is represented to be $J = \lambda^6 A^2 \eta$.

1.3.3 Current status of CKM parameters

As shown in the previous subsection, A, λ, and η determine the size of *CP* violation in the Standard Model. They are also used in theoretical calculations to predict the branching ratio of $K_L^0 \to \pi^0\nu\bar{\nu}$ decay, as will be described in the next section. Thus, we briefly summarize the current status of constraints on the CKM parameters, which are imposed from a combination of various experiments.

The $\lambda = |V_{us}|$ is determined by the decay rates of strange particles. The current average value is reported to be $|V_{us}| = 0.2255 \pm 0.0019$. The A can be determined with the λ and the measurement of the $|V_{cb}|$ as shown in Eq. 1.22 and Eq. 1.28. The $|V_{cb}|$ is obtained from the semi-leptonic decays in B mesons to be $|V_{cb}| = (41.2 \pm 1.1) \times 10^{-3}$.

The constraints on $(\bar{\rho}, \bar{\eta})$ plane, where $\bar{\rho} = \rho(1-\lambda^2/2)$ and $\bar{\eta} = \eta(1-\lambda^2/2)$, respectively, are imposed from several experimental measurements. The $|\epsilon|$ and $\sin 2\phi_1$ are typical parameters in the K and B meson systems, respectively.

The $|\epsilon|$ is connected to $(\bar{\rho}, \bar{\eta})$ through the relation:

$$\epsilon = \bar{\eta} A^2 B_K \left[1.248(1-\bar{\rho}) A^2 (\frac{m_t}{170(\mathrm{GeV})})^{1.52} + 0.31 \right], \tag{1.33}$$

where B_K is the ratio of the true matrix element to that obtained using vacuum insertion, and it is estimated to be 0.85 ± 0.15.

The decay processes of $b \to c\bar{c}s$ give, in the time-dependent CP violation, an important parameter $\sim 2\phi_1$, where ϕ_1 is an angle of the unitary triangle in the $(\bar{\rho}, \bar{\eta})$ plane. The present experimental results from BELLE and BaBar experiments determine it to be:

$$\sin 2\phi_1 = 0.681 \pm 0.025. \tag{1.34}$$

All the constraints on the $(\bar{\rho}, \bar{\eta})$ nicely overlap in one region as shown in Fig 1.1 [17]. The measurement in the K meson system, $|\epsilon|$, and the measurement in the B meson system, $\sin 2\phi_1$, well agree. The global fit for the Wolfenstein parameters, as defined in Eq. 1.28, gives

$$\lambda = 0.2257^{+0.0009}_{-0.0010}, \ A = 0.184^{+0.021}_{-0.022}, \tag{1.35}$$

$$\bar{\rho} = 0.135^{+0.031}_{-0.016}, \ \bar{\eta} = 0.349^{+0.015}_{-0.017}. \tag{1.36}$$

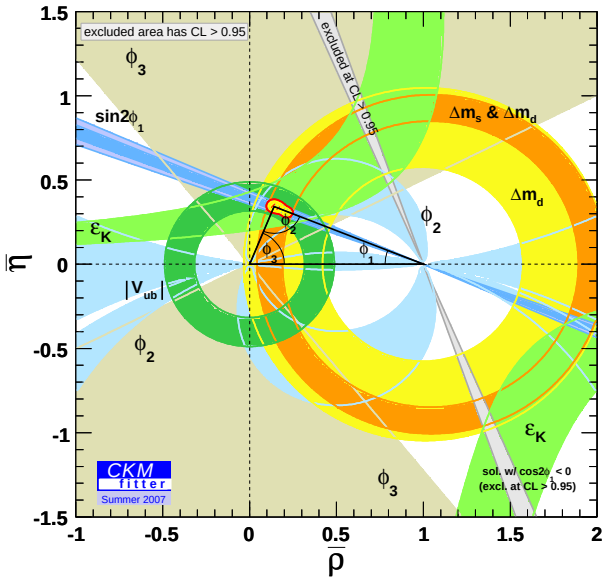

Figure 1.1: Constraints on the $(\bar{\rho}, \bar{\eta})$ plane with recent experimental measurements, obtained by the CKMfitter group [17]. ε_K in the figure means the measurement on $|\epsilon|$.

1.4 $K_L^0 \to \pi^0\nu\bar{\nu}$ decay in the SM

In this section, we discuss the relation between the $K_L^0 \to \pi^0\nu\bar{\nu}$ decay and CP violation, and the benefit in studying this decay mode.

Due to the small value of ϵ, the amplitude of the $K_L^0 \to \pi^0\nu\bar{\nu}$ decay is approximated to be the amplitude of the $K_2 \to \pi^0\nu\bar{\nu}$ process. The decay is dominated by the short-distance process and is mediated by the second order diagrams of the electroweak interactions as shown in Fig. 1.2. Because the contribution of the top quark as the intermediate state dominates in Fig. 1.2 [18], the amplitude of $K_2 \to \pi^0\nu\bar{\nu}$ can be expressed as:

$$A(K_2 \to \pi^0\nu\bar{\nu}) \propto V_{td}^* V_{ts} - V_{ts}^* V_{td} \propto 2i\eta. \tag{1.37}$$

Thus, the branching ratio of the $K_L^0 \to \pi^0\nu\bar{\nu}$ decay, $\mathrm{BR}(K_L^0 \to \pi^0\nu\bar{\nu})$, is proportional to η^2. This means that the $K_L^0 \to \pi^0\nu\bar{\nu}$ decay is directly related to the CP violation, and that we can deduce the "height" of the unitary triangle drawn in $(\bar{\rho}, \bar{\eta})$ plane by measuring the $K_L^0 \to \pi^0\nu\bar{\nu}$ decay.

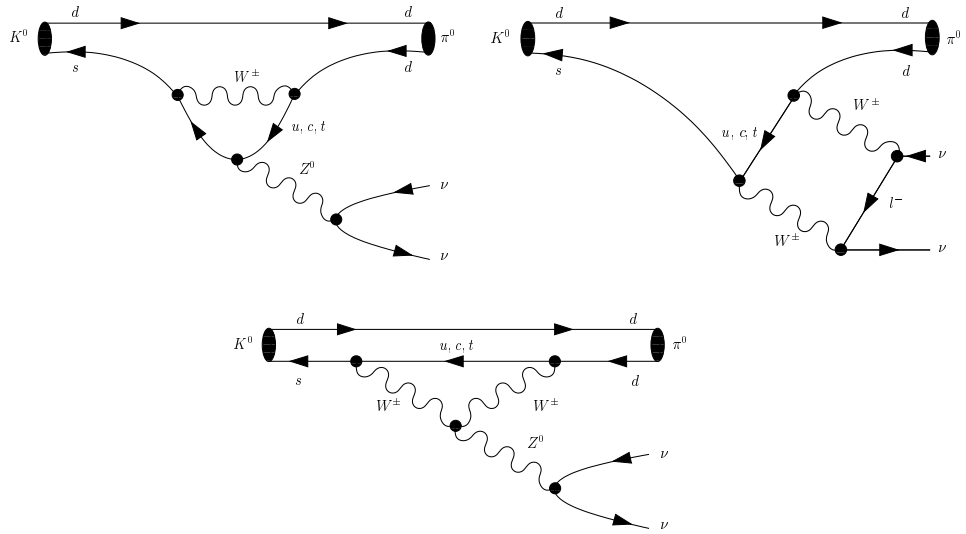

Figure 1.2: Feynman diagrams of the $K_L^0 \to \pi^0 \nu\bar{\nu}$ decay. The decay is mediated by penguin and box diagrams with FCNC, and the top quarks dominates the loop diagram. Figures are quoted from [18].

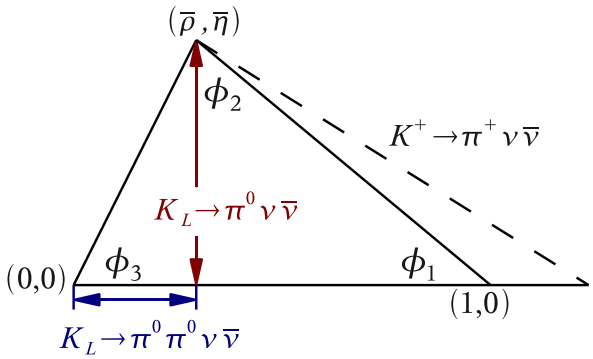

Figure 1.3: Unitary triangle of the CKM matrix, reconstructed by the Kaon decays.

For the $K_L^0 \to \pi^0\nu\bar{\nu}$ decay mode, the effective Hamiltonian of short-distance force can be written as:

$$\mathcal{H}_{eff} = \frac{G_F}{\sqrt{2}} \frac{\alpha}{2\pi \sin\theta_W} \sum_{l=e,\nu,\tau} V_{ts}^* V_{td} X(x_t) (\bar{s}d)_{V-A} (\bar{\nu}_l \nu_l)_{V-A} + h.c., \tag{1.38}$$

where x_t is the ratio of the top mass to the W mass, $x_t = m_t^2/m_W^2$. $X(x_t)$ is the value of the Inami-Lim loop function, expressed as:

$$X(x_t) = \frac{x_t}{8}[-\frac{2+x_t}{1-x_t} + \frac{3x_t - 6}{(1-x_t)^2} \ln x_t]. \tag{1.39}$$

Because the hadronization part can be extracted from the $K^+ \to \pi^0 e^+ \nu_e$ decay with the correction for the isospin-breaking effect, the $\mathrm{BR}(K_L^0 \to \pi^0\nu\bar{\nu})$ is expressed as

$$\mathrm{BR}(K_L \to \pi^0\nu\bar{\nu}) = 6.87 \times 10^{-4} \times \mathrm{BR}(K^+ \to \pi^0 e^+ \nu) \times A^4 \lambda^8 \eta^2 X^2(x_t), \tag{1.40}$$

where $\mathrm{BR}(K^+ \to \pi^0 e^+ \nu_e)$ denotes the branching ratio of the $K^+ \to \pi^0 e^+ \nu_e$ decay.

The most important benefit in studying the $K_L^0 \to \pi^0\nu\bar{\nu}$ decay is that it has small theoretical uncertainties in the estimation of $\mathrm{BR}(K_L^0 \to \pi^0\nu\bar{\nu})$. The reasons for the small theoretical uncertainty is that the contributions from the long distance interaction is negligibly small, and that the hadronic matrix elements are extracted directly from experimental measurements of the $\mathrm{BR}(K^+ \to \pi^0 e^+ \nu_e)$.

Substituting the fitted CKM parameters, as described in Sec. 1.3.3, the branching ratio of the $K_L^0 \to \pi^0\nu\bar{\nu}$ decay is estimated to be [18]

$$\mathrm{BR}(K_L \to \pi^0\nu\bar{\nu}) = (2.49 \pm 0.39) \times 10^{-11}, \tag{1.41}$$

where the uncertainty is dominated by the experimental value of CKM parameters and top mass.

1.5 $K_L^0 \to \pi^0\nu\bar{\nu}$ decay beyond the SM

Owing to the small theoretical uncertainty in the estimation of $\mathrm{BR}(K_L^0 \to \pi^0\nu\bar{\nu})$, the significant excess or deficiency of $\mathrm{BR}(K_L^0 \to \pi^0\nu\bar{\nu})$ directly indicates the existence of a new physics beyond the Standard Model. In this section, first, we introduce the model-independent upper limit calculated by the branching ratio of the closely-related process $K^+ \to \pi^+\nu\bar{\nu}$. Next, we show several possibilities to modify $\mathrm{BR}(K_L^0 \to \pi^0\nu\bar{\nu})$ from viewpoints of new physics model beyond the SM.

1.5.1 Grossman-Nir limit

The rare decay of charged kaon, $K^+ \to \pi^+\nu\bar{\nu}$, is strongly related to the $K_L^0 \to \pi^0\nu\bar{\nu}$ decay. Y. Grossman and Y. Nir pointed out the correlation between the $K_L^0 \to \pi^0\nu\bar{\nu}$ decay and the $K^+ \to \pi^+\nu\bar{\nu}$ decay [19]. The diagram of $K^+ \to \pi^+\nu\bar{\nu}$ process can be obtained simply by replacing the d quark with the u quark in the $K^0 \to \pi^0\nu\bar{\nu}$ diagram. We can derive the correlation between these two modes from the isospin symmetry. A model independent upper limit for the $\mathrm{BR}(K_L^0 \to \pi^0\nu\bar{\nu})$, called the Grossman-Nir limit, can be expressed to be

$$\mathrm{BR}(K_L \to \pi^0\nu\bar{\nu}) < 4.4 \times \mathrm{BR}(K^+ \to \pi^+\nu\bar{\nu}). \tag{1.42}$$

The $K^+ \to \pi^+\nu\bar{\nu}$ decay is experimentally observed by the AGS E787/E949 experiment at the Brookhaven National Laboratory. They set the branching ratio of the $K^+ \to \pi^+\nu\bar{\nu}$ decay, mainly based on two and one observed events in the E787 and E949 experiment, respectively, to be [20]

$$\mathrm{BR}(K^+ \to \pi^+\nu\bar{\nu}) = [14.7^{+13.0}_{-8.9}] \times 10^{-11}. \tag{1.43}$$

By substituting the upper limit calculated by Eq. 1.43 into Eq. 1.42, the upper limit to the $\mathrm{BR}(K_L^0 \to \pi^0\nu\bar{\nu})$ can be obtained as

$$\mathrm{BR}(K_L \to \pi^0\nu\bar{\nu}) < 1.7 \times 10^{-9} \quad (90\%\ \mathrm{C.L.}). \tag{1.44}$$

1.5.2 Several examples of theories beyond the Standard Model

The $K_L^0 \to \pi^0\nu\bar{\nu}$ decay occurs via loop diagrams and directly violates the *CP* symmetry. When there is any contribution from new particles which appear in loop diagrams and/or from a new source of *CP* violation, the branching ratio of the $K_L^0 \to \pi^0\nu\bar{\nu}$ decay may vary. Thus, one can probe a new physics by measuring the deviation of $\mathrm{BR}(K_L^0 \to \pi^0\nu\bar{\nu})$ from the SM prediction.

One of major models of new physics beyond the Standard Model is Minimal Supersymmetric Standard Model (MSSM), which is the minimal extension to the SM, including sypersymmetry (SUSY). Buras *et al.* studied on the allowed region of $\mathrm{BR}(K_L^0 \to \pi^0\nu\bar{\nu})$ and $\mathrm{BR}(K^+ \to \pi^+\nu\bar{\nu})$ in the general MSSM by scanning the allowed range of the SUSY particle parameters [21]. In the general MSSM, it is possible to have new *CP* violation phases; this results in a possibility to have the $\mathrm{BR}(K_L^0 \to \pi^0\nu\bar{\nu})$ to be a few times 10^{-10}, which is about 10 times larger than the SM prediction. Also, the amount of *CP* violation in the $K_L^0 \to \pi^0\nu\bar{\nu}$ decay could be different from that in the indirect *CP* violation, such as K^0 – $\overline{K^0}$ and B^0 – $\overline{B^0}$ mixing. This implies that the unitary triangle of CKM matrix measured by K system ($K_L^0 \to \pi^0\nu\bar{\nu}$ and $K^+ \to \pi^+\nu\bar{\nu}$) and B system ($B \to J/\psi K_S$ and $\Delta m_{B_d}/\Delta m_{B_s}$) could differ, as shown in Fig. 1.4.

In contrast, the Minimal Flavor Violation hypothesis (MFV) is designed that all flavor and *CP*-violating interactions are linked to the known structure of CKM matrix. Thus, deviations of the $\mathrm{BR}(K_L^0 \to \pi^0\nu\bar{\nu})$ from the Standard Model prediction become small ($\sim 20\%$) in MFV models [22, 23]. Other predictions from hypothesis: littlest higgs model with T-parity (LHT) [24, 25], minimal 3-3-1 model [26] and four generations (4-Gen.) [27], are summarized in Fig. 1.5, which is taken from the reference [28], including the results from the general MSSM and the MFV models.

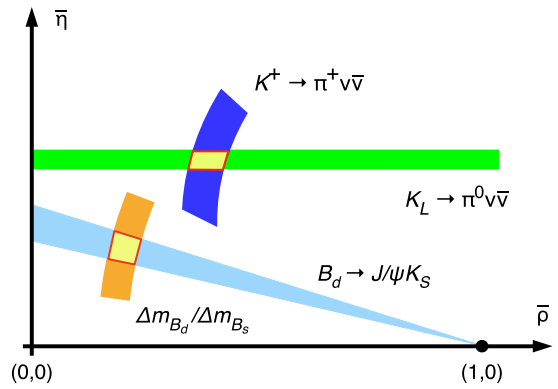

Figure 1.4: Schematic determination of (ρ, η) from the B system ($B_d \to J/\psi K_S$ and $\Delta m_{B_d}/\Delta m_{B_s}$) and from $K \to \pi\nu\bar{\nu}$.

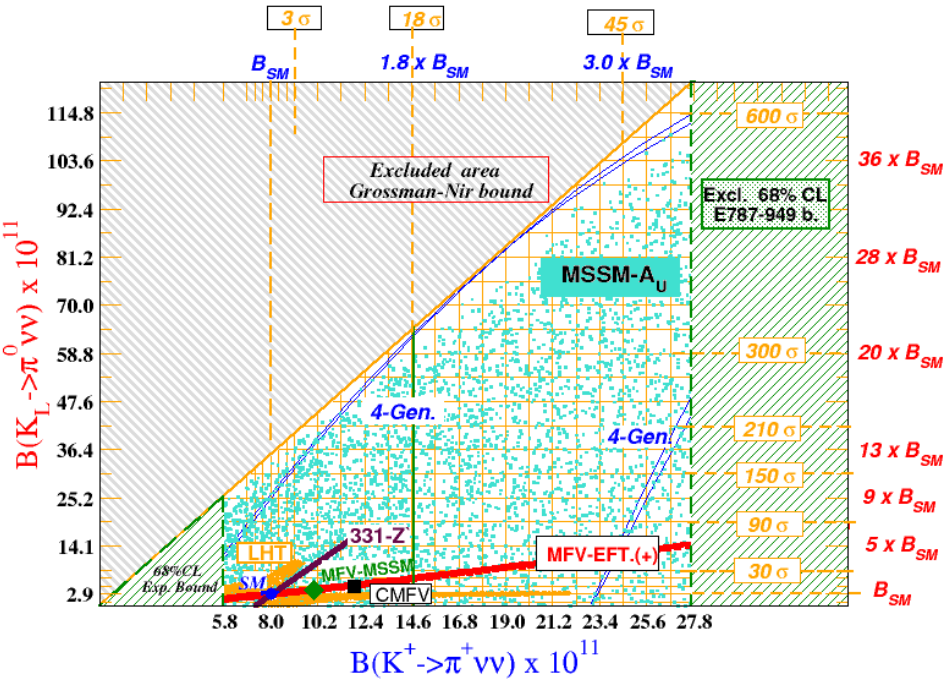

Figure 1.5: The correlation between $\mathrm{BR}(K_L^0 \to \pi^0\nu\bar{\nu})$ and $\mathrm{BR}(K^+ \to \pi^+\nu\bar{\nu})$ by showing the allowed region with various new physics models. The figure was quoted from the reference [28].

1.6 History of $K_L^0 \to \pi^0\nu\bar{\nu}$ search

In the experimental view of the $K_L^0 \to \pi^0\nu\bar{\nu}$ decay, there have been made five searches to the decay mode by increasing the sensitivity. Due to the quite small value of $\mathrm{BR}(K_L^0 \to \pi^0\nu\bar{\nu})$, only upper limits to the decay have been given. Figure 1.6 shows the history of the experimental upper limits to the $K_L^0 \to \pi^0\nu\bar{\nu}$ decay.

The first search was performed by Littenberg [29] in 1989 by extracting a limit from the data of Cronin *et al.* for the $K_L^0 \to \pi^0\pi^0$ decay [5]. The limit given by Littenberg was followed by several experimental searches. In these searches, two approaches were tried to identify the π^0 in the final state; one is to use the $\pi^0 \to e^+e^-\gamma$ decay and the other is to use the $\pi^0 \to \gamma\gamma$ decay. The merit to use the $\pi^0 \to e^+e^-\gamma$ decay is that π^0 decay vertex can be reconstructed with two tracks of e^+ and e^-. Thus, the invariant mass of $e^+e^-\gamma$ can be reconstructed and one can require it to be m_{π^0}, which provides a strong kinematic constraint. On the other hand, the small branching ratio of the $\pi^0 \to e^+e^-\gamma$ decay ($\sim 1\%$) causes small acceptance to the signal mode. The advantage and disadvantage of using the $\pi^0 \to \gamma\gamma$ decay is opposite to the $\pi^0 \to e^+e^-\gamma$ case: larger acceptance due to larger branching ratio of $\pi^0 \to \gamma\gamma$ ($\sim 99\%$), and weaker kinematical constraints.

In the KTeV experiment, both two approaches were tried. By using the $\pi^0 \to \gamma\gamma$ decay, an upper limit on the branching ratio was set to be [30]

$$\mathrm{BR}(K_L^0 \to \pi^0\nu\bar{\nu}) < 1.6 \times 10^{-6} \ \text{(at 90\% C.L.)}, \tag{1.45}$$

based on a special run taken in one day. In this search, one event was observed in the signal region with the estimated number of background of 3.5 ± 0.9 events. The best limit to the $K_L^0 \to \pi^0\nu\bar{\nu}$ decay before our experiment was given by using the $\pi^0 \to e^+e^-\gamma$ decay. An upper limit was set to be [31]

$$\mathrm{BR}(K_L^0 \to \pi^0\nu\bar{\nu}) < 5.9 \times 10^{-7} \ \ (\text{at } 90\% \text{ C.L.}), \tag{1.46}$$

based on the data taken for 46 days. In these searches, the dominant background source was hyperon decays such as $\Lambda \to n\pi^0$ and $\Xi \to \Lambda\pi^0$.

In order to improve the sensitivity to the $K_L^0 \to \pi^0\nu\bar{\nu}$ decay, we carried out the E391a experiment at the 12 GeV proton synchrotron in High Energy Accelerator Research Organization (KEK) [32]. The E391a experiment performed three periods of physics data taking as Run-1, Run-2, and Run-3. As a first result of the $K_L^0 \to \pi^0\nu\bar{\nu}$ search, an upper limit was obtained by analyzing part of Run-1 data (taken in one week) as [33, 34]

$$\mathrm{BR}(K_L^0 \to \pi^0\nu\bar{\nu}) < 2.1 \times 10^{-7} \ \ (\text{at } 90\% \text{ C.L.}). \tag{1.47}$$

The sensitivity was limited by background from neutron interactions caused by a material which was unexpectedly drooped in the beam. The problem was fixed during an intermission between Run-1 and Run-2. The analysis on the Run-2 full data gave an upper limit to the $\mathrm{BR}(K_L^0 \to \pi^0\nu\bar{\nu})$ as [35, 36]:

$$\mathrm{BR}(K_L^0 \to \pi^0\nu\bar{\nu}) < 6.7 \times 10^{-8} \ \ (\text{at } 90\% \text{ C.L.}). \tag{1.48}$$

In this thesis, we show the final result of the E391a by using the full data sample of Run-2 and Run-3, with improvements on the analysis to increase the signal acceptance.

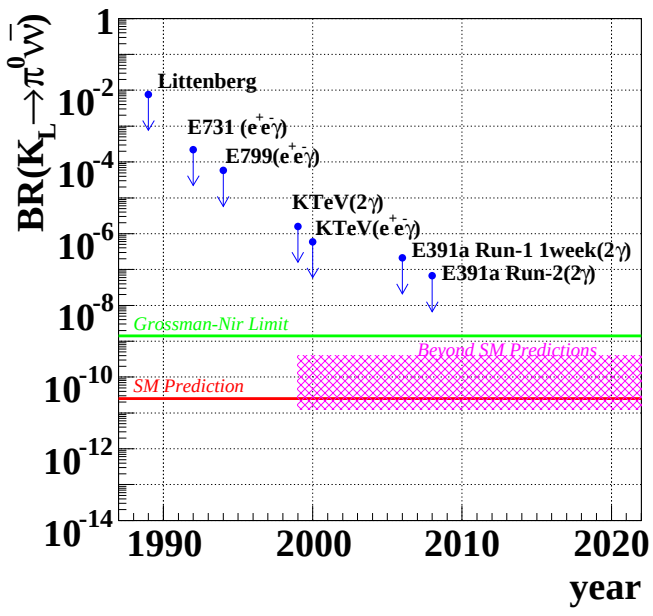

Figure 1.6: History of $K_L^0 \to \pi^0\nu\bar{\nu}$ search.

1.7 Outline of the thesis

Here we overview the composition of this paper. In this chapter, we have discussed the importance of the measurement of the $K_L^0 \to \pi^0\nu\bar{\nu}$ decay, by introducing the theoretical backgrounds

and the current status of experimental searches. In the next chapter, Chap. 2, we present the experimental concept to search for the $K_L^0 \to \pi^0\nu\bar{\nu}$ decay in the E391a experiment. The actual apparatus of the E391a experiment is described in Chap. 3, including the explanations on the data taking.

In the Chap. 4, we give a broad overview of the analysis to be described in this thesis. The event reconstruction, including the photon and π^0 reconstruction, will be introduced in Chap. 5. Chap. 6 describes the Monte Carlo simulation, which was used to estimate the sensitivity to the signal mode and the number of background events. Since these values were estimated by using the simulation, the reproducibility of the simulation will be also discussed. We describe the event selections to the $K_L^0 \to \pi^0\nu\bar{\nu}$ mode in Chap. 7, with descriptions on their optimization. Chap. 8 shows the estimation of the background events, and Chap. 9 describes the number of collected K_L^0 decays. The final result of the analysis is presented in Chap. 10. The estimations of systematic uncertainties are summarized in Chap. 11. Finally, we conclude the results of this paper in Chap. 12, and the prospects of this research are discussed as well.

Chapter 2

Experimental Method

Brief summary

In this chapter, we introduce the basic concept of the E391a experiment to search for the $K_L^0 \to \pi^0\nu\bar{\nu}$ decay. In this experiment, the signature of the $K_L^0 \to \pi^0\nu\bar{\nu}$ decay is determined by detecting two photons and nothing else, because there are only one π^0 as a visible particle in the final state of $K_L^0 \to \pi^0\nu\bar{\nu}$ and π^0 is dominantly decays into two photons. To determine the condition of "two photons and nothing else", the decay region was surrounded by the hermetic veto detector system which covered all solid angle. We also used a narrow shaped beam, called "pencil beam", to obtain the kinematic information of the decay. The sharply shaped beam had a benefit to prevent the beam neutrons from interacting with detector materials and generating sole π^0, which could fake a signal. Also, the decay region was evacuated at ultra-high vacuum with differential pumping method in order to suppress neutron interactions with residual gas. Following sections describe the overview of the experimental principle of E391a and make some detailed explanation on each feature.

2.1 Signature of the $K_L^0 \to \pi^0\nu\bar{\nu}$ decay

The ultimate goal of the $K_L^0 \to \pi^0\nu\bar{\nu}$ search is to measure $\mathrm{BR}(K_L^0 \to \pi^0\nu\bar{\nu})$ with better sensitivity than the Standard Model prediction. In the previous experiment, this decay was searched as a by-product of other physics themes and the upper limit of the decay was set as $\mathrm{BR}(K_L^0 \to \pi^0\nu\bar{\nu}) < 5.9 \times 10^{-7}$ at 90% confidence level. Since there remains four orders of magnitude difference between the previous experimental limit and the SM prediction, we decided to take a step-by-step approach, in which we make several experiments with gradually improving the sensitivity. The E391a is the first dedicated experiment in the world to search for the $K_L^0 \to \pi^0\nu\bar{\nu}$ decay, and designed as the first step of the step-by-step approach. The purpose of the experiment is to confirm the experimental concept for measuring the $K_L^0 \to \pi^0\nu\bar{\nu}$ decay, including estimation for the sensitivity, backgrounds, and systematic uncertainties.

The E391a experiment utilized the 12 GeV proton synchrotron in KEK (KEK-PS) to produce K_L^0's. Primary protons from the KEK-PS struck on the target and secondary emitted K_L^0's were transported through a neutral beamline to a decay region. Since two neutrinos are virtually undetectable, the final state of the $K_L^0 \to \pi^0\nu\bar{\nu}$ decay only contains one π^0 as a visible particle. This nature makes it difficult to identify this decay mode experimentally. In the E391a experiment, the $K_L^0 \to \pi^0\nu\bar{\nu}$ decay is identified by detecting two photons decayed from π^0 and

no other particles. Previous search was made by detecting $\pi^0 \to e^+e^-\gamma$ instead of $\pi^0 \to \gamma\gamma$. The benefit of using $\pi^0 \to \gamma\gamma$ is in its larger branching ratio, which is roughly 80 times larger than that of $\pi^0 \to e^+e^-\gamma$. We can achieve higher sensitivity with the same amount of K_L^0's, in exchange for direct vertex measurement.

It is also difficult to obtain the information of parent K_L^0. Thus, the measurement can only be made of the energy and position of the two photons in a calorimeter located downstream of the K_L^0 decay region, and there is no direct information of the incident particle. Kinematic constraints are weak for definitive identification of the decay. Our identification method is to extract signal candidates by eliminating all possible backgrounds.

2.2 Background sources

Because the key concept of E391a is to eliminate all backgrounds, we need to understand the possible background sources and their mechanism to become backgrounds. In the E391a experiment, backgrounds mainly come from other K_L^0 decay modes and interactions of beam neutrons.

K_L^0-decay-originated backgrounds are the events from other K_L^0 decays such as $K_L^0 \to \pi^0\pi^0$ or $K_L^0 \to \pi^+\pi^-\pi^0$. These decay modes can become backgrounds when we failed to detect extra particles. Thus, identification of extra particles is important in order to eliminate these backgrounds. For neutral decay modes like $K_L^0 \to \pi^0\pi^0\pi^0$ and $K_L^0 \to \pi^0\pi^0$, photon detection efficiency takes an important role to reduce backgrounds, and for charged decay modes like $K_L^0 \to \pi^+\pi^-\pi^0$ and $K_L^0 \to \pi^\pm l^\mp \nu$ ($l = e, \mu$), detection efficiency of charged particles takes an important role.

Beam-neutron-induced backgrounds are made by the interactions of neutrons contained in the beam and in the region surrounding the beam (beam halo). For the background originated by the neutrons in the beam (core neutrons), it is important to reduce the material inside the beam region. For the background originated by the neutrons in the beam halo (halo neutrons), it is needed to detect secondary particles emitted in the interactions, as well as to have a sharply shaped beam.

Hyperons produced at the target can also cause backgrounds through processes such as $\Lambda \to n\pi^0$; these hyperon events are strongly suppressed in the present experiment because most of them decay away in our 10 m long neutral beamline.

2.3 Features of the E391a experiment

To reduce the backgrounds mentioned in the last section, E391a had several features. In this section, we introduce the key components in the E391a experiment.

2.3.1 Hermetic high-sensitivity veto system

The most important tool to reduce backgrounds is detection of extra particles. In all K_L^0 decay modes other than $K_L^0 \to \pi^0\nu\bar{\nu}$, except for $K_L^0 \to \gamma\gamma$, two photons are accompanied with at least two additional photons or charged particles. Thus, we can strongly suppress the backgrounds from K_L^0 decays by surely detecting extra particles with high sensitivity. To obtain this rejection, the decay volume was surrounded by highly sensitive veto detectors, as shown in Fig 2.1. For hermeticity, we even covered the beam region, where the neutral beam passed through.

Inefficiencies of photon and charged particle detection cause backgrounds. The decay $K_L^0 \to \pi^0\pi^0$ is the most serious background source because it has only two extra photons in the final

state. The inefficiency of photon detection was investigated in a series of experiments [37], which showed that the inefficiency monotonically decreased with the incident photon energy. It was also found that photon detection with a very low energy threshold is necessary to achieve a small overall inefficiency, even for high-energy photons. If an extremely low energy threshold around 1 MeV could be set, the backgrounds from other K_L^0 decays were reduced to a negligible level within the sensitivity of the experiment.

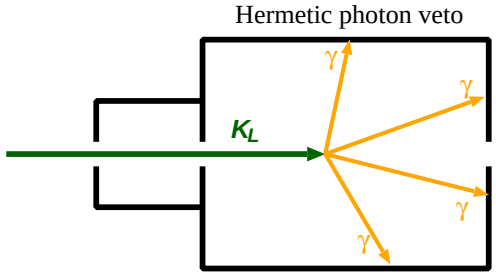

Figure 2.1: Concept of hermetic veto detector system in E391a.

2.3.2 Pencil beamline

We introduced a small-diameter K_L^0 beam (called "pencil beam") in our experiment. Although the K_L^0 flux is reduced, the pencil beam has several advantages. First, the beam hole at the center of the calorimeter, which degrades hermeticity, can be minimized. This helped to suppress the backgrounds caused by the geometrical inefficiency of veto detectors. Second, the K_L^0 decay vertex position ($Z_{\rm VTX}$) can be reconstructed with an assumption that the vertex is on the beam axis, as follows.

Figure 2.2 shows the concept of the π^0 reconstruction in the E391a experiment. The energies and positions of two photons were measured with the CsI calorimeter, which was located at the downstream end of the decay region. With assumption of the invariant mass of two photons to be π^0 mass, the opening angle of two photons (θ) can be calculated by following equation:

$$M_{\pi^0}^2 = 2E_1E_2(1-\cos\theta), \tag{2.1}$$

where M_{π^0} is the π^0 mass, and E_1 and E_2 are the energies of photons. The angle θ can be written with the positions of two photons, which were observables, and the decay vertex. The pencil beam enabled us to assume the decay vertex was on the beam axis, and thus, Eq. 2.1 can be reduced to quadric equation of $Z_{\rm VTX}$. Equation 2.1 has two solutions, each corresponding to the front and back side of the CsI, and the fake solution in the back side of the CsI calorimeter (called "ghost") was discarded. After the vertex position of the K_L^0 decay was determined, we calculated the momentum of π^0 by summing the momentum-vectors of two photons. We also defined transverse component of the π^0 momentum to the beam axis (P_T). The detailed description on the π^0 reconstruction can be found in Sec. 5.2.

The signal region for $K_L^0 \to \pi^0\nu\bar{\nu}$ decay can be defined in the plane of $Z_{\rm VTX}$ and P_T, as also shown in Fig. 2.2. Requiring a sufficiently large missing transverse momentum eliminates contamination from the $K_L^0 \to \gamma\gamma$ decay and also reduces the contamination of other K_L^0 decays. Most of the K_L^0's decay into multiple particles, a π^0 has low momenta in the K_L^0 rest frame, and hence low P_T in the laboratory frame, as shown in Fig. 2.3. The $Z_{\rm VTX}$ should be in the region away from detectors and P_T should be in the range from 120 to 240 MeV/c, where the maximum momentum of π^0's in the K_L^0-rest frame is 231 MeV/c for $K_L^0 \to \pi^0\nu\bar{\nu}$.

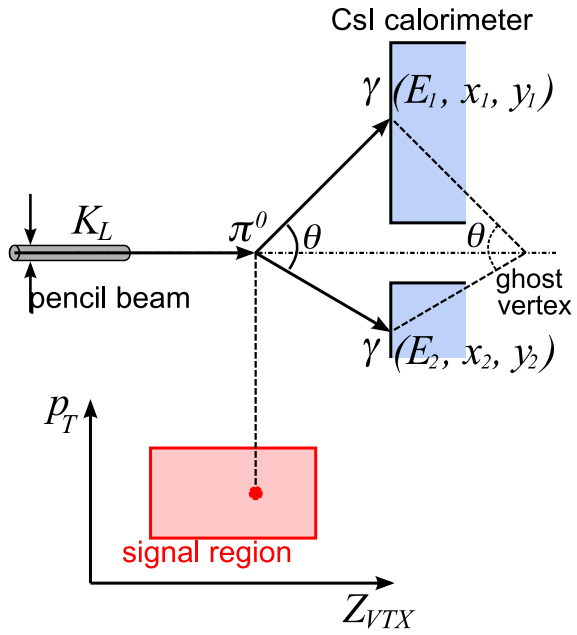

Figure 2.2: Concept of π^0 reconstruction in E391a. Top figure illustrates the geometry of π^0 decay and the reconstruction of π^0. Bottom figure shows the signal region defined in $Z_{\rm VTX}$-$P_T$plane.

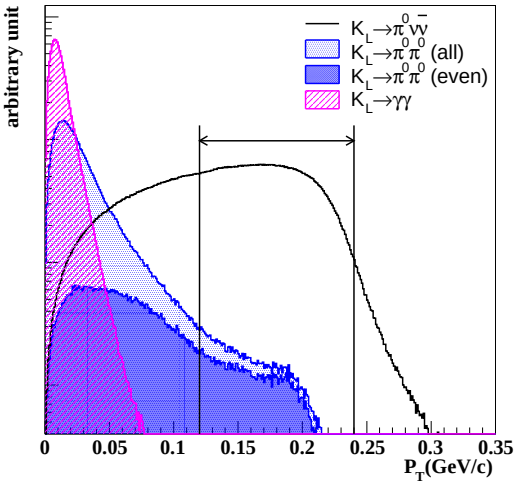

Figure 2.3: Reconstructed P_T distributions of two photon system for the signal mode and the $K_L^0 \to \pi^0\pi^0$ and $K_L^0 \to \gamma\gamma$ background modes obtained by a Monte Carlo simulation. In $K_L^0 \to \pi^0\pi^0$ decays, "even" events means that both of the photons come from the same π^0. The signal region is set as a region between two vertical lines in this experiment.

2.3.3 Methods to reduce the neutron interactions

To reduce the backgrounds caused by the interactions of neutrons, we implemented two features in the E391a. First, to reduce the interaction between the halo neutrons and the detectors located near the beam, the edge of the neutral beam was sharply shaped by a collimator system. Secondly, to reduce the interaction between the core neutrons and the residual gas in the decay region, the decay region was evacuated at a high vacuum of 10^{-4} Pa. To achieve this high vacuum, we developed a differential evacuation system, where the vacuum region was divided into high vacuum region and low vacuum region and the two regions were pumped differentially. Details of these features will be described in Chap. 3.

Chapter 3

Experimental Apparatus and Runs

Brief summary

In this chapter, we describe the experiment apparatus of the E391a experiment to realize the key concepts described in the last chapter.

K_L^0 were generated by striking the primary protons from KEK-PS on a target rod, and were transported through a neutral beamline. The beamline was designed to have a small aperture in order to realize the "pencil beam". In addition, the beamline was designed not to have remaining flux outside the beam. It helped to reduce the backgrounds caused by the interactions between halo neutrons and the detectors near the beam.

Photons produced by the K_L^0 decays were detected by a calorimeter located at the downstream end of the decay volume. The decay volume was surrounded by a hermetic veto detector system, consisting of both photon and charged particle veto detectors.

To reduce the backgrounds from the interaction between the beam neutrons and residual gas, the decay volume was evacuated at the pressure of 10^{-5} Pa by utilizing the differential pumping method.

The data were processed by ADC, TDC, and MTDC, and recorded via VME, TKO, and CAMAC systems. We prepared several triggers for physics data, calibrations, and so on. In addition to the physics runs, we also carried out the special runs to study properties of background events. Details of each components will be described in the following sections.

3.1 Beamline

The E391a experiment was performed in the East Counter Hall (ECH) of KEK 12 GeV Proton Synchrotron (KEK-PS). Figure 3.1 shows the layout of ECH. Neutral long-lived kaons produced in a target entered the experimental area through the neutral beamline.

3.1.1 Primary proton beamline and K_L^0 production target

At KEK-PS, the primary protons were accelerated up to the kinetic energy of 12 GeV, and extracted to the East Counter Hall (ECH) through EP2-C beamline. Extractions of the protons were made by the slow extraction mode, having 2 second duration every 4 second repetition cycle. The extraction duration is usually called as "spill". The intensity of the primary beam was monitored by a secondary emission chamber (SEC) and the typical value was 2.5×10^{12}

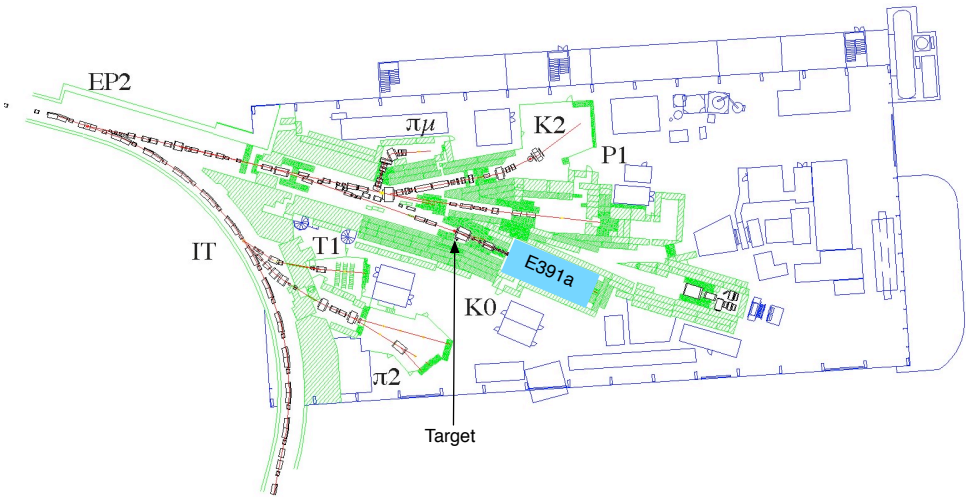

Figure 3.1: Layout of the East Counter Hall at KEK. K_L^0's are produced at the target and extracted to the K0 beamline. The arc in the left-hand side is a part of the PS. The E391a experimental area is the blue shaded region.

protons on target (POT) per a spill. The size of the beam at the target was $\sigma_X = 3.3$ mm and $\sigma_Y = 1.1$ mm along the X (horizontal) and Y (vertical) axes, respectively.

The K_L^0 production target was made of platinum (Pt) with a cylindrical shape of 60 mm in length and 8 mm in diameter. The length of the target corresponded to 0.68 interaction length (λ_I) and 20 radiation length (X_0). The neutral beamline was extended to 4-degree direction with respect to the primary proton beam. The target rod was aligned with the direction of the neutral beamline. It minimized the target image viewed from the detector system. The amount of secondary particles produced at the target was monitored by a counter telescope (TMON), which was directed toward the target center at 90°.

3.1.2 Neutral beamline

Concept

The neutral beamline of E391a was designed to create a narrow shaped beam ("pencil beam"). There were two reasons to utilize the pencil beam. The first one was to obtain a kinematic constraint for selecting the $K_L^0 \to \pi^0\nu\bar{\nu}$ decay. Since the decay position and transverse momentum of π^0's were reconstructed by assuming the decay vertex to be on the beam axis, the larger dispersion of the beam would worsen the transverse momentum resolution. The second reason was to reduce the inefficiency in detection of extra particles. It is difficult to detect extra photons or charged particles escaping inside the beam, because the beam caused many activities in the detector. Using the pencil beam, we could reduce the solid angle of the beam hole viewed from the decay volume, and reduce the inefficiencies.

In addition to the "pencil beam" feature, the neutral beamline was designed to suppress remaining flux in the beam halo. The neutrons in the beam halo interacts with the detectors near the beam and can produce π^0, which may become backgrounds. Reduction of the halo-neutron flux contributes to background suppression.

Beamline components

The neutral beamline consisted of the complex of two dipole magnets, collimator systems, and two absorbers, as shown in Fig. 3.2. Two dipole magnets (D1, D2) were located to sweep charged particles out of the beam. The field strengths of the magnets were 4 T·m and 3 T·m for D1 and D2, respectively.

The collimator system were consisted of six collimators (C1-C6) to shape the "pencil beam" and to reduce the flux in the halo region. Five collimators (C1-C3, C5, and C6) were made of tungsten. The C2 and C3 collimators were used to define the beam with the designed apertures. They were arranged to form the aperture with a half cone angle of 2 mrad from the target center. The last two collimators, C5 and C6, were used to trim the beam halo. The most upstream collimator C1 reduced the size of the beam immediately after the target without producing a large penumbra. The total thickness of these five collimators was approximately 6 m. A thermal-neutron absorber, which was made of polyethylene terephthalate (PET) sheets containing Gd_2O_3 40% in weight, was used for C4. The aperture of C4 was set to be larger than that of the other collimators. The distance from the target to the exit of the last collimator was 10 m, which was long enough to reduce hyperon decays, such as $\Lambda \to n\pi^0$, and the total thickness of the collimators corresponded to $47\lambda_I$, where λ_I denotes the interaction length.

Movable absorbers, made of lead (Pb) and beryllium (Be), were placed inside the beam between C1 and C2 to reduce the number of photons and neutrons relative to the K_L^0's. The absorbers were 10-mm-diameter rods with the lengths of 5 cm and 30 cm for Pb and Be, respectively. The downstream region, starting with a window of 100-μm-thick stainless steel at the upstream end of C4, was evacuated to approximately 1 Pa.

Profiles of the neutral beamline

The profiles of the neutral beam was studied by a Monte Carlo simulation and confirmed by a beam survey experiment, which was held before starting the E391a experiment. The peak momentum of the K_L^0 as determined from the beamline simulations was 2 GeV/c at the exit of C6, as shown in Fig. 3.3. The initial transverse momentum spread due to the beam divergence of 2 mrad was approximately 4 MeV/c. The neutron-to-K_L^0 ratio was 60 and the halo-to-core ratio was approximately 10^{-5} for both neutrons and photons with energies above 1 MeV, as shown in Fig. 3.4. By inserting the Be absorber, the neutron-to-K_L^0 ratio was reduced to 40, with roughly a 45% loss in K_L^0 flux. Profiles of the K_L^0 beam are shown in Fig. 3.5. Details of the beamline has been reported elsewhere [38, 39].

During the experiment, the position and divergence of the neutral beam was monitored by measuring the $K_L^0 \to \pi^0\pi^0\pi^0$ decay. Since the $K_L^0 \to \pi^0\pi^0\pi^0$ decay mostly produces six photons, we used the center of energy of six-photon events in the calorimeter. The center of energy was defined to be $\boldsymbol{r}_c = \sum E_i \, \boldsymbol{r}_i$, where E_i are the photon energies and $\boldsymbol{r}_i$ are the photon hit positions at the CsI calorimeter. The central position of the neutral beam in the decay region was adjusted to be within 0.2 mm during the runs. The diameter of the beam at the CsI calorimeter was $\sigma = 40$ mm, which was consistent with the beam divergence.

Punch-through muons were emitted in the direction parallel to the beam axis. Their position distribution was almost flat and the flux density was larger than the cosmic ray flux by roughly one order of magnitude. These muons were used to calibrate several detectors located along the beam axis, as described in a later section.

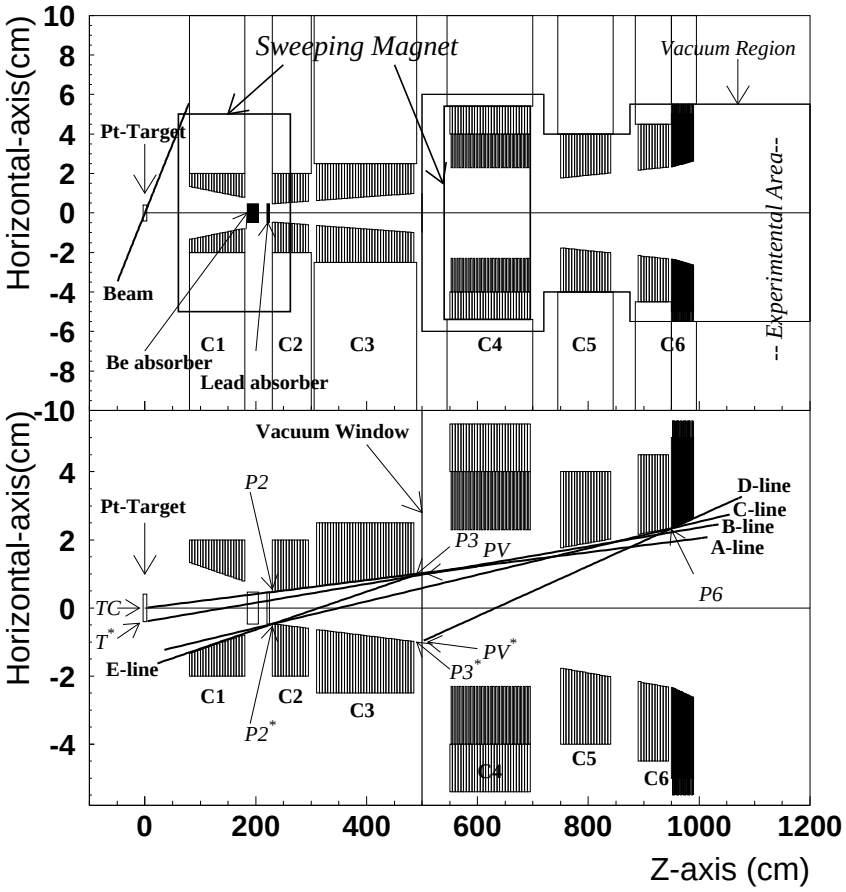

Figure 3.2: Schematic view of the neutral beamline: (top) the arrangements of the components and (bottom) the collimation scheme. C1-C3, C5, and C6 were tungsten collimators, assembled as a stack of cylindrical blocks 5-cm thick with circular holes of different diameters. Each collimator approximated the cone-shaped aperture as indicated by the A-E lines in the bottom figure. The $Z = 0$ coordinate is at the center of the production target.

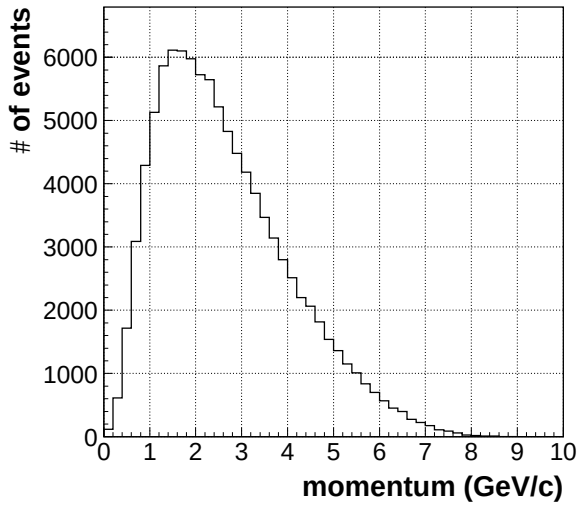

Figure 3.3: Momentum spectrum of K_L^0 at the exit of C6, obtained from beamline simulations.

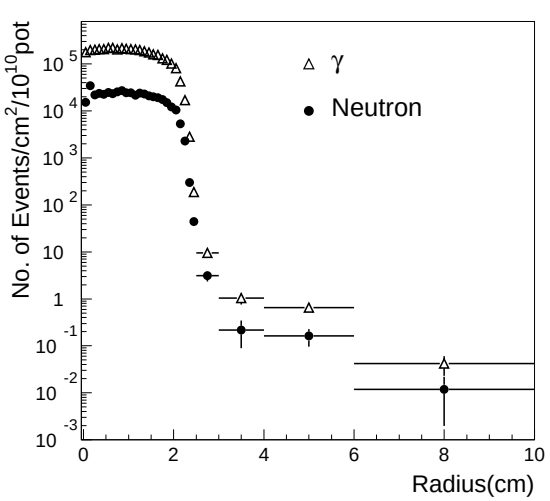

Figure 3.4: Beam profiles of neutrons and photons above 1 MeV at the exit of C6 collimator, obtained from beamline simulations.

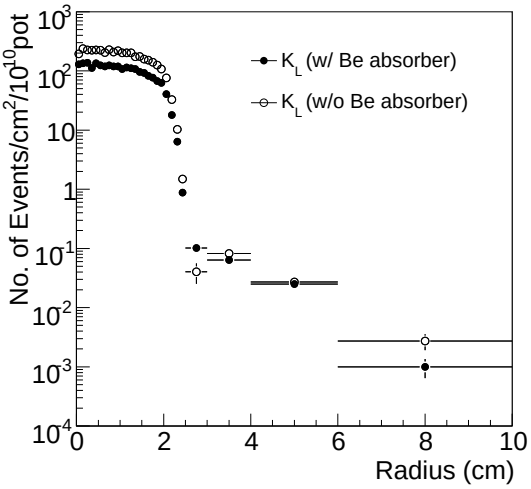

Figure 3.5: Beam profile of K_L^0 at the exit of C6 collimator, obtained from beamline simulations. Filled and open circles show the case with and without the Be absorber, respectively.

3.2 Detectors

3.2.1 Overview

The E391a detection system was located at the end of the beamline. The detector subsystems were cylindrically arranged around the beam axis, and most of them were placed inside a large vacuum vessel, as shown in Fig. 3.6. From here on, the origin of the coordinate system is defined to be at the upstream end of the E391a detector, as shown in Fig. 3.6. This position was approximately 12 m from the production target.

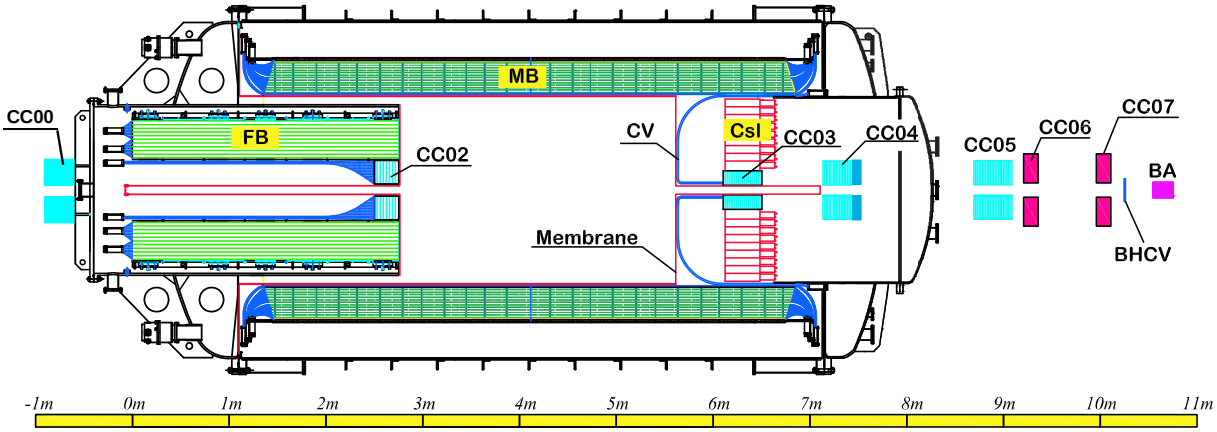

Figure 3.6: E391a detection system.

3.2.2 CsI calorimeter

The energy and hit position of the two photons were measured by using a electromagnetic calorimeter placed at the downstream end of the decay region. The calorimeter was made of 576 undoped CsI crystals and assembled in a support cylinder with an inner diameter of 1.9 m, as shown in Fig. 3.7. A collar counter (CC03) was installed inside of the calorimter with 12 cm $\times$ 12 cm hole, which is described later. The CsI calorimeter was placed at $z = 614.8$ cm. Most of the crystals had a square shape, with the exception of crystals located at the outer edge. In order to fill the gap at the periphery of the cylinder between the square-shaped crystals and the support structure, specially shaped CsI crystals (Edge CsI) and lead-scintillator sandwich counter (Sandwich module) were placed at the outer edge of main CsI crystals.

CsI crystals

Two different sizes of crystals were used in the array: 496 crystals, called "Main CsI", had a dimension of 7 cm $\times$ 7 cm $\times$ 30 cm ($= 16X_0$) and 24 crystals, called "KTeV CsI"[1], had a dimension of 5 cm $\times$ 5 cm $\times$ 50 cm ($= 27X_0$).

Each Main CsI crystal was wrapped with a 100 μm thick Teflon sheet and then wrapped with a 20 μm thick Aluminized mylar, in order to isolate each crystal optically and to improve the light collection. The Main CsI crystal yielded typically 15 photoelectrons per an enrgy deposition of

[1] borrowed from the KTeV experiment.

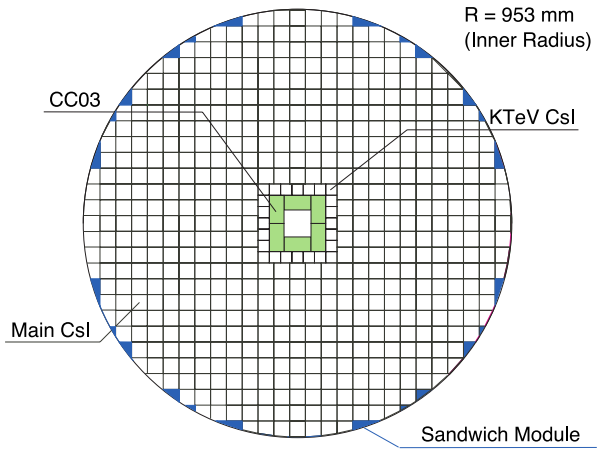

Figure 3.7: Assembly of detector subsystems in the downstream end-cap.

1 MeV. The scintillation light produced by the electromagnetic showers in the CsI crystals was detected by a photo-multiplier tubes (PMT) mounted on the back of each crystal. Figure 3.8 shows schematic drawings of CsI modules. Each crystal was viewed by a 2 inch Hamamatsu R4275-02 PMT through a 3 mm thick silicone cookie and a UV transmitting filter that reduces the slow component of the scintillation light from the CsI crystal. Since these modules were operated in vacuum, the PMT's voltage divider was modified to reduce power dissipation and heat conduction from the divider to the PMT. It was achieved by decreasing the divider current and taking a larger gap between the PMT and the divider circuit board, as shown in Fig. 3.8. In addition, the divider was filled with a 5 mm thick heat conductive glue (METACAST 5448), and was connected to a cooling water pipe.

Each KTeV CsI was wrapped with a 13 μm thick Aluminized mylar. The KTeV CsI yielded typically 25 photoelectrons per MeV. Each KTeV CsI was viewed by a 1.5 inch Hamamatsu R580-UV PMT through a 5 mm thick silicone cookie and a UV transmitting filter, as shown in Fig. 3.8. The voltage divider with the same design as that for the Main CsI crystal was used for KTeV CsI crystals. The divider was filled with a heat conductive glue (EN11) and was connected to a cooling water pipe.

56 crystals used at the outer edge of the array had 7 types of trapezoidal shapes to fit the calorimeter inside the support structure, as shown in Fig. 3.9. Their length was 30 cm, and the optical treatment and their light yields were almost the same as the Main CsI. $1\frac{1}{8}$ inch Photonis XP2978 PMTs were used for smaller 32 crystals and 2 inch Hamamatsu R4275-02 PMTs were used for the others. These PMTs were directly attached to the crystals.

Sandwich module

In order to fill gaps between the CsI crystals and the support structure, we used 24 lead-scintillator sampling counters (Sandwich module). The Sandwich modules consisted of alternating layers of 1 mm thick lead and 5 mm thick plastic-scintillator plates. As shown in Fig. 3.10, there were three types: type-A, type-B, and type-C, according to the number of layers. The scintillation light by the electromagnetic shower in the Sandwich module was absorbed by wavelength-shifting (WLS) fibers. The WLS fibers we used were KURARAY Y-11 with 1 mm in diameter and multi-clad structure. They were glued to grooves on the surface of the scintillator plate. The light from the WLS fibers was detected by a $1\frac{1}{8}$ inch Hamamatsu H1398 PMT. The opposite end of the fiber was polished and coated with aluminum. Typical

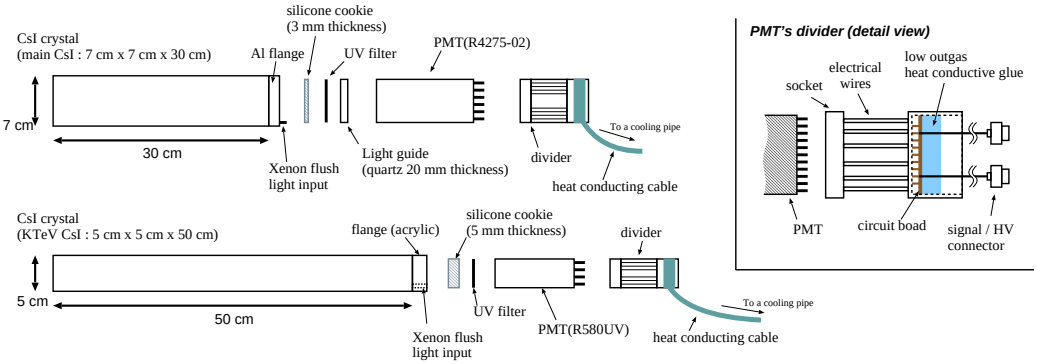

Figure 3.8: Schematic drawing of the CsI module. Figures in upper-left and lower-left explain the components of Main and KTeV CsI module, respectively.

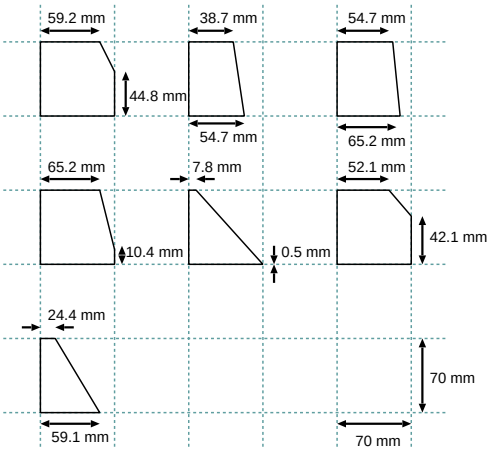

Figure 3.9: Cross-sectional shapes of Edge CsI.

light yield was 10–20 photoelectrons per 1 MeV energy deposition.

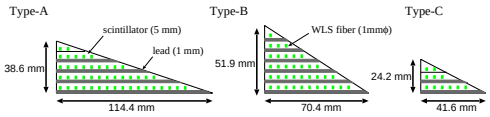

Figure 3.10: Cross-sectional drawings of the Sandwich module.

Xenon gain monitoring system

Figure 3.11 shows a schematic view of the calibration system to monitor the stability of the PMT gain. A Xenon lamp flashing at 1.1 Hz was located in the temperature-controlled box. The light from the Xenon lamp was distributed into each PMT through a clear fibers. There were seven PMTs in the same box. One of them was used for triggering, and three of them were used to monitor the light yield of the Xenon lamp itself by directly connecting clear fibers from the lamp to the PMTs. The remaining three were used to monitor the light yields after the distribution to each CsI module. We checked the stability of each PMT with a stable light source attached on the front surface of each PMT.

Figure 3.12 shows the average gain of a CsI PMT as a function of operation days. The fluctuation of the gain was found to be within about ±3%.

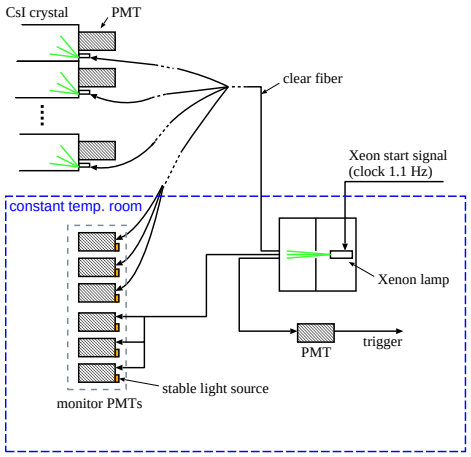

Figure 3.11: Schematic view of the Xenon gain monitoring system.

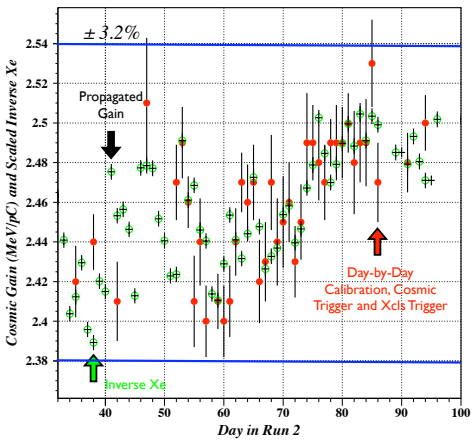

Figure 3.12: Gain stability of CsI's PMT as a function of the operation days. Red dots show the gain factor calibrated by the cosmic-ray data. Green open circles show the gain factor corrected by the Xe system.

Performance of the electromagnetic calorimeter

Prior to the E391a experiment, we evaluated the energy resolution of the calorimeter. A part of the E391a calorimeter, a 5×5 array of Normal CsI crystals, were tested by using a positron beam in the energy range from 0.5 to 3 GeV. Figure 3.13 shows the result of the energy resolution as a function of the incident energy E by the measurement. We obtained the energy resolution:

$$\frac{\sigma_E}{E(\mathrm{GeV})} \sim \frac{1\%}{\sqrt{E(\mathrm{GeV})}} \oplus 1\%, \tag{3.1}$$

where $\oplus$ denotes addition in quadrature.

We continually monitored and calibrated the energy scale factor during the operation by using cosmic ray muons and minimum ionization particles from the beam during the operation [40, 41].

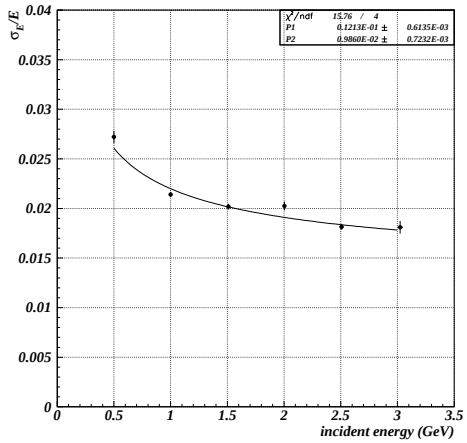

Figure 3.13: Energy resolution as a function of the incident energy, as measured with a positron beam with 5×5 Normal CsI crystals. The curve in the plot is represented as $\sigma_E/E = P1/\sqrt{E} + P2$.

3.2.3 Charged veto counter

Main K_L^0 decay modes such as $K_L^0 \to \pi^\pm e^\mp \nu$, $K_L^0 \to \pi^\pm \mu^\mp \nu$, and $K_L^0 \to \pi^+\pi^-\pi^0$ have at least two charged particles in the final states. In order to remove the events caused by these decay modes, a set of plastic scintillation counters (named "charged veto" or "CV") were placed in front of the CsI calorimeter.

Figure 3.14 shows the composition of the CV modules. A total of 32 sector-shaped modules (outer CV) were placed at a distance of 50 cm from the front face of the CsI calorimeter. The outer CV modules were arranged to have overlaps between adjacent modules. At the outside of the calorimeter, outer CV modules were bent and extended to the PMTs for readout. The beam region from the outer CV to the CsI was covered by the inner CV, which was a square pipe formed with four plastic scintillator plates. The inner and outer CVs were closely connected with aluminum fixtures, and inner CV was extended over the outer CV in order to eliminate the gaps between them. Both outer and inner modules had a thickness of 6 mm, and were read out by 2 inch Hamamatsu R329 PMTs.

Figure 3.15 shows the relative light yield of outer CV as a function of the incident position from the beam center. The data was obtained by punch-through muons and the incident position was measured by using the hit position in the CsI. The figure also shows the model function implemented in the Monte Carlo simulation, described in Chap. 6. The light yield increases at

the far end due to the taper shape of scintillator modules; the light collection efficiency increased by the reflection at the edge. The detailed study on the CV modules are summarized in the reference [42].

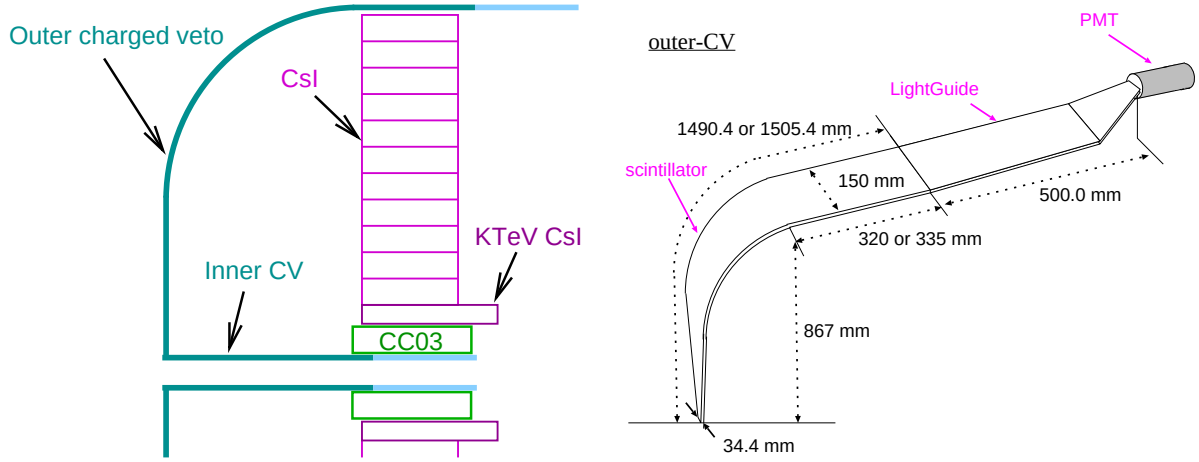

Figure 3.14: (Left) Schematic drawings of CV; (Right) structure of the outer CV.

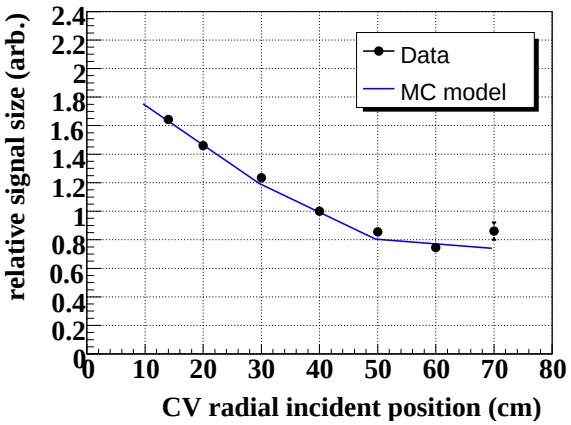

Figure 3.15: Relative light yield of outer CV as a function of the incident position from the beam center. The dots show the data obtained by punch-through muons and the solid line shows the model function used in the MC simulation in order to reproduce the position dependence.

3.2.4 Barrel counters

The decay region was surrounded with two large lead-scintilaltor sandwich counters: the main barrel (MB) and the front barrel (FB). The lamination was parallel to the beam axis, and the lengths of the MB and FB modules were 5.5 m and 2.75 m, respectively. The MB and FB was consisted of 32 and 16 modules with a segmentation in azimuthal direction. Figure 3.16 shows the cross-sectional end view of MB and FB. As shown in the figure, the direction of gaps between the modules was tilted from the radial direction in order to avoid the inefficiency caused by gaps between modules. The construction of barrel modules was summarized in Ref. [43].

Main barrel

The MB was located at the middle of detector system, as shown in Fig. 3.6. The purpose of the MB was to detect the extra photons and veto the background events from the $K_L^0 \to \pi^0\pi^0\pi^0$ and

$K_L^0 \to \pi^0\pi^0$ decays. The MB cylindrically surrounded the decay region. As shown in Fig. 3.17, MB modules were supported by a vacuum vessel. Each MB module had a trapezoid shape as shown in Fig. 3.18. One module consisted of 45 pairs of a plastic-scintillator plate and a lead sheet. The inner 15 layers, called "inner module", had lead sheets with the thickness of 1 mm, and the outer 30 layers, called "outer module", had lead sheets with the thickness of 2 mm. In both the inner and outer modules, the thickness of plastic scintillator was 5 mm. The total thickness of the module corresponded to 13.5 X_0.

We developed a new type of plastic scintillator made of a resin mechanically strengthened with a mixture of styrene and methacrylate [44], infused with the fluors PPO (1%) and POPOP (0.02 %). The emitted light was transmitted through wavelength-shifting (WLS) fibers, which were glued to each scintillator plate with a pitch of 10 mm. The WLS fiber was 1 mm in diameter with a multicladding structure (KURARAY Y-11). The green light emitted from Y11 was read by a newly developed photomultiplier tube with a high quantum efficiency for green light (E329-EGP PMT) [45]. In order to increase the quantum efficiency, E329-EGP PMTs had a prism-shape photo cathode as shown in Fig. 3.19, and had a modified material of photo-cathode, which was more sensitive to green light; to match the sensitive region with the emission spectrum of the Y-11 WLS fiber. There were 4 PMTs equipped for 1 module; from upstream and downstream ends of inner and outer modules.

The PMT gain of MB was monitored by an LED calibration system. A blue LED was located at outside the vacuum vessel and the its light was transmitted through an acrylic flange and clear fibers to each PMT. The LED light was flashed with 1.1 Hz, and the corresponding data was taken with a special trigger for the LED calibration.

The performance of MB was measured by using cosmic ray muons. Figure 3.20 shows the light yields for 4 readout channels of one MB module, obtained from cosmic-ray events. A typical light yield was 35 and 10 photo-electrons per MeV at the nearest and farthest point from the PMT, respectively. The timing resolution was 0.6 (0.5) nsec for inner (outer) module, as shown in Fig. 3.21. Details of the barrel counters has been reported in Ref. [46].

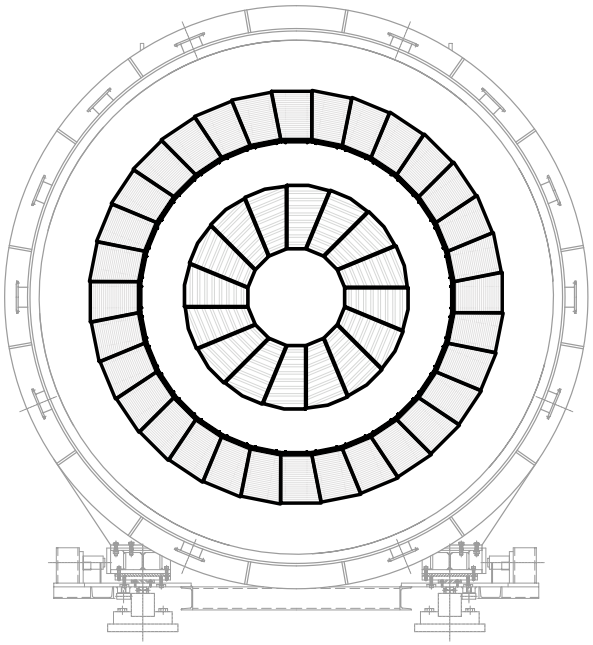

Figure 3.16: Cross-sectional end view of MB and FB. The outer ring shows MB and the inner ring shows FB, respectively.

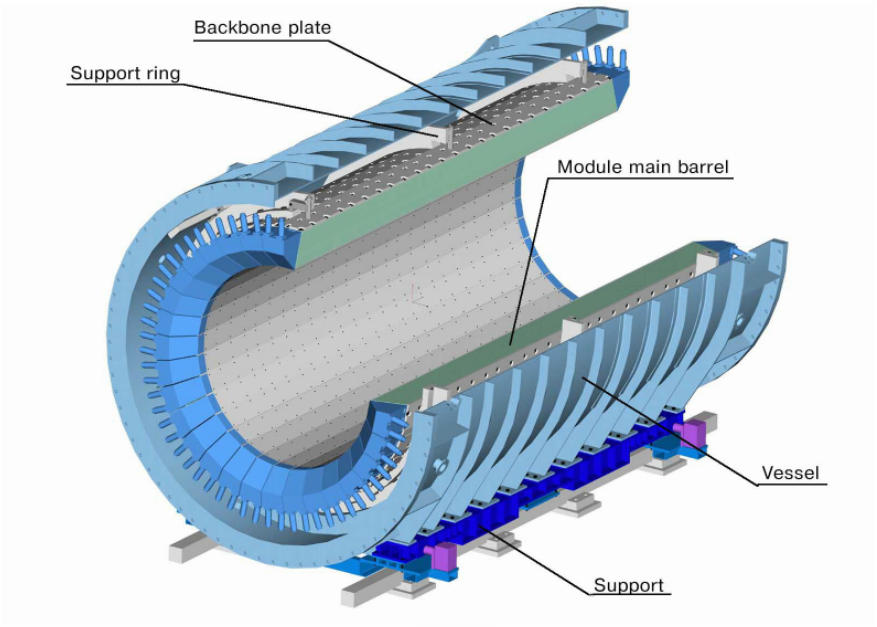

Figure 3.17: Drawing of Main Barrel and its support structure. The MB modules are supported by the vacuum vessel.

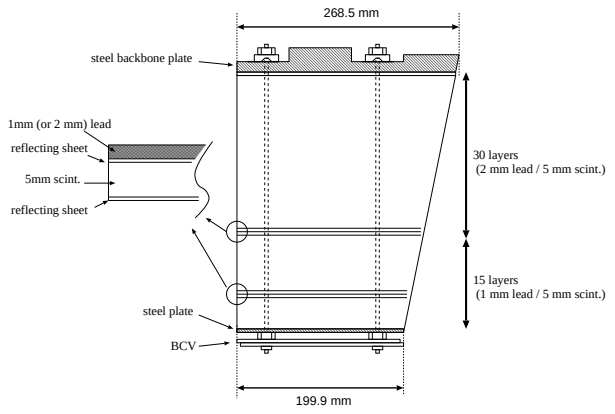

Figure 3.18: Structure of MB module.

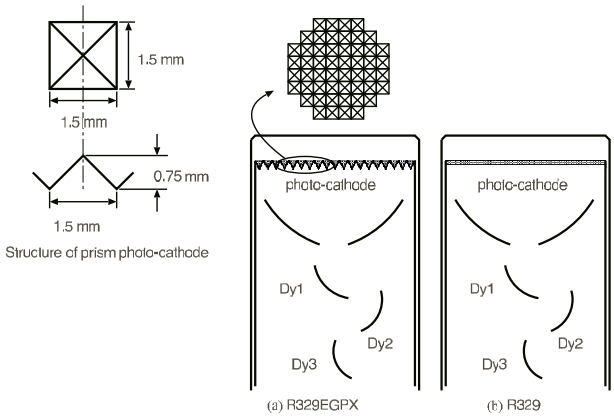

Figure 3.19: Schematic drawings of photo-cathode for the EGP-PMT (left) and normal one (right).

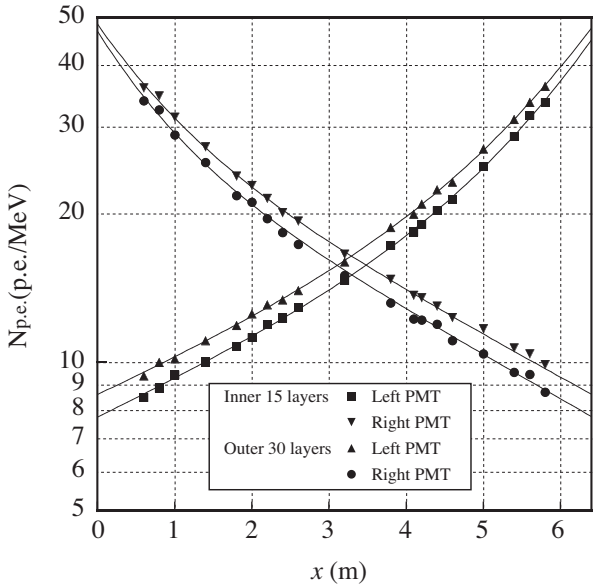

Figure 3.20: Light yield of MB module as a function of the distance from the PMT, quoted from the reference [46]. The result of four PMTs: upstream-inner, upstream-outer, downstream-inner, and upstream-outer, are shown.

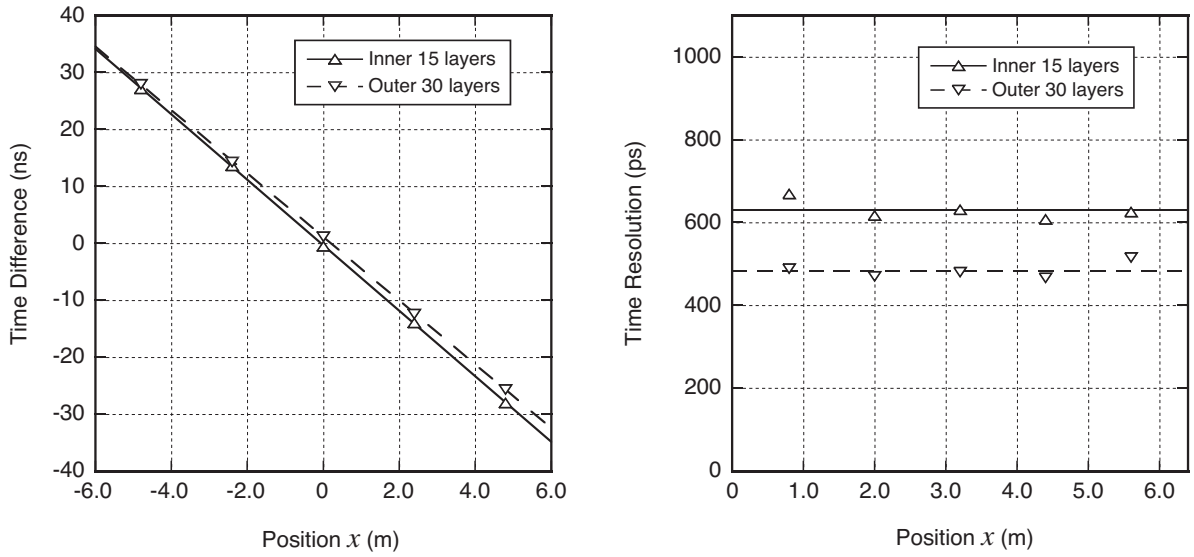

Figure 3.21: Linearity (left) and timing resolution (right) of a MB module as a function of the distance from the PMT, taken from the reference [46].

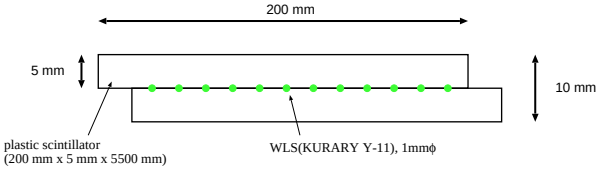

Figure 3.22: Schematic drawing of a BCV module. The green dots indicate the WLS fibers.

Barrel charged veto

In order to detect charged particles hitting the barrel region, a veto counter, named barrel charged veto (BCV), was located inside the MB. Since the inner surface of the MB was covered

with a steel plate for its mechanical support (See Fig. 3.18), an additional layer of plastic scintillator was placed inside the MB module in order to keep the efficiency to charged particles. BCV had 32 modules of plastic scintillator plates, and each module was mounted on a MB module, as shown in Fig. 3.18.

Figure 3.22 shows the schematic drawing of one BCV module. Two scintillator plates, each of which had a dimension of 5.5 m in length, 20 cm in width, and 5 mm in thickness, were glued together with optical cement. The scintillation light was transmitted through WLS fibers (KURARAY Y-11), which were sandwiched between two plates with a 5 mm pitch. The transmitted light was read out by the 1 inch PMT (Hamamatsu R7899-EGP) at the both ends of WLS fiber, which had the same features as the PMT used in the MB.

Front barrel

The front barrel (FB) surrounded the upstream of the K_L^0 decay region. The FB was needed to reject the events originated upstream of the decay region, such as K_L^0 decays and halo neutron interactions in the upstream region. It also worked to detect the extra photons escaping toward the upstream direction in the $K_L^0 \to \pi^0\pi^0\pi^0$ and $K_L^0 \to \pi^0\pi^0$ events. The FB was constructed in a upstream part of vacuum vessel, as shown in Fig. 3.23. Each FB module included 59 pairs of a 5 mm thick scintillator plate and a 1.5 mm thick lead sheet. The total thickness of the FB corresponded to 17.2 X_0.

The scintillation light was transmitted through WLS fibers having 1 mm diameter with multi-cladding structure (BICRON BCF-91a). The fibers were of inner 27 layers and outer 32 layers were separately bundled, and each bundle was read out by a 2 inch PMT (Hamamatsu R392-EGP). WLS fibers were connected to PMTs at the upstream ends, and their downstream edges were covered by Aluminized-mylar reflectors.

The performance of FB was measured by using cosmic ray muons. A typical light yield was 20 and 10 photo-electrons per 1 MeV energy deposit with the muon hit at the nearest and farthest point from the PMT, respectively.

3.2.5 Counters along the beam

Multiple collar-shaped counters, CC00, CC02 – CC07, were placed along the beam axis. These detectors were needed to detect photons passing just outside the beam region. The size and basic parameters of the counters are summarized in Table 3.1.

The upstream counters, CC02 – CC04, were placed inside the vacuum vessel, and the downstream CC05 – CC07, BHCV, and BA (discussed later) were placed outside the vessel, as shown in Fig. 3.24. A vacuum duct, which was directly connected to the vacuum vessel, penetrated CC05 - CC07 and the vacuum region was extended up to the front face of BHCV.

CC00

Counter CC00 was installed in front of the FB and outside the vacuum vessel to reduce the effects of halo neutrons. It consisted of 11 layers of a 5-mm-thick plastic scintillator interleaved with 10 layers of 20-mm-thick tungsten, as illustrated in Fig. 3.25. The scintillator plates were divided into the top and bottom parts; each part was read out from both left and right sides by the PMTs through light guides. However, CC00 did not significantly reduce the neutron halo because it was not placed as close to the beam as the other collar counters.

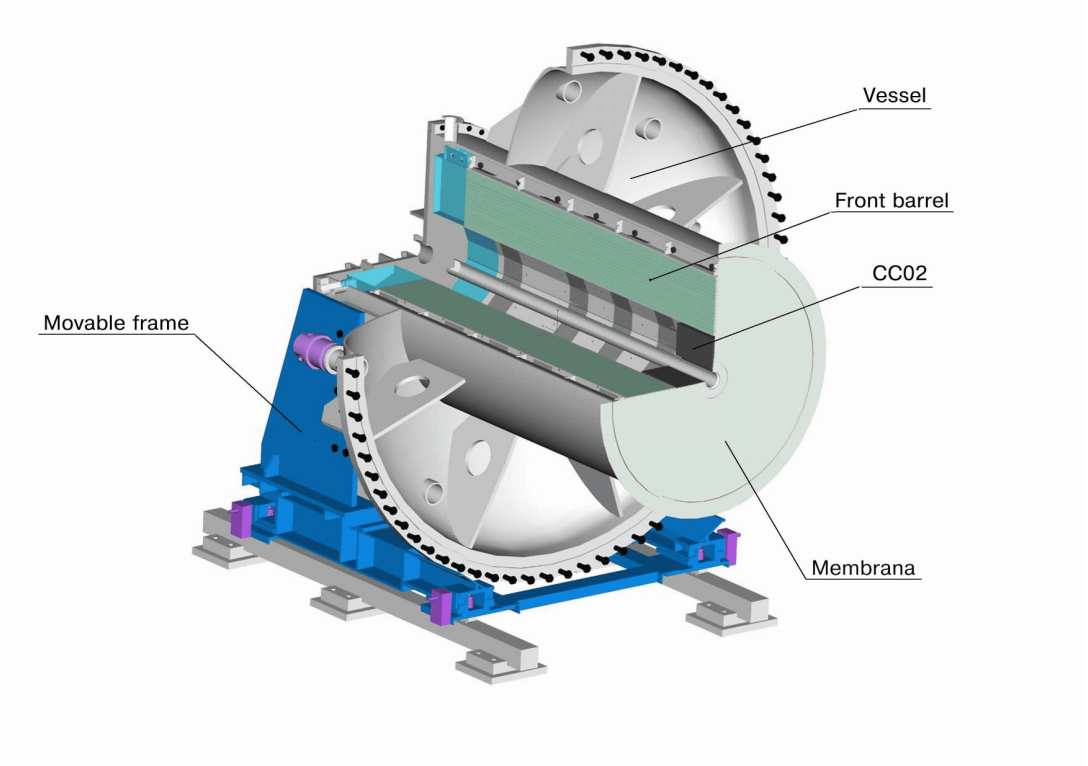

Figure 3.23: Overview of the upstream detectors, including FB and CC02. The figure is viewed from the downstream side.

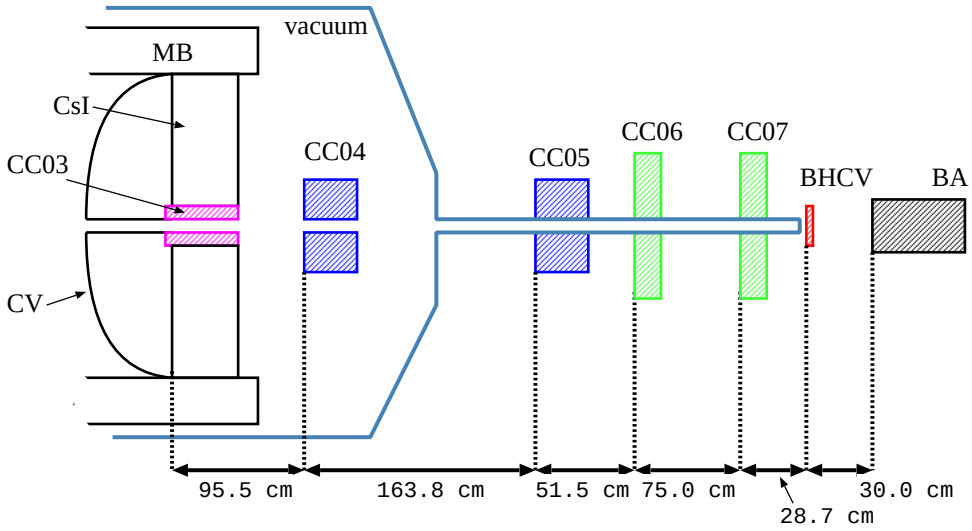

Figure 3.24: The location of downstream counters; CC03 – CC07, BHCV, and BA.

Table 3.1: Size and basic parameters of detectors along the beam. The origin of the z position corresponds to the start of the E391a detector. In the sizes of cross section and hole, dia. and sq. represents diameter and square, respectively. Visible fraction (R_{vis}) is defined as the ratio of the energy deposit in the active material to that in the whole volume. The thickness is expressed in units of radiation length.

detector	z position (cm)	outer size (cm)	inner size (cm)	configuration	R_{vis}	thickness (X_0)
CC00	-85.5	21.0 dia.	8.2 dia.	tungsten/scint.	0.024	57
CC02	239.1	62.0 dia.	15.8 dia.	lead/scint.	0.32	15.7
CC03	609.8	25.0 sq.	12.0 sq.	tungsten/scint.	0.23	7.6†
CC04	710.3	50.0 sq.	12.6 sq.	lead/scint.	0.28	11.8
CC05	874.1	50.0 sq.	12.6 sq.	lead/scint.	0.28	11.8
CC06	925.6	30.0 sq.	15.0 sq.	lead glass	1.0	6.3
CC07	1000.6	30.0 sq.	15.0 sq.	lead glass	1.0	6.3
BHCV	1029.3	23.0 sq.	no	plastic scint.	1.0	0.007
BA(Run-2)	1059.3	24.5 sq.	no	quartz	1.0	1.5
				lead/scint.	0.31	13.3
BA(Run-3)	1059.3	24.5 sq.	no	quartz	1.0	1.2
				PWO	1.0	16.8

† The lamination of CC03 was parallel to the beam.

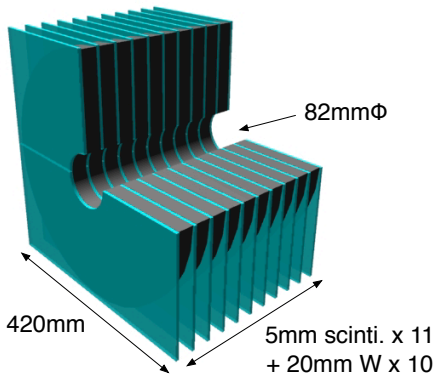

Figure 3.25: Cross-sectional drawing of CC00.

CC02

Counter CC02 was located at the downstream end of FB, lining the inner bore of FB, as shown in Fig. 3.23. The role of CC02 was to reject the events with the extra photons escaping toward upstream direction in $K_L^0 \to \pi^0\pi^0\pi^0$ and $K_L^0 \to \pi^0\pi^0$ decays. It also worked to eliminate the events in which K_L^0's decayed upstream of the decay volume.

The schematic drawing of CC02 is shown in Fig. 3.26. As in the figure, CC02 consisted of 8 modules and formed an octagonal shape. CC02 module had 43 layers of a lead sheet and a 5-mm-thick plastic scintillator plane. The thickness of the lead plate was 1 mm for the 7 layers from both upstream and downstream ends and 2 mm for the inner layers, resulting in a total thickness of $15.73X_0$. The scintillation light was read out by WLS fibers piercing the lamination ("Shashlik type"). WLS fibers used in the CC02 was the same as that used for FB, and the length of them were 2.5 m. The transmitted light was read out by 2 inch PMTs (Hamamatsu R329-EGP). A typical light yield was 10 photo-electron per one MeV energy deposit.

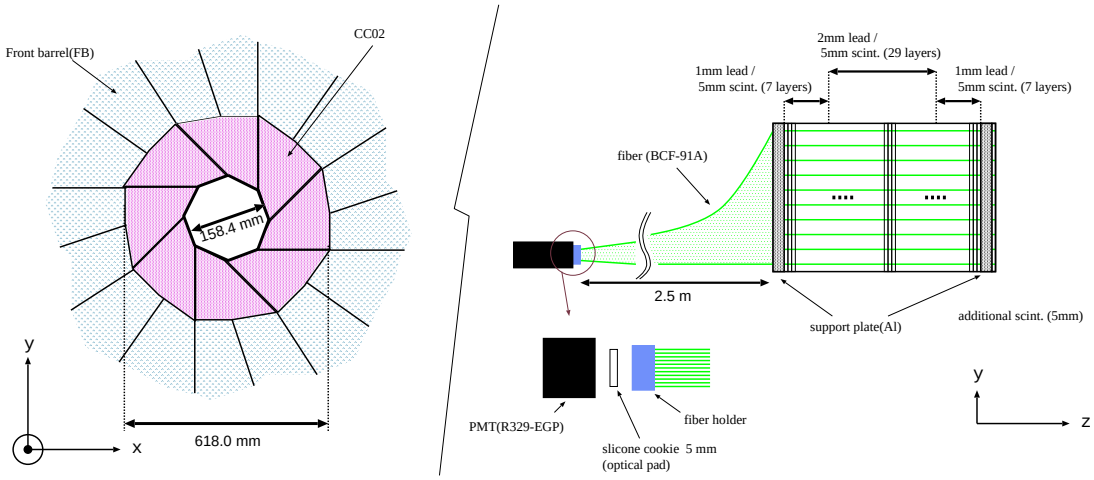

Figure 3.26: Cross-sectional view of CC02 (left) and detailed composition of the CC02 module (right).

CC03

Counter CC03 was located inside the CsI calorimeter, *i.e.* at the end of the decay region. It was worked to remove the events with K_L^0's decayed inside the beam hole of the CsI calorimeter. The CC03 consisted of 6 modules, each was a tungsten-scintillator sandwich with 26 pairs of a 1 mm thick tungsten plate and a 3.4 mm thick plastic scintillator. The lamination direction was parallel to the beam axis.

CC04 and CC05

Counters CC04 and CC05 were located downstream of the CsI calorimeter in order to detect extra particles escaping from the decay region through the beam hole of CsI. The location of CC04 was inside the vacuum vessel, and CC05 was positioned outside the vessel, where it was penetrated by a beam pipe.

As shown in Fig. 3.27, CC04 consisted of 32 pairs of a 5 mm thick scintillator and a 2 mm thick lead plate. In front of the first lead/scintillator layer, two additional scintillator plates with higher PMT gains were added in order to veto charged particles effectively.

CC05 also consisted of 32 pairs of a 5 mm thick scintillator and a 2 mm thick lead plate, as similar to the CC04. There were two additional scintillator plates with higher PMT gains at the downstream side of CC05 in order to detect charged particles effectively.

For both CC04 and CC05, the total thickness corresponded to $11.4X_0$. The scintillation light was read out by 2 inch PMTs (Hamamatsu H1161) through WLS fibers.

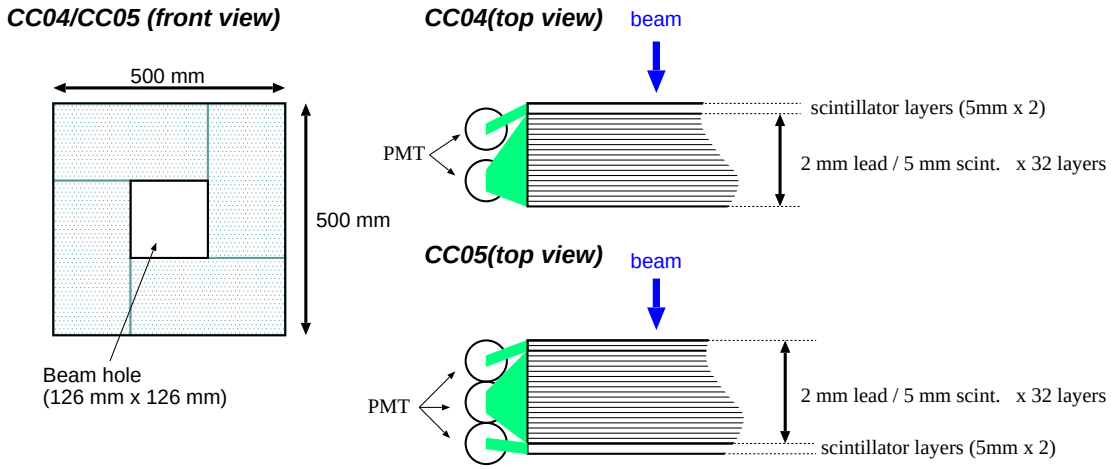

Figure 3.27: Schematic drawings of CC04 and CC05.

CC06 and CC07

Counters CC06 and CC07 was located at the downstream of CC05, and their role is to veto photons escaping away from the decay region through the beam hole. As shown in Fig. 3.28, CC06 and CC07 had the same mechanical structures: they were composed of 10 blocks of SF5 lead-glass with a refractive index of 1.7. The total radiation length was $6.3X_0$.

In the CC06 and CC07, Cherenkov light, which was emitted from electrons and positrons in a electro-magnetic shower, was emitted in a lead-glass block and detected by a 5 inch PMT (Hamamatsu R1250). The PMTs were directly attached to the lead-glas blocks with optical cement.

3.2.6 Beam counters

In order to detect photons and charged particles escaping into the neutral beamline, two counters, back anti (BA) and beam hole charged veto (BHCV), was located inside the beamline.

Back anti

The back anti (BA) was located at the end of the beamline in order to detect photons escaping into the beam core region. Since its location was inside the beam core, a large amount of neutrons hit the BA. When neutron signals were accidentally mis-identified as photon signals,

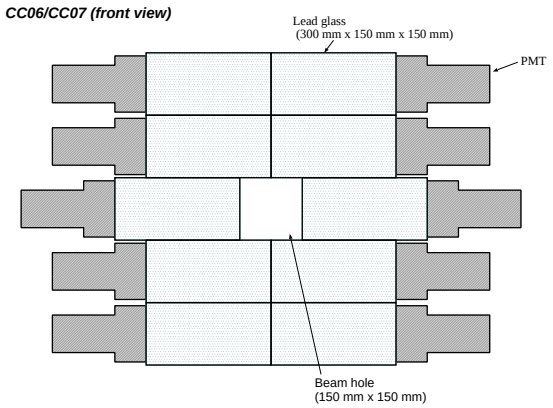

Figure 3.28: Front view of CC06 and CC07.

the acceptance for the $K_L^0 \to \pi^0\nu\bar{\nu}$ signal would be lost. Thus, BA was required to discriminate photon hits from neutron hits.

In order to satisfy the requirement, the BA consisted of two types of modules: scintillator module and Cherenkov module. Figure 3.29 shows the structure of BA; we used different types of BA in Run-2 and Run-3. In the Run-2, the BA consisted of six layers, each of which contained a calorimeter module and a Cherenkov module. The calorimeter module consisted of seven 2-mm-thick lead sheets and 5-mm-thick plastic-scintillator plates, alternatively. The Cherenkov module consisted of seven quartz crystals with a dimension of 35 mm $\times$ 245 mm in the cross section and 30 mm thick in the beam direction. The quartz had a refractive index of 1.46. In the Cherenkov module, a photon produces a number of electrons and positrons in the electromagnetic shower. Since these e^- and e^+ exceed the Cherenkov threshold, a large number of Cherenkov lights was emitted. On the contrary, slow secondary particles produced in neutron interactions, such as protons, deposit large energy in the scintillator, while they do not exceed the Cherenkov threshold, resulting in a small signal in the Cherenkov module. Thus, the photon hits and neutron hits can be separated.

In the Run-3 period, the BA consisted of five layers, each of which contained a calorimeter module and a Cherenkov module. The calorimeter module in Run-3 consisted of 16 blocks of PWO crystals, each having a dimension of 30 mm $\times$ 120 mm in the cross section and 30 mm thick in the beam direction. Each PWO crystal was read out by a $1\frac{1}{8}$ inch PMT (Photonis XP2978), which was directly contacted to the crystal. The Cherenkov module was kept the same as the Run-2 case. The detailed description on the Run-3 BA can be found in the reference [47].

The radiation length of the BA was $14X_0$ in Run-2 and $18X_0$ in Run-3, respectively.

Beam hole charged veto

A thin layer of plastic scintillator, the beam hole charged veto (BHCV), was placed inside the beam in front of the BA. It was an effective device to reject the $K_L^0 \to \pi^0\pi^+\pi^-$ decay, with π^+ or π^- escaping into the beam core region.

The BHCV consisted of eight plastic scintillator plates with a thickness of 3 mm. They were aligned perpendicularly to the beam direction, being overlapped with adjacent plates to eliminate gaps between the plates, as shown in Fig. 3.30. The scintillation light was read out by PMTs, which were directly connected to the scintillator plates. The PMT was EMI 9954B and its voltage divider was an active divider developed by the KTeV experiment.

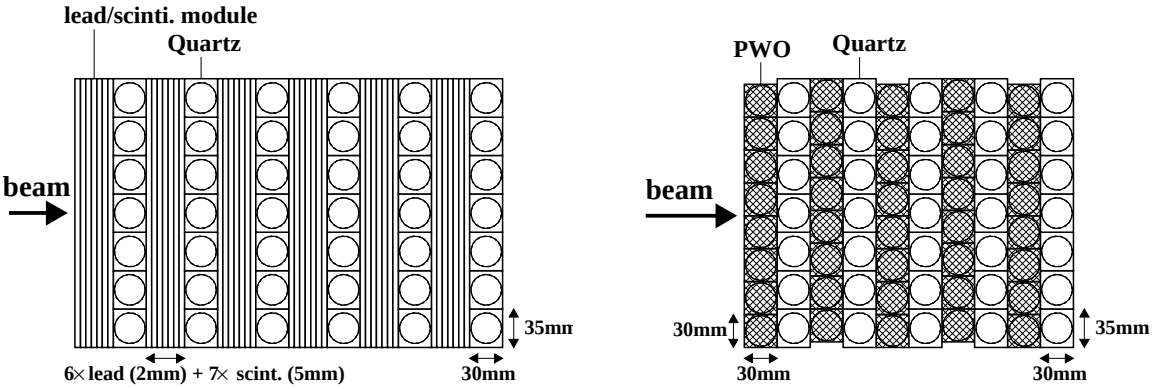

Figure 3.29: Side view of BA used in Run-2 (left) and Run-3 (right).

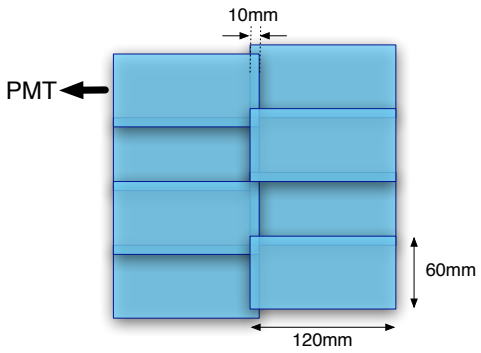

Figure 3.30: Schematic front view of BHCV.

Aerogel photon counter

In Run-3, an additional counter in the beam, named as aerogel photon counter (APC), was placed between the BHCV and BA. The APC was a threshold-type Cherenkov counter. The primary purpose of the APC was to discriminate photon events from others for the n–γ separation study of the BA. In addition we wanted to examine the performance of the Cherenkov detector using aerogel, since the APC was a prototype of the BA-like counter in the next generation experiment.

Figure 3.31 shows the structure of the APC. As a Cherenkov radiator, 27 aerogel tiles (Matsushita YI-50) with a dimension of 10 $\times$ 10 $\times$ 1.7 cm^3 were stacked with a structure of 3 $\times$ 3 $\times$ 3 in (X, Y, Z) direction, resulting in a total size of 30 cm $\times$ 30 cm in the cross section and 5.1 cm in the thickness along the beam. The refractive index of the aerogels was 1.05. The Cherenkov light was transfered to a PMT with a light collection system. The light collection system consisted of a flat mirror and a funnel, which was shaped as a Winston cone. A 5 inch PMT (Hamamatsu R1250) was used to detect the transmitted Cherenkov lights. The detailed study on the APC was summarized in the reference [48].

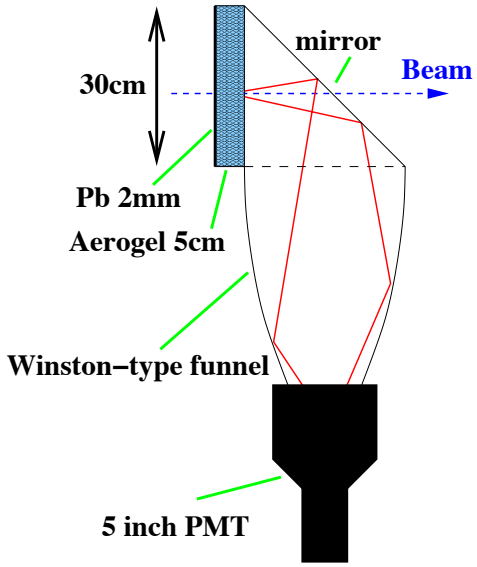

Figure 3.31: Schematic drawing of APC.

3.3 Vacuum

As discussed in the Sec. 2.3.3, the decay region was needed to be evacuated in order to reduce the backgrounds caused by the interaction of beam core neutrons to the residual gas. The decay region had to be maintained below 10^{-5} Pa in order to suppress these backgrounds to a negligible level at the sensitivity corresponding to the SM prediction of $K_L^0 \to \pi^0\nu\bar{\nu}$.

It is difficult to evacuate down to the 10^{-5} Pa level with the detector inside, because of the large amount of out-gassing from the detector materials. Thus, the detector components are needed to be separated from the high vacuum region. It is also required that the amount of dead material between the decay region and the detector system should be minimized in order to achieve a high detection efficiency even to low energy particles. To satisfy these requirements, we adopted a differential pumping method, where the vacuum region was divided into two regions as "high vacuum" and "low vacuum" regions, as shown in Fig. 3.32.

The entire detection system was placed in a large vacuum vessel, as shown in Fig. 3.6. The detectors were located in the low vacuum region, where the pressure was around 0.1 Pa. The pressure in the high vacuum region, through which the beam passed, was 1×10^{-5} Pa. The volume and surface area of two regions are summarized in Table 3.2.

The two regions were separated by a laminated membrane sheet with a thickness of 20 mg/cm^2. As shown in Fig. 3.33, the sheet was a lamination of four films. The EVAL film had low transmission for oxygen gas (mostly air) and the nylon film strengthened the sheet. The polyethylene layers on both sides were used to make a tight connection by using a heat iron press. The bag-shaped membrane covered the inner surface of the CsI detectors by using a skeleton structure of thin aluminum pipe, similar to a camping tent.

The outer low vacuum region was connected to a manifold through eight ports, and the manifold was evacuated by two pairs of rotary and root pumps. The pumping speed of each pair was 1200 m^3/hour. Four turbo molecular pumps, each having the pumping speed of 800 l/sec, were connected between the inner high vacuum region and the manifold. They produced the necessary pressure difference of an additional five orders of magnitude.

For the PMTs installed in vacuum, the pressure had to be less than 10 Pa to prevent high voltage discharges, according to our study on the discharge voltage as a function of pressure, as shown in Fig. 3.34. The PMT operation in vacuum additionally caused a cooling problem due to the absence of convection. We implemented a cooling system inside the vacuum, as described in Ref. [40]. The temperature was stable within $\pm 0.1^\circ$ for the CsI calorimeter.

Table 3.2: Total volume and surface area for the high vacuum region and the low vacuum region as shown in Fig. 3.32.

Region	Volume	Surface area	Pressure in the operation
High vacuum region	10 m^3	40 m^2	10^{-5} Pa
Low vacuum region	100 m^3	220 m^2	$\sim$0.1 Pa

3.4 Data acquisition

The data acquisition (DAQ) system in the E391a experiment was developed to collect data with high efficiencies. About 1000 PMTs were used as readout devices for all detectors. Here, we describe the readout scheme of the data and the hardware triggers developed to obtain the physics and calibration data.

3.4.1 Electronics

Signals from the detectors in the vacuum vessel were extracted through individual feed-through connectors. A connector was made of a coaxial cable simply molded to a metal flange with a resin.

Figure 3.35 shows the scheme of the E391a DAQ system. All detector signals were fed to Amplifier-Discriminator (AD) modules, which were newly developed for the experiment. An AD module accepted 16 PMT signals and generated 16 analog signals, 16 discriminated signals, and two 8-channel linear sums. Because early discrimination prevents time deterioration due to

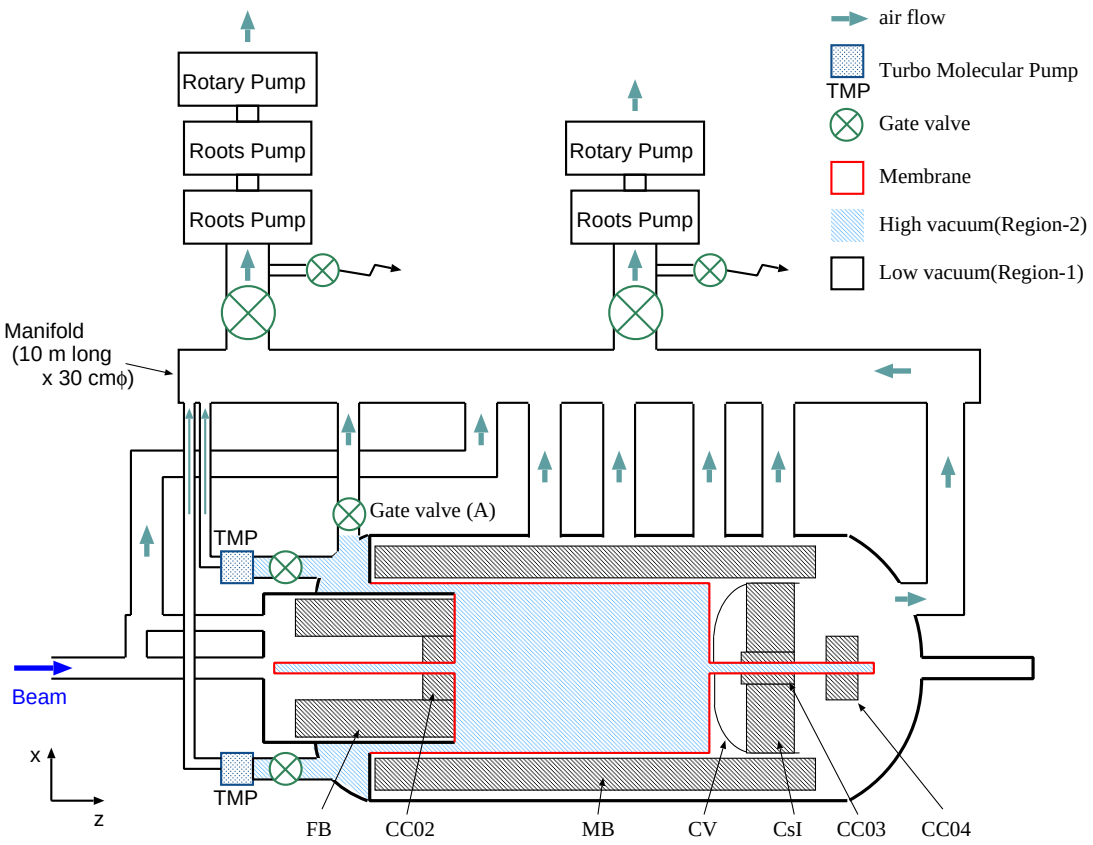

Figure 3.32: E391a vacuum system. The evacuation scheme was as follows: first we turned on the rotary pump and evacuated the whole region down to ∼10 Pa. Next, root pump was turned on and the whole area was evacuated down to ∼ 1 Pa. Finally, we separate the high vacuum region from low vacuum region by closing the gate valve (A), and the turbo molecular pumps (TMP) were turned on.

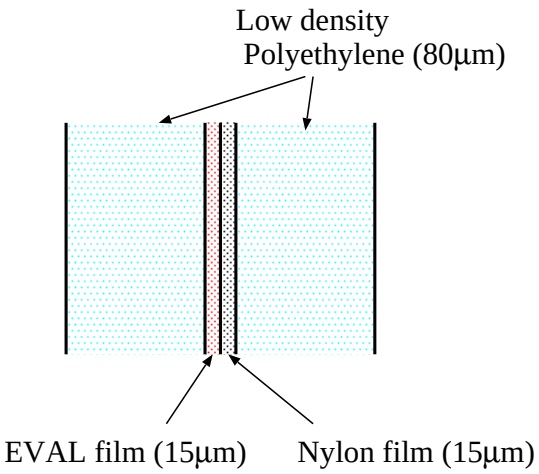

Figure 3.33: Membrane used for the vacuum separation.

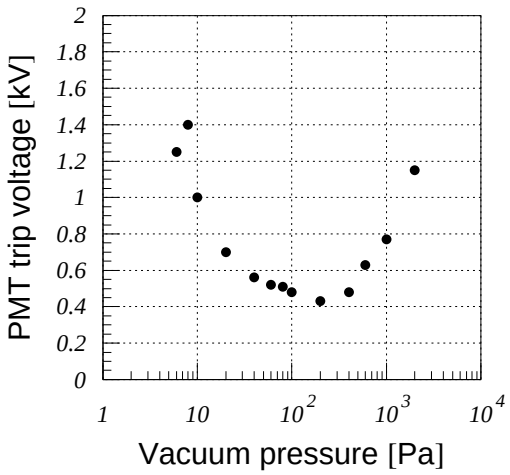

Figure 3.34: The discharge voltage of a PMT as a function of the vacuum pressure. Typical high voltage value in the actual operation was 1.0 kV to 1.6 kV.

distortion of the signal shape in the cable, the AD modules were placed near the vacuum vessel to shorten the cables.

Energy signal

The analog output signal, which was related to the energy deposit in each channel, was derived from each input signal with a throughput of 95%. It was sent to a charge-sensitive analog-to-

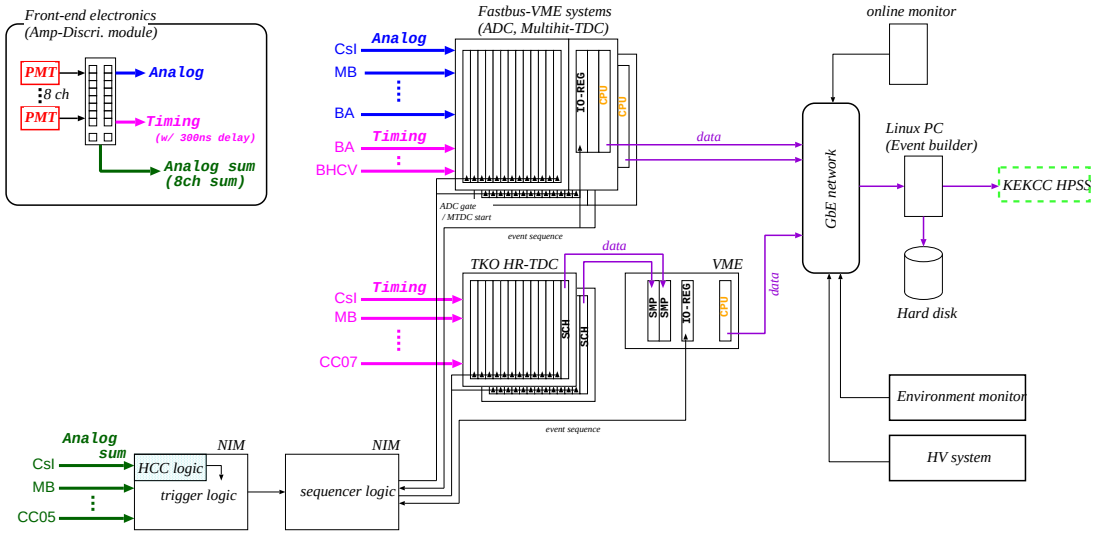

Figure 3.35: Schematic view of the E391a DAQ system.

digital converter (ADC) in the counting hut through a 90-m coaxial cable. The delay of analog signal was 300 ns compared to the timing of linear-sum signal with a cable length of 30 m, by considering a propagation velocity of 20 cm/ns. The ADC module, LeCroy FASTBUS 1885F, had 96 input channels, each channel having the equivalent dynamic range of a 15-ibt ADC in its 12-bit data by using a bi-linear technique. The typical resolution at a low energy range was 0.13 MeV/bit for the CsI calorimeter, and 0.035 MeV/bit for photon veto detectors. The gate width for the CsI calorimeter was 200 ns. All cables from the vacuum vessel to the counting hut were placed inside trays covered with copper-plated iron sheets in order to minimize ground noise caused by alternating magnetic fields. The pedestal widths of almost all the ADC channels were less than 1 bit.

Timing signal

The discriminator output, which was related to the timing of hits, was generated with a very low threshold of 1 mV. The threshold corresponded to an energy deposit of 1 MeV for the CsI calorimeter and below 1 MeV for the other detectors. The discriminator output was sent to a time-to-digital converter (TDC) in the counting hut through 30 m of twisted-pair cable after passing through a fixed delay of 300 ns in the AD module. The TDC module in the TKO (Tristan KEK Online-system), which was an electronics platform developed in KEK [49], was operated at a full range of 200 ns and a resolution of 50 ps. For BA and BHCV, the timing information was fed into a multi-hit TDC (MTDC) module (LeCroy FASTBUS 1877), which can store timing of multi signals.

Summed signal

The signal summed over 8 inputs was sent to the counting hut through 30 m of coaxial cable. These signals were used to form trigger signals for data acquisition.

DAQ system

The E391a DAQ system consisted of two Fastbus-VME systems, one TKO-VME system and one Linux PC for the event-building. In addition, it consisted of several Linux PCs for an online monitoring, an environment monitor and a HV control. All the CPUs and PCs were connected each other through the gigabit ethernet (GbE) network.

Two Fastbus modules, 1885F and 1877, were mounted in two Fastbus crates and their data was read out by the two Fastbus-VME system. We used two sets of a Fastbus-VME interface (SIS4100 NGF) and a VME CPU (FORCE54 UltraSPARCH 500 MHz boads). After waiting for the 1885F conversion time of 256 μs, an event sequence signal started the data transfer both from the 1885F and the 1877 to NGF's FIFO buffer (2 kByte) in a DMA block transfer mode. The data in the FIFO was moved to the CPU's memory every event. The data in the CPU's memory was transferred to the Linux PC for the event-building every spill. The data structure on the Linux PC was based on MIDAS [50]. Total processing time was 600 μs/event.

The data of TDC modules on the TKO platform was read out by the TKO-VME system. It consisted of two TKO-SCH controllers with the TKO crates and one VME CPU. After waiting for the conversion time of 100 μs, an event sequence signal started the data transfer. The TKO-SCH module controlled the data transfer from the TDC to the VME memory module (SMP) every event. The data in the SMP was transferred to the Linux PC for the event-building every spill. Total processing time was 500 μs/event.

In order to confirm that partial data in the three data buffers were from the same event, an 8-bit event ID was sent to each buffer.

The data from the Fastbus-VME systems and the TKO-VME system were combined and written in the local Hard-Disk-Drive (HDD). The data in the local HDD was transferred to a large storage system in the KEK Computing Center (HPSS system) through the KEK Giga-bit network every run.

The typical data size was 3 MByte/spill, and 60 GByte/day. The DAQ live ratio was ∼90 % with 300 triggers per spill, or 150 Hz.

3.4.2 Triggers

In the E391a, we employed a hardware-based single-level trigger system. There were several kinds of triggers according to the requirements. We mainly describe the physics trigger, a main trigger to obtain the $K_L^0 \to \pi^0\nu\bar{\nu}$ signal, and briefly mention other triggers such as calibration triggers.

Physics trigger

In order to obtain the $K_L^0 \to \pi^0\nu\bar{\nu}$ signal events and other K_L^0 decays for the normalization, a physics trigger was developed. As described in Sec. 2.1, the $K_L^0 \to \pi^0\nu\bar{\nu}$ decay was identified as the condition with two photons form a π^0decay and no other particles. To select the events with these characteristics, we counted the number of photon hits in the CsI calorimeter by using hardware cluster counter (HCC), and rejected events with extra activities by requiring no energy deposition in several veto counters.

In the HCC, the signals from eight adjacent CsI blocks (a segment) were collected into a summed signal by using the summed output of the AD modules. The CsI crystals were divided into 72 segments as shown in Fig. 3.36. The segments were used to form a trigger signal. A 40-mV threshold, which corresponded to an energy deposit of 80 MeV, was applied to each summed signal, and the number of segments whose summed signal was above the threshold, $\mathrm{N_{HC}}$, was counted. The distribution of the N_{HC} is shown in Fig. 3.37, where many events with $N_{\mathrm{HC}} = 1$ were due to beam associated events. We required $\mathrm{N_{HC}} \geq 2$ for the physics trigger.

We also required an anti-coincidence of several veto counters, CV, MB, FB and CC02 - CC05 with a rather high threshold. Table 3.3 summarizes the thresholds applied in the online veto. Later, in the offline analysis, these conditions were set tighter: a higher threshold for photon detection and lower thresholds for the vetos.

The K_L^0 decay rate in the decay region was approximately 1.6×10^5 events per 2 second spill with typical intensity of 2.6×10^{12} protons on the target. After the requirements described above, the trigger rate was reduced to 300 events per 2 second spill.

Other triggers

In addition to the physics trigger, we prepared several triggers for the calibration of the detector system and for the analysis.

Gain-monitoring triggers: Xenon trigger was used to flash the Xenon lamp with a 1.1 Hz clock for monitoring the CsI, as described in Sec. 3.2.2. LED trigger was used to flash the LED with a 1.1 Hz clock, for monitoring gains of PMTs used in MB and other veto counters. The frequency of 1.1 Hz was chosen not to synchronize with the spill. They were used to monitor

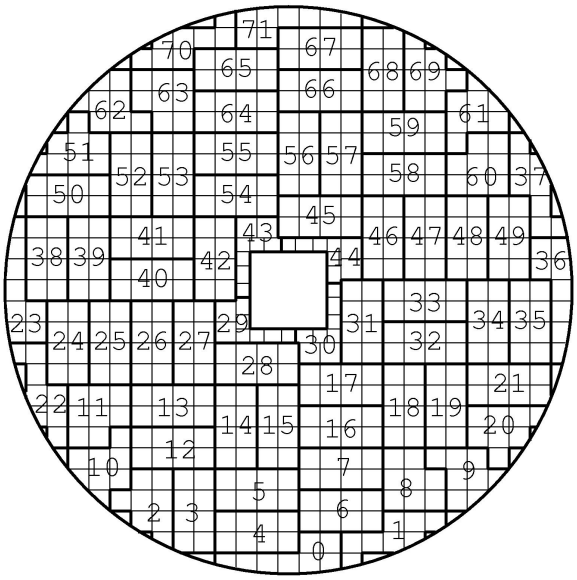

Figure 3.36: Segments of CsI blocks for the hardware clustering.

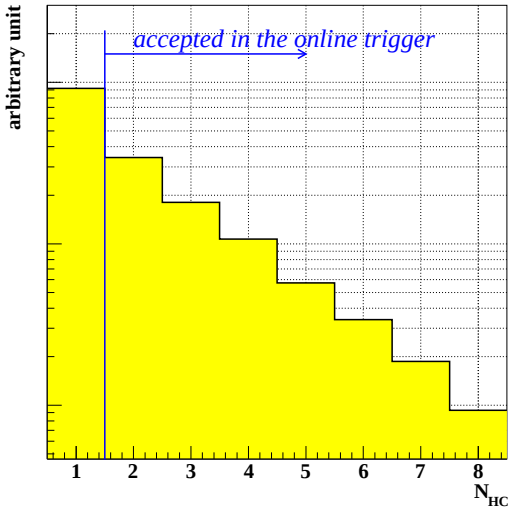

Figure 3.37: Distribution of the number of the hardware clusters (N_{HC}) obtained from the real data.

Table 3.3: Online veto thresholds for veto counters. The events exceeded the listed value were rejected. E_{cls} is a summed energy in each eight channel in the detector. E_{tot} is the total energy deposit in the detector. For MB, the energy at the trigger stage was measured at the upstream end.

Detector	Online threshold	Detector	Online threshold
CV	$E_{cls} \leq 1.2$MeV	MB	$E_{tot} \leq 20$MeV
FB	$E_{cls} \leq 25$MeV	CC02	$E_{tot} \leq 15$MeV
CC03	$E_{tot} \leq 15$MeV	CC04	$E_{tot} \leq 40$MeV
CC05	$E_{tot} \leq 25$MeV		

short-term drifts in the PMT gains. Also, the trigger was used to study the effects of beam loading by flashing them within and outside the beam spills.

Calibration triggers: Triggers for cosmic ray muons and punch-through muons were prepared for the calibration of the detector system. The cosmic-ray muon trigger was made by the hits penetrating the MB module and used for the calibration of the CsI, CC03, Sandwich, MB, BCV, and FB. The punch-through muon trigger was made by the synchronous hit of CC02 and CC06 or made by the BA hits. These events were used to calibrate the CV, CC02, CC04-07, and beam counters as BHCV and BA.

Minimum bias triggers: In order to check the performance of the physics trigger, we created a set of triggers with relaxed conditions with prescaling. One was the trigger requiring $N_{\rm HC} \geq 1$ without any vetoes. Another was the trigger requiring $N_{\rm HC} \geq 2$ without any vetoes.

Accidental triggers: We prepared two types of triggers to record accidental hits in the detector system by using an electronic pulse generator and the TMON, which was a counter telescope near the target. The accidental activities observed in the two types of triggers were consistent with each other for all detectors except the BA and BHCV. While the pulsar trigger had no correlation with the event time and was randomized with respect to the asynchronous timing of events, the TMON trigger reflected intensity variations of the primary beam. The TMON trigger data were normally used because we observed the micro time-structure of the beam extraction.

3.5 Calibration

The gains of the detectors were calibrated through a constant in units of MeV/bit. The gain constants of all detectors were basically calibrated in situ, after assembling and in vacuum, by using cosmic-ray muons and/or punch-through muons coming from the upstream region of the primary beamline. While the cosmic-ray muons primarily traveled in the downward direction, the punch-through muons were parallel to the beam. In the case of sandwich detectors, we selected the muons so that their primary direction was perpendicular to the lamination.

The CsI module was initially calibrated by using a cosmic-ray track as shown in Fig. 3.38.

The punch-through muons were used to cross check the cosmic-ray calibration because their directions were perpendicular to each other and their penetration lengths were different (7 cm for cosmic-ray muons and 30 cm for punch-through muons). The gain constants were refined by using the two photons from a π^0 produced in a special run in which an aluminum plate was installed on the beam axis. Finally, the gain constants were refined by an iteration process based on the kinematic constraints of $K^0_L \to \pi^0\pi^0\pi^0$ decay. The short-term variation of the gain was corrected by using xenon-lamp light pulses. The reconstructed K^0_L mass and the width were well stabilized, as shown in Fig. 3.39.

The timings were determined relative to one of the photon clusters in the CsI calorimeter. First, TDC constants (ns/count) were measured for all TDC channels by using a fixed delay, and the time-zero value was calibrated from the data. Cosmic-ray and/or punch-through muons were also used for the time-zero calibration. They were determined step-by-step by utilizing the overlapping parts of different detectors with respect to the muon tracks.

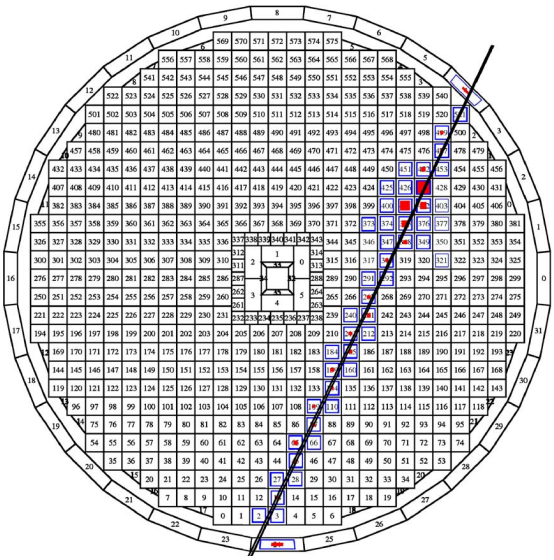

Figure 3.38: Cosmic ray track used for calibration. The outer ring shows the MB.

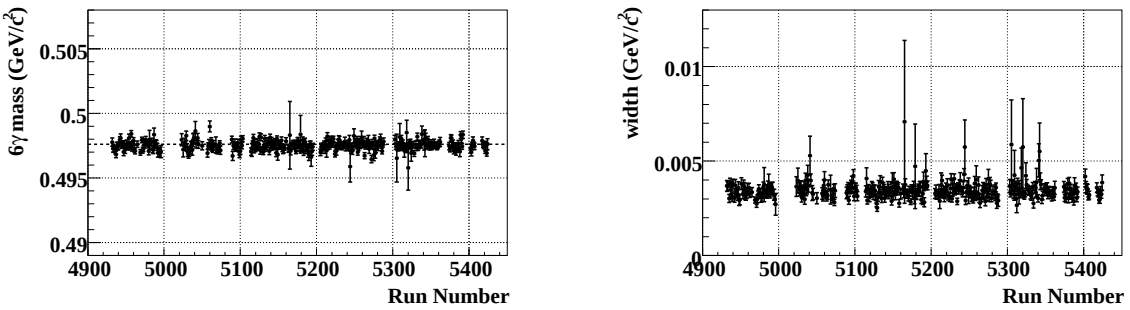

Figure 3.39: Stability of the kinematic variables over the entire period of Run-3. The left and right graphs show the peak and width of the effective mass distribution of $3\pi^0$ from the $K_L^0 \to \pi^0\pi^0\pi^0$ decay, respectively.

The time-zero values among CsI modules were determined by using cosmic ray tracks. Finally the calibration was refined by using six photons from $K_L^0 \to \pi^0\pi^0\pi^0$ decays. The time difference between two photons was determined with a standard deviation of 0.3 ns, as shown in Fig. 3.40, where the timing of a photon cluster was estimated from the timing of the central block that had the local maximum energy deposit.

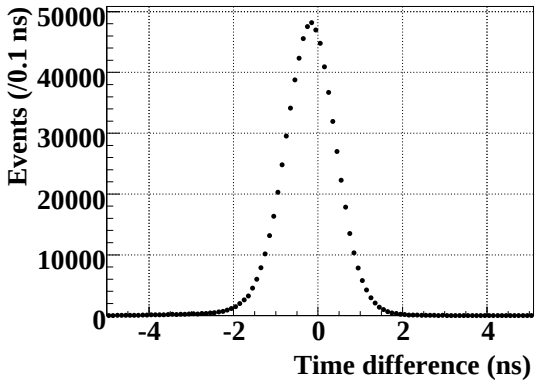

Figure 3.40: Time difference between two photons from the $K_L^0 \to \pi^0\pi^0\pi^0$ decay, obtained by subtracting the timing of lower energy photon from that of higher energy photon.

3.6 Data taking

3.6.1 Run periods

We carried out three periods of physics data taking. The first period (Run-1) was carried out from February 2004 to June 2004. The data quality of Run-1 was severely affected because the membrane for vacuum separation drooped into the beam core, causing many beam interactions. To reduce the background caused by the core beam interactions, the acceptance to the $K_L^0 \to \pi^0\nu\bar{\nu}$ mode was forced to be reduced in the Run-1 analysis [33, 51].

In the second period, Run-2, was carried out from February 2005 to April 2005, after fixing the problem of the membrane. In Run-2 (and Run-3), a beryllium (Be) absorber was inserted into the neutral beamline in order to improve the K_L^0 to neutron ratio.

The third period (Run-3) was carried out from October 2005 to December 2005. In Run-3, the BA was upgraded and the APC was installed as described in Sec. 3.2.6. Table 3.4 summarizes the features of three physics runs.

3.6.2 Physics run

In the physics run, the physics trigger and other triggers with pre-scaling were used in the data taking. The typical proton intensity was 2.5×10^{12} POT per spill. With the Be and Pb absorbers, and the HCC threshold at 40 mV (80 MeV), the trigger rate was 300 events per spill.

We monitored the number of reconstructed $K_L^0 \to \pi^0\pi^0\pi^0$ events every spill during the physics runs. Since this number depended on the proton intensity, the detector stability, etc., we were able to monitor the data quality at the online stage.

3.6.3 Calibration runs

Several runs were carried out to calibrate the detector system, using cosmic-ray muons and punch-through muons.

During the beam time, there were scheduled accelerator stops for the maintenance of ∼1/3 days in a week. In these times, we took the cosmic data, where the cosmic-ray muon trigger was taken without the pre-scaling. The gains of CsI, MB, BCV, FB, CC03, and Sandwich were calibrated by using these data samples.

Just after returning from the regular accelerator stops, *i.e.* once per week, we took a punch-through muon data. In this run, we used punch-through muons came from the upstream of the neutral beamline through the collimators and the radiation shield. The muons entered the detector uniformly and almost perpendicularly. When the shutter in the collimator system was closed, neutral particles in the beam were blocked and only the high energy muons could be enhanced. The gains of CC00, CC02, CC04–07, CV (outer module), BHCV, and BA were calibrated by using the punch-through muon data.

3.6.4 Al-plate run

Another special run, called "Al-plate run", was carried out for the background study. In the Al-plate run, an aluminum (Al) target with a thickness of 5 mm and a diameter of 10.6 cm was inserted in the beam at 6.5 cm behind the CC02. The conditions of the Al-plate run is summarized in Table. 3.5. Since the Al-palte run was taken in a period where the primary protons from the accelerator were shared to other experiment, the intensity of the primary proton beam was about half of the intensity in the physics run. Thus, Be absorber was taken out in order to increase the beam particles. In order to reduce the low energy contribution by the neutrons and photons produced in the Al plate, the threshold for HCC was raised to 150 mV (corresponded to 300 MeV), *i.e.* two hits in the CsI, each having the energy deposit greater than 300 MeV, were required in the trigger.

The data obtained in the Al-plate run was used to study the hadronic interaction of neutrons and to study the photo-nuclear interactions in the CsI. The detailed description on the Al-plate run is in Sec. 6.6.2 and 6.6.3.

Table 3.4: Summary of three physics runs.

Run	Run period	POT	Remarks
Run-1	Feb.-Jun. 2004	2.1×10^{18}	Membrane problem
Run-2	Feb.-Apr. 2005	1.4×10^{18}	Be absorber
Run-3	Oct.-Dec. 2005	1.1×10^{18}	New BA

Table 3.5: Run conditions of Al-plate run

Parameter	Physics run	Al-plate run
Proton intensity (Typ.)	2.5×10^{12}	1.0×10^{12}
Total protons	2.6×10^{18}	5.57×10^{16}
Be absorber	IN	OUT
Pb absorber	IN	IN
HCC threshold	80 MeV	300 MeV
Physics trigger rate	300 events/spill	550 events/spill

Chapter 4

Analysis Overview

Brief summary

In this chapter, we describe the analysis overview of the $K_L^0 \to \pi^0\nu\bar{\nu}$ search in this thesis. A previous analysis ("Analysis-2008") was made by using the whole data of the Run-2 sample in E391a. In the Analysis-2008, we found that the dominant background source was the halo neutron interactions with detectors near the beam. π^0's and η's produced in the interactions decayed into two photons and faked the signal. To reduce the halo neutron background, the event selection was needed to be tightened, and thus the sensitivity to the $K_L^0 \to \pi^0\nu\bar{\nu}$ decay was limited.

Because we found in Analysis-2008 that the halo neutron interaction was the dominant background source in our experiment, the improvement was focused on the treatment of the halo neutron background. After that, for the process of the combined data of Run-2 and Run-3, we improved the analysis method to achieve better sensitivity.

In this chapter, the review on the results obtained by the Analysis-2008 will be presented in Sec. 4.1. Section 4.2 describes the outline of the current analysis, in which we focus on the efforts to make improvement from the previous analysis.

4.1 Analysis-2008

The results of the Analysis-2008 is reported elsewhere [35]. The Analysis-2008 was carried out with a blind analysis, which means that the signal candidate events were not examined until the final selection criteria were fixed. This method was adopted to prevent us from knowing information which might lead to conscious or unconscious bias, and invalidate the results.

For the complete Run-2 data sample, the single event sensitivity, or S.E.S., was $(2.91\pm0.31)\times 10^{-8}$. No candidate events were observed in the data after imposing the final selection criteria, with the estimated number of background of 0.42 ± 0.14. The upperlimit of $\mathrm{BR}(K_L^0 \to \pi^0\nu\bar{\nu})$ was set to be 6.7×10^{-8} at the 90% CL.

Table 4.1 shows the estimated number of backgrounds in the Analysis-2008. As shown in the table, the contribution from the halo neutron backgrounds was expected to be the largest among the background sources. The halo neutron background was from three sources: CC02-π^0, CV-π^0, and CV-η.

The CC02-π^0 background was caused by π^0's produced in the CC02 by the interaction of halo neutron. In the CC02-π^0 background, the computed Z_{VTX} could be shifted downstream when

the energy of photons was mis-measured due to shower leakage or photo-nuclear interactions in the CsI calorimeter.

The CV-π^0 background was caused by π^0's produced in the CV by the interaction of halo neutron. In the CV-π^0 background, $Z_{\rm VTX}$ could be shifted upstream when the energy of photons was measured to be larger due to the fusion of multiple photons or the overlap of other hits in the calorimeter.

The CV-η background was caused by η's produced in the CV by the interaction of halo neutron. In the CV-η background, $Z_{\rm VTX}$ could be shifted upstream by applying the π^0 assumption in the reconstruction of the two photons.

Table 4.1: Estimated number of backgrounds (BG) in the Analysis-2008, taken from Ref. [36]

Background source		Estimated number of BG
Halo neutron BG	CC02-π^0	0.16 ± 0.05
	CV-π^0	0.08 ± 0.05
	CV-η	0.06 ± 0.02
K_L^0 decay BG	$K_L^0 \to \pi^0\pi^0$	0.12 ± 0.12
Total		0.42 ± 0.14

In the Analysis-2008, the background level was estimated by a different method for each background source. A special run with an Al plate (the Al-plate run explained in previous chapter) was used to estimate the background level for CC02-π^0. A bifurcation method was used to estimate the CV-π^0 background. A Monte Carlo simulation (MC) was used to estimate the CV-η background. The difference of the methods to estimate these backgrounds made it complicated to carry out optimizations with the objective of obtaining the best signal-to-noise ratio, S/N. The estimation by separate methods made it difficult to carry out optimizations to obtain the best signal-to-noise ratio, S/N.

4.2 Key points of the current analysis

To improve the analysis, we developed a new method to simulate hadronic interactions caused by the halo neutron. We used the hadron-interaction code FLUKA [52], and implemented an early-veto algorithm to save the CPU time. By using this method, we were able to generate sufficient amount of statistics of the halo neutron background events.

Generally, it is difficult to reproduce hadronic interactions by simulations because the hadronic interactions have a complicated nature. Thus, we first confirmed the reproducibility of the FLUKA simulation by using the data obtained from the Al-plate run. We confirmed that the numbers of produced π^0's and η's were reproduced by the simulation, as will be described in Sec. 6.6.2.

After the reproducibility of the simulation was confirmed, we generated beam-halo interactions with approximately 8 times larger than the total number of real data obtained in Run-3. With the sufficient amount of Monte Carlo data for the halo neutron background, we optimized the selection criteria to obtain the largest acceptance while the S/N ratio being kept in the MC data, as will be described in Sec. 7.2. Here, S is the number of events inside the signal region ($340 < Z_{\rm VTX} < 500$ cm and $120 < P_T < 240$ MeV/c) for the $K_L^0 \to \pi^0\nu\bar{\nu}$ events, and N is

the number of background events caused by beam-halo interactions. Since the optimization was based on the MC simulation, we were able to avoid potential bias, which might be caused by seeing the actual data sample. It also helped us to avoid a bias in reanalyzing the Run-2 data.

For the data processing, we first masked the events in the signal region for both Run-2 and Run-3 in order to perform the blind analysis. Once we fixed all the selection criteria by the optimization described above, we compared the data and MC for the events outside the signal region, as in Sec. 8.4. After confirming the consistency, we finally examined the events inside the signal region (Sec. 10.2).

Chapter 5

Event Reconstruction

Brief summary

As described in previous chapters, the $K_L^0 \to \pi^0\nu\bar{\nu}$ decay was identified by measuring two photons from the π^0 decay. The energies and positions of the photons at the CsI calorimeter were reconstructed from the pattern of energy deposits in the crystals ("photon reconstruction").

After the photon reconstruction was performed and two photon events were selected, π^0 was reconstructed as follows. The decay vertex of π^0 reconstructed by assuming both that the invariant mass of two photons was the π^0 mass and that the transverse position of the decay vertex was on the beam axis. By using the obtained vertex position, the momentum vector of the two photons, and then that of π^0 was calculated ("π^0 reconstruction").

In addition, the energies of the photons were corrected in order to compensate the effect of shower leakage out of the CsI. The positions of the photons at the CsI were also corrected for the shifts caused by the incident angle. The both correction ("photon correction") depended on the energy and incident angle of photons, where the incident angle was calculated from π^0 reconstructions. The correction was made iteratively, repeating π^0 reconstruction and photon correction.

In this chapter, we describe the reconstruction methods of photons and π^0, and the correction on the energy and position of photons.

5.1 Photon reconstruction

When a photon hits the CsI calorimeter, it generates an electromagnetic shower in the CsI blocks. The energy deposit of the electromagnetic shower spreads over multiple CsI crystals. Figure 5.1 shows an example of $K_L^0 \to \pi^0\pi^0\pi^0$ decay, in which each π^0 decays into two photons, and six photons in total hit the CsI calorimeter. As shown in the figure, six photons created six groups of activities, each of which contains several CsI blocks with finite energy deposits.

The purpose of photon reconstruction was to determine the energy and position of each photon from the pattern of energy deposits in the CsI crystals.

5.1.1 Cluster finding

We defined a "cluster" as a group of neighboring CsI crystals with finite energy deposit. Figure 5.2 shows the schematic drawing of cluster finding. The clusters were searched as following schemes. First, we picked CsI crystals with their energy deposit of more than 5 MeV (called

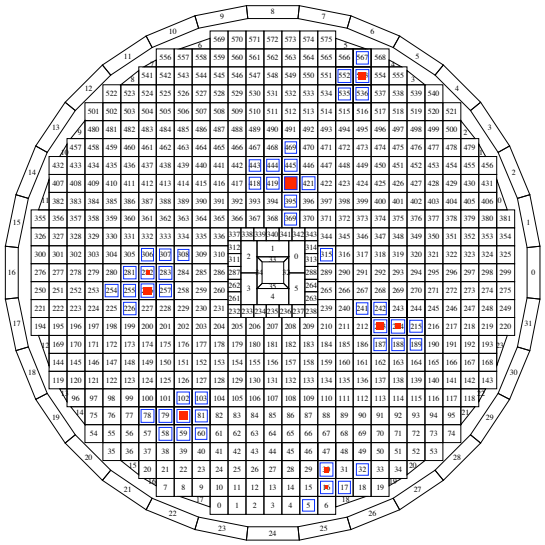

Figure 5.1: An example of six photon events in the CsI calorimeter. In this example, a $K_L^0 \to \pi^0\pi^0\pi^0$ decay occurred and produced three π^0's, each decaying into two photons. The size of the red filled boxes indicates the amount of energy deposit obtained from ADC values. The blue opened boxes were marked on the crystals with TDC hits.

"cluster seeds"). Then, we grouped the neighboring cluster seeds to form clusters. The neighboring crystals were defined as crystals which shared a side. We started this procedure from the CsI crystal which has a maximum energy deposit among the cluster seeds, because such a crystal is generally at the center of an electromagnetic shower generated by a photon. This process continued until all cluster seeds were used. To be recognized as a photon cluster, the group was required to contain more than two crystals with the energy deposit greater than 5 MeV. Finally, the neighboring crystals with the energy deposit greater than 1 MeV were added to the cluster, which were not used to calculate the energy and position of the photon, but were used to estimate the parameters relating to the shape of the cluster (See Sec. 7.4.1).

The remaining CsI crystals that had energy deposits and were not used in the photon clusters were treated as single crystal hits. They were considered as extra activities in the CsI and used to veto the events, as will be described in Sec. 7.3.1.

Figure 5.3 shows the distribution of the number of crystals contained in one photon cluster by comparing the six photon events of data and $K_L^0 \to \pi^0\pi^0\pi^0$ MC. The number of crystals was obtained by counting the crystals having the energy deposit greater than 5 MeV. The size of the cluster was well reproduced by the simulation.

5.1.2 A criterion to reject non-isolated clusters

After the cluster finding, the number of local maxima in each cluster was counted. A local maximum was defined as a crystal whose energy was greater than any of the neighboring crystals. If a cluster had two or more local maxima, as illustrated in Fig. 5.4, it was defined as a non-isolated cluster. The events containing non-isolated clusters were rejected, because those clusters had a potential to have more than one photons, which could result in the inefficiency to the extra particles. On the other hand, even a single photon can produce a cluster with multiple local maxima due to a fluctuation of the electromagnetic shower. The acceptance loss caused by this selection was estimated by a Monte Carlo study to be 8% for the $K_L^0 \to \pi^0\nu\bar{\nu}$ decay.

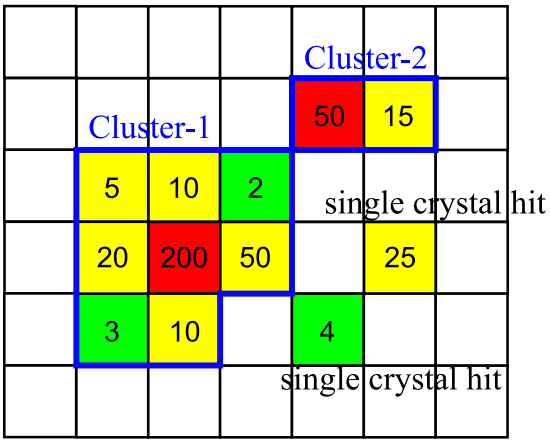

Figure 5.2: An example of cluster finding algorithm. The value shown in each box denotes the energy deposit in the CsI crystal in MeV unit. The red box shows the crystal having the maximum energy deposit in each cluster, and it is used as the start point for the cluster growth. The yellow boxes show the crystals having the energy deposit greater than 5 MeV, and the green boxes show the crystals having the energy deposit greater than 1 MeV. This example is reconstructed as two photon clusters as surrounded by blue lines (Cluster-1 and Cluster-2) and two single crystal hits.

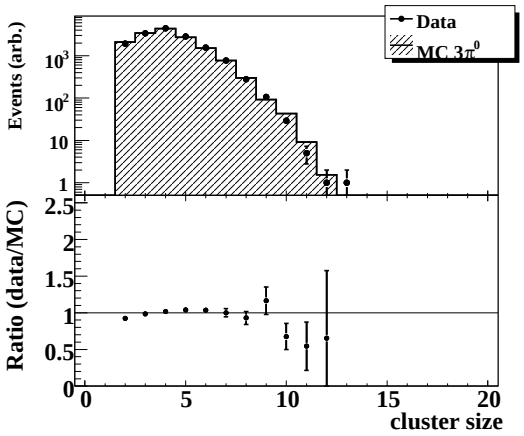

Figure 5.3: Distribution of the number of crystals having the energy deposit greater than 5 MeV in a photon cluster, comparing the data and $K_L^0 \to \pi^0\pi^0\pi^0$ MC. The top portion shows a comparison between the number of events in the data and MC, and the bottom portion shows the ratio between them. All analysis cuts for the $K_L^0 \to \pi^0\pi^0\pi^0$ mode, as will be described in Sec. 9.2.2 , are imposed.

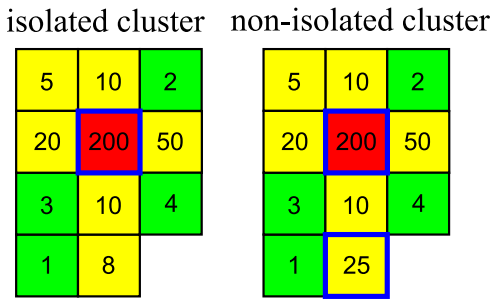

Figure 5.4: Schematic diagram of isolated (left) and non-isolated (right) clusters. The local maxima of the clusters are surrounded by blue lines; the cluster in the left figure has single local maximum and the cluster in the right has two local maxima.

5.1.3 Energy and position calculation

The energy deposit of each photon was calculated by summing the energies of crystals in a cluster:

$$E_{dep} \equiv \sum_{i=1}^{n} e_i, \quad (e_i \geq 5\text{MeV}) \tag{5.1}$$

where e_i is the energy deposit in each crystal and n denotes the number of crystals in the cluster.

The position of the photon, was initially defined by the energy weighted mean:

$$x_{COE} = \frac{\sum_{i=1}^{n} x_i e_i}{\sum_{i=1}^{n} e_i}, \; y_{COE} = \frac{\sum_{i=1}^{n} y_i e_i}{\sum_{i=1}^{n} e_i}, \quad (e_i \geq 5\text{MeV}) \tag{5.2}$$

where x_i and y_i is the center position of each CsI crystal.

The E_{dep}, x_{COE}, and y_{COE}, calculated in this stage, deviated from the true energy and position because of the leakage of the electromagnetic shower out of the CsI crystals and because of the incident angle of photons to the surface of CsI. Thus, the energies and positions were needed to be corrected. The method of the correction will be described in Sec. 5.3.

5.1.4 Sorting of events

The events were sorted into several samples according to the number of reconstructed photon clusters. The two-photon sample was used to search for the $K_L^0 \to \pi^0\nu\bar{\nu}$ decay and for monitoring the $K_L^0 \to \gamma\gamma$ decay. The four-photon and six-photon samples were used for monitoring the $K_L^0 \to \pi^0\pi^0$ and $K_L^0 \to \pi^0\pi^0\pi^0$ decays, respectively.

5.2 π^0 reconstruction

By using the positions and energies of two photon clusters, the decay vertex and the momentum of the π^0 were reconstructed. In the π^0 reconstruction, we assumed that two photons came from a π^0decay and their invariant mass was equal to the π^0mass. Also, the decay vertex was assumed to be on the beam axis, *i.e.* $(0, 0, Z_{\text{vtx}})$

Figure 5.5 shows the relation between several parameters used in the calculation. The distance between the vertex and the CsI calorimeter is defined as $dz \equiv Z_{\text{CsI}} - Z_{\text{vtx}}$. There are following geometrical relations:

$$r_{12}^2 = d_1^2 + d_2^2 - 2d_1 d_2 \cos\theta, \tag{5.3}$$

$$d_1 = \sqrt{r_1^2 + (dz)^2}, \tag{5.4}$$

$$d_2 = \sqrt{r_2^2 + (dz)^2}., \tag{5.5}$$

where r_{12} is the distance the two photons at the calorimeter surface, θ is the angle between the direction of the two photons, d_1 and d_2 are the distances between the decay vertex and the hit positions, r_1 and r_2 are the distances of the hit positions from the z-axis. In addition, assuming the invariant mass of the two photons to be the π^0 mass (M_{π^0}), we obtain:

$$\cos\theta = 1 - \frac{M_{\pi^0}^2}{2E_1 E_2}, \tag{5.6}$$

where E_1 and E_2 are the energies of the photons.

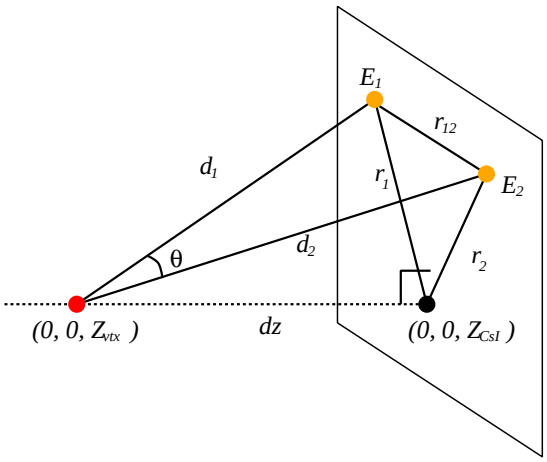

Figure 5.5: Schematic view of parameters used to reconstruct the π^0 vertex.

Using these equations, the z-coordinate of the decay vertex ($Z_{\rm VTX}$) was calculated to each combination of two photons. Also the standard deviation of the decay vertex, $\sigma_{\rm vtx}$, was calculated from the standard deviation of the measured quantities: σ_{E_i}, σ_{x_i}, and σ_{y_i}, for each photon ($i = 1, 2$), by propagating through these equations.

After reconstructing $Z_{\rm VTX}$, the momentum vector of the π^0 was calculated as the sum of two photon momenta. The transverse momentum of the π^0, or P_T, is calculated as:

$$P_{\rm T} = \sqrt{(P_x^{\pi^0})^2 + (P_y^{\pi^0})^2}, \tag{5.7}$$

where $P_x^{\pi^0}$ and $P_y^{\pi^0}$ are x and y components of the reconstructed π^0 momentum, respectively. The P_T is approximately independent of the reference frame, and stays within a kinematic limit. This feature played an important role in background suppression, as to be discussed in Chap. 9.

5.3 Energy and position corrections

After reconstructing π^0, we can calculate the incident angle of the two photons to the surface of the CsI. The energies and positions of the photons were corrected by using the information of incident angles.

To make these correction, we carried out a special Monte Carlo study. We prepared MC samples in which photons with various energies, positions, and angles were injected into an array of 11 $\times$ 11 CsI crystals. Two types of look-up tables were developed to make correction. The first one was used to correct the energy leakage out of the CsI crystals, either going out from front-side face and back-side end. Figure 5.6 shows dependence of the energy leakage on the incident angle. The second table was prepared to correct the positions: from the center of energy to the incident position, as shown in Fig. 5.7. An example of the correction table is shown in Fig. 5.8. Positions calculated as the center of energy (x_{COE}, y_{COE}) were apart from the true incident position, and they were corrected according to this table.

Since the π^0 reconstruction was affected by the energy and position correction, the correction process was carried out iteratively, as shown in Fig. 5.9. The iteration was continued until the difference before and after the correction became convergent. Typically, the correction process was finished within three iterations.

The effect of the correction was demonstrated in Fig. 5.10. As shown in the figure, the position and energy resolution of the photons were improved, and thus, the resolution of the

π^0 reconstruction was also improved.

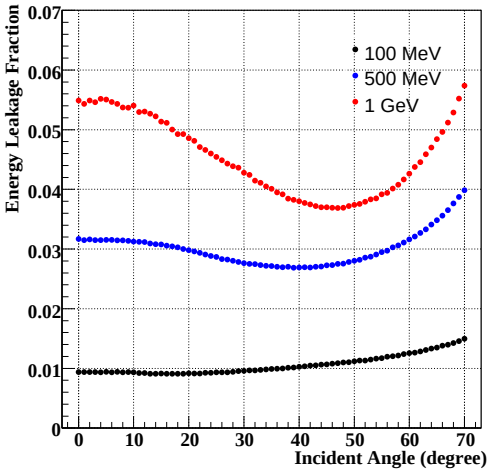

Figure 5.6: Correlation between the incident angle and the fraction of leaked energy, obtained by the simulation. At the small incident angle, the leakage fraction is dominated by the leakage from the back-side end of the CsI. As increasing the incident angle, the path length of the CsI increases and the energy leakage from the back-side end decreases. At the large incident angle, the leakage from the front-side face of the CsI makes the large fraction of leaked energy.

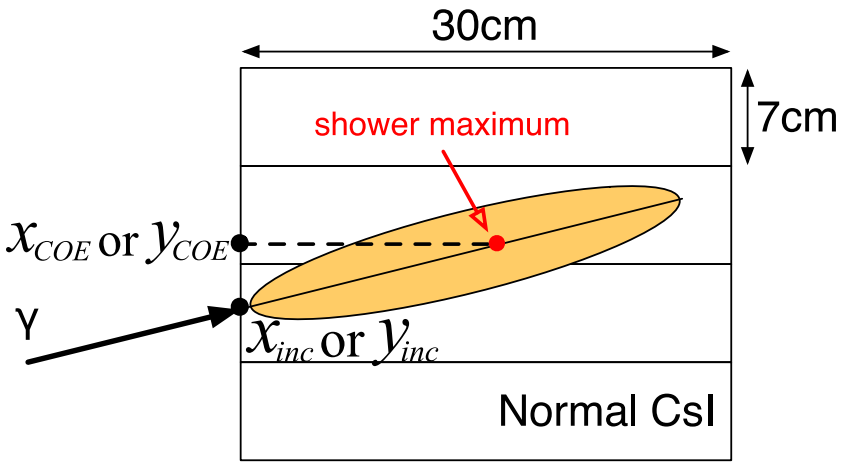

Figure 5.7: Schematic illustration of the position correction. The incident position (x_{inc} or y_{inc}) can be calculated from the length of electromagnetic shower (L), the position of the center of energy (x_{COE} or y_{COE}), and the incident angle.

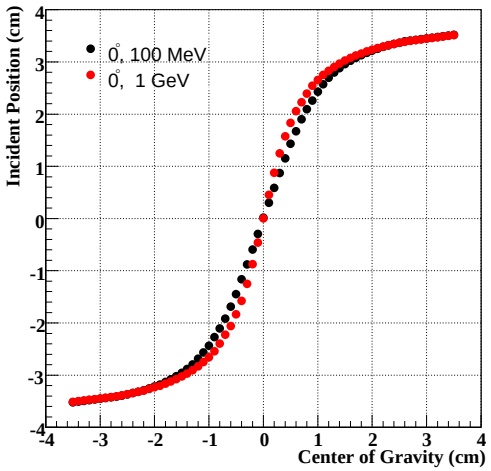

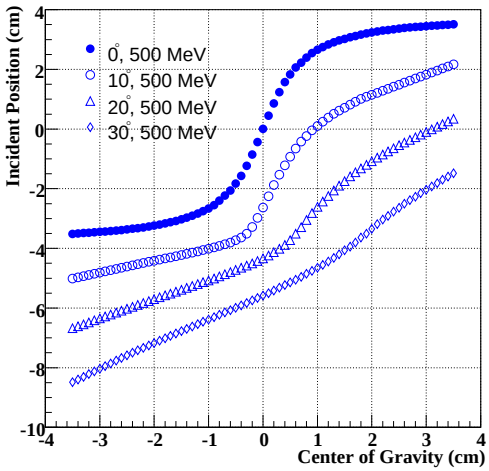

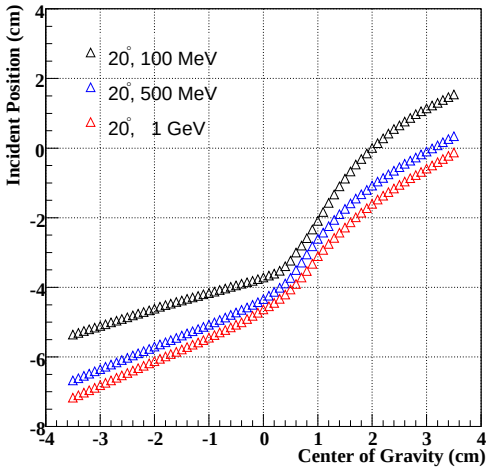

Figure 5.8: Correlations between the true hit position and x_{COE} in MC. Each plot shows dependency of the correlation on the energy and the incident angle of photons. The CsI crystal had the size of 7×7 cm^2, thus 0 cm and 3.5 cm corresponded to the center and the edge of the crystal, respectively. Since the position of the x_{COE} is tended to be reconstructed near the center of the CsI crystal having the largest energy deposition, the correction function becomes sigmoidal curve to recover this tendency. Note that the vertical scales are different among the plots.

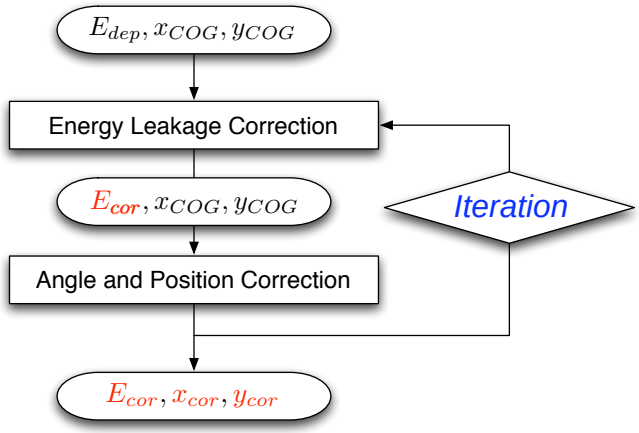

Figure 5.9: Scheme of the energy and position correction for the photon cluster. E_{cor}, x_{cor}, and y_{cor} means the corrected energy and positions.

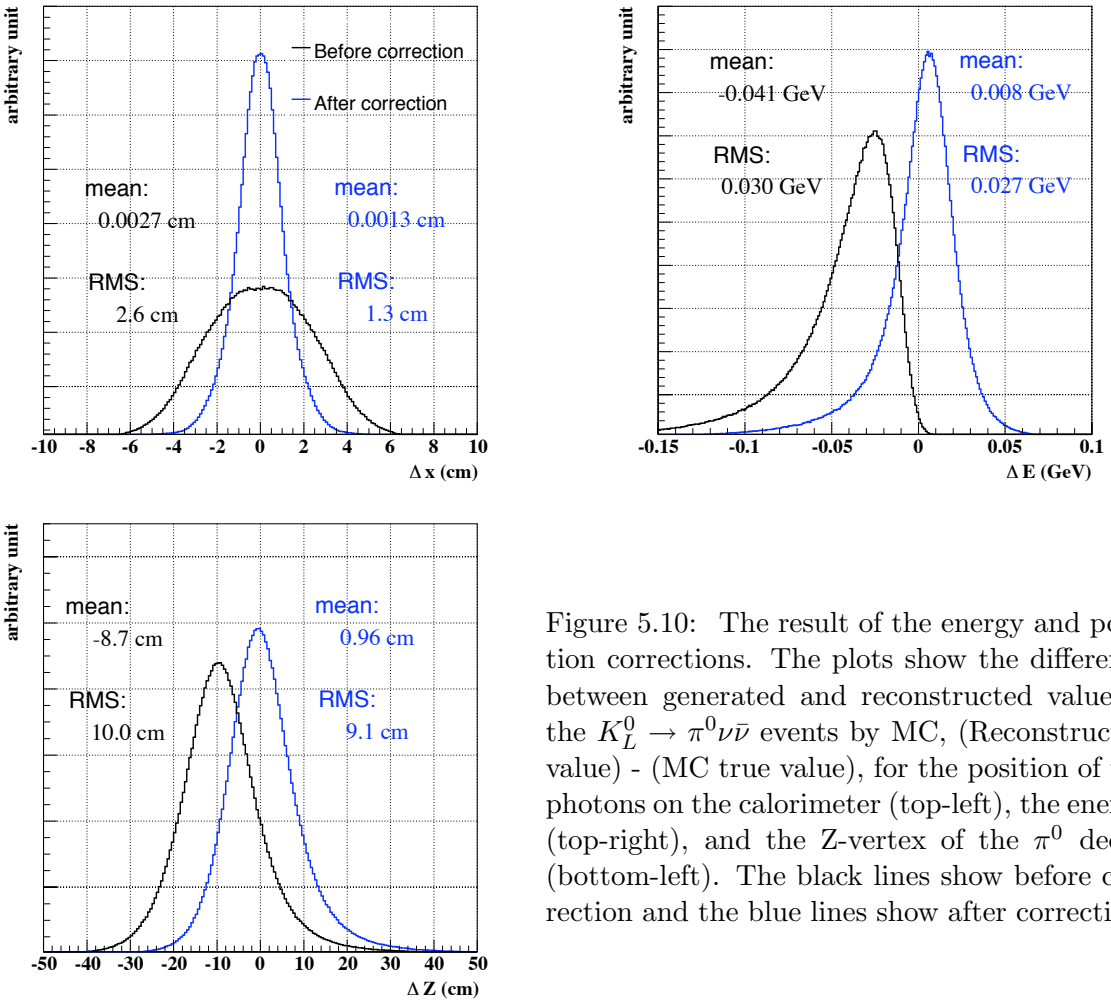

Figure 5.10: The result of the energy and position corrections. The plots show the difference between generated and reconstructed value of the $K_L^0 \to \pi^0\nu\bar{\nu}$ events by MC, (Reconstructed value) - (MC true value), for the position of the photons on the calorimeter (top-left), the energy (top-right), and the Z-vertex of the π^0 decay (bottom-left). The black lines show before correction and the blue lines show after correction.

Chapter 6

Monte Carlo Simulations

Brief summary

In this chapter, we present the Monte Carlo (MC) simulation used in the current analysis. We carried out several types of MC study to estimate the acceptance of the signal and normalization modes, and to estimate background events. To optimize event selections and obtain the best sensitivity, it is essential to estimate background events with confidence. It is also crucial to estimate the ratio of acceptances between the signal and normalization modes, because the ratio was used to set the sensitivity of our experiment.

We divided the process of the MC simulation into several steps, as shown in Fig 6.1. As the first stage of the simulation, a beamline simulation was carried out to estimate the flux of K_L^0's, photons, and neutrons in the neutral beamline. After the beamline simulation, the simulation process was divided into two streams. One is to estimate the K_L^0 decay, including the signal mode and the normalization modes, by using the GEANT3 simulation package. The response of the detector is also estimated by this simulation. The other one is to estimate the halo neutron backgrounds. In this process, we simulated the interaction between halo neutrons and detectors by using the FLUKA hadronic package. The results of the halo neutron simulation were fed into the detector simulation, which utilized GEANT3.

The reproducibility of these simulations was confirmed by real data obtained by physics runs and special runs. Following sections describe the methods of these simulations and the results of the reproducibility confirmation.

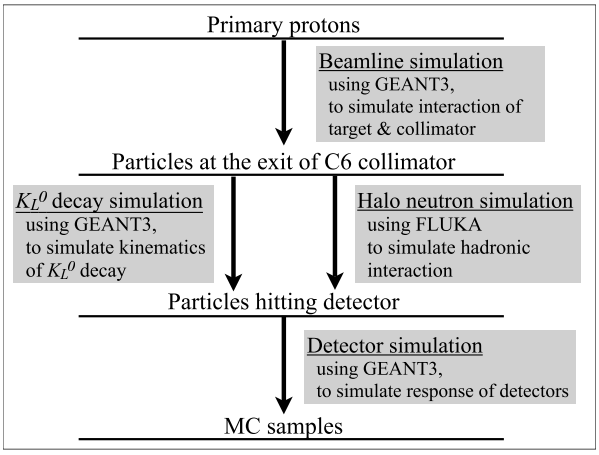

Figure 6.1: Flowchart of MC simulation.

6.1 Beamline simulation

To estimate the K_L^0, photon, and neutron fluxes in the neutral beamline, a beamline simulation was carried out. First, we collected the information of the secondary particles produced at the target. The primary protons having the kinetic energy of 12 GeV were generated and stroke on the platinum target, and all kinds of the secondary particles were collected.

Second, we simulated the performance of the neutral beamline. The collimators (C1-C6), two absorbers (Pb and Be), and the magnetic field (D1 and D2 magnets) were implemented in the simulation according to their measured positions. The particles collected at the previous step were transported through the beamline components. The momentum, position, and angle distributions at the exit of the last collimator (C6) were recorded. In these simulation, we used the GEANT3 simulation package [53] with the GFLUKA plug-in code for hadronic interactions.

The momentum distribution of the K_L^0 beam at C6 is shown in Fig. 3.3. Figure 6.2 shows the distribution of the beam density and the momentum at C6 for the core and halo neutrons. We defined the "halo neutrons" as the neutrons which goes outside the beam region when extrapolated to the position of CC05. The ratio of the halo to the core neutrons was approximately 10^{-4}, as shown in Fig. 6.2.

The amount of statistics of the beamline simulation corresponded to 4×10^{11} of the primary protons on the target (POT).

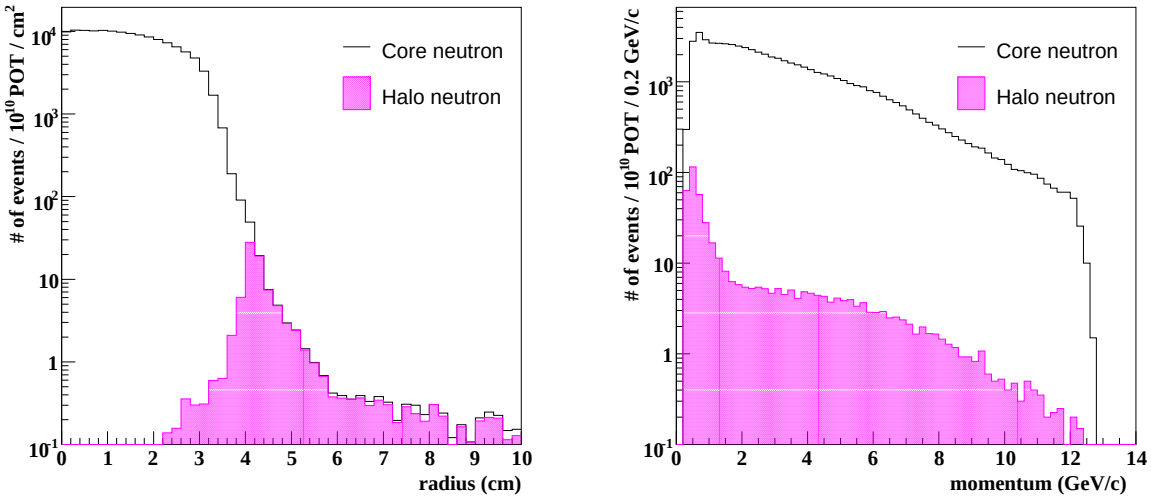

Figure 6.2: Distributions of the beam density (left) and the momentum (right) for the core (solid lines) and halo (pink shaded areas) neutrons, respectively. The distributions were obtained at the exit of C6 for the neutrons with momentum above 0.3 GeV/c.

6.2 K_L^0 simulation

We developed a K_L^0 simulation to estimate the K_L^0 decays in the detector system. In this simulation, we first generate K_L^0's at the exit of C6 collimator. The position, momentum, and direction of K_L^0's were determined according to the results of the beamline simulation. Second, K_L^0's were transfered through the detector system and decayed according to the lifetime of K_L^0,

where the lifetime of K_L^0 was taken from Ref. [10]. In the signal acceptance study, K_L^0's were forced to decay into the $K_L^0 \to \pi^0\nu\bar{\nu}$ signal mode, and for the study on the normalization and the K_L^0 background estimation, K_L^0's were forced to decay into respective modes such as $K_L^0 \to \pi^0\pi^0\pi^0$, $K_L^0 \to \pi^0\pi^0$, etc.. We describe the generation of the K_L^0 beam and the simulation of the K_L^0 decay in the following subsections.

6.2.1 Parameterization for K_L^0 beam

The kinematic parameters of K_L^0, the momentum, position, and direction, were determined by the functions that were obtained by fitting the results of beamline simulation.

The momentum and the radial position distribution used in the K_L^0 generation was shown in Fig 6.3. For the momentum (p), we used the following function:

$$\frac{dN}{dp} = N_0 \exp(-\frac{(p-\mu)^2}{2\sigma^2}), \tag{6.1}$$

where

$$\sigma = \sigma_0(1 - (A + S \cdot P)(p - \mu)), \tag{6.2}$$

N_0 denotes an arbitrary normalization factor, μ (mean) = 1.788529, σ_0 (dispersion) = 1.291137, A (asymmetric offset) = -0.3290585, and S (asymmetric slope) = 0.0303398.

For the radial position (r), we used the following function:

$$\frac{dN}{dr} = \frac{N_0}{1 + \exp((r - x_0)/s)}, \tag{6.3}$$

where N_0 is a normalization factor, x_0 (falling edge) = 1.85893, and s (slope of the beam shape) = 0.20780.

The angle of the K_L^0 was defined with the polar angle (θ) and the azimuthal angle (ϕ) to the beam axis. Basically, the direction of K_L^0 can be obtained by connecting the radial position at C6 and the target position. Since there remained an ambiguity due to the size of the target, small fluctuation was added to θ to implement this ambiguity. The ϕ distribution was initially set to be flat from 0 to 2π radian and later tuned with the data,

6.2.2 K_L^0 decay

The generated K_L^0's were traveled through the detector system until it decayed. The decay position was determined by the life time of K_L^0 (τ) and its Lorentz-boost factor. The distribution of the decay vertex (z) with a momentum ($p_{K_L^0}$) can be expressed as:

$$\propto \exp(-\frac{z}{\Delta z}), \tag{6.4}$$

where

$$\Delta z = c\tau\beta\gamma = c\tau \times \frac{p_{K_L^0}}{m_{K_L^0}}. \tag{6.5}$$

At the decay, K_L^0 was forced to decay into secondary particles of a specific decay mode. The secondary particles decayed according to the branching ratios as defined in the GEANT3 package. For $K_L^0 \to \pi^0\nu\bar{\nu}$, $K_L^0 \to \pi^\pm e^\mp \nu$, and $K_L^0 \to \pi^\pm \mu^\mp \nu$ (K_{l3}) decays, the Daliz plot

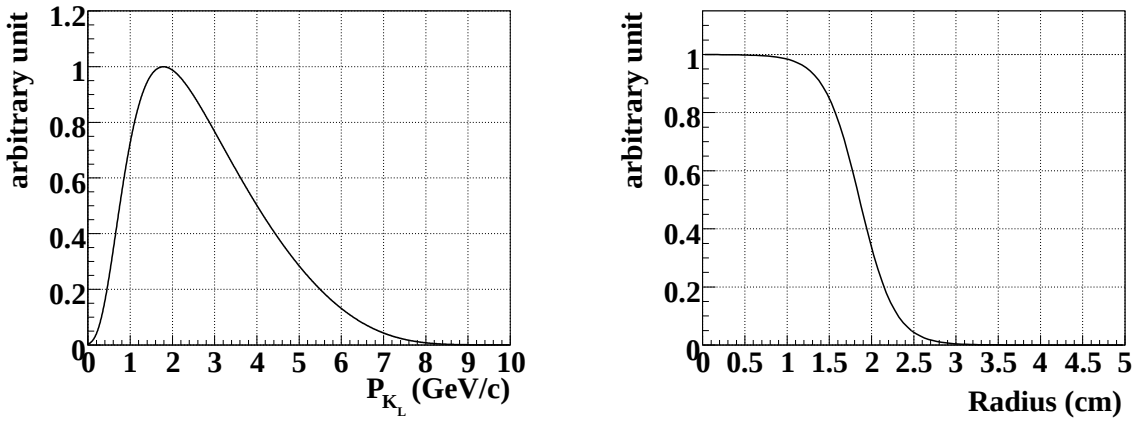

Figure 6.3: Functions used to determine the initial state of K_L^0's. Left plot shows momentum distribution expressed by Eq. 6.1 and right shows radial position distribution expressed by Eq. 6.3.

distribution was calculated by assuming the V-A interaction, implemented with the form factor taken from [10].

For the $K_L^0 \to \pi^0\nu\bar{\nu}$ decay, the distribution of the π^0 momentum was calculated as follows [29, 54]. In the Standard Model calculation substituting the neutrino mass to zero, the differential decay rate can be represented as

$$\frac{d\Gamma}{dE_\pi} \sim \lambda f_+^2[(m_K^2 - m_\pi^2 - q^2)^2 - \frac{2}{q^2}(\frac{q^2\lambda^2}{3} + 2m_\pi^2 q^4)], \tag{6.6}$$

where m_K is the mass of K_L^0, and E_π and m_π are the energy and the mass of the π^0, respectively, and

$$q^2 \equiv m_K^2 + m_K^2 - 2m_K E_\pi, \tag{6.7}$$

$$\lambda \equiv [(m_K^2 + m_\pi^2 - q^2)^2 - 4m_K^2 m_\pi^2]^{1/2}. \tag{6.8}$$

The form factor, f_+, was parameterized as $f_+ = 1 + \lambda_+ q^2/m_\pi^2$ with $\lambda_+ = 0.032$, which was measured by experiments [10]. The kinetic constraint,

$$m_\pi \leq E_\pi \leq (m_K^2 + m_\pi^2)/2m_K, \tag{6.9}$$

was also required.

Once the π^0's energy was chosen, by following the spectrum expressed in Eq. 6.6, its direction was determined isotropically in the K_L^0 rest frame. The π^0 was then boosted in the K_L^0 direction, and immediately decayed into two photons with a branching ratio of 98.8%.

6.3 Neutron simulation

Since the dominant background source in Run-2 analysis was the halo neutron background, it was important to estimate the amount of halo neutron background by using MC simulation in order to optimize the signal to background ratio. As described in Chap. 3.1.2, the neutron flux of the neutral beamline consisted of core neutron and halo neutron. We carried out core

neutron simulation to prove the reproducibility of hadronic code by examining the results of Al plate run. Halo neutron simulation was carried out to estimate the amount of halo neutron background in the physics run.

6.3.1 Halo neutron generation

Since halo neutrons were produced by the scattering or interaction in the absorbers or collimators, their direction could not be described by a simple formula. Thus, in generating of neutrons, the parameters of each event collected in the beamline simulation was directly used, instead of fitting functions as in the case of K_L^0 generation. The particles' position at C6 was represented by (R, ϕ_R), where R is the radial position from the center of beamline and ϕ_R denotes the azimuthal angle with respect to x-coordinate. Also the particles' direction was represented by $(\theta, \phi_R + \Delta\phi)$, where θ is the polar angle and $\Delta\phi$ is difference of the azimuthal angle from ϕ_R, as illustrated in Fig. 6.4.

To obtain enough statistics for the halo neutron simulation, we decided to take the method to recycle the collected neutrons by adding the small fluctuation with the Gaussian distribution. An example of adding the fluctuation for the momentum is:

$$p' = p(1 + g(\sigma_p)), \tag{6.10}$$

where $g(\sigma)$ is a Gaussian random function with the standard deviation of σ and the mean of 0. We set σ's to be 5% for the momentum, 2% for the R, 2% for the θ, and 0.5% for the $\Delta\phi$. For ϕ_R, we used uniform distribution. These smearing parameters were chosen as small enough not to change the distribution of each parameters, and as large enough not to affected by the particular events remaining in the beamline simulation.

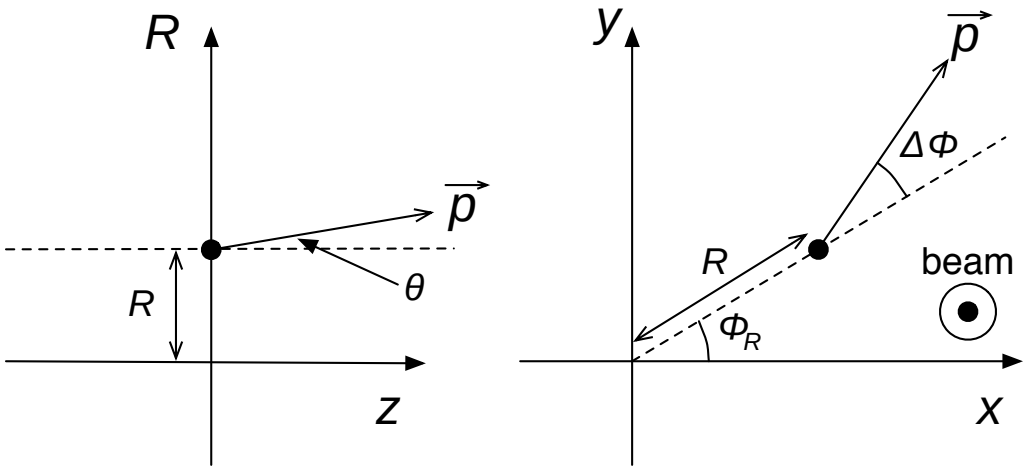

Figure 6.4: Definition of the parameters used in the halo neutron generation.

6.3.2 Simulation of neutron interaction in the detector

In the Analysis-2008, the interaction of halo neutron was simulated by using the GFLUKA hadronic package, which was integrated in the GEANT3 simulation code. The simulation code

had several problems for realistic estimation of the halo neutron background. First, it did not generate η particles. Second, the ratio between the number of produced π^0's at CC02 and that at CV was different from the actual data. Third, the amount of statistics was not sufficient due to its time-consuming simulation method. Because of these problems, the halo neutron background was estimated in different ways for CC02-π^0, CV-π^0, and CV-η, in the Analysis-2008.

To overcome these problems, we developed a Monte Carlo simulation using the FLUKA hadronic interaction model [52]. In the FLUKA package, η particles are produced intrinsically, the ratio between the numbers of produced π^0's at the CC02 and that at CV was confirmed by the real data, and the amount of statistics was increased by an early veto logic, which is described later. The reproducibility of the FLUKA hadronic code was confirmed by the Al-plate run, as will be described in Sec. 6.6.2. The results of the halo neutron simulation will be described in Sec. 8.1.

In the simulation, neutrons were generated according to the parametrization described in the previous subsection. The detectors located upstream from the CsI calorimeter, including the support structure of CV, were implemented. The generated neutrons were transfered into the detector system, and the interactions in the upstream detectors were simulated. The secondary particles hitting the CsI or escaping into the beam hole were recorded and fed into the detector simulation written by the GEANT3.

To save the CPU time needed for the simulation, we implemented an early veto logic, in which the events were discarded when the energy deposit in the upstream veto detector exceeded the veto threshold. This feature reduced the CPU time by roughly 1/10 of the case without it.

6.4 Detector Response

We simulated the detector response using the GEANT3 package. The interactions, such as pair production, multiple scattering, etc., were simulated with detector materials according to their cross sections. We traced particles until their energy became below a cut-off energy. The cut-off energy was set at 0.05 MeV for electrons, positrons, and photons, and 0.1 MeV for hadrons and muons.

We summed visible energy depositions in the sensitive detector material. The hit "timing" was simulated as the time when the summed energies exceeded the discriminator threshold used in the data taking. The summed energy deposition in each detector channel was defined as the "energy" in the detector except for MB, BCV, CV, APC, and BA. For the energy in CsI, we added the special treatment to simulate the energy resolution and photo-nuclear interaction. For other exceptive detectors, we implemented additional treatment to simulate the light propagation in these detectors.

The information of the energy deposit and timing of each detector were stored having the same data structure as the real data, and both the real and simulated data can be analyzed by the same analysis program.

6.4.1 Energy smearing for CsI

Energy resolution

The energy resolution σ_E/E can be represented [10] as

$$\frac{\sigma_E}{E} = a \oplus \frac{b}{\sqrt{E}} \oplus \frac{c}{E}, \tag{6.11}$$

where $\oplus$ represents addition in quadrature and E is in the unit of GeV. The constant term a comes from non-uniformity and calibration uncertainty, b is a stochastic term, and c is a noise term, which was known to be negligible in our electronics system. Since the a and b terms could not be reproduced by the interaction in the simulation, we imposed the additional fluctuation, called "smearing", to the energy in each CsI crystal, in order to adjust the energy resolution of MC to data.

The parameters for two types of CsI crystals were found to be different due to the difference of their light yields. Table 6.1 shows the parameters used to the energy smearing for each type.

Table 6.1: Parameters for the crystal-by-crystal smearing. Note that the noise term (c) was negligible in our experiment and set to be 0.

Crystal Type	Constant Term (a)	Stochastic Term (b)
Normal CsI	0.4%	0.8%
KTeV CsI	0.4%	0.6%

Photo-nuclear interaction

The photo-nuclear interaction is the interaction between photon and nucleus, like $\gamma + N \rightarrow p + N'$ or $n + N'$. When the photon makes photo-nuclear interaction in the CsI calorimeter, the visible energy can become smaller, especially in the case that neutron is emitted in the final state. Due to the loss in the visible energy caused by this interaction, the reconstructed position of π^0 was blurred in general. In particular, the effect of photo-nuclear interactions became important in analyzing the Al-plate run and the CC02-π^0 background. Since the photo-nuclear interaction was not implemented in the GEANT3 package, we needed to add an additional fluctuation to the visible energy of photon.

The effect of the photo-nuclear interaction was evaluated by a simulation using GEANT4. In the simulation, we compared the visible ratio of the photon energy in the CsI with and without the photo-nuclear interaction. Figure 6.5 shows the results of the comparison, where the input photon energy was 200 MeV. We see an increase in the number of events having the smaller visible energy in the case with the photo-nuclear interaction. By subtracting the results without the photo-nuclear interaction from that with the interaction and by normalizing them with the total number of events in the simulation, we obtain the probability of losing the visible energy by the effect of photo-nuclear interaction, as shown in Fig. 6.6.

We made the simulation with varying the photon input energy from 50 MeV to 1000 MeV with an interval of 50 MeV. Several lookup tables of the correlation between the visible ratio and the probability were prepared for various photon energies. The energies of two photons were reduced according to the lookup tables with an event weight. For the case that incident energies of two photons were E_1 and E_2, and their visible ratios were v_1 and v_2, the event weight was calculated as

$$w(v_1E_1, v_2E_2) = p(v_1, E_1) \cdot p(v_2, E_2), \tag{6.12}$$

where $p(v_i, E_i)$, $(i = 1, 2)$ denotes the probability of having the visible ratio of v_i for the input energy of E_i. The π^0 reconstruction was redone with the photon energies of v_1E_1 and v_2E_2. The results of the implementation of photo-nuclear effect will be described in Sec. 6.6.3.

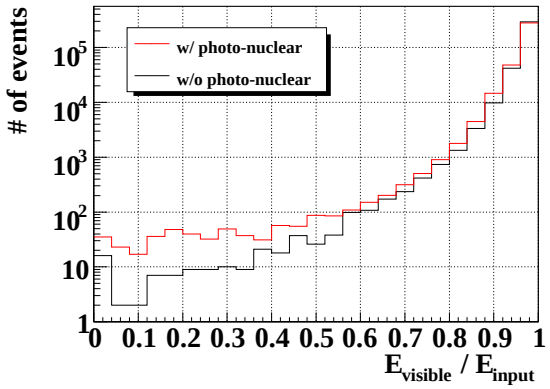

Figure 6.5: Distribution of visible ratio of the photon energy, obtained at the input energy of 200 MeV. Red (black) line shows the case with (without) the photo-nuclear interaction, respectively.

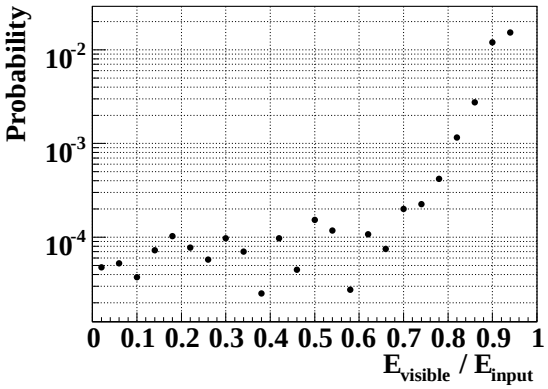

Figure 6.6: Probability to lose the visible ratio of the photon energy by the photo-nuclear interaction, obtained at the input energy of 200 MeV.

6.4.2 Other detectors

MB, BCV

Since the barrel detectors, MB and BCV, were 5 m long, the attenuation of scintillation light should be taken into account. The scintillation light was transmitted through WLS fibers and detected by PMTs at the both ends of the fibers. When a particle hit MB or BCV at a distance l from a PMT, the energy measured by the PMT was expressed as

$$E = E_0(a_l e^{-\frac{l}{\lambda_l}} + a_s e^{-\frac{l}{\lambda_s}}), \tag{6.13}$$

where E_0 is the energy deposition at the incident position, λ_l (λ_s) is the attenuation length and a_l (a_s) is a normalization factor for the long (short) term component, respectively. The energy to be detected at the PMTs was normalized for minimum ionization particles (MIPs) passing through the center of the barrel. It is 15 MeV for the MB inner module, 30 MeV for the MB outer module, and 2 MeV for BCV.

The hit timing of the incident particles at the PMTs was also simulated by taking the light propagation into account. Using cosmic ray muons, we measured the attenuation length and the light propagation speed. They are summarized in Table 6.2

Table 6.2: Parameters for the attenuation in the barrel detectors [46].

Detector	Light propagation speed (cm/ns)	λ_l (cm)	λ_s (cm)
MB	17.7 ± 0.1	608.0 ± 56.1	112.5 ± 14.8
BCV	18.2 ± 0.1	481.1 ± 54.5	87.7 ± 23.2

CV

As mentioned in Sec. 3.2.3, CV had an "strange" shape; it had a tapered shape and a 90°-bending at the middle. As a consequence, the relative light yield as a function of the hit position had a non-exponential dependence, as shown in Fig. 3.15. We corrected the effective light yield of the outer CV by using the relative light yield as the function of the hit position, as shown in Fig. 3.15.

APC

In the APC, Cherenkov lights emitted in aerogel blocks were read by a PMT. We simulated the optical transmission of Cherenkov lights in the APC module. The emitted Cherenkov lights were transmitted through the aerogel blocks, reflected by a mirror system, which was consisted of flat mirror and Winston-cone-shaped funnel, and detected at the PMT position. We implemented the transmittance of the aerogel blocks, which was measured by a LED, and the reflectance of the mirrors.

BA

BA consisted of the lead-scintillator (Run-2) / PWO scintillator (Run-3) and quartz modules. Since the quartz is a Cherenkov radiator, the light yield was calculated with β of each particle. The emitted photons was traced within the quartz blocks with the condition of the total reflection and detected at the positions of the PMTs.

6.5 Accidental activity

Since there were accidental activities in the detectors, those effect had to be added to the simulation. In the real experiment, the detector had many accidental activities, which were caused by particle coming either from the target or from other reactions. These accidental activities caused additional energy deposition in the detector, and affected the acceptance.

In order to check the effect of the accidental activities, we overlaid the experimental data collected by the accidental trigger on the generated MC events. The energy deposition was simply added together channel by channel. As for the timing information, we took the arrival time of the earliest hit. Acceptance loss due to the accidental activities was estimated independently, as described in Sec. 9.2.3.

6.6 Reproducibility of the MC simulations

Because the estimation for the acceptance and the background events was based on the Monte Carlo simulation, it was important to confirm the reproducibility of the simulation. First, we checked the distributions of kinematic variables for the $K_L^0 \to \pi^0\pi^0\pi^0$ decay mode. Second, the inefficiencies of the detector system was confirmed by checking the contamination from the $K_L^0 \to \pi^0\pi^0\pi^0$ decay to the four photon events. Also, the reproducibility of the FLUKA hadronic package was confirmed by the Al-plate run.

6.6.1 K_L^0 simulation

After imposing the treatments mentioned in the Sec. 6.4, we confirmed the reproducibility of the simulation by comparing the six photon events of the real data and the simulation. We found a mismatch in the radial shape of the Kaon beam, as shown in Fig. 6.7, where the radial position was calculated by taking the center of energy of six photons. This mismatch was caused by the difference in the beam shape at the last collimator C6; we generated K_L^0's according to a cylindrically-symmetric function, but the shape was oval in the real case. To adjust the difference, we applied an empirical weight function to the reconstructed values of MC events as:

$$w = 1.305 - 0.192559 r_{gen}^2 + 0.0029822 r_{gen}^4, \tag{6.14}$$

where r_{gen} is the radius of the generated K_L^0 at C6.

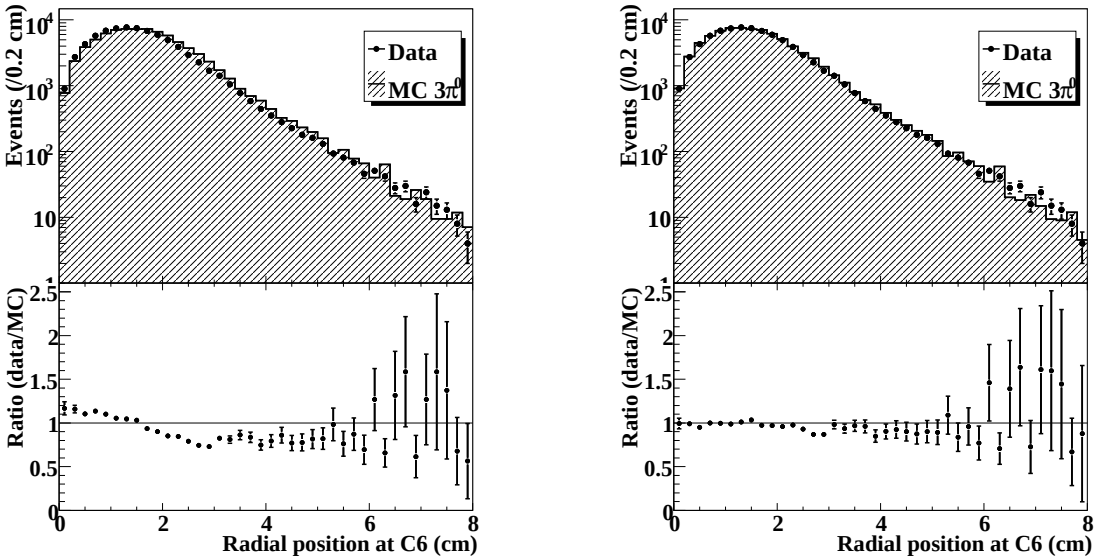

Figure 6.7: Reconstructed radial position distribution from the $K_L^0 \to \pi^0\pi^0\pi^0$ mode at the last collimator (C6). The left figure shows the case before the radial position correction and the right figure shows after the correction. In each plot, the top figure shows a comparison between the number of events in the data and MC, and the bottom figure shows the ratio between them. The MC data were normalized by the total number of events after imposing all analysis cuts for the $K_L^0 \to \pi^0\pi^0\pi^0$ mode, which is to be described in Sec. 9.2.2, except for the selection on the radial position.

Typical results of K_L^0 decay simulations: reconstructed mass, vertex position, momentum, and transverse momentum for the six-photon data samples are shown in Fig. 6.8. Here, the radial position corrections were included and the both veto cuts and kinematical selections were implemented, which will be described in Chap. 7. Each distribution is reproduced by the simulation of the $K_L^0 \to \pi^0\pi^0\pi^0$ decays. The method used to reconstruct the six-photon events and the event selections are described in a later section.

In addition to the distributions of kinematic variables for the $K_L^0 \to \pi^0\pi^0\pi^0$ decay mode, the events with four photons reconstructed in the calorimeter were analyzed in order to verify the detection inefficiency of photon counters in the simulation. Figure 6.9 shows the reconstructed mass distribution for four-cluster events. In addition to the $K_L^0 \to \pi^0\pi^0$ events at the K_L^0 mass,

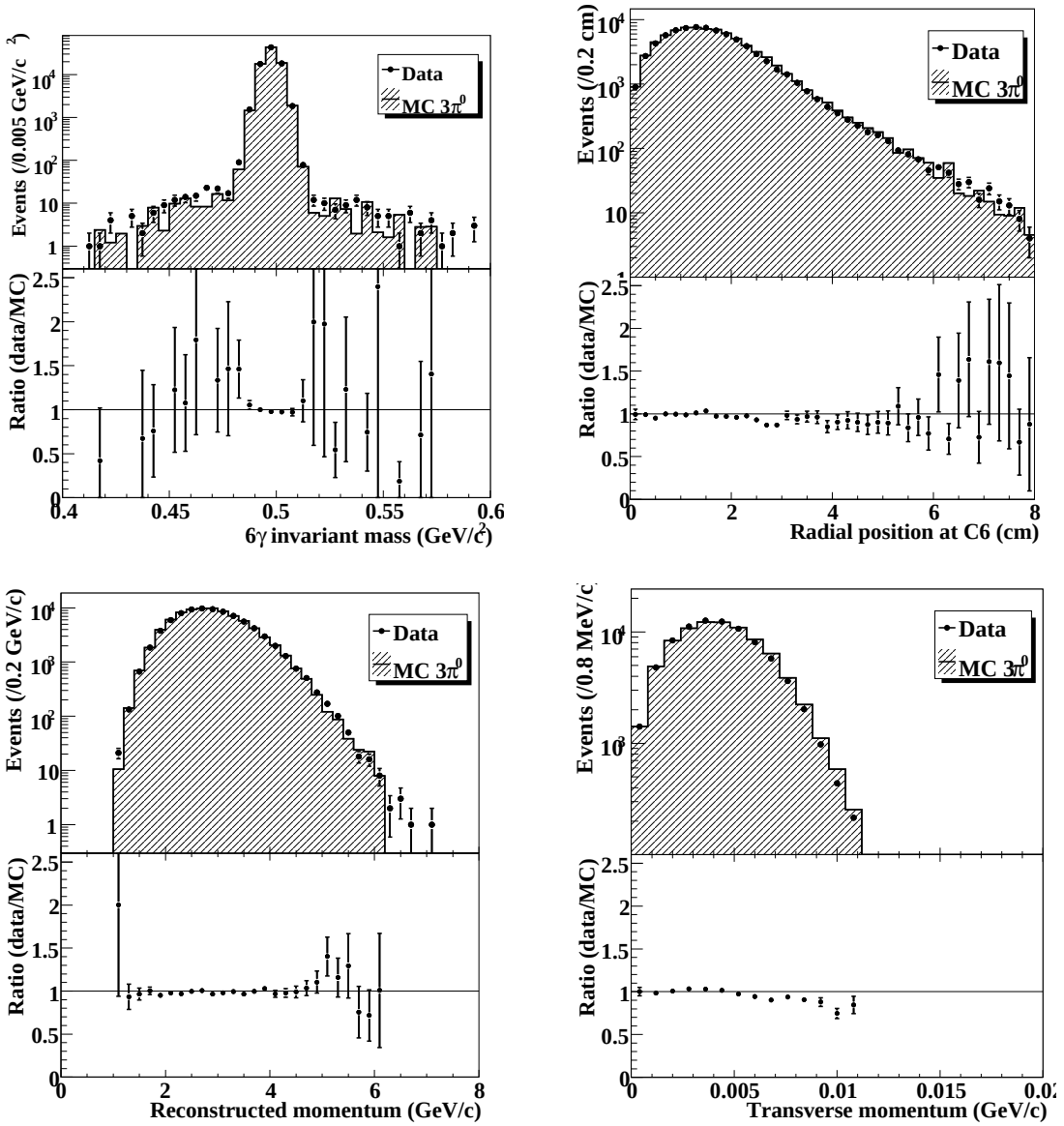

Figure 6.8: Distributions of reconstructed mass (top left), vertex position (top right), momentum (bottom left), and transverse momentum (bottom right) obtained from the six-photon data samples, compared to the data and the $K_L^0 \to \pi^0\pi^0\pi^0$ MC. In each plot, the top figure shows a comparison between the number of events in the data and MC, and the bottom figure shows the ratio between them.

there was a tail in the lower mass region due to contamination from $K_L^0 \to \pi^0\pi^0\pi^0$ events with two undetected photons out of six photons from the decay. The number of events in the tail was reproduced by our simulations.

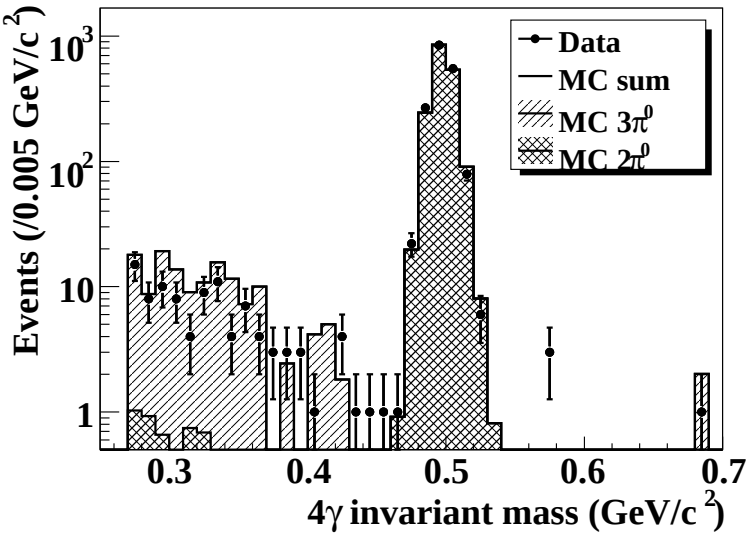

Figure 6.9: Reconstructed invariant-mass distribution of events with four photons in the calorimeter. The points show the data and the histograms indicate the contribution of $K_L^0 \to \pi^0\pi^0$ and $K_L^0 \to \pi^0\pi^0\pi^0$ decays (and their sum), as expected from the simulation, normalized by the number of events in the $K_L^0 \to \pi^0\pi^0$ peak.

6.6.2 Neutron simulation

In order to confirm the reproducibility of the FLUKA hadronic-interaction package, a simulation with the FLUKA code was carried out to the Al-plate run. In the Al plate run, a 0.5-cm-thick aluminum plate was inserted into the beam at 6.5 cm downstream of the rear end of CC02, as shown in Fig. 6.10. Because the position of the Al plate is known, the invariant mass of two photons can be reconstructed from the energy and position of two photons, as

$$M_{2\gamma}^2 = 2E_1E_2(1-\cos\theta)\ , \tag{6.15}$$

where E_1 and E_2 are the energies of two photons, and the opening angle between two photons, θ, can be calculated by assuming the vertex to be located at the Al target. Figure 6.11 shows the reconstructed mass distribution of two photons in the Al-plate run, by comparing the data and MC simulation. The MC events were normalized by the number of protons on target (POT). The number of events in the π^0 mass (0.14 GeV/c^2) and η mass (0.55 GeV/c^2) were reproduced by the simulation.

6.6.3 Photo-nuclear interaction

The effect of shower leakage and photo-nuclear interactions in the CsI was also examined by using the two photon events obtained in the Al-plate run. As described in Sec. 5.2, the decay

vertex of π^0 can be reconstructed by assuming that the invariant mass of two photons is π^0 mass. If the photon energy is incorrectly measured as being low due to the shower leakage or photo-nuclear interactions, the π^0 vertex position is reconstructed downstream of the true position. Because the true $Z_{\rm VTX}$ is known in the Al plate run, we can estimate the effect of these processes by using the tail in the distribution of the reconstructed $Z_{\rm VTX}$.

As described in the Sec. 6.4.1, the effects of the photo-nuclear interactions were estimated from GEANT4 simulations, and the results were fed into the detector simulation, which was based on GEANT3 package. Figure 6.12 shows the distribution of $Z_{\rm VTX}$ obtained from the Al-plate run by comparing the data and MC with and without the photo-nuclear effects. A tail on the downstream side of the peak is reproduced by the simulations with photo-nuclear interactions.

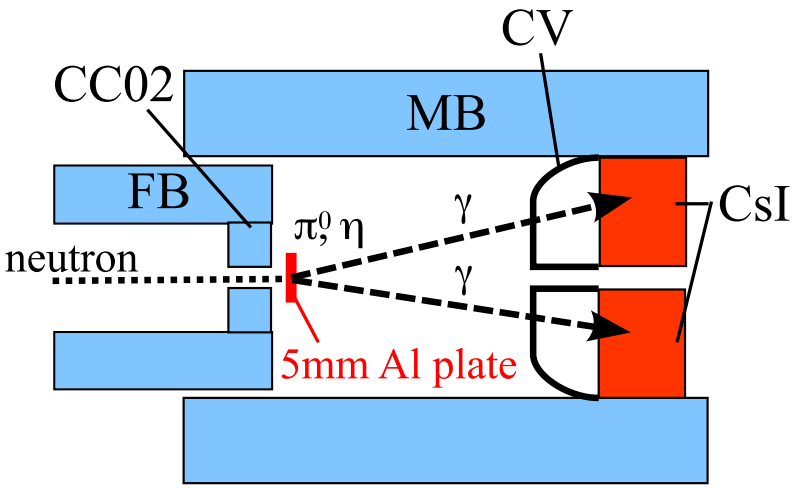

Figure 6.10: Schematic layout of the Al plate run.

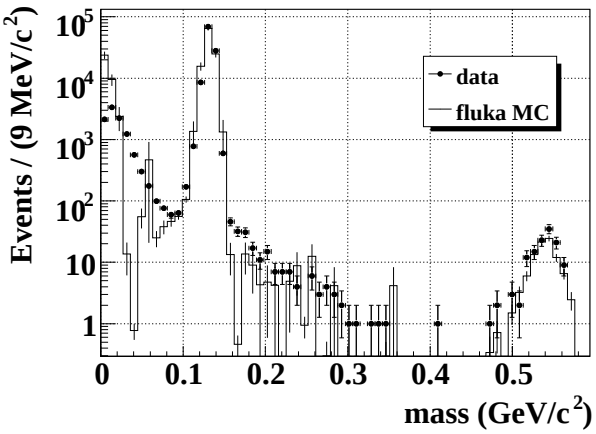

Figure 6.11: Reconstructed invariant mass distribution of the two-photon event in the Al-plate run. The points represent data and the solid line is from FLUKA simulations. The peaks at 0.14 GeV/c^2 0.55 GeV/c^2 correspond to $\pi^0$and η particles, respectively.

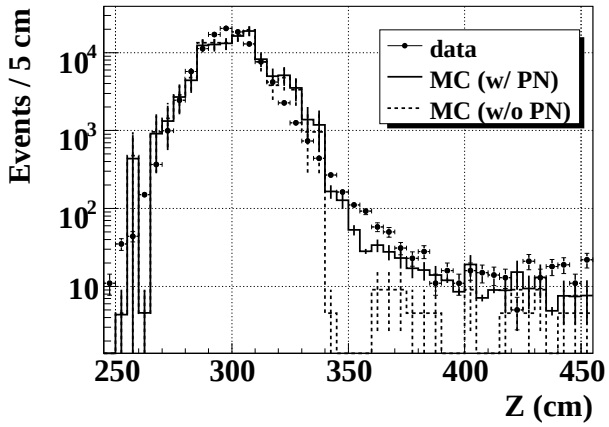

Figure 6.12: Reconstructed Z_{VTX} distribution of two photon events in the Al plate run. The points represent the real data and the solid (dashed) line is obtained from the FLUKA MC simulaiton with (without) the effects of photo-nuclear interaction.

Chapter 7

Event Selection

Brief summary

In this chapter, we introduce the method of event selections used in the $K_L^0 \to \pi^0\nu\bar{\nu}$ analysis. The event selections were consisted of veto cuts and kinematic selections. In the veto cuts, extra particles were rejected by using the hermetic veto detector system. The kinematic selections utilized the information of two photon clusters to obtain further separation between the signal and backgrounds.

The event selections were optimized based on the MC simulation for the signal and background events. We set the principle of the optimization as obtaining the maximum signal acceptance with keeping the signal-to-background ratio (S/N) as same as the Analysis-2008. During the optimization, the signal region was kept hidden in order to avoid biasing.

After reviewing the characteristics of each background source in Sec. 7.1, the principle of the optimization will be described in Sec. 7.2. Sections 7.3, 7.4, and 7.5 will discuss the details of the each veto cuts, kinematic selections, and signal region.

7.1 Characteristics of the signal and background events

Before describing the event selection and its optimization, we introduce the characteristics of the signal mode and each background source. Figure 7.1 shows the scatter plot in the P_T vs $Z_{\rm VTX}$ plane obtained by the Monte Carlo simulations for the signal mode (a) and main background sources (b – e). Some detailed descriptions on the signal mode and each backgrounds will be described subsequently.

7.1.1 The $K_L^0 \to \pi^0\nu\bar{\nu}$ signal

Figure 7.1(a), shows the distribution of the $K_L^0 \to \pi^0\nu\bar{\nu}$ signal events in the P_T-$Z_{\rm VTX}$ plane. As shown in the figure, the signal events were distributed almost uniformly in the fiducial region along $Z_{\rm VTX}$. For the P_T distribution, the maximum value was extended up to 1/2 of K_L^0 mass, and its peak was located at the 1/3 of K_L^0 mass. The signal region for the $K_L^0 \to \pi^0\nu\bar{\nu}$ signal is shown as the box surrounded by solid lines in the figure. The definition of the signal region will be described in Sec. 7.5.

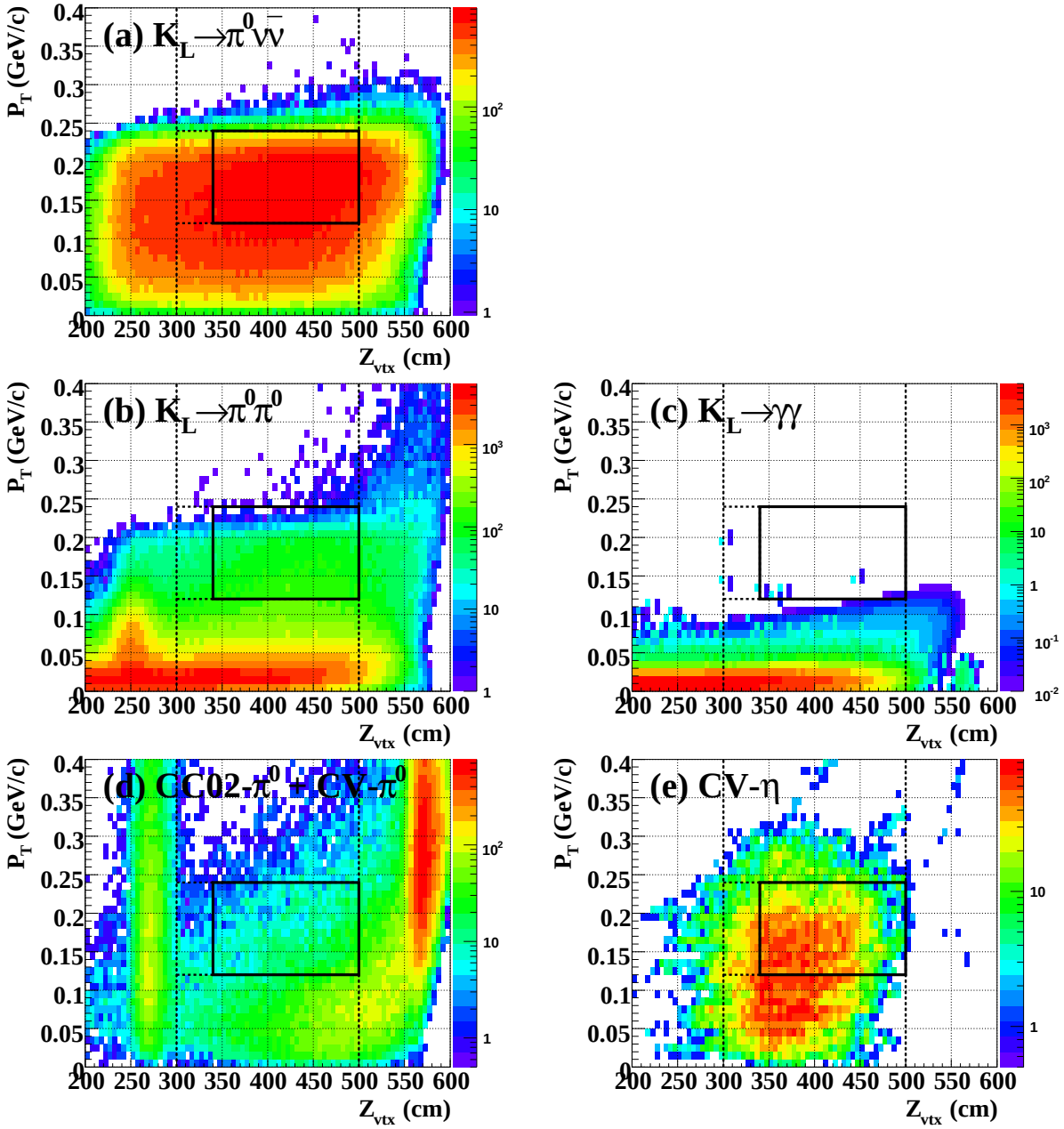

Figure 7.1: P_T vs. Z_{VTX}distributions of the reconstructed π^0's for the signal mode and background modes by MC simulation. The top left figure (a) shows the case of the $K_L^0 \to \pi^0\nu\bar{\nu}$ signal mode. Middle two figures show the case of kaon decay backgrounds: left is for $K_L^0 \to \pi^0\pi^0$ (b) and right is for $K_L^0 \to \gamma\gamma$ (c). Bottom two figures show the case of halo neutron backgrounds, where the left figure (d) shows the background caused by the π^0 production, *i.e.* CC02-π^0 and CV-π^0, and the right figure (e) shows the case of CV-η background. For all plots except for the $K_L^0 \to \pi^0\pi^0$ case, all veto cuts are imposed and no kinematic selections are applied. For the $K_L^0 \to \pi^0\pi^0$ background, only loose veto cuts without the timing requirement are applied to enhance the $K_L^0 \to \pi^0\pi^0$ events.

7.1.2 Kaon backgrounds

Because all major K_L^0 decay modes, except for the $K_L^0 \to \gamma\gamma$ decay, have at least two extra particles, vetoing the extra activities were the primary tool to reject these backgrounds. The $K_L^0 \to \gamma\gamma$ events could be strongly suppressed by the kinematic selection. Following, we describe the basic characteristics of K_L^0 decays.

Neutral decay modes

Among the backgrounds caused by the kaon decays, the $K_L^0 \to \pi^0\pi^0$ mode made the largest contribution. The $K_L^0 \to \pi^0\pi^0$ decay becomes background when two photons among four were undetected. Figure 7.1(b) shows the distribution of $K_L^0 \to \pi^0\pi^0$ events in P_T-$Z_{\rm VTX}$ plane with only loose veto cuts (Sec. 7.3) were applied. The reasons to make the mis-detection were: 1. photon detection inefficiency, and 2. "fused" cluster, where the two overlapping photons were reconstructed as one cluster in the CsI calorimeter.

As described in Sec. 2.3, the $K_L^0 \to \pi^0\pi^0$ "even" background events remained even after being imposed kinematic constraints on P_T. Because, in the $K_L^0 \to \pi^0\pi^0$ even background, the two photons in the CsI calorimeter are originated by a true π^0 decay, the kinematic selections on the two photons are not effective to suppress them. Thus, the contribution of the $K_L^0 \to \pi^0\pi^0$ background was measured by the detection inefficiency to the extra photons.

The $K_L^0 \to \gamma\gamma$ events are impossible to be removed by the photon veto cuts because the decay has only two photons in the final state. However, they can be strongly suppressed by applying kinematic selections, which use the nature of two body decay: the total transverse momentum of two photons becomes around zero, as shown in Fig. 7.1(c), and two photons are emitted in back-to-back direction in the K_L^0-rest frame.

Charged decay modes

Charged decay modes of K_L^0's, like $K_L^0 \to \pi^+\pi^-\pi^0$ or $K_L^0 \to \pi^\pm l^\mp \nu$ ($l = e, \mu$), were also possible to become background sources. The inefficiency of CV can cause to make them backgrounds. Especially, the $K_L^0 \to \pi^- e^+ \nu$ mode is the dangerous background source because,

- π^- can be missed by a charge-exchange interaction ($\pi^- + p \to \pi^0 + n$), and
- e^+ can be missed by a annihilation ($e^+ + e^- \to \gamma\gamma$),

where the photons in the final states can create photon clusters in the CsI.

The $K_L^0 \to \pi^+\pi^-\pi^0$ decay can also become background when the two photons from π^0 are detected in the CsI and π^+ and π^- are missed by the inefficiency of CV or BHCV.

7.1.3 Halo neutron backgrounds

Halo neutron backgrounds were the events made by the hadronic interaction between halo neutrons and the detectors located near the beamline. In these interactions, π^0's or η's were produced and decayed into two photons, resulting in imitating the signal mode. The extra particle veto again takes the dominant role to reduce these backgrounds, because the hadronic interactions of halo neutrons are often accompanied by extra particles such as protons or pions. To obtain the further reduction to the halo neutron backgrounds, several kinematical selections were implemented by using the characteristics of CC02-π^0, CV-π^0, and CV-η events.

CC02-π^0events

The CC02-π^0 events were the background caused by the interaction between the halo neutrons and the CC02. In the hadronic interaction, such as $n + N \to \pi^0 X$, π^0 may create two photon events and be reconstructed with large P_T.

Figure 7.1(d) shows the distribution in P_T-$Z_{\rm VTX}$ plane for the case that the π^0's were produced by the halo neutron interactions. As seen in the clustered events at $Z_{\rm VTX} = 275$ cm in the figure, the CC02-π^0 events should be reconstructed at the position of downstream face of CC02 ($Z = 275$ cm) and not reconstructed in the signal region. However, if the energy of either photon was mis-measured as being lower due to the shower leakage or photo-nuclear interaction in the CsI, $Z_{\rm VTX}$ could be shifted to the downstream. Also, the finite accuracy of the vertex reconstruction, due to the limitation in the position and energy resolution in the calorimeter, worsened the separation between the signal and background.

The difficulty in rejecting the CC02-π^0 events was that the two photons were real photons produced by a π^0 decay. Thus, it was difficult to reduce them by photon quality selections, which discriminated the cluster made by photons from that made by other activities. We introduced a kinematic selection using the information of reconstructed π^0 to reduce this background.

CV-π^0 events

The CV-π^0 events were made by the halo-neutron interaction in the CV, like $n + N \to \pi^0 + X$.

The P_T-$Z_{\rm VTX}$ distribution of CV-π^0 events are shown in Fig. 7.1(d). Ideally, the CV-π^0 events should be reconstructed at the position of CV, which was downstream of the signal region, as presented in the clustered events at $Z_{\rm VTX} = 560$ cm in the figure. On the contrary to the case of CC02-π^0, the CV-π^0 events became background if the reconstructed vertex were shifted upstream. This could occur when the energy of photon was mis-measured as being larger due to the fusion of multiple photons or the overlap of other hits in the calorimeter. The CV-π^0 events also became background when one cluster was made by a photon and the other cluster was made by other hadronic activities, such as neutrons.

To reduce these events, the selections on the cluster quality takes important role. These selections discriminate the genuine photon cluster from that made by other particles or contaminated by other activities.

CV-η events

In the CV-η events, the η particle was produced by the interaction like $n + N \to \eta + X$, where the η decays into two photons with the branching ratio of 39%. Since the two photon events were reconstructed with the π^0-mass assumption, $Z_{\rm VTX}$ could be shifted upstream and moved inside the signal region as shown in Fig. 7.1(e).

To reject the CV-η events, a special neural-network selection on the shape of photon cluster was developed, where the cluster shape was different due to the difference in the incident angle of photons. The special selection strongly reduced the number of background events.

7.2 Optimization principle for the event selections

In the current analysis, the optimization for the event selections was made based on the results of the Analysis-2008. We set the policy of the optimization as: maximizing the signal acceptance with keeping the S/N as the same level as in the Analysis-2008. In the optimization, the number

of signal events, or S, was determined by the signal MC simulation, and the number of noise (background) events, or N, was determined as the sum of the $K_L^0 \to \pi^0\pi^0$ and halo neutron backgrounds obtained by each MC simulation. During the optimization, the signal region for the real data, including both Run-2 and Run-3 data, was kept hidden in order to avoid human-biasing.

Figure 7.2 shows an example of the optimization. In this example, we show the case of a neural-network parameter called "CV-η neural network", which will be described in Sec. 7.4. We calculated the number of the signal, number of background events, and its ratio (S/N) by varying the selection threshold for the target value. Then we selected the optimum value that had the largest signal acceptance with the same S/N to the Analysis-2008 case as shown in the bottom left plot in Fig. 7.2.

The actual optimization was carried out simultaneously in a multidimensional parameter space. In order to equally optimize to suppress the three major background sources, CC02-π^0, CV-π^0, and CV-η backgrounds, the parameters suppressing each background source were selected to be optimized. The parameters of a fusion neural network (for CV-π^0suppression), CV-η neural network (for CV-η), π^0 projection (for CV-η), missing momentum (for CC02-π^0), and angle neural network (for CV-π^0 and CV-η) were optimized at the same time, where each parameter worked to suppress the background noted in the parenthesis. The explanation of the parameters will be found in Sec. 7.4.

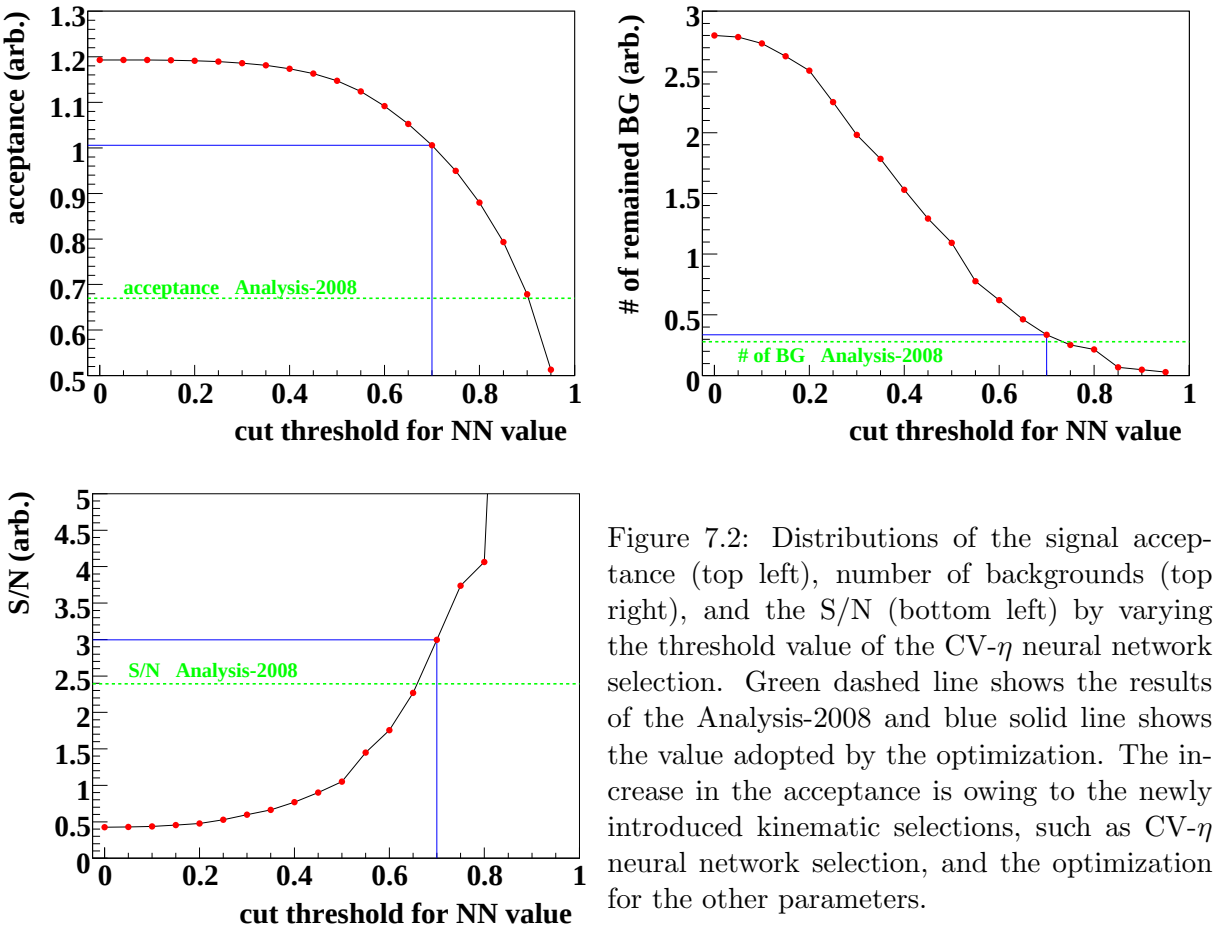

Figure 7.2: Distributions of the signal acceptance (top left), number of backgrounds (top right), and the S/N (bottom left) by varying the threshold value of the CV-η neural network selection. Green dashed line shows the results of the Analysis-2008 and blue solid line shows the value adopted by the optimization. The increase in the acceptance is owing to the newly introduced kinematic selections, such as CV-η neural network selection, and the optimization for the other parameters.

7.3 Veto cuts

As described in the Sec. 7.1, the particle veto with a hermetic detector system was the primary method to reject possible background sources, both for K_L^0 decay backgrounds and halo neutron backgrounds.

Several veto counters were applied two kinds of energy thresholds; loose one and tight one. For loose veto thresholds (typically, 10 MeV), no timing requirement was made, and for tight veto thresholds (typically, 1–2 MeV), events with a TDC value within roughly $\pm 5\sigma$ from the on-time peak were rejected. The reason to use two kinds of veto thresholds is described below. In order to reduce the acceptance loss caused by accidental hits, it is better to require the strict on-timing information for vetoing. Though, when such a strict timing is required, there could be a veto inefficiency caused by accidental hits, because, by using the single-hit TDC, the timing information at the veto timing might be masked by the accidental hit before the veto timing. Combining the two veto conditions, we balanced the efficiencies of detecting extra particles and the suppression of the acceptance loss caused by accidental hits. The actual thresholds are summarized in Table 7.1.

7.3.1 CsI veto cut

In addition to its main role of measuring the energy and position of photons, the CsI also served as a veto detector for extra photons. Extra activities that were not reconstructed as photon clusters, *i.e.* "single crystal hits," were rejected with this cut. However, a photon occasionally creates a single crystal hit near its genuine cluster due to fluctuations in the electromagnetic processes. Thus, applying a tight energy threshold for a single crystal hit near the photon cluster can cause acceptance loss for signal candidates. To recover this loss, the energy threshold for a single crystal hit was determined as a function of the distance to the closest cluster, d, as shown in Fig. 7.3:

- $E_{\text{thres.}} = 10$ MeV for $d < 17$ cm,
- $E_{\text{thres.}} = 5 - (3/8)(d - 17)$ MeV for $17 < d < 25$ cm,
- $E_{\text{thres.}} = 2$ MeV for $d > 25$ cm,

where $E_{\text{thres.}}$ is the energy threshold for a single crystal hit.

7.3.2 Other photon veto cuts

Main barrel

Because the MB was 5.5-m-long and the scintillation light was attenuated in propagating through the fibers to the PMTs, the energy deposit (E_{MB}), which was used for veto, was determined as the geometrical mean of the visible energies in both sides in order to cancel the position dependence of the light yield. Considering that the signal size at the PMT can be expressed as $E_{\text{PMT}} = E_0 \exp(-z/\lambda)$, where z is the distance to the PMT and λ is the light attenuation length of fibers (See Fig. 3.20.), E_{MB} can be written as,

$$E_{\text{MB}} = c\sqrt{E_{up} \cdot E_{dn}} \tag{7.1}$$

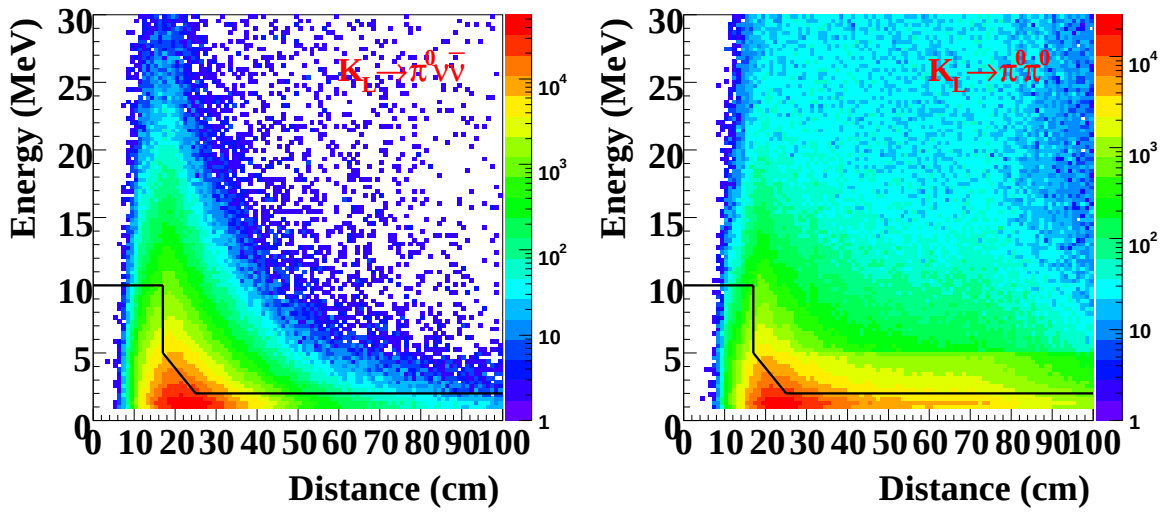

Figure 7.3: Energy deposition in a single hit crystal versus the distance from the nearest photon cluster of the two-photon events from the $K_L^0 \to \pi^0\nu\bar{\nu}$ (top) and $K_L^0 \to \pi^0\pi^0$ (bottom) simulations. The difference between two cases is that the $K_L^0 \to \pi^0\nu\bar{\nu}$ case does not include the single hit crystals made by extra photons, whereas the $K_L^0 \to \pi^0\pi^0$ case includes the single hit crystals caused by extra photons. Events above the solid line were rejected. Rejected events in the $K_L^0 \to \pi^0\nu\bar{\nu}$ sample represents the self-veto of the signal mode and those in the $K_L^0 \to \pi^0\pi^0$ sample represents the rejection of background events, respectively.

$$= c\sqrt{E_0 \exp(-\frac{z}{\lambda}) \cdot E_0 \exp(-\frac{L-z}{\lambda})} \quad (7.2)$$

$$= cE_0 \exp(-\frac{L}{\lambda}), \quad (7.3)$$

where c is calibration factor to each counter, $E_{up(dn)}$ is the signal recorded in the PMT at the upstream (downstream) end, E_0 is the energy deposition of the incident photon, z is the distance from the hit position to the upstream PMT, and L is the total length of the MB. Here, the $E_{\rm MB}$ is determined to be independent to the incident position of photon.

Because the timing in the MB was broadly distributed in the halo neutron backgrounds, we were not able to set a tight timing requirement for the tight energy threshold. Thus, the timing requirement for the MB was set as wide as the width of ADC gate ($\sim$ 200 nsec). When a photon hit the CsI calorimeter, low-energy photons and electrons that were created in an electromagnetic shower occasionally went backward and hit the MB. This process caused a larger acceptance loss in the MB as compared to the loss in other veto detectors.

Collar counters and BA

For the downstream collar counters (CC06 and CC07), the energy threshold was the looser one, in order to reduce accidental losses due to beam-induced activities. The BA located inside the beamline rejected photons escaping into the beam hole. The energy thresholds for these counters are summarized in Table 7.1.

7.3.3 Charged particle veto cuts

Background events produced by charged K_L^0 decay modes were mostly rejected by cuts on the charged particle veto detectors, mainly CV, BCV, and BHCV. As in the case of MB, energy deposit in the BCV was determined as the geometrical mean of the hits in the upstream and downstream ends, and the timing requirement was loosened. The energy thresholds for these counters are summarized in Table 7.1.

7.4 Kinematic selections

Kinematic selections were applied to discriminate the signal from background events by using the information of two photons in the CsI calorimeter. These selections can be categorized into three types: photon-cluster quality selections, two-photon selections, and π^0 selections. The detailed descriptions on these selections are in the following subsections. The values used in the kinematic selections are summarized in Table 7.2.

7.4.1 Photon-cluster quality selections:

Photon-cluster quality selections were developed using the information of each photon cluster. The cuts were applied to ensure that two photon clusters were from the $K_L^0 \to \pi^0\nu\bar{\nu}$ decay and were distinguished from fake clusters created by hadronic showers or photons produced by halo neutron interactions.

Table 7.1: Summary of loose and tight veto energy threshold for each detector. The timing requirements for the tight veto are also shown. The timing width was determined by the spread in the timing distribution of each detector.

Detector	Loose threshold	Tight threshold	(timing width)
CC00	—	2 MeV	($\pm$20.7 nsec)
FB	10 MeV	1 MeV [1]	($^{-44.9}_{+33.7}$ nsec)
CC02	10 MeV	1 MeV	($^{-12.0}_{+30.0}$ nsec)
BCV	—	0.75 MeV [2]	($\sim$200 nsec [6])
MB Inner	—	1 MeV [2]	($\sim$200 nsec [6])
MB Outer	—	1 MeV [2]	($\sim$200 nsec [6])
CV Outer	—	0.3 MeV	($\pm$7.7 nsec)
CV Inner	—	0.7 MeV	($\pm$12.6 nsec)
CC03	10 MeV	2 MeV	($^{-13.9}_{+20.9}$ nsec)
CsI	—	2–10 MeV [3]	($^{-10.5}_{+17.5}$ nsec)
Sandwich	—	2 MeV	($^{-7.0}_{+10.6}$ nsec)
CC04 Scintillator	10 MeV	0.7 MeV	($^{-11.6}_{+17.4}$ nsec)
CC04 Calorimeter	10 MeV	2 MeV	($^{-11.7}_{+17.6}$ nsec)
CC05 Scintillator	10 MeV	0.7 MeV	($\pm$12.0 nsec)
CC05 Calorimeter	10 MeV	3 MeV	($\pm$7.7 nsec)
CC06	20 MeV	10 MeV	($\pm$16.4 nsec)
CC07	50 MeV	10 MeV	($\pm$16.4 nsec)
BHCV	—	0.1 MeV	($\pm$7.3 nsec)
BA Scintillator (Run-2)	—	20 MeV [4]	($\pm$21.6 nsec)
BA PWO (Run-3)	—	50 MeV [4]	($^{-50.0}_{+30.0}$ nsec)
BA Quartz	—	0.5 MIPs [5]	($\pm$13.5 nsec)

[1] Sum of inner and outer layers.

[2] Geometrical mean of upstream and downstream ends.

[3] Depends on d. See the text for details.

[4] Summed over layers.

[5] Determined by AND logic of scintillator/PWO and quartz.

[6] The width corresponded to the ADC gate width.

Photon energy selection

The energies of two photons were required to be $E_H > 250$ MeV and $E_L > 150$ MeV, where E_H and E_L are the energies of the higher- and lower-energy photons, respectively. This selection helped to suppress the clusters made by hadronic showers, which tended to have lower energy. It also reduced the photon clusters having poor information, in which the other photon-cluster quality selections could not work effectively.

Cluster size selection

Selection on the number of the CsI crystals in one cluster ("cluster size") were imposed. Figure 7.4 shows an example of the photon cluster. The parameters "csize-5" and "csize-1" are the numbers of CsI crystals with the energy deposition greater than 5 MeV and 1 MeV, respectively. We required csize-5 ≥ 3 and csize-1 ≥ 5.

This selection worked similar to the photon energy selection; removing the clusters with low energy or poor information. It also worked to reject the clusters made by minimum ionizing particles from the charged decay modes.

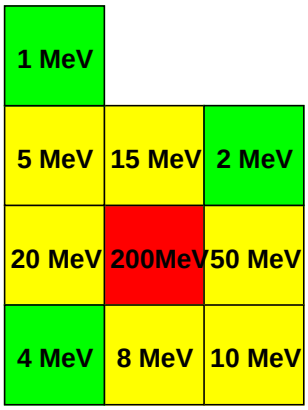

Figure 7.4: Example of the photon cluster.

Energy ratio

The parameter energy ratio or E_R was defined as:

$$E_R = \begin{cases} e_1/E_{sum} & \text{csize-1} \leq 2 \\ (e_1+e_2)/E_{sum} & \text{csize-1} = 3 \\ (e_1+e_2+e_3)/E_{sum} & \text{csize-1} \geq 4 \end{cases} \tag{7.4}$$

where csize-1 is the number of the crystals having the energy deposit greater than 1 MeV in the cluster, E_{sum} is the total energy deposit in the cluster, and e_1, e_2, and e_3 are the largest, second largest, and third largest energy deposit in the crystals, respectively. E_R was required to be greater than 0.88. This selection was effective to remove the wide-spread hadronic shower by the neutrons hits.

Timing dispersion selection

We defined the timing dispersion, TDI, as:

$$\mathrm{TDI} = \frac{1}{N}\sqrt{\sum_{i=1}^{N}(T_i - T_m)^2} \ \ (e_i > 1\mathrm{MeV}), \tag{7.5}$$

$$T_m \equiv \frac{1}{n}\sum_{i=1}^{n} T_i \ \ (e_i > 5\mathrm{MeV}), \tag{7.6}$$

where e_i is the energy deposit in each crystal, n and N are csize-5 and csize-1, respectively. T_m is the average time of the crystals in the cluster. This cut was to suppress the clusters contaminated by accidental hits. We required TDI to be less than 2.0.

Hit position selection

We required the position of the photons in the CsI calorimeter should be outside the 18.0 cm $\times$ 18.0 cm square area centered at the CsI calorimeter. This selection was to remove photons with shower leakage into the beam hole. It also worked to suppress the photons produced by the halo-neutron interactions in CV, because these photons tended to hit close to the beam hole.

We also required that all the photons in the CsI calorimeter should be within 88 cm from the center of the CsI calorimeter. This was to remove photons with shower leakage out of the calorimeter.

Fusion neural network selection

To remove the photon clusters contaminated by other activities, or "fusion clusters", a selection with neural network (NN) technique was developed. This selection worked against the $K_L^0 \to \pi^0\pi^0$ and CV-π^0 backgrounds. In the case of $K_L^0 \to \pi^0\pi^0$ background, a fusion cluster becomes a source of inefficiency to extra photons; in the case of CV-π^0 background, it results in a larger photon energy, with which the event vertex were shifted into the signal region.

By using the difference in the shape of the cluster, the fusion NN selection separated the fusion clusters from normal clusters. A fusion cluster have generally a wider shape compared to a normal cluster made by single photon hit, as illustrated in Fig. 7.5. As input parameters to the neural network, we used the energy deposits in the $3 \times 3 = 9$ crystals around the center of the cluster, and the cluster position and its azimuthal angle on the CsI face. This neural network was trained by single and fusion clusters obtained from the $K_L^0 \to \pi^0\pi^0$ MC samples. The rejection power of the fusion neural network selection is shown in Fig. 7.6; it shows the distribution of the output values from the neural network for the signal and CV-π^0 background events.

CV-η neural network selection

Another neural network selection on the cluster shape was developed to reject the CV-η background. Figure 7.7 illustrates geometric features of the CV-η background. Because η particles were mainly produced in the CV support structure or the inner CV module, the two photons produced by η decay tended to have large incident angles to the CsI calorimeter. The distribution of incident angle of photons in the $K_L^0 \to \pi^0\nu\bar{\nu}$ signal events and the CV-η events are shown in Fig. 7.8. The difference in the incident angle caused a different shape of photon cluster in

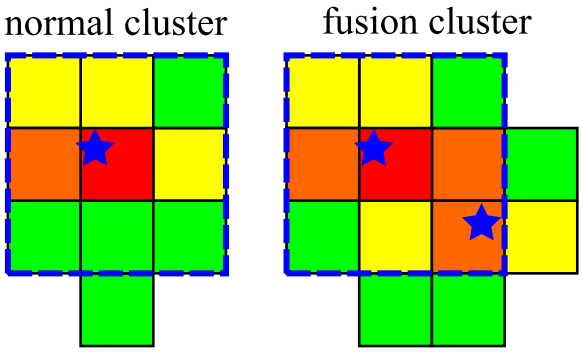

Figure 7.5: An illustration of normal (left) and fusion (right) cluster. The color of the boxes present the energy deposit of CsI crystals, where red (green) shows larger (smaller) energy. Blue stars mean the incident position of particle hitting the CsI. The energy deposits of 9 crystals surrounded by dashed lines are used as input parameters for the neural network in this example.

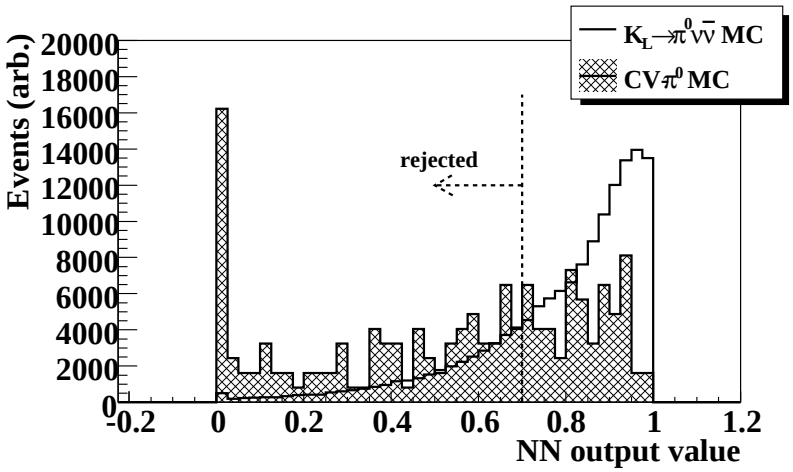

Figure 7.6: Distributions of the output values obtained by the fusion neural network selection for the signal mode (hollow) and the CV-π^0 background events (hatched). For the signal mode, all analysis cuts except for the fusion neural network selection are imposed. Several cuts are loosened for the background case in order to enhance the events. Note that the output values are calculated by combining the information of two photon clusters.

the CsI; the photon clusters in the CV-η background tended to have longer shape in the radial direction compared to the case of the signal events, as indicated in the right drawing of Fig. 7.7. By using this difference, the CV-η background were able to be separated from the signal mode.

An example of the discriminant can be presented as the "size" of photon clusters along the radial direction. Here we define a value showing the size of cluster along the radial direction, $\mathrm{RMS}_{\mathrm{radial}}$, as

$$\mathrm{RMS}_{\mathrm{radial}} = \sqrt{\frac{\sum_{i=1}^{N} r_i^2 E_i}{E_{tot}}} \quad (N = \text{csize-1}) \ , \tag{7.7}$$

where csize-1 is the number of crystals with the energy deposit larger than 1 MeV contained in a photon cluster. r_i is the radial component of the relative position of i-th crystal in a photon cluster E_i is the energy deposit of i-th crystal, and E_{tot} is the total energy deposit of the cluster. The comparison of this value between the CV-η background and the signal mode is shown in Fig. 7.9. As discussed above, the CV-η events had larger RMS values than the $K_L^0 \to \pi^0\nu\bar{\nu}$ events.

In order to reject the CV-η background effectively, we developed a selection using neural network technique. As input parameters to the neural network, we used radial and rotational position, and energy deposit of each crystal in a photon cluster. This neural network was trained by the MC samples of $K_L^0 \to \pi^0\nu\bar{\nu}$ and CV-η background. Figure 7.10 shows the performance of the CV-η neural network selection, where the signal events were clearly separated from the CV-η background events by the discriminant obtained by the neural network.

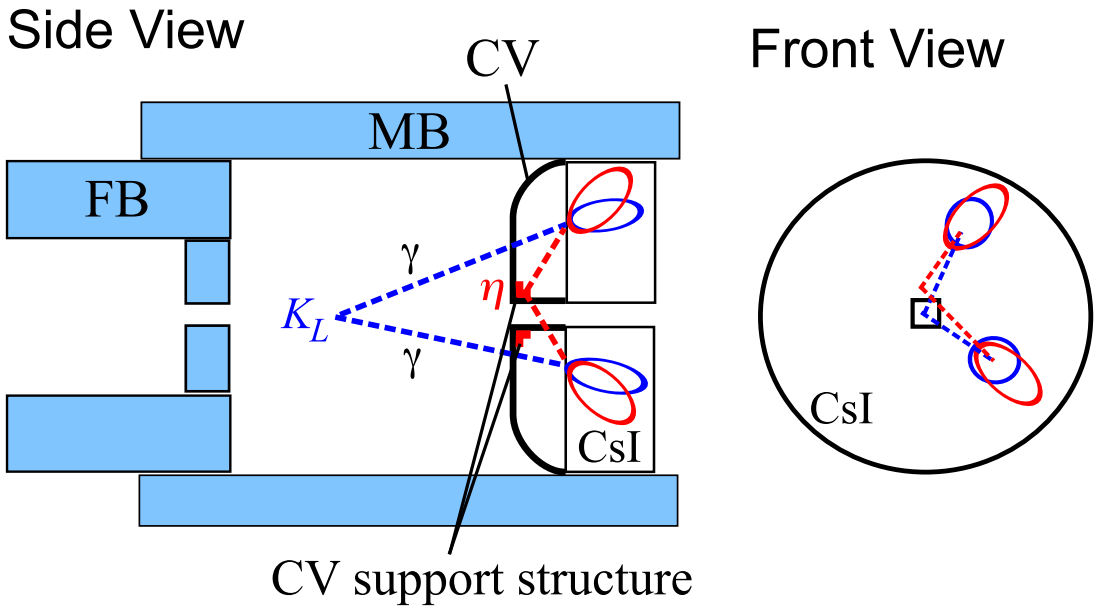

Figure 7.7: Schematic drawing of geometric features of the CV-η background compared to the $K_L^0 \to \pi^0\nu\bar{\nu}$ signal mode. Left drawing shows the cross-sectional view of the detection system, and right shows the front-side view of the CsI calorimeter. Red and blue ovals in both figures represent the spread of electro-magnetic shower in the CsI for the CV-η and the signal events, respectively.

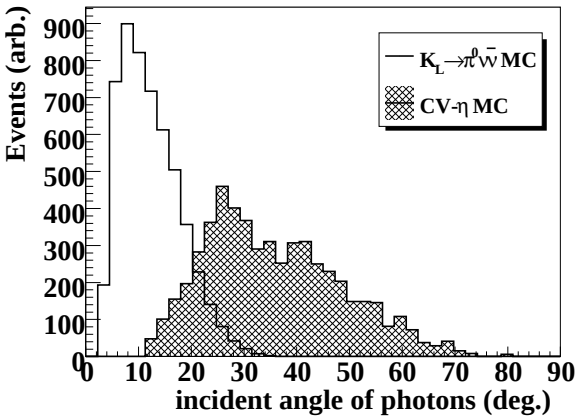

Figure 7.8: Incident angle distribution of photons for the $K_L^0 \to \pi^0\nu\bar{\nu}$ signal (hollow) and the CV-η background (hatched) events obtained by the MC simulation. All veto cuts and fiducial region selection in P_T-$Z_{\rm VTX}$ plane are imposed.

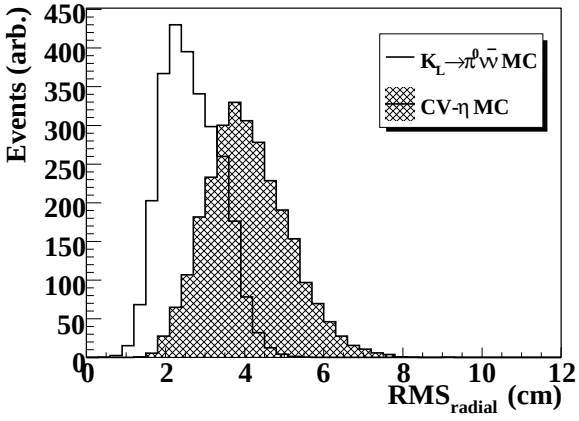

Figure 7.9: Distribution of RMS along the radial direction for the $K_L^0 \to \pi^0\nu\bar{\nu}$ signal (hollow) and the CV-η background (hatched) events, obtained by the MC simulation. All veto cuts and fiducial region selection in P_T-$Z_{\rm VTX}$ plane are imposed.

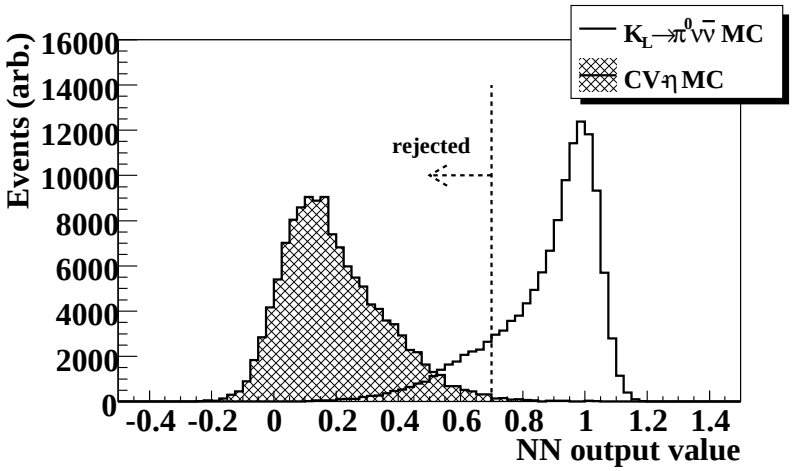

Figure 7.10: Distributions of the output values obtained by the CV-η neural network selection for the signal mode (hollow) and the CV-η background events (hatched). For the signal mode, all analysis cuts except for the CV-η neural network selection are imposed, and several cuts are loosened for the background.

7.4.2 Two photons selections

Two photons selections focused on the correlative properties of two photons in an event. These selections were basically worked against the accidental hits.

Distance selection

We required the distance between two photons to be greater than 15 cm. This selection was imposed to avoid the mis-identification of one photon for two.

Time difference selection

The timing difference between two photons were required to be $-9.6 < T(E_H) - T(E_L) < 18.4$ ns, where $T(E_H)$ and $T(E_L)$ are the timing of the higher and lower energy photons, respectively. This selection removed the events contaminated by the accidental activity.

Energy balance selection

In addition, the energy balance of two photons defined as $(E_H - E_L)/(E_H + E_L)$, was required to be less than 0.75. This selection was needed to reject the events including a soft cluster caused by accidental activities.

7.4.3 π^0 selections

By using the information for reconstructed π^0's, several selection criteria were imposed. These selections were used for rejecting the $K_L^0 \to \gamma\gamma$ and halo neutron backgrounds.

Kinetic energy selection

We required the kinetic energy of the reconstructed π^0's to be less than 2 GeV to suppress neutron backgrounds with high energy.

π^0 projection selection

In order to remove the CV-η background, we imposed another kinematic selection. We defined "π^0-projection" using $P_R \equiv P_T/P_Z$ vs. Z plot (where P_Z is longitudinal momentum). In the P_R-Z plane, events above the line defined by connecting (0.2, 300 cm) and (0.34, 500 cm) are discarded.

In this selection P_R represents the direction of π^0, thus $P_R \times (Z_{CsI} - Z_{vtx})$ means the projection of the trajectory of the π^0 on the CsI surface.

Missing momentum selection

If we knew the invariant mass of the $\nu\bar{\nu}$ system, we would be able to reconstruct the momentum of K_L^0 from the π^0 momentum in the $K_L^0 \to \pi^0\nu\bar{\nu}$ decay. We defined the "missing momentum" of the $\nu\bar{\nu}$ system in each event by assuming the invariant mass of the $\nu\bar{\nu}$ system ($m_{\nu\bar{\nu}}$) to be 0, *i.e.*, assuming a two-body decay.

We calculated the missing momentum (P_{miss}) with the constraint that P_T of the whole system should be balanced:

$$\begin{aligned} m_{\nu\bar{\nu}} &\equiv 0 \\ A &= E^2 - P_Z^2 \\ B &= \tfrac{1}{2}(m_{K_L^0}^2 - m_{\pi^0}^2) - P_T^2 \\ D &= (B \cdot P_Z)^2 - A[E^2 \cdot (P_T^2 + m_{\nu\bar{\nu}}^2) - B^2] \\ P_{miss} &= (B \cdot P_Z - \sqrt{D})/A \\ P_{min} &= P_{miss} + P_Z \end{aligned} \tag{7.8}$$

where E, P_T and P_Z are the total energy, the transverse momentum, and the longitudinal momentum of π^0, respectively. P_{min} is the minimum value of the reconstructed momentum of K_L^0 consistent with the $K_L^0 \to \pi^0\nu\bar{\nu}$ decay. P_{min} was found to be larger in the CC02 background events than the typical signal events, as shown in Fig. 7.11. The P_{min} was required to be smaller than 2 GeV/c.

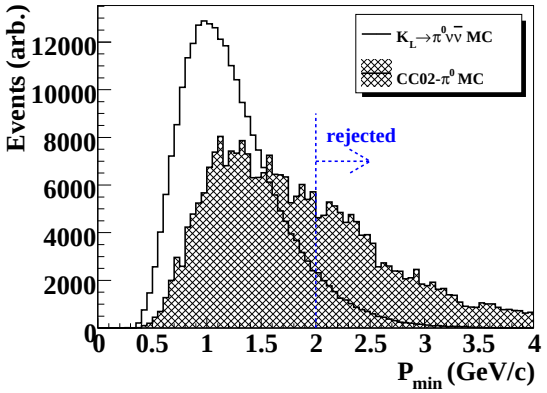

Figure 7.11: Distributions of the P_{min} parameters obtained by the signal and CC02-π^0 MC simulation.

Projected opening angle selection

For the $K_L^0 \to \gamma\gamma$ backgrounds, the primary method to remove them was the P_T requirement because the $K_L^0 \to \gamma\gamma$ events cannot have large P_T. However, if one of the photons was mismeasured due to the photo-nuclear interaction or the large leakage of the electromagnetic shower, the $K_L^0 \to \gamma\gamma$ events could result in high P_T. In order to suppress such events, a selection using the geometry of the $K_L^0 \to \gamma\gamma$ events was developed. We calculated the opening angle between the two photon directions projected onto the CsI calorimeter plane (θ_{proj}), as shown in Fig. 7.12. The projected opening angle was required to be less than 135 degrees. Figure 7.13 shows the rejection power of the selection to the $K_L^0 \to \gamma\gamma$ background.

Angle neural network selection

A neural-network selection was applied to the discrepancy between two angles. One angle was calculated by connecting the incident position of photons and the position of reconstructed π^0's (θ_{rec}), and the other angle was estimated by the neural network based on the cluster shape (θ_{NN}).

The neural network was trained by a MC sample in which the photons were injected to the 15×15 CsI crystals with a flat distribution of incident angle. The information of 3×3 crystals were fed into the neural network. The performance of the angle estimation is shown in Fig. 7.14

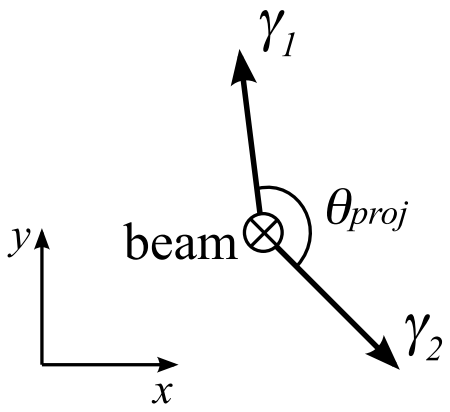

Figure 7.12: Schematic view of the projected opening angle. The figure is viewed along the beam direction.

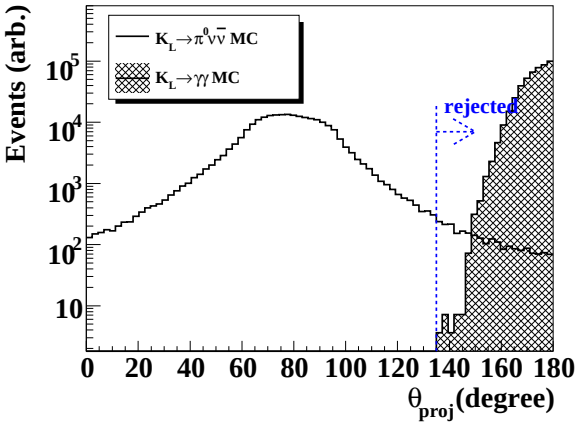

Figure 7.13: Distributions of the θ_{proj} parameters obtained by the $K_L^0 \to \pi^0\nu\bar{\nu}$ and $K_L^0 \to \gamma\gamma$ MC simulation.

by taking the correlation between the true incident angle and the angle obtained by the neural network.

We calculated the difference between two angles as $\Delta\theta = \theta_{rec} - \theta_{NN}$ for each photon. We required $\Delta\theta \geq -20$degrees for both photons. This selection suppressed CV-π^0 and CV-η backgrounds because the discrepancy of the angle increased in these processes. The rejection power of the selection is demonstrated in Fig. 7.15.

7.5 Signal region

We set the signal region in the $Z_{\rm VTX}$-P_T plane to be square shape of $340 \leq Z_{VTX} \leq 500$ cm and $0.12 \leq P_T \leq 0.24$ GeV/c. The requirement on $Z_{\rm VTX}$ was determined to avoid background π^0's coming from the CC02 (upstream) and CV (downstream). The lower limit for P_T was set to reduce the $K_L^0 \to \pi^0\pi^0$ and CV-η backgrounds; these events cluster in the low P_T region due to kinematics and a large halo neutron flux near the beam center, respectively. The upper bound for P_T was determined by the kinematic limit of the $K_L^0 \to \pi^0\nu\bar{\nu}$ decay, whose maximum value is 0.231 GeV/c.

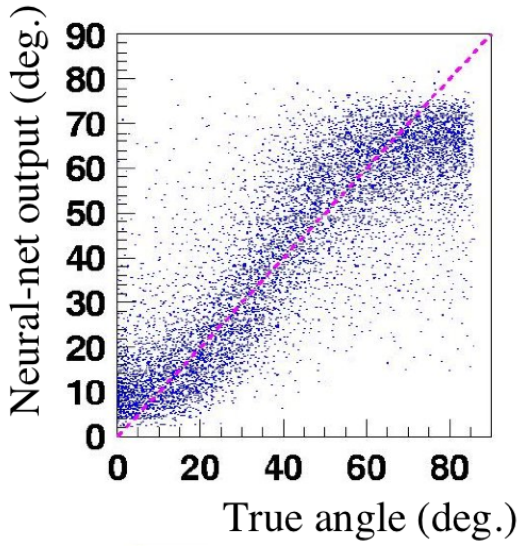

Figure 7.14: Performance of the angle neural network. The correlation between the MC true incident angle and the angle obtained by the neural network is shown.

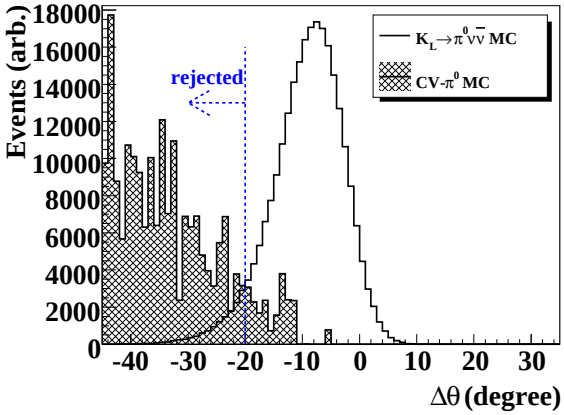

Figure 7.15: Distributions of the $\Delta\theta$ parameters by comparing the $K_L^0 \to \pi^0\nu\bar{\nu}$ signal and CV-π^0 background MC samples.

Table 7.2: Kinematic selections for the $K_L^0 \to \pi^0\nu\bar{\nu}$ events.

Selection		Min.	Max.
Photon quality selections	higher energy	250 MeV	
	lower energy	150 MeV	
	cluster size (5 MeV)	3	
	cluster size (1 MeV)	3	
	energy ratio	0.88	
	TDI		2.0
	hit position	18 cm (sq.)	88 cm (radial)
	fusion NN	0.7	
	CV-η NN	0.7 (ave.)	
Two photon selection	distance	15 cm	
	timing difference	-9.6 ns	18.4 ns
	energy balance		0.75
π^0 selections	kinetic energy		2 GeV
	π^0projection	(see text)	
	missing momentum		2.0 GeV
	projected opening angle		135°
	angle NN	-20°	

Chapter 8

Background Estimation

Brief summary

In this chapter, we estimate the number of backgrounds after imposing all analysis cuts. The estimation was mainly based on the MC simulation for each process. The background was consisted of the halo neutron background, K_L^0 background, and other background.

The number of halo neutron background events were estimated by the simulation based on the FLUKA hadronic-interaction package. The reproducibility of the background estimation was confirmed by comparing the P_T-Z_{VTX} distribution of the data and the simulation. The number of halo neutron background events in the simulation was normalized by using the number of events in the upstream of the fiducial region. We estimated the number of backgrounds for CC02-π^0, CV-π^0, and CV-η backgrounds to be 0.66, <0.36, and 0.19, respectively.

The K_L^0 background was estimated by the simulation based on GEANT3. Among the K_L^0 backgrounds, the $K_L^0 \to \pi^0\pi^0$ decay made the largest contribution, and the number of remaining events was estimated to be 0.02. For $K_L^0 \to \gamma\gamma$, the events were suppressed by large P_T requirement and projected angle selection, and for charged decays, the events were suppressed by the charged vetoes. In both cases, the number of the remaining events was estimated to be negligibly small.

In addition to the halo neutron and K_L^0 backgrounds, two other mechanisms were considered as background sources: the backward-going π^0 and the residual gas background. The backward-going π^0 background was caused by hadronic interactions of halo neutrons in the vacuum vessel, which was located downstream of the CsI calorimeter, and the residual gas background was caused by hadronic interactions between core neutrons and residual gas in the decay volume. The backward-going π^0 background was estimated by the FLUKA-based simulation, and the residual gas background was estimated by a dedicated run under the atmospheric pressure. Both background was estimated to be small enough in the current analysis.

8.1 Halo neutron background

The halo neutron background was estimated by combined MC simulations with FLUKA and GEANT3, where the hadronic interaction was estimated by FLUKA and the detector response was estimated by GEANT3. Because the veto cuts on the upstream detectors (CC00, FB, CC02, MB, BCV, and CV) were already applied as an early veto in the halo neutron MC generation, as described in Sec. 6.3.2, the veto cuts on these counters were removed in estimating the halo

neutron background.

Figure 8.1 shows the distribution of background events in the $Z_{\rm VTX}$-P_T plane as estimated from the MC samples of halo neutrons and the $K_L^0 \to \pi^0\pi^0$ backgrounds (described later), with an comparison to the data. The outside of the signal box was divided into four regions, as shown in Fig. 8.1. These were normalized to the number of events in the upstream region (shown as Region-(1)). The normalization factor was 0.318, which corresponded to 3.15 times larger statistics as compared to the combined data sample of Run-2 and Run-3. The factor can be compared to that calculated by the number of protons on target (POT). The value obtained by the POT was 0.213; the MC predicted larger backgrounds than the actual data by 50%. This 50% difference was reasonable by considering the ambiguity in simulating the hadronic interactions.

The numbers for events outside the signal box were compared between the data and the MC, as listed in Table 8.1. The numbers of events in each region are consistent within the statistical uncertainties between the data and the MC. Possible impacts of discrepancies outside the signal box on the estimation inside the signal box are included in the systematic uncertainties below, and will be discussed in detail in a later section (Sec. 11.2).

8.1.1 CC02-π^0 background

For estimating the CC02-π^0 background, the effect of shower leakage and photo-nuclear interactions described in Sec. 6.4.1 were taken into account. Figure 8.2 shows the distribution of the $Z_{\rm VTX}$distribution by comparing the data and MC simulation, where the shape in the downstream from the position of CC02 (Z = 275 cm) was reproduced by the simulation.

After applying all event selections, we estimated $0.66 \pm 0.33_{\rm stat} \pm 0.20_{\rm syst}$ background events in the signal box for the combined data sample of Run-2 and Run-3. Estimation of the systematic uncertainty is described in a later chapter.

8.1.2 CV-π^0 background

For CV-π^0 events, a fusion cluster or a cluster made by a neutron produces background. These events were suppressed by the fusion neural network and the angle neural network selections. After applying all event selections, no events inside the signal box were obtained with 3.15 times larger statistics as compared to the data, as shown in Fig. 8.4. Thus, we set an upper limit of 0.36 events at the 1σ level for this process.

8.1.3 CV-η background

For the CV-η background, the events were recycled 10 times for the same event seeds in order to increase the statistics. CV-η events were strongly suppressed by the dedicated neural network selection on the cluster shape, as shown in Fig. 8.5. A value of $0.19 \pm 0.08_{\rm stat} \pm 0.10_{\rm syst}$ events was estimated for this process. In estimating the statistical error, the events coming from same event seeds were treated as grouped.

8.2 K_L^0 background

The K_L^0 background was estimated by using GEANT3-based MC simulations that were performed separately for Run-2 and Run-3 conditions. Table 8.2 summarizes the MC event samples used to estimate K_L^0 backgrounds.

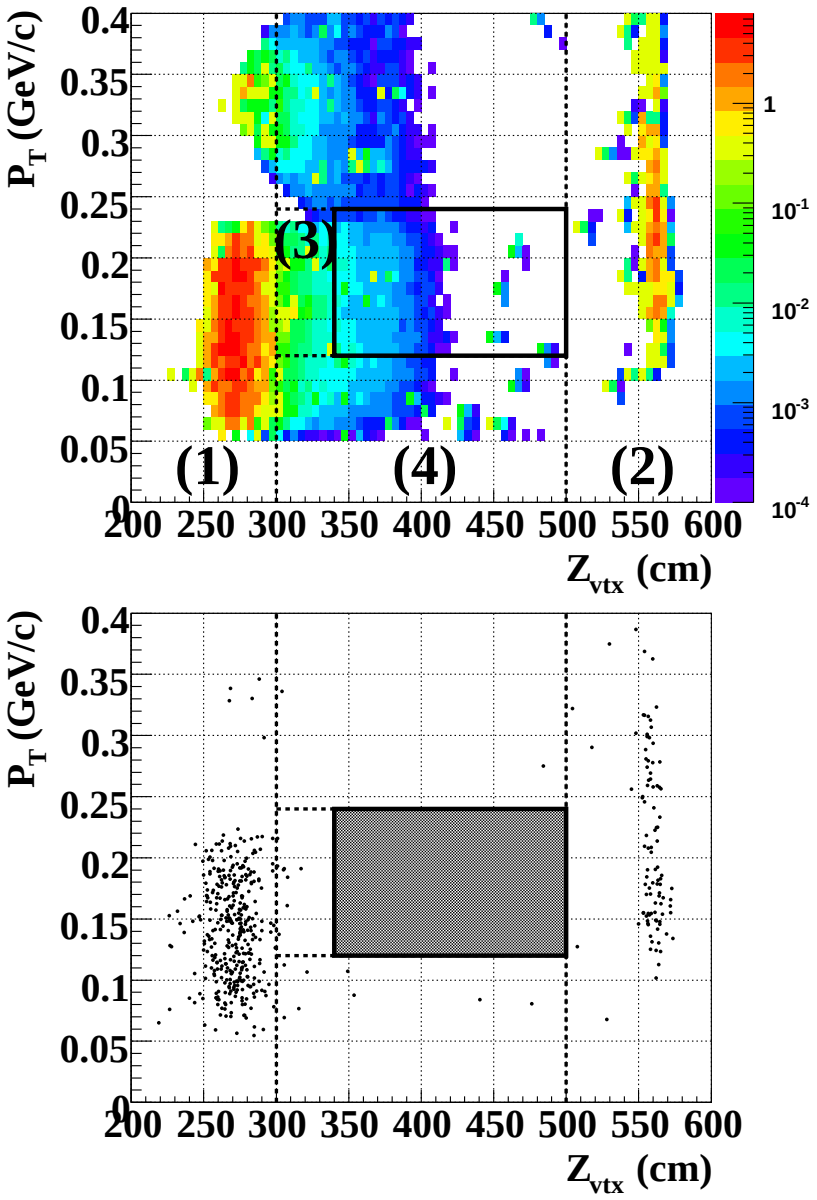

Figure 8.1: Scatter plot of P_T vs. the reconstructed Z position after applying all cuts to the MC samples for background simulation (top) and the real data (bottom). The MC samples include halo neutron and $K_L^0 \to \pi^0\pi^0$ backgrounds. The data includes both Run-2 and Run-3 samples, where the signal region is masked. The region bounded by the solid line shows the signal box. Events around $Z_{VTX} = 275$ cm are halo neutron events reconstructed at the position of CC02, and those around $Z_{VTX} = 560$ cm are events reconstructed at the CV. The numbers of events in each region are listed in Table 8.1.

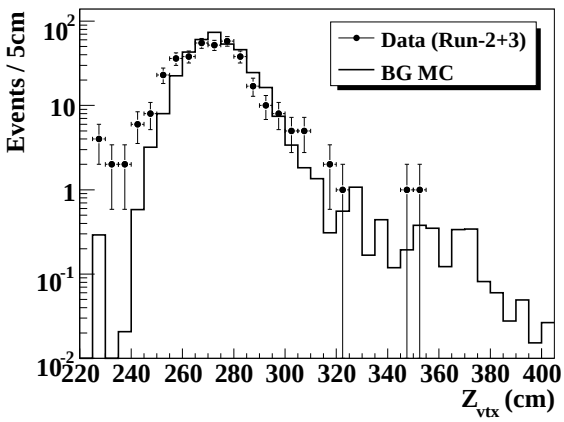

Figure 8.2: Distribution of the reconstructed vertex position for the CC02-π^0 events, by comparing the data (dots) and MC simulation (solid line).

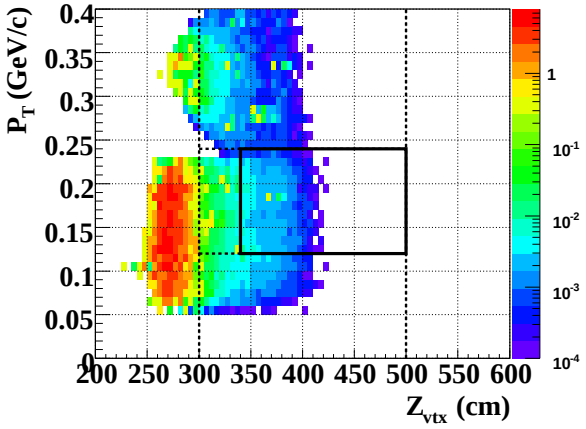

Figure 8.3: $Z_{\rm VTX}$-P_T distribution of CC02-π^0 background events after imposed all analysis cuts.

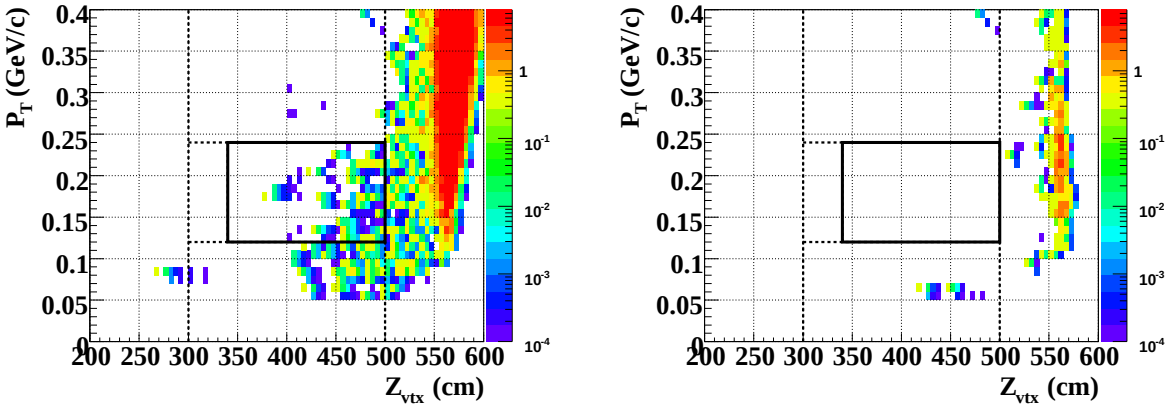

Figure 8.4: $Z_{\rm VTX}$-P_T distribution of CV-π^0 background events. In the left plot, the fusion neural network and angle neural network selections are removed from the all analysis cuts in order to enhance the CV-π^0 events. All analysis cuts are imposed in the right figure.

Table 8.1: Estimated numbers of events outside the signal region, compared with the combined data samples of Run-2 and Run-3. Note that the numbers of events estimated by the MC simulation were normalized in Region-(1). Errors in the MC estimates indicate statistical uncertainties.

Region		Data	MC estimation
Region-(1)	(CC02)	360	360.0 ± 15.6
Region-(2)	(CV)	101	77.2 ± 5.6
Region-(3)	(upstream)	8	5.9 ± 1.1
Region-(4)	(low-P_T)	8	2.9 ± 0.9
Signal box		(masked)	0.87 ± 0.34

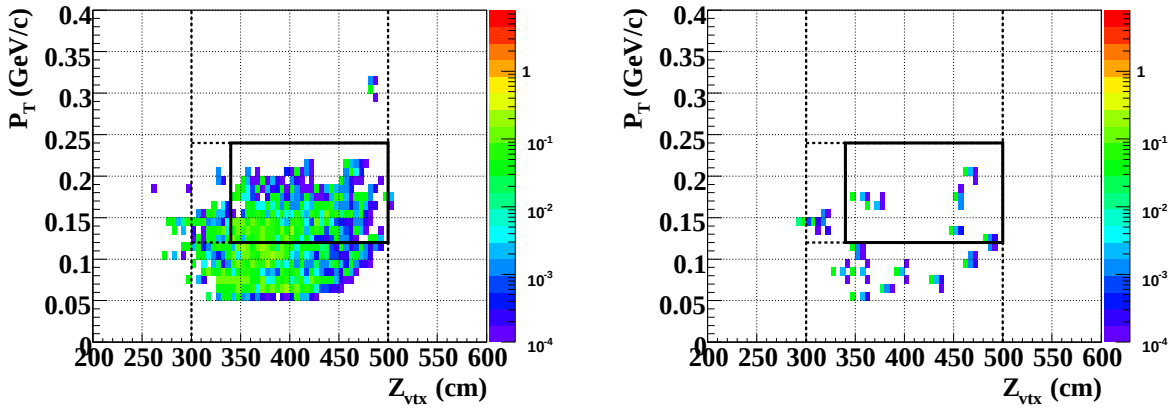

Figure 8.5: Z_{VTX}-P_T distribution of CV-η background events. In the left plot, the CV-η neural network selection is removed from all analysis cuts in order to enhance the CV-η events. All analysis cuts are imposed in the right figure.

Table 8.2: Summary of MC samples used to estimate K_L^0 backgrounds. N_{decay} is the number of decays in the fiducial volume and sample size is the equivalent amount of statistics compared to the Run-2 and Run-3 data.

Mode	Branching ratio	K_L^0 at C6	N_{decay}	Sample size
$K_L^0 \to \pi^0\pi^0$	$(8.69 \pm 0.04) \times 10^{-4}$	1.4×10^{10} (Run-2)	3.0×10^8	$\times 67$ of Run-2
		8.5×10^9 (Run-3)	1.8×10^8	$\times 59$ of Run-3
$K_L^0 \to \gamma\gamma$	$(5.48 \pm 0.05) \times 10^{-4}$	5.0×10^8 (Run-2)	1.1×10^7	$\times 3.8$ of Run-2
		8.0×10^8 (Run-3)	1.7×10^7	$\times 8.7$ of Run-3
$K_L^0 \to \pi^- e^+ \nu$	$(20.27 \pm 0.08)\%$	1.0×10^9 (Run-2)	2.1×10^7	2.1% of Run-2
		1.0×10^9 (Run-3)	2.1×10^7	3.0% of Run-3
$K_L^0 \to \pi^+\pi^-\pi^0$	$(12.56 \pm 0.05)\%$	2.0×10^9 (Run-2)	4.3×10^7	6.6% of Run-2
		2.0×10^9 (Run-3)	4.3×10^7	9.5% of Run-3

8.2.1 $K_L^0 \to \pi^0\pi^0$ background

Among the backgrounds from K_L^0 decay, the $K_L^0 \to \pi^0\pi^0$ mode made the largest contribution. The amount of Monte Carlo statistics for the $K_L^0 \to \pi^0\pi^0$ mode was roughly 70 (60) times that for the real data of the Run-2 (Run-3) sample. In Run-2, two events remained after applying all event selections in the simulations, and in Run-3, no events remained. The estimated number of background events from $K_L^0 \to \pi^0\pi^0$ decay was $(2.4 \pm 1.8_{\rm stat} \pm 0.2_{\rm syst}) \times 10^{-2}$ for the combined data sample of Run-2 and Run-3. In the calculation, the event weight from the radial position correction, as described in Sec. 6.6.1, were taken into account.

We examined the event topology of the remained events by checking the particle information in the MC. In both cases, two photon clusters were made by the photons decayed from the same π^0, *i.e.* even event, and two extra photons were missed. One missed photon was a energetic photon (882 and 1169 MeV) directed to the CsI and passed through it (called a "punch-through" photon). The other photon was a low energy photon (15 and 9.3 MeV) hitting the MB and was missed due to the sampling effect. This indicated that we need more radiation length for the CsI and the sampling fraction of the MB, especially in inner region, should be increased in order to obtain further reduction to the $K_L^0 \to \pi^0\pi^0$ events.

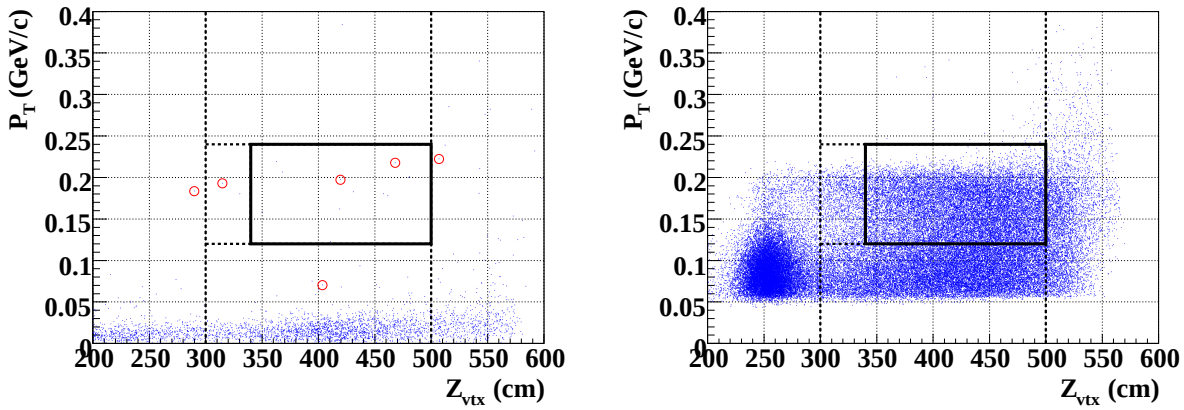

Figure 8.6: Distribution of the $K_L^0 \to \pi^0\pi^0$ MC events in the $Z_{\rm VTX}$-P_T plane after imposing the photon veto cuts (left) and kinematic selections (right). In the left figure, the dots with red circle shows the events remaining after imposing all event selections.

8.2.2 $K_L^0 \to \gamma\gamma$ background

For the MC $K_L^0 \to \gamma\gamma$ samples whose statistics corresponded to 3.8 and 8.7 times the Run-2 and Run-3 data, respectively, all of the event selections except for the projected opening angle selection were imposed and no events remained in the signal region, as shown in Fig. 8.7. Furthermore, the projected opening angle selection strongly suppressed the $K_L^0 \to \gamma\gamma$ events, with a typical rejection of 1×10^5. We concluded that the background due to $K_L^0 \to \gamma\gamma$ was negligible in this analysis.

8.2.3 Charged decay backgrounds

For charged modes, the branching ratios of the $K_L^0 \to \pi^+\pi^-\pi^0$ and $K_L^0 \to \pi^\pm l^\mp \nu$ $(l = e, \mu)$ modes are too large to generate sufficient statistics in the simulations. The background from

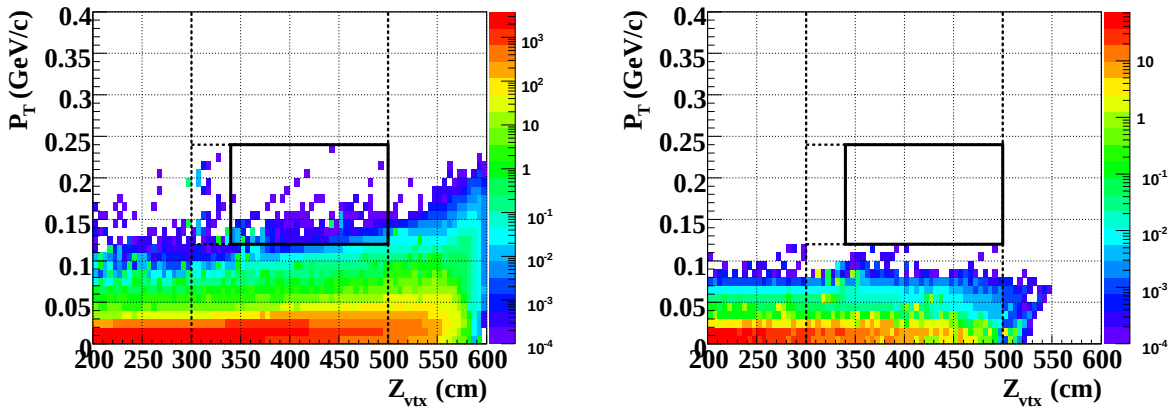

Figure 8.7: Distributions of the $K_L^0 \to \gamma\gamma$ events in the $Z_{\rm VTX}$-P_T plane, when imposed all veto cuts (left) and all analysis cuts except for the projected angle selection (right).

these modes were estimated by assuming that the inefficiency of charged-particle vetos was 1.0×10^{-4} for the CV, and 1.0×10^{-3} for BCV and BHCV [55]. By applying the event weight calculated from the inefficiency, the numbers of background events from these modes were estimated to be 4.2×10^{-4} for $K_L^0 \to \pi^- e^+ \nu$ and less than 1.0×10^{-4} for $K_L^0 \to \pi^+ \pi^- \pi^0$. Here, the $K_L^0 \to \pi^- e^+ \nu$ mode had the largest contribution to the background events among $K_L^0 \to \pi^\pm l^\mp \nu$ modes because a charge-exchange interaction of a π^- ($\pi^- + p \to \pi^0 + n$) and annihilation of e^+ prevent the detection of charged particles. Figure 8.8 shows the distribution of the $K_L^0 \to \pi^- e^+ \nu$ events in the $Z_{\rm VTX}$-P_T plane after applying the event weight.

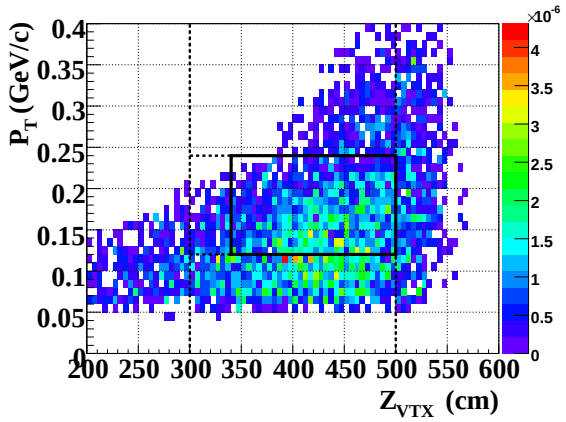

Figure 8.8: Distribution of the $K_L^0 \to \pi^- e^+ \nu$ backgrounds after applying all analysis cuts except for the CV, BCV, and BHCV vetoes. Events are weighted according to the inefficiencies of charged veto detectors, as described in the text.

8.3 Other background sources

In addition to the backgrounds from halo neutron and K_L^0 decay, two other possible background sources were considered: the backward-going π^0 background and the residual gas background.

8.3.1 Backward-going π^0 background

Figure 8.9 illustrates the mechanism of the backward-going π^0 background. When the halo neutrons interacts in the end cap of the vacuum vessel located 2 m behind the CsI, π^0's are

occasionally produced and emitted in the upstream direction. Because we were unable to discriminate whether photons came from the front or the back, these events were reconstructed as coming from the front. The vertex position was reconstructed at the position where the distance from the front surface of the CsI (l' in the figure) was similar to the distance between the back surface of CsI and the end cap (l). Thus, the events tended to be reconstructed inside the signal box.

We estimated this background by using FLUKA simulations with 20 times the amount of statistics as compared to the combined data sample of Run-2 and Run-3. Distribution of the backward-going π^0 background in the $Z_{\rm VTX}$-P_T plane was shown in Fig. 8.10, where only all veto cuts are imposed. After applying kinematic selections, no events remained. The number of background events was determined to be less than 0.05 events.

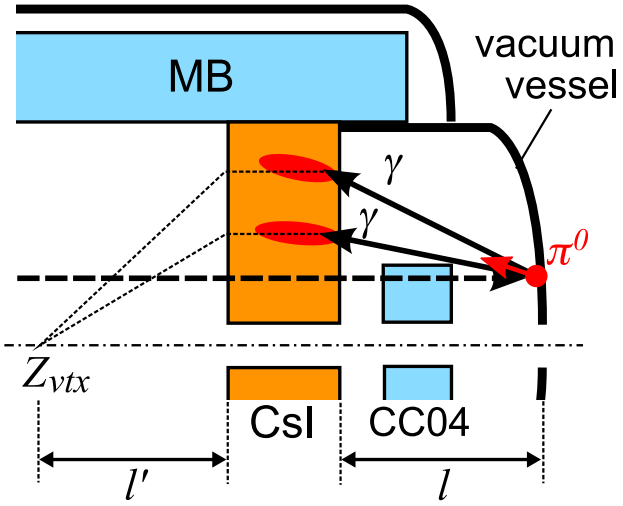

Figure 8.9: Mechanism of backward-going π^0 background.

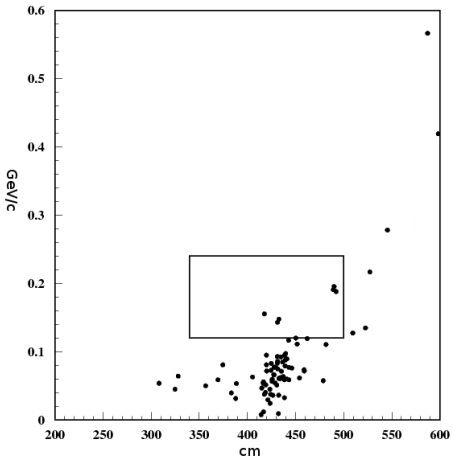

Figure 8.10: P_T vs. $Z_{\rm VTX}$ distributions of the backward-going π^0 background with all veto cuts are imposed.

8.3.2 Residual gas background

The second additional background source is the residual gas background that occurs from interactions of beam neutrons with the residual gas. This process is well suppressed by a high-vacuum system that provided a very low pressure of 10^{-5} Pa. To estimate the background, we carried out a dedicated run at atmospheric pressure, accumulating statistics that were roughly equivalent to 0.6% of the combined data sample of Run-2 and Run-3. We obtained 6867 candidate events with loose event selections. By considering a reduction factor of 10^{-10} due to the air pressure, this background was concluded to be negligible.

8.4 Total number of estimated backgrounds

In total, the estimated number of background events became

$$N_{\rm BG} = 0.87 \pm 0.41 \ , \tag{8.1}$$

Table 8.3: Estimated number of background events for the combined data sample of Run-2 and Run-3.

Background source		Estimated number of BG
Halo neutron BG	CC02-π^0	0.66 ± 0.39
	CV-π^0	< 0.36
	CV-η	0.19 ± 0.13
K_L^0 decay BG	$K_L^0 \to \pi^0\pi^0$	$(2.4 \pm 1.8) \times 10^{-2}$
	$K_L^0 \to \gamma\gamma$	negligible
	charged modes	negligible ($\mathcal{O}(10^{-4})$)
Other BG	backward π^0	< 0.05
	residual gas	negligible ($\mathcal{O}(10^{-4})$)
Total		0.87 ± 0.41

where the CV-π^0 and the backward-going π^0 backgrounds were not included. Table 8.3 summarizes estimates for the numbers of background events. The rejection power of the kinematic selections to the halo neutron backgrounds is shown in Fig. 8.11, with comparing the case of the signal mode. In the figure, the acceptance of each selection was calculated "exclusively", where the acceptance was calculated with all other selections imposed, like

$$A_i = \frac{N(\text{with all selections})}{N(\text{all selections without } i\text{-th selection})} , \tag{8.2}$$

where the A_i denotes the exclusive acceptance of i-th selection and $N(\textit{condition})$ denotes the number of remaining events under the *condition*.

As shown in Fig. 8.11, the CC02-π^0 background was suppressed by the γ position, missing momentum, and CV-η neural network selections. The reason of the CC02-π^0 background to be suppressed by the CV-η NN selection was that the CC02-π^0 events had relatively high energy photons compared to the $K_L^0 \to \pi^0\nu\bar{\nu}$ signals, and made wide-spread clusters in the CsI. The CV-π^0 background was suppressed by the cluster size (csize-1) and angle neural network selections. Because the CV-π^0 events tended to have lower energy photons compared to the $K_L^0 \to \pi^0\nu\bar{\nu}$ signal, these events were rejected by the cluster size (csize-1) selection. Also, the CV-π^0 events should have a discrepancy between the angle calculated by the reconstructed position of the π^0's and that estimated by the neural network based on the cluster shape, as described in Sec. 7.4.3, and the events were suppressed by the angle NN selection. The CV-η background was strongly suppressed by the CV-η neural network selection, as expected in the explanation in Sec. 7.4.1.

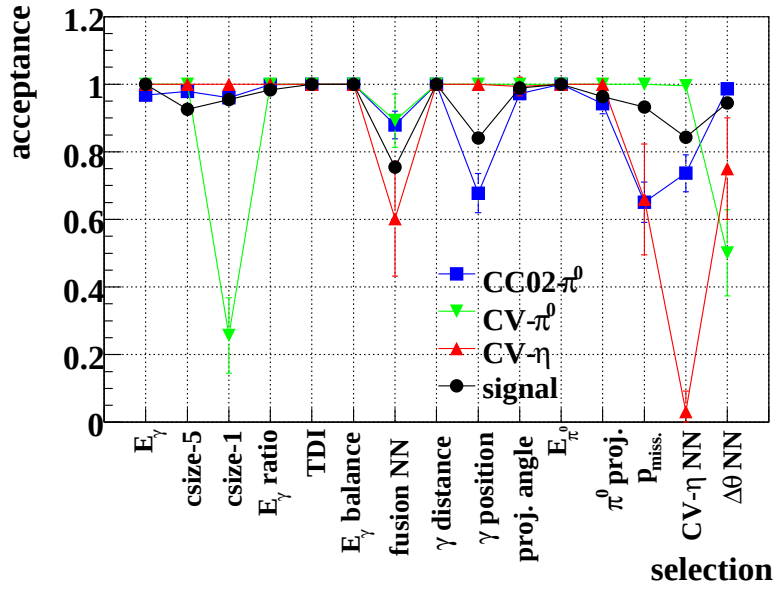

Figure 8.11: Acceptance of each kinematic selection to the halo neutron backgrounds and the signal mode. $\Delta\theta$ NN means the angle neural network selection.

Chapter 9

Normalization

Brief summary

In this chapter, we describe the method to estimate the sensitivity and the estimation of the number of K_L^0 decays. To calculate the sensitivity of our experiment, we need to estimate the number of K_L^0 decays obtained in the physics runs. We used three decay modes: $K_L^0 \to \pi^0\pi^0\pi^0$, $K_L^0 \to \pi^0\pi^0$, and $K_L^0 \to \gamma\gamma$ decays to calculate the number of K_L^0 decays. The estimated numbers of K_L^0 decays by three decay modes were consistent to each other.

First, in Sec. 9.1, we introduce the principle of normalizing the data sample to the sensitivity. In Sec. 9.2, the analysis for the normalization modes are described, including the estimation of the acceptance loss due to accidental activities. Sec. 9.3 shows the results of the number of K_L^0 decays.

9.1 Principle of normalization

In this section, we describe the method to normalize the number of observed decays to obtain the value of sensitivity.

9.1.1 Acceptance

During the following discussion, an acceptance to the $K_L^0 \to \pi^0\nu\bar{\nu}$ signal mode and normalization modes are defined as the ratio of the number of events that passed all the event selections divided by the number of K_L^0's that decayed through the signal and normalization mode in the fiducial region ($340 < Z_{\rm VTX} < 500$ cm), *i.e.*

$$A_{mode} = \frac{N^{\rm MC}(\text{accepted as the } mode)}{N^{\rm MC}(K_L^0 \text{ decays of the } mode)} \ , \tag{9.1}$$

where A_{mode} is the acceptance to the decay *mode* (*mode* can be the signal or normalization modes), $N^{\rm MC}$(accepted as the *mode*) is the number of accepted events after imposing all the event selections for the *mode*, and $N^{\rm MC}(K_L^0$ decays of the *mode*) is the number of K_L^0's that decayed through the *mode* in the fiducial region. The acceptance to the signal and normalization modes was estimated by using the MC simulation of each decay mode.

9.1.2 Single Event Sensitivity

Here, we introduce a parameter called "single event sensitivity" (S.E.S), which is defined as:

$$\text{S.E.S.}(K_L^0 \to \pi^0\nu\bar{\nu}) = \frac{1}{N(\text{total } K_L^0 \text{ decays}) \times A_{\text{signal}}} , \tag{9.2}$$

where A_{signal} denotes the acceptance to the signal mode, and $N(\text{total } K_L^0 \text{ decays})$ is the number of total K_L^0 decays obtained in an experiment. Assuming that a certain number of signal events (n_{signal}) was observed in an experiment, the branching ratio of the signal mode can be calculated to be

$$\begin{aligned} \text{BR}(K_L \to \pi^0\nu\bar{\nu}) &= \frac{n_{\text{signal}}}{N(\text{total } K_L^0 \text{ decays}) \times A_{\text{signal}}} & (9.3) \\ &= n_{\text{signal}} \times \text{S.E.S.}(K_L^0 \to \pi^0\nu\bar{\nu}) . & (9.4) \end{aligned}$$

Thus, the S.E.S. means the branching ratio at which the experiment can observe single event, and so, this parameter directly represents the sensitivity of the experiment.

To estimate the S.E.S., we need to evaluate the $N(\text{total } K_L^0 \text{ decays})$ and A_{signal}. The value $N(\text{total } K_L^0 \text{ decays})$ can be determined by using the normalization mode as

$$N(\text{total } K_L^0 \text{ decays}) = \frac{N_{\text{norm.}}^{\text{data}}}{A_{\text{norm.}} \times BR_{\text{norm.}}} , \tag{9.5}$$

where $N_{\text{norm.}}^{\text{data}}$ is the number of observed events from the normalization mode and $A_{\text{norm.}}$ and $BR_{\text{norm.}}$ represent the acceptance and branching ratio of the normalization mode, respectively. Substituting Eq. 9.5 into Eq. 9.2, the S.E.S. is obtained to be

$$\text{S.E.S.} = \frac{1}{N_{\text{norm.}}^{\text{data}}} \times \frac{A_{\text{norm.}}}{A_{\text{signal}}} \times BR_{\text{norm}}. \tag{9.6}$$

Here, the S.E.S can be calculated from the number of remaining events in the normalization mode and the ratio of acceptances between the signal and the normalization modes. By taking the ratio of the acceptance, uncertainties arising from variations in beam condition, *etc.*, can be canceled.

We examined three decay modes, namely, $K_L^0 \to \pi^0\pi^0\pi^0$, $K_L^0 \to \pi^0\pi^0$, and $K_L^0 \to \gamma\gamma$, as the normalization modes to obtain the number of K_L^0 decays, because they were fully reconstructed and clearly identified. Because these three decay modes have different numbers of photons in the final states, we could cross-check the reliability of the photon identification method. The mean values of the accepted K_L^0 momentum were also different, as shown in Fig. 9.1, which provided a check in the full range of the accepted K_L^0 momentum for the $K_L^0 \to \pi^0\nu\bar{\nu}$ mode. The following sections describe the estimation for $N(\text{total } K_L^0 \text{ decays})$ in our experiment by using three normalization modes.

9.2 Analysis of normalization modes

9.2.1 K_L^0 reconstruction

For the $K_L^0 \to \pi^0\pi^0\pi^0$ and $K_L^0 \to \pi^0\pi^0$ modes, K_L^0's were reconstructed from the six and four photons in the CsI calorimeter, respectively. In the reconstruction, the number of possibile

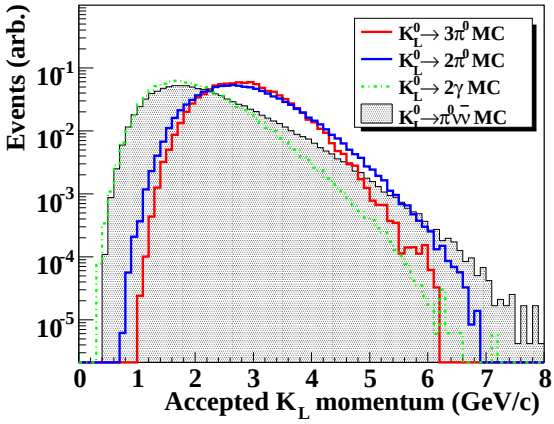

Figure 9.1: Momentum distributions of K_L^0 for the $K_L^0 \to \pi^0\pi^0\pi^0$, $K_L^0 \to \pi^0\pi^0$, and $K_L^0 \to \gamma\gamma$ decays, by comparing the case of the signal mode, obtained by the MC simulation. All analysis cuts except for the photon energy selection are imposed.

combinations of pairs of the two photons was $({}_6C_4 \times_4 C_2 \times_2 C_2)/3! = 15$ for $K_L^0 \to \pi^0\pi^0\pi^0$ and $({}_4C_2 \times_2 C_2)/2! = 3$ for $K_L^0 \to \pi^0\pi^0$. The decay vertex location can be calculated from the energy and position of the two photons of each pair by assuming the π^0 mass. To find the best combination of the photons, the variance in the reconstructed vertex points was calculated, named "pairing χ^2_Z," for all the possible combinations. The pairing χ^2_Z was defined as

$$\chi^2_Z = \sum_{i=1}^{n} \frac{(Z_i - \bar{Z})^2}{\sigma_i^2}\,, \tag{9.7}$$

where Z_i is the vertex point of i-th two-photon pair, σ_i is the resolution in reconstructing Z_i calculated from the energy and position resolutions of the two photons, and

$$\bar{Z} = \frac{\sum_{i=1}^{n} Z_i/\sigma_i^2}{\sum_{i=1}^{n} 1/\sigma_i^2}\,. \tag{9.8}$$

The index n is equal to 3 for $K_L^0 \to \pi^0\pi^0\pi^0$ and 2 for $K_L^0 \to \pi^0\pi^0$. The decay vertex of the K_L^0 was determined as $\bar{Z}$ for the combination with minimum χ^2_Z. We required the minimum pairing χ^2_Z to be less than 3.0 and the difference between the next-to-minimum one to be greater than 4.0, in order to reduce incorrect pairing.

For the $K_L^0 \to \gamma\gamma$ mode, K_L^0's were reconstructed from the two photons in the CsI calorimeter by assuming the K_L^0 mass.

9.2.2 Event selection

Several analysis cuts were imposed on the events in each decay mode to remove contaminations of other decay modes. Photon veto cuts were important to detect the modes with extra photons, such as $K_L^0 \to \pi^0\pi^0\pi^0$ to the $K_L^0 \to \pi^0\pi^0$ events, and $K_L^0 \to \pi^0\pi^0$ to the $K_L^0 \to \gamma\gamma$ events. The energy threshold for the veto in each subsystem was the same as that used in the $K_L^0 \to \pi^0\nu\bar{\nu}$ analysis (see Table 7.1).

In addition to the photon veto cuts, we imposed several mode-dependent kinematic selections. The values used in the selection are summarized in Tables 9.1, 9.2, and 9.3.

For the photon quality selections and two photon selection, the photon energy selection, hit position selection, fusion NN selection, and photon distance selection were imposed. Explanations for these selections can be found in Chap. 7.

In the analysis of $K_L^0 \to \pi^0\pi^0\pi^0$ and $K_L^0 \to \pi^0\pi^0$ decays, we imposed several selections on the correlations between the reconstructed K_L^0 and π^0. After reconstructing K_L^0, we took the differences between Z_i and $Z(K_L^0)$ for all the combinations, and required them to be less than 10 (5) cm for the $K_L^0 \to \pi^0\pi^0\pi^0$ ($K_L^0 \to \pi^0\pi^0$) selection. We also re-calculated the invariant mass using the $Z(K_L^0)$ for each π^0 and required its deviation from M_{π^0} (135 MeV/c^2) to be less than 5.125 (5) MeV/c^2 for $K_L^0 \to \pi^0\pi^0\pi^0$ ($K_L^0 \to \pi^0\pi^0$) selection.

For the $K_L^0 \to \gamma\gamma$ decay, we imposed the projected opening angle and angle neural network selections, where the projected opening angle was required to be consistent with back-to-back condition.

After applying the selections described above, the reconstructed mass of six photons in the $K_L^0 \to \pi^0\pi^0\pi^0$ events and four photons in the $K_L^0 \to \pi^0\pi^0$ events had to be consistent with the K_L^0 mass (from 0.481 to 0.513 GeV/c^2). The decay vertex point of K_L^0 also had to be located in the fiducial region (from 340 to 500 cm), as in the case of $K_L^0 \to \pi^0\nu\bar{\nu}$. The selected regions were shown in Figs. 9.2, 9.3, and 9.4, for $K_L^0 \to \pi^0\pi^0\pi^0$, $K_L^0 \to \pi^0\pi^0$, and $K_L^0 \to \gamma\gamma$, respectively.

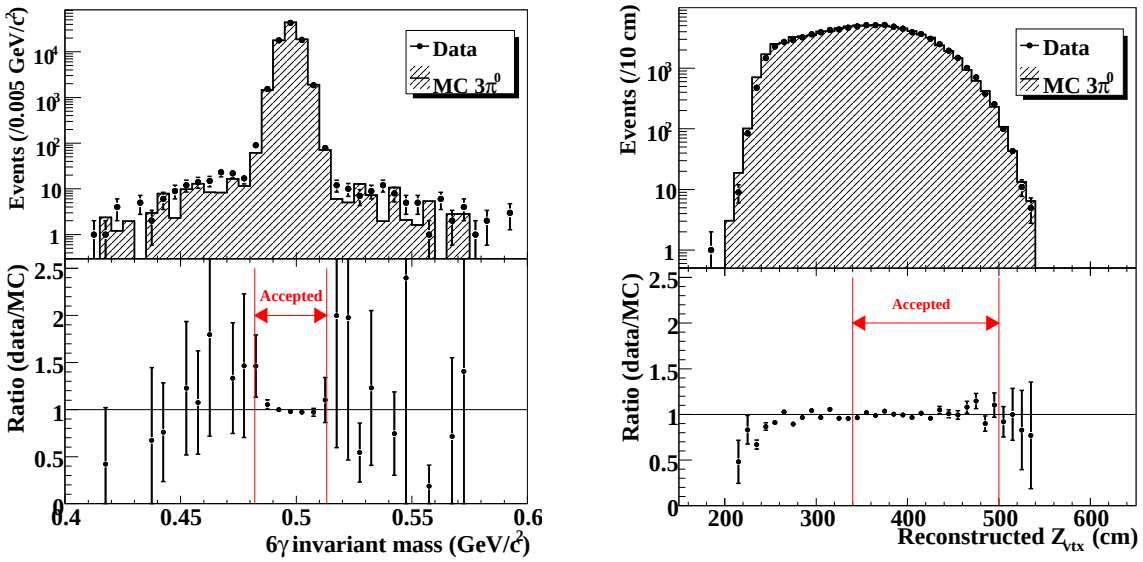

Figure 9.2: Accepted regions for the reconstructed mass (left) and vertex position (right), for six-photon data samples. The distributions show the case after imposing all veto and kinematic selections. The accepted regions are shown by red arrows in the bottom figures.

9.2.3 Accidental loss

In the actual experiment, detector had many accidental activities, which were caused by particles coming either from the target, K_L^0 decays, or other reactions. These accidental activities caused additional energy deposit in the detector, and resulted in an acceptance loss by making false veto hits.

We estimated the acceptance loss caused by accidental activities in two methods. One was to analyze data taken by the accidental trigger and multiply estimated loss to the results from the analysis on raw MC sample, called the "Pure" MC. The other was to overlay the accidental data on the MC sample event-by-event, called the "Add-BG" MC. In the latter, we took the earliest time among the native MC output and the accidental to merge their timing information

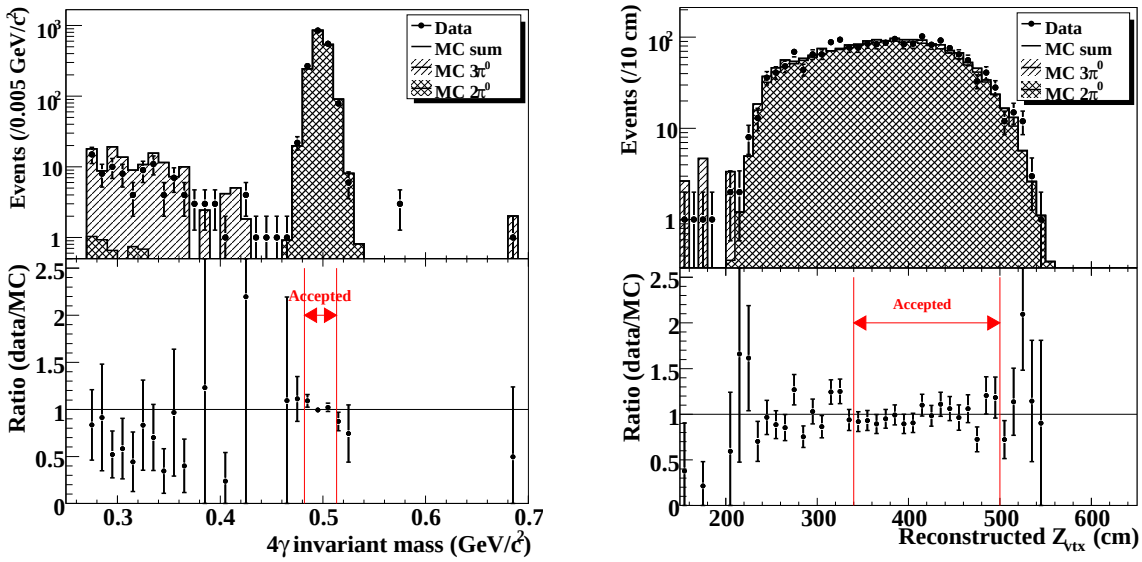

Figure 9.3: Accepted regions for the reconstructed mass (left) and vertex position (right), for four-photon data samples. The distributions show the case after imposing all veto and kinematic selections. The accepted regions are shown by red arrows in the bottom figures.

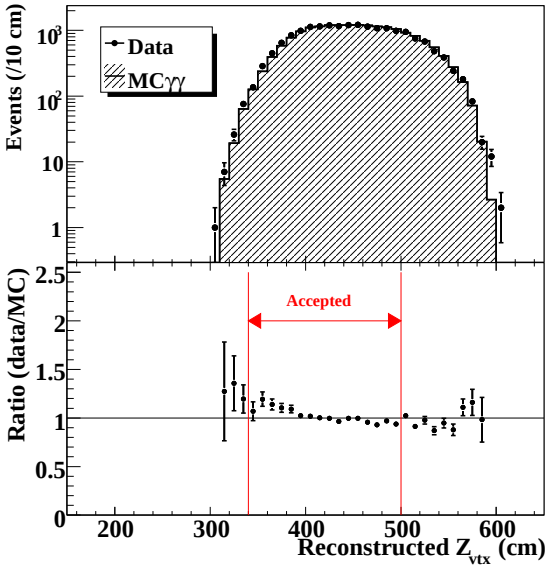

Figure 9.4: Accepted region for the reconstructed vertex position for two-photon data samples with $K_L^0 \to \gamma\gamma$ selections. The accepted region is shown by red arrow in the bottom figure.

for each channel. We set the same time window on the Add-BG MC as the data.

For the Pure MC, we calculated an inefficiency due to accidental loss as follows. This quantity, named as "Inefficiency due to Accidental Loss", can be expressed as;

$$\text{Inefficiency due to Accidental Loss} = 1 - B \cdot C_1 \cdot C_2 \ , \tag{9.9}$$

where B is the efficiency with the loss due to all the photon veto cuts except for the CsI calorimeter, C_1 is the efficiency with the loss due to additional clusters in CsI, and C_2 is the efficiency with the mode-specific loss in the CsI due to accidental activity that did not produce any extra cluster. B was estimated by examining accidental data and counting the number of events that were vetoed by the detectors other than CsI. C_1 was estimated by counting the fraction that contained one or more reconstructed cluster in the CsI in the accidental triggers. We imposed no photon quality selections on these events.

The CsI hits which did not belong to any cluster should be specially treated because the veto condition was a function of the distance from photon clusters, as explained in Sec. 7.3.1. The effect could not be estimated from accidental data alone. Also it depended on the number of genuine clusters, thus, on the decay modes. C_2 was estimated by taking the ratio of the exclusive acceptance of the CsI veto with the Pure and Add-BG MC, as

$$C_2 = \frac{A(\text{CsI veto; Add-BG MC})}{A(\text{CsI veto; Pure MC})} \ , \tag{9.10}$$

where the A(CsI veto; Add-BG MC) and A(CsI veto; Pure MC) is the acceptance of the CsI veto calculated by the Add-BG and Pure MC, respectively. Here, the acceptance of the CsI veto was calculated "exclusively", *i.e.* with all the other selections were imposed, as presented in Eq. 8.2.

The results of the accidental loss estimation are summarized in Table 9.4. Contributions of each veto detectors to the total accidental loss are listed in Table 9.5.

9.3 Number of K_L^0 decays

The acceptance of each mode was estimated with Monte-Carlo simulations. Because, in the simulations, K_L^0's were generated at the exit of the last collimator (C6), the probability of K_L^0 decay in the fiducial region, $p_{decay} = (2.14 \pm 0.02)\%$, was calculated separately and was taken into account in calculating the number of K_L^0 decays. Losses due to accidental activities in the detector were also included in the acceptance.

The acceptance for the normalization mode can be calculated as:

$$A_{\text{norm.}} = \frac{N_{\text{norm.}}^{\text{remain}}}{N_{\text{norm.}}^{\text{gen}} \times p_{decay}} \times (1 - \text{Inefficiency due to Accidental Loss}) \ , \tag{9.11}$$

where $N_{\text{norm.}}^{\text{remain}}$ is the number of remaining events in the simulation after applying all event selections, and $N_{\text{norm.}}^{\text{gen}}$ is the number of generated K_L^0's in the simulation. In the Pure MC case, the accidental loss, which was estimated in the previous section, was applied, and in the Add-BG MC, it was not applied.

By substituting the values obtained by Eq. 9.11 to Eq. 9.5, the number of K_L^0 decays was calculated. Table 9.6 shows the summary of estimated numbers of K_L^0 decays for Run-3 data by comparing the Pure MC and Add-BG MC methods for the three decay modes. The obtained

values by the two methods were consistent within statistical errors. The differences among the three modes were also within the systematic uncertainties, and considered to come from the CsI veto, because it has the largest systematic uncertainties as well as dependence on the number of photons. The consistency between these three decay modes indicated that our simulation of the K_L^0 decay and the detector response was reliable.

As the final value of the number of K_L^0 decays, we adopted the value obtained from $K_L^0 \to \pi^0\pi^0$ Pure MC case, because the energy distribution of photons in the CsI calorimeter from $K_L^0 \to \pi^0\pi^0$ was similar to that expected to $K_L^0 \to \pi^0\nu\bar{\nu}$. Thus, the number of K_L^0 decays was obtained to be

$$N(\text{total } K_L^0\text{decays}) = (8.70 \pm 0.17_{\text{stat.}} \pm 0.59_{\text{syst.}}) \times 10^9 \ . \tag{9.12}$$

Table 9.7 shows the estimations of $N(\text{total } K_L^0\text{decays})$, for the Run-2, Run-3, and the combined data sample of them. The estimations by using three decay modes for the combined data sample of Run-2 and Run-3 are summarized in Table 9.8. Estimates of the systematic uncertainties are described later.

Table 9.1: Kinematic selections for $K_L^0 \to \pi^0\pi^0\pi^0$ mode.

Selection		Min.	Max.
Photon quality selections	energy	150 MeV	
	hit position	17.5 cm (sq.)	88 cm (radial)
	fusion NN	0.5	
Two photon selection	distance	17.5 cm	
K_L^0 selections	best χ^2_Z		3.0
	2nd best - best χ^2_Z	4.0	
	π^0 Z difference		10 cm
	π^0 mass difference		5.125 MeV/c^2
	R^2 at C6		4.5 cm^2
	M(6γ)	0.481 GeV/c^2	0.513 GeV/c^2
	Z(K_L^0)	340 cm	500 cm
	$P_T(K_L^0)^2$		1.25×10^{-4}(GeV/c)^2

Table 9.2: Kinematic selections for $K_L^0 \to \pi^0\pi^0$ mode.

Selection		Min.	Max.
Photon quality selections	energy	150 MeV	
	hit position	17.5 cm (sq.)	88 cm (radial)
	fusion NN	0.7	
Two photon selection	distance	15.0 cm	
K_L^0 selections	best χ^2_Z		3.0
	2nd best - best χ^2_Z	4.0	
	π^0 Z difference		5 cm
	π^0 mass difference		5.0 MeV/c^2
	R^2 at C6		4.0 cm^2
	M(4γ)	0.481 GeV/c^2	0.513 GeV/c^2
	Z(K_L^0)	340 cm	500 cm
	$P_T(K_L^0)^2$		1.25×10^{-4}(GeV/c)^2

Table 9.3: Kinematic selections for $K_L^0 \to \gamma\gamma$ mode.

Selection		Min.	Max.
Photon quality selections	higher energy	250 MeV	
	lower energy	150 MeV	
	energy ratio	0.88	
	hit position	15 cm (sq.)	88 cm (radial)
	fusion NN	0.7	
Two photon selection	distance	15.0 cm	
K_L^0 selections	angle NN	-20°	
	projected angle	170°	
	Z(K_L^0)	340 cm	500 cm
	$P_T(K_L^0)^2$		9×10^{-4}(GeV/c)^2

Table 9.4: Accidental losses of Run-3 data for the normalization modes. The parameters B, C_1, and C_2 are defined in the text. The errors are statistical only.

Mode	$K_L^0 \to \pi^0\pi^0\pi^0$	$K_L^0 \to \pi^0\pi^0$	$K_L^0 \to \gamma\gamma$
B	81.44 ± 0.01 %		
C_1	99.33 ± 0.04 %		
C_2	98.45 ± 1.43 %	97.99 ± 1.35 %	97.95 ± 0.57%
Total	79.64 ± 1.16 %	79.27 ± 1.12 %	79.24 ± 0.48%
Weighted average	79.40 %		

Table 9.5: Accidental losses of each detector obtained by the Run-3 data. The errors are statistical only. Loose veto means the sum of all veto detectors for the loose veto threshold without timing requirement. Detectors having the value less than 0.05% are not listed. Note that the total value was calculated by applying all vetoes at once.

Detector	Accidental loss (%)
FB	1.39 ± 0.00
MB	7.35 ± 0.01
BCV	0.54 ± 0.00
CC07	0.18 ± 0.00
BHCV	0.26 ± 0.00
BA	6.40 ± 0.01
Loose veto	3.99 ± 0.01
Total	18.56 ± 0.01

Table 9.6: Estimated numbers of K_L^0 decays for Run-3 data. calculated from the three decay modes and comparing the Pure and Add-BG MC. $N_{\text{norm.}}^{\text{data}}$ is the number of events obtained from the real data after imposing all the analysis cuts. Uncertainties in the acceptances are statistical ones due to the amount of the MC samples. Statistical uncertainties in the number of K_L^0 decays include an ambiguity in $N_{\text{norm.}}^{\text{data}}$, and systematic ones include an ambiguity from the reproducibility of the MC (described later) and statistical uncertainties of the MC in the acceptance estimate.

Mode		$N_{\text{norm}}^{\text{data}}$	$A_{\text{norm.}}$	N(total K_L^0decays)
$K_L^0 \to \pi^0\pi^0\pi^0$	(Pure)	48280	$(7.28 \pm 0.06) \times 10^{-5}$	$(3.39 \pm 0.03_{\text{stat.}} \pm 0.18_{\text{syst.}}) \times 10^9$
	(Add-BG)		$(7.30 \pm 0.06) \times 10^{-5}$	$(3.38 \pm 0.03_{\text{stat.}} \pm 0.21_{\text{syst.}}) \times 10^9$
$K_L^0 \to \pi^0\pi^0$	(Pure)	1079	$(3.47 \pm 0.03) \times 10^{-4}$	$(3.57 \pm 0.11_{\text{stat.}} \pm 0.21_{\text{syst.}}) \times 10^9$
	(Add-BG)		$(3.54 \pm 0.03) \times 10^{-4}$	$(3.51 \pm 0.11_{\text{stat.}} \pm 0.23_{\text{syst.}}) \times 10^9$
$K_L^0 \to \gamma\gamma$	(Pure)	14682	$(7.51 \pm 0.02) \times 10^{-3}$	$(3.57 \pm 0.03_{\text{stat.}} \pm 0.13_{\text{syst.}}) \times 10^9$
	(Add-BG)		$(7.62 \pm 0.02) \times 10^{-3}$	$(3.52 \pm 0.03_{\text{stat.}} \pm 0.16_{\text{syst.}}) \times 10^9$

Table 9.7: Estimated numbers of K_L^0 decays by comparing Run-2, Run-3, and the combined data sample of Run-2 and Run-3. These values are obtained by the $K_L^0 \to \pi^0\pi^0$ decay modes with Pure MC method.

Data sample	N(total K_L^0decays)
Run-2	$(5.13 \pm 0.40) \times 10^9$
Run-3	$(3.57 \pm 0.24) \times 10^9$
Run-2 + Run-3	$(8.70 \pm 0.61) \times 10^9$

Table 9.8: Estimated numbers of K_L^0 decays calculated from the three decay modes in the combined sample of Run-2 and Run-3 data. $N_{\text{norm.}}^{\text{data}}$ is the number of events obtained from the real data after imposing all the analysis cuts. In the $K_L^0 \to \pi^0\pi^0$ mode, $N_{\text{norm.}}^{\text{data}}$ is obtained by subtracting the contamination from the $K_L^0 \to \pi^0\pi^0\pi^0$ mode. Uncertainties in the acceptances are statistical ones due to the amount of the MC samples. Statistical uncertainties in the number of K_L^0 decays include an ambiguity in $N_{\text{norm.}}^{\text{data}}$, and systematic ones include an ambiguity from the reproducibility of the MC (described later) and statistical uncertainties of the MC in the acceptance estimate.

Mode	$N_{\text{norm.}}^{\text{data}}$	$A_{\text{norm.}}$	N(total K_L^0decays)
$K_L^0 \to \pi^0\pi^0\pi^0$	118334	$(7.21 \pm 0.06) \times 10^{-5}$	$(8.41 \pm 0.03_{\text{stat.}} \pm 0.53_{\text{syst.}}) \times 10^9$
$K_L^0 \to \pi^0\pi^0$	2573.9	$(3.42 \pm 0.03) \times 10^{-4}$	$(8.70 \pm 0.17_{\text{stat.}} \pm 0.59_{\text{syst.}}) \times 10^9$
$K_L^0 \to \gamma\gamma$	35367	$(7.18 \pm 0.03) \times 10^{-3}$	$(9.02 \pm 0.05_{\text{stat.}} \pm 0.51_{\text{syst.}}) \times 10^9$

Chapter 10

Results

Brief summary

In this chapter, we describe the results of the present analysis. First, the acceptance to the $K_L^0 \to \pi^0\nu\bar{\nu}$ decay was estimated based on the MC simulations. The acceptance losses caused by the accidental activities and the selections using timing informations were taken into account by separated calculations. The acceptance to the signal mode was obtained to be $(1.06 \pm 0.08)\%$ and $(1.01 \pm 0.06)\%$ for the Run-2 and Run-3 data, respectively. The single event sensitivity was calculated by using the number of K_L^0 decays and was found to be $(1.11 \pm 0.10) \times 10^{-8}$ for the combined data sample of Run-2 and Run-3.

Finally, the signal candidates in the P_T-Z_{VTX} plane was examined for the Run-2 and Run-3 data. We observed zero events inside the signal box. Thus, we set a new upper limit on the $\mathrm{BR}(K_L^0 \to \pi^0\nu\bar{\nu})$ to be 2.6×10^{-8} at 90% C.L. based on the Poisson statistics.

10.1 Acceptance and single event sensitivity

10.1.1 Signal acceptance

The acceptance for the $K_L^0 \to \pi^0\nu\bar{\nu}$ decay was estimated from Monte-Carlo simulations based on the GEANT3 package. The definition of the acceptance was the ratio of the number of remaining events after applying all the selection criteria divided by the number of K_L^0 decays in the fiducial region, as introduced in Eq. 9.1.

The "raw" acceptance was calculated by dividing the number of remaining events after imposing all the analysis cuts by the number of $K_L^0 \to \pi^0\nu\bar{\nu}$ decays generated in the simulation. For the $K_L^0 \to \pi^0\nu\bar{\nu}$ MC sample, we generated 5.0×10^8 (8.0×10^8) K_L^0's at the downstream end of the neutral beamline, which corresponded to 1.07×10^7 (1.71×10^7) K_L^0 decays, for the Run-2 (Run-3) case, respectively. After imposing all event selections, we obtained 150334 (237871) remaining events. Thus, the raw acceptance was calculated as 1.40% and 1.39% for the Run-2 and Run-3 data.

In the raw acceptance, the losses caused by geometrical acceptance, veto cuts, kinematic selections, and selection on fiducial region were included. The geometrical acceptance to detect two photons in the CsI was 19.5%. The loss by veto cuts, or self-vetoing, was 47.4%, which was dominated by the CsI and MB vetoes: the loss in the CsI veto was caused by hits accompanied by the genuine photon cluster, as shown in Fig. 7.3, and the loss in the MB was caused by photons escaping from the front face of the CsI and hitting the MB. The acceptance of the kinematic

selections except for two time-dependent selections (discussed later) was 25.0%. The acceptance of selecting the signal region in the P_T-$Z_{\rm VTX}$ plane was 51.6%. These values were estimated through MC simulations of the $K_L^0 \to \pi^0\nu\bar{\nu}$ mode. The evaluation of the acceptance loss was supported by the fact that the acceptance losses in the normalization modes ($K_L^0 \to \pi^0\pi^0\pi^0$, $K_L^0 \to \pi^0\pi^0$, and $K_L^0 \to \gamma\gamma$) were reproduced by the simulation, as discussed in Sec. 9.3.

The acceptance loss due to accidental activities in the detector was estimated from real data taken with the TMON trigger, as described in Sec. 9.2.3. The accidental loss was estimated to be 20.6% for the Run-3 data, in which the losses in MB (7.4%) and BA (6.4%) were major contributions. For Run-2, the accidental loss was estimated to be 17.4%; the difference between Run-2 and Run-3 was due to the difference in the BA counters used in the data taking.

The acceptance loss caused by the selections on the timing dispersion of each photon cluster and on the timing difference between two photons was estimated separately by using real data, because the timing reproducibility of the MC simulation was not sufficient. For the timing dispersion selection, we estimated the acceptance to be 96.7% for each photon, and for the timing difference selection, the acceptance was estimated as 97.4%. Thus, the acceptance loss caused by the timing selections was $(1 - 0.967^2 \times 0.974) = 8.9\%$.

The total acceptance for the $K_L^0 \to \pi^0\nu\bar{\nu}$ was calculated to be

$$A_{\rm signal} = (1.06 \pm 0.08)\% \ \text{(for Run-2)}, \tag{10.1}$$

$$A_{\rm signal} = (1.01 \pm 0.06)\% \ \text{(for Run-3)}, \tag{10.2}$$

where the errors are dominated by the systematic uncertainties that are discussed later. The acceptance of each selections and reasons are summarized in Tables 10.1 and 10.2. Fig. 10.1 shows the distribution of the MC $K_L^0 \to \pi^0\nu\bar{\nu}$ events in the scatter plot of P_T-$Z_{\rm VTX}$ after imposing all of the other cuts.

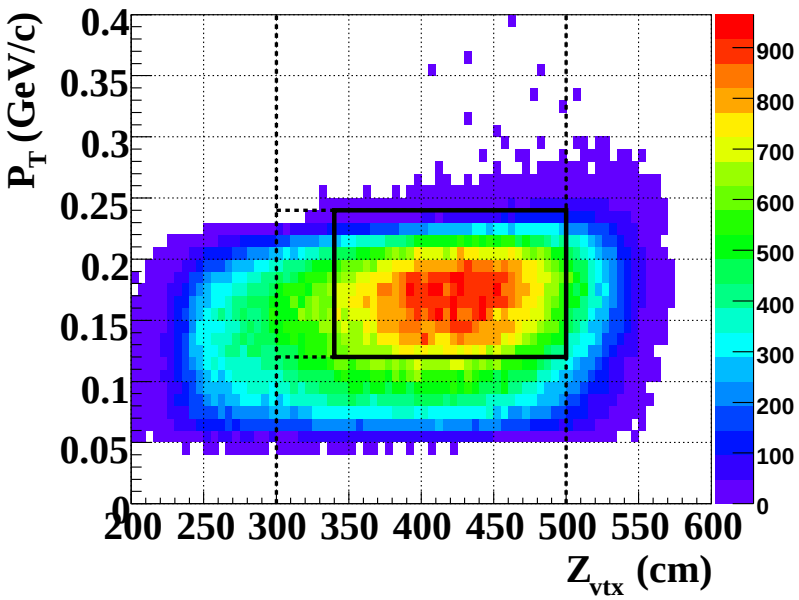

Figure 10.1: Distribution of P_T vs. the reconstructed Z position for the $K_L^0 \to \pi^0\nu\bar{\nu}$ Monte Carlo events after imposing all of the analysis cuts. The box indicates the signal region for $K_L^0 \to \pi^0\nu\bar{\nu}$.

Table 10.1: Acceptance to the $K_L^0 \to \pi^0\nu\bar{\nu}$ signal events. Values outside and inside the parenthesis shows the Run-2 and Run-3 case, respectively. Acceptance of the kinematic selections includes two time-dependent selections: time dispersion and timing difference selections.

Selections / Reasons	Acceptance
Geometrical acceptance	19.5 %
Veto cuts	47.4 %
Kinematic selections	22.8 %
P_T-Z_{VTX} selection	51.6 %
Accidental activities	92.6 (89.4) %
Total	1.06 (1.01) %

Table 10.2: Breakdown lists of the signal acceptance for the veto cuts (left) and the kinematic selections (right).

Detector	Acceptance
CC00	100.0 %
FB	99.6 %
CC02	99.9 %
BCV	94.3 %
MB	83.4 %
CV	98.8 %
CC03	99.6 %
CsI	65.8 %
sand	99.8 %
CC04	95.8 %
CC05	99.5 %
CC06	99.8 %
CC07	99.9 %
BHCV	100.0 %
BA	100.0 %
Total	47.4 %

Selection	Acceptance
Photon energy	99.9 %
Cluster size (csize-5)	92.4 %
Cluster size (csize-1)	95.6 %
Energy ratio	93.3 %
Timing dispersion	93.5 %
Photon hit position	84.5 %
Fusion NN	75.4 %
CV-η NN	84.2 %
2-γ distance	100.0 %
2-γ time difference	97.4 %
2-γ energy balance	100.0 %
π^0 kinetic energy	100.0 %
π^0 projection	96.5 %
π^0 missing momentum	93.4 %
Projected opening angle	98.9 %
Angle NN	94.4 %
Total	22.8 %

10.1.2 Single event sensitivity

By using the number of K_L^0 decays and the total acceptance, the single event sensitivity for $K_L^0 \to \pi^0\nu\bar{\nu}$ can be calculated by using the Eq. 9.2. The S.E.S. value was obtained to be

$$\text{S.E.S.} = (1.84 \pm 0.05_{\text{stat.}} \pm 0.19_{\text{syst.}}) \times 10^{-8} \text{ for Run-2,} \quad (10.3)$$

$$\text{S.E.S.} = (2.80 \pm 0.09_{\text{stat.}} \pm 0.23_{\text{syst.}}) \times 10^{-8} \text{ for Run-3.} \quad (10.4)$$

By combining the Run-2 and Run-3 samples, we obtained

$$\text{S.E.S.} = (1.11 \pm 0.02_{\text{stat.}} \pm 0.10_{\text{syst.}}) \times 10^{-8} \text{ in total.} \quad (10.5)$$

10.2 Results

After finalizing all of the event selection cuts, the candidate events inside the signal region were examined. No events were observed in the signal region, as shown in Fig. 10.2. An upper limit for the $K_L^0 \to \pi^0\nu\bar{\nu}$ branching ratio was set to be

$$BR(K_L^0 \to \pi^0\nu\bar{\nu}) < 2.6 \times 10^{-8} \quad (10.6)$$

at the 90% confidence level (C.L.), based on Poisson statistics. The result improves the previous limit given by the early analysis of Run-2 by a factor of 2.6.

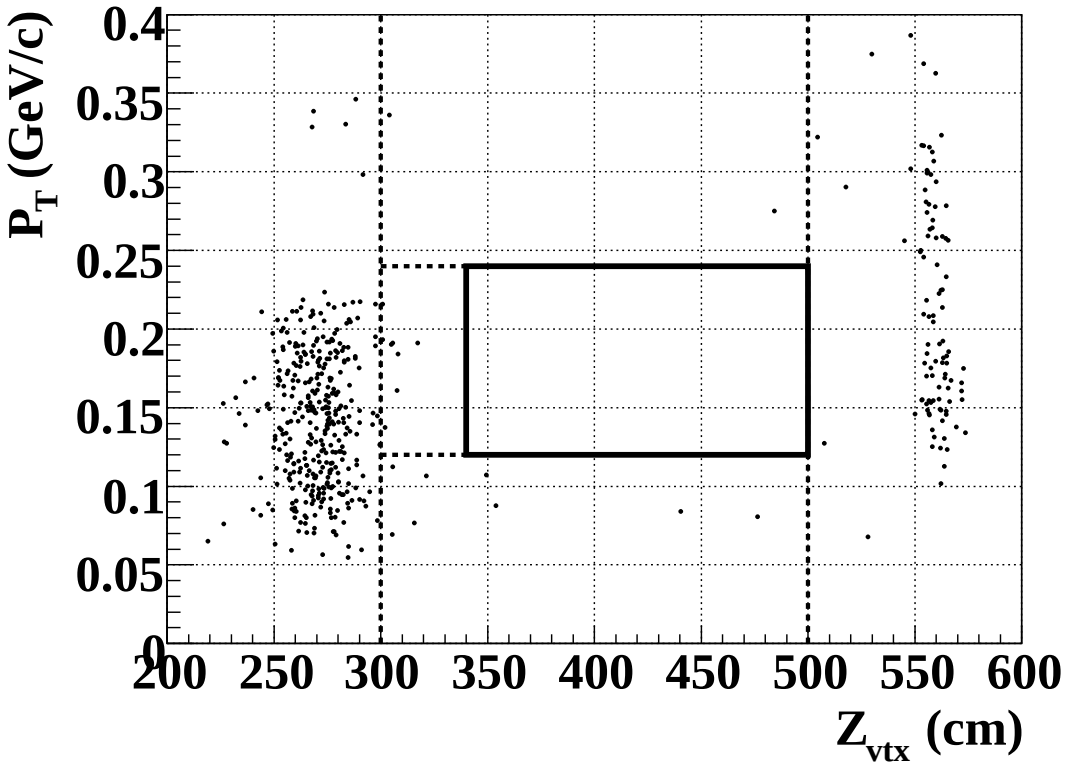

Figure 10.2: Scatter plot of P_T vs. the reconstructed Z position for the events with all of the selection cuts imposed. The box indicates the signal region for $K_L^0 \to \pi^0 \nu\bar{\nu}$.

Chapter 11

Systematic Uncertainties

Brief summary

In this chapter, we will describe our treatment for various systematic uncertainties to provide thorough understanding of the experiment. The systematic uncertainties were evaluated for the single event sensitivity and background estimates due to halo neutrons. The method to estimate the systematic errors and the results of them will be discussed in following sections.

11.1 Uncertainty of the single event sensitivity

The systematic uncertainty of the single event sensitivity was evaluated by summing the uncertainties of the number of K_L^0 decays and the acceptance of the $K_L^0 \to \pi^0\nu\bar{\nu}$ decay. Because the calculation of the former also includes the acceptance of the normalization modes, both of them are relevant to the acceptance evaluation by the Monte Carlo simulations. To estimate the uncertainties in the acceptance calculation, we utilized the fractional difference between data and the simulation in each selection criterion, defined by the equation

$$F^i = \frac{A^i_{\rm data} - A^i_{\rm MC}}{A^i_{\rm data}}, \tag{11.1}$$

$$A^i = \frac{N(\text{with all selections})}{N(\text{all selections without } i\text{-th selection})}, \tag{11.2}$$

where $A^i_{\rm data}$ and $A^i_{\rm MC}$ denote the acceptance values of the i-th cut, calculated as the ratio of numbers of events with and without the cut, for the data and MC simulations, respectively. In calculating F^i, the acceptance was calculated with all the other cuts imposed, *i.e.* "exclusively" as shown in Eq. 8.2. Figure 11.1 shows the calculated fractional difference of the exclusive acceptance to the $K_L^0 \to \pi^0\pi^0$ mode with the Pure MC sample.

The systematic uncertainty of the acceptance was evaluated by summing all the fractional differences in quadrature, weighted by the effectiveness of each cut, as

$$\sigma^2_{\rm syst.} = \frac{\sum_{i=\rm cuts}(F^i/A^i_{\rm data})^2}{\sum_{i=\rm cuts}(1/A^i_{\rm data})^2}\ . \tag{11.3}$$

For the three decay modes used in the normalization, $K_L^0 \to \pi^0\pi^0\pi^0$, $K_L^0 \to \pi^0\pi^0$, and $K_L^0 \to \gamma\gamma$, the calculated uncertainties were 5.2%, 5.7%, and 3.6% (in Run-3), respectively. The

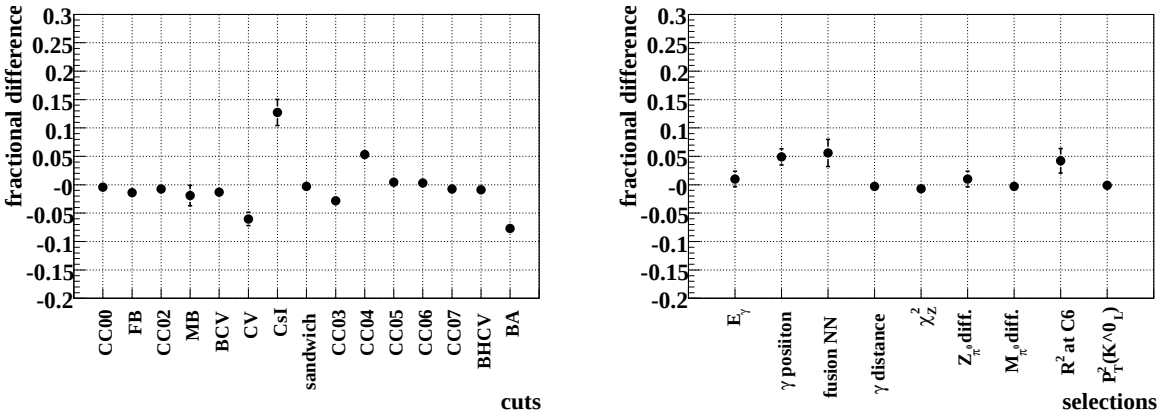

Figure 11.1: Fractional difference of the exclusive acceptance for the Pure MC. A positive value indicates the acceptance loss was larger in the MC than in the data.

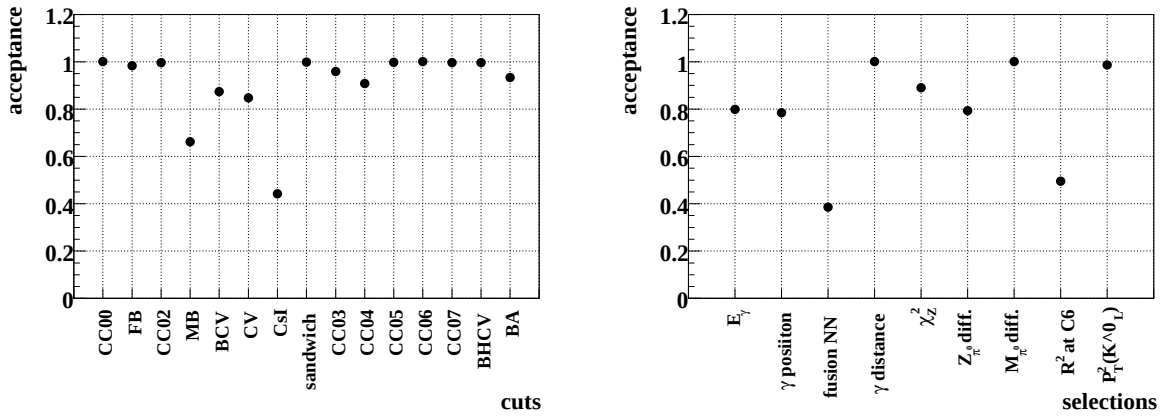

Figure 11.2: Acceptance of veto cuts and kinematic selections for the $K_L^0 \to \pi^0\pi^0$mode. The values are obtained by using four-photon events in the Run-3 data.

contribution of each veto cut and kinematic selection is listed in Table 11.1, with comparing the results obtained by Pure MC and Add-BG MC. As shown in the table, the acceptances of the CsI veto cut had the largest uncertainties in all decay modes. The number of K_L^0 decays was obtained by using the $K_L^0 \to \pi^0\pi^0$ mode, and thus its uncertainty is quoted as the same value for the $K_L^0 \to \pi^0\pi^0$ mode.

Table 11.1: Contribution of each veto cut and kinematic selection to the total systematic uncertainties for the $K_L^0 \to \pi^0\pi^0$ Pure MC and Add-BG MC samples obtained with the Run-3 condition. The vetoes and kinematic selections having the systematic error smaller than 1% is collected as the "others" by summing them in quadrature.

cut/selection	Pure MC	Add-BG MC
CsI	4.47%	5.01%
CV	1.10%	1.13%
MB	0.45%	1.40%
fusion NN	2.26%	2.59%
$R^2(K_L^0)$	1.32%	1.45%
others	1.50%	1.52%
total	5.67%	6.38%

For the acceptance of the $K_L^0 \to \pi^0\nu\bar{\nu}$ mode, the same systematic uncertainties as the $K_L^0 \to \pi^0\pi^0$ mode were adopted because there were no signal candidates in the data to be compared with the MC simulations.

The systematic error of the single event sensitivity was evaluated to be a quadratic sum of the uncertainties of the number of K_L^0 decays and the acceptance of the $K_L^0 \to \pi^0\nu\bar{\nu}$ decay. It was 10.3% in Run-2 and 8.2% in Run-3, respectively.

11.2 Uncertainty of the halo neutron backgrounds

The systematic errors of halo neutron backgrounds were estimated by combining the errors coming from the veto cuts, kinematic selections, and normalization; as

$$\sigma_{\text{syst.}} = \sigma_{\text{syst.}}(\text{veto cuts}) \oplus \sigma_{\text{syst.}}(\text{kinematic selections}) \oplus \sigma_{\text{syst.}}(\text{normalization}). \tag{11.4}$$

Systematic uncertainties from veto cuts and kinematic selections were estimated by utilizing fractional differences between data and the simulations. It was similar to in the case of S.E.S., described in the previous section, with small modification to treat the features in the background estimation.

For the veto cuts, the method was unable to be used directly because veto cuts had been applied in the early stages of the MC simulations to save the computing time. Thus, for the systematic uncertainty due to veto cuts, the same value obtained in the $K_L^0 \to \pi^0\pi^0$ analysis was assigned, as $\sigma_{\text{syst.}}(\text{veto cuts}) = 4.9\%$

For the kinematic selections, the difficulty was in the lack of statistics: we had no events after applying all selections in the data. Thus, in the estimation of fractional differences, expressed by Eq. 11.1, we calculated the A^i with all veto cuts imposed except the kinematic selections,

like

$$A^i = \frac{N(\text{with veto cuts and } i\text{-th selection})}{N(\text{with veto cuts})}, \tag{11.5}$$

where N was counted in the signal box. Figure 11.3 shows the fractional difference of the acceptance calculated to the kinematic selections.

The systematic error of the remaining number of backgrounds from the kinematic selections was evaluated by summing the fractional differences in quadrature, weighted by the effectiveness of each cut to the each background sources, as represented in Eq. 11.3. Note that in the calculation of systematic errors, A^i of Eq. 11.3 was calculated exclusively by using the MC samples of CC02-π^0, CV-π^0, and CV-η cases.

Thus, the systematic uncertainties due to the reproducibility of kinematic selections were calculated to be $\sigma_{\text{syst.}}$(kinematic selections) = 30.3%, 31.7%, and 43.7% for CC02-π^0, CV-π^0, and CV-η backgrounds, respectively.

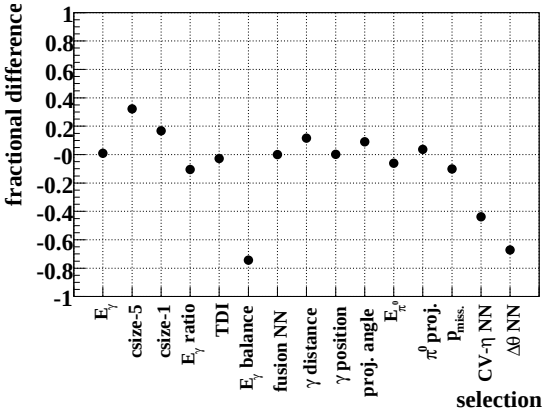

Figure 11.3: Fractional difference of the acceptance calculated to the each kinematic selection.

In addition, the uncertainties in the normalizations of the MC simulations were taken into account. Because the normalization was determined by using the number of events in the CC02 region (Region-(1)), there can be ambiguity in estimating the CV-related backgrounds. As shown in Table 8.1, there was a 24% difference between data and MC simulation in the downstream region (Region-(2)). Even though they were statistically consistent, we assigned the difference as an additional systematic uncertainty of CV-π^0. For the CV-η case, further ambiguity due to the reproducibility of η production should be considered. It was estimated to be 24% from the difference between data and MC simulations in the numbers of η events in the Al plate run, as shown in Fig. 6.11.

The total systematic uncertainties were calculated by summing up the contributions quadratically, to be 31%, 40%, and 55% for CC02-π^0, CV-π^0, and CV-η backgrounds, respectively. The contributions of each source to the total systematic error are summarized in Table 11.2.

Table 11.2: Systematic uncertainties in the background estimation, for the CC02-π^0 (left), CV-π^0 (middle), and CV-η (right) backgrounds, respectively. The "others" include the contributions of all kinematic selections except for the listed ones.

selection	syst. error
fusion NN	19.3%
$\Delta\theta$ NN	15.6%
CV-η NN	13.6%
others	10.8%
veto cuts	4.9%
normalization	none
total	30.7%

selection	syst. error
$\Delta\theta$ NN	23.6%
fusion NN	14.6%
csize-1	11.5%
others	10.1%
veto cuts	4.9%
normalization	23.6%
total	39.8 %

selection	syst. error
CV-η NN	43.7%
others	5.1 %
veto cuts	4.9%
normalization	33.6%
total	55.3%

Chapter 12

Conclusion and Discussion

12.1 Conclusion of the present analysis

The E391a experiment at the KEK-PS was the world-first dedicated experiment for the $K_L^0 \to \pi^0\nu\bar{\nu}$ decay. Combining the Run-2 and Run-3 data, the single event sensitivity reached 1.11×10^{-8}. No events were observed inside the signal region and the new upper limit on the branching ratio of the $K_L^0 \to \pi^0\nu\bar{\nu}$ decay was set to be

$$\mathrm{BR}(K_L^0 \to \pi^0\nu\bar{\nu}) < 2.6 \times 10^{-8} \text{ at the 90\% C.L..} \tag{12.1}$$

The result improves the previous published limit given by the Run-2 analysis (Analysis-2008) by a factor of 2.6, and the E391a experiment as a whole has improved the limit from previous experiments by a factor of 20. The improvement in the history of $K_L^0 \to \pi^0\nu\bar{\nu}$ search is plotted in Fig. 12.1

The E391a experiment was also the first step of our step-by-step strategy toward the accurate measurement of the $K_L^0 \to \pi^0\nu\bar{\nu}$ decay. The experiment was planned to confirm our experimental strategy, and this purpose was well achieved. Several points need to be noted.

First, we found the solutions to several technical issues, such as the pencil beamline, differential pumping for ultra-high vacuum, low-threshold particle detection with a hermetic configuration, in situ calibration, *etc.*, which can be successively used in the next step. We encountered some technical problems that exist in the current apparatus, such as insufficient thickness and segmentation of the CsI calorimeter, the structure of the CV, the limitation of the BA in an environment with high counting rate, *etc.*. They will be improved in the next experiment.

Second, we were able to control the systematic uncertainties small enough in the estimate of the single event sensitivity, as described in Chap. 9. A small systematic error is essential for an accurate determination of the branching ratio. We are confident that the branching ratio of the decay $K_L^0 \to \pi^0\nu\bar{\nu}$ can be measured accurately with this method.

A third point concerns the understanding and estimation of backgrounds. In the experiment for the decay $K_L^0 \to \pi^0\nu\bar{\nu}$, elimination of all possible backgrounds is the only effective way to identify the decay, and it can be achieved by complete understanding of backgrounds.

The dominant source of backgrounds was the result of beam interactions. Although the background from this source was considered to be as serious as those from K_L^0 decays in the experiment, its understanding and estimation were very difficult before the work reported here. The background mechanisms were clearly understood and divided into three different sources, CC02, CV-π^0, and CV-η. Methods were developed to estimate them with rather small systematic

errors. Based on this experience, we clearly know the direction of upgrades to minimize the beam backgrounds in the next step.

The backgrounds from other K_L^0 decays were able to be reduced to negligibly small level in the present experiment, mainly due to the success of applying tight vetoes with a hermetic configuration. One of the important results is the invariant mass distribution of the events with four photons, shown in Fig. 6.9. The distribution was well reproduced by the simulations. In particular, the low-mass region was well described by $K_L^0 \to \pi^0\pi^0\pi^0$ decays with a small contamination by mis-combination events of four photons from $K_L^0 \to \pi^0\pi^0$ decays. The relation between $K_L^0 \to \pi^0\pi^0\pi^0$ and $K_L^0 \to \pi^0\pi^0$ is similar to the relation between $K_L^0 \to \pi^0\pi^0$ and $K_L^0 \to \pi^0\nu\bar{\nu}$. By taking their branching ratios into account, it was found that the low-mass region could to be reproduced after reducing the $K_L^0 \to \pi^0\pi^0\pi^0$ yield by several orders of magnitude. Reproduction could not be achieved without good simulations of small signals from the detector, to which a tight veto was applied. This achievement indicates that a similar direction will be promising in the next step.

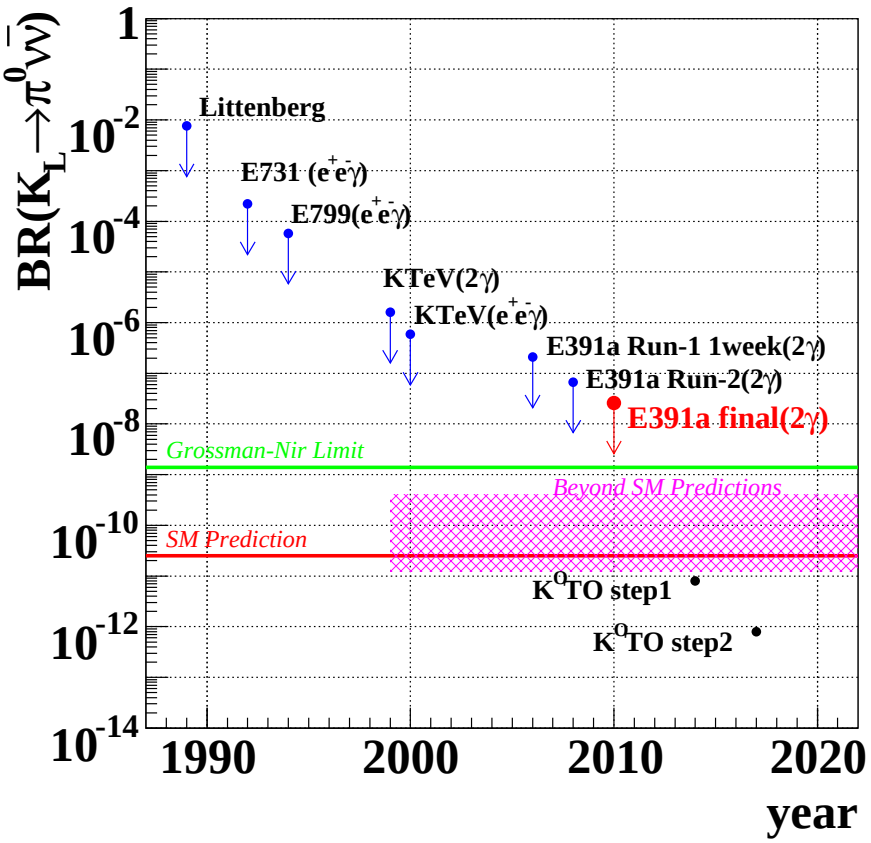

Figure 12.1: History of the $K_L^0 \to \pi^0\nu\bar{\nu}$ search with the result reported in this thesis.

12.2 K^{O}TO experiment : $K_L^0 \to \pi^0\nu\bar{\nu}$ search in near future

As discussed through the present thesis, we developed an effective method to search the $K_L^0 \to \pi^0\nu\bar{\nu}$ decay. Based on the same experimental concept, a successor experiment, K^{O}TO [56] at the new J-PARC accelerator [57], is now in preparation. The K^{O}TO (J-PARC E14) experiment plans to proceed in two steps as Step-1 and Step-2. The goal of the Step-1 is the first observation of the $K_L^0 \to \pi^0\nu\bar{\nu}$ decay with the S/N ratio of 1.4, and the Step-2 aims to accumulate more than 100 Standard Model events with the S/N of 4.8. Here, we overview the improvements from the E391a in Step-1 to achieve their goal.

The K^{O}TO experiment uses the J-PARC 30GeV proton synchrotron and they reuses the E391a detector with a number of required upgrades in the Step-1 phase. The sensitivity of the E391a experiment was three orders of magnitude far from the SM prediction, and the background level was O(1) even with such sensitivity. The K^{O}TO experiment implements many features to overcome this gap from the E391a. The improvement in the K^{O}TO experiment can be divided into two things: the increase in the sensitivity to $K_L^0 \to \pi^0\nu\bar{\nu}$ and the reduction in the background events. The precise understandings of the background events in E391a, as discussed in this thesis, play an important role to set the direction of improvements in the K^{O}TO experiment, especially in the reduction of background events.

12.2.1 Improvements in sensitivity

The primary difference from the E391a to K^{O}TO experiment is in the accelerator. The J-PARC 30GeV proton synchrotron is to provide ∼100 times larger number of protons compared to the KEK 12GeV PS. Table 12.1 summarizes the beam parameters of K^{O}TO compared to the E391a one.

The improvements in the sensitivity is summarized in Table 12.2. As listed in the table, the increase in the proton intensity of the primary beam results in a factor of ∼30 increase in the K_L^0 yield. Also the run time is planned to be expanded from 2 months (E391a) to 12 months [1] (K^{O}TO). The decay probability of K_L^0 in the fiducial region increases by a factor of 2, because of the softer momentum distribution of K_L^0, as shown in Fig. 12.2, and the longer fiducial region, $300cm < Z_{\rm VTX} < 500$ cm (K^{O}TO), than that of E391a, $340cm < Z_{\rm VTX} < 500$ cm.

The acceptance is estimated to increase by a factor of 3.6, because the background events are suppressed by the hardware improvements, as will be described in the next section, and they can loosen the selection criteria.

The sensitivity of the K^{O}TO experiment is estimated to reach 9.3×10^{-12}, which corresponds to the 2.7 $K_L^0 \to \pi^0\nu\bar{\nu}$ events observation with SM prediction.

12.2.2 Improvements in background suppression

In the E391a experiment, we figured out that the most serious background was the halo neutron background. To reduce the halo neutron background, the K^{O}TO experiment constructs a new beamline, which can suppress the halo neutron flux. In addition, several upgrades in the detector system are planned for further suppression.

[1] These numbers indicates net running periods. Gross calendar period is thought to be 3 times larger.

Table 12.1: Comparison between the E391a and K^{O}TO beamline. The value for the K^{O}TO experiment are taken from Ref. [58].

	E391a	K^{O}TO
Proton energy	12 GeV	30 GeV
Number of protons per spill	2.5×10^{12}	2×10^{14}
Spill length / Beam repetition	2 sec / 4 sec	0.7 sec / 3.3 sec
Extraction angle	4°	16°
Solid angle	12.6 μsr	9 μsr
K_L^0 yield / spill	3.3×10^5	7.8×10^6

Table 12.2: Comparison between the E391a and K^{O}TO experiment. The value for the K^{O}TO experiment are taken from Ref. [58].

	E391a	K^{O}TO	Improvement (K^{O}TO/E391a)
K_L^0 yield / spill	3.3×10^5	7.8×10^6	×29 per unit time
Net run time	2 months	12 months	×6
Decay probability	2%	4%	×2
Acceptance	1.0%	3.6%	×3.6
			×1250 in total

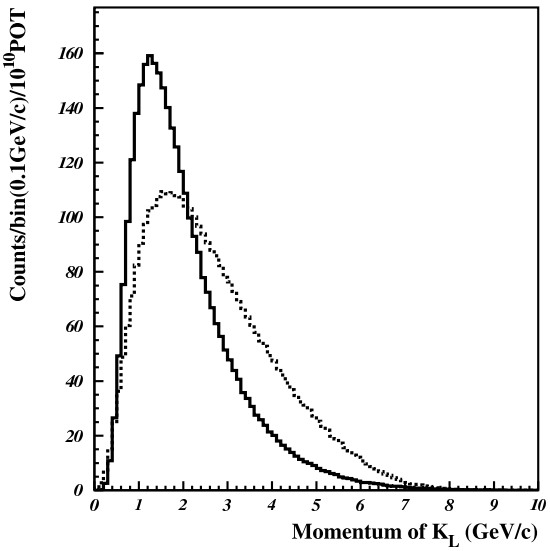

Figure 12.2: The momentum distribution of the K_L^0 for the K^{O}TO (solid line) and E391a (dashed line) experiment, taken from [58].

Well-collimated neutral beamline

The primary tool to suppress the halo neutron background in the K^{O}TO experiment is a new well-collimated neutral beamline. The beamline consists of two collimator modules and the total length of the beamline is 21 m. The collimators are optimized to have sufficient suppression to the halo neutron flux. Figure 12.3 shows the performance of the new beamline, quoted from Ref. [58]. The halo neutron flux is suppressed to 5 orders of magnitude compared to the core neutron flux, which corresponds to 10 times improvement from the E391a. The larger production angle (16°), compared to 4° in the E391a, improves the ratio of number of K_L^0 to that of neutrons. The improvement in the halo neutron to K_L^0 ratio becomes a factor of 66 compared to the E391a.

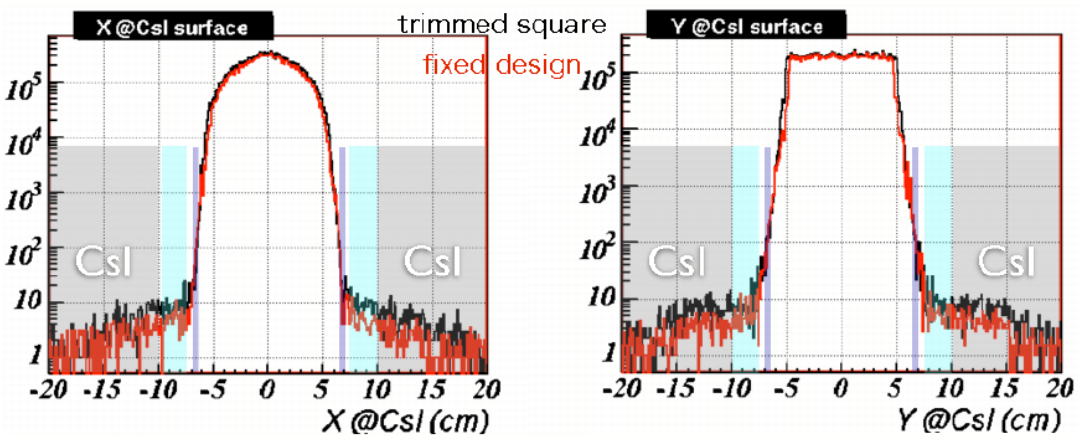

Figure 12.3: Estimated horizontal (left) and vertical (right) profiles of the neutral beamline at the face of the CsI calorimeter [58]. Red histogram indicates the result with final design, while black one is an example of the results during the optimization of the design.

Upgraded CsI calorimeter

Another way to reduce backgrounds is to improve the photon reconstruction in the CsI calorimeter. The thickness of the CsI calorimeter in E391a was not sufficient, which resulted in non-negligible effects due to shower leakage and photo-nuclear interactions in the energy measurement. It caused the background in the signal region from the interactions at CC02. The increase in the thickness of the CsI was also required to suppress the $K_L^0 \to \pi^0\pi^0$ background because, as described in Sec. 8.2.1, the remaining $K_L^0 \to \pi^0\pi^0$ backgrounds in the simulation were caused by the inefficiency due to punch-through in the CsI. The segmentation of the CsI calorimeter in E391a was also not sufficient because the Moliere radius in CsI (3.5 cm) is smaller than the crystal size (7 cm × 7 cm); this resulted in the loss of cluster shape information.

To solve these problems, the CsI calorimeter is planned to be upgraded. In E391a, the CsI calorimeter consisted of 496 crystals with the dimension of $7 \times 7 \times 30$ cm. As shown in Fig. 12.4, in the K^{O}TO experiment, the calorimeter consists of 2240 CsI crystals with a dimension of $2.5 \times 2.5 \times 50$ cm and 476 crystals with a dimension of $5 \times 5 \times 50$ cm, both of which are borrowed from the KTeV experiment. The thickness of the CsI calorimeter increases from 30 cm to 50 cm, which can increase the energy resolution by reducing the energy leakage and photo-nuclear

interactions. The granularity of the CsI calorimeter is also improved, which can provide more information on the shape of the clusters, and they can distinguish the genuine photons from the fake hits caused by possible background sources.

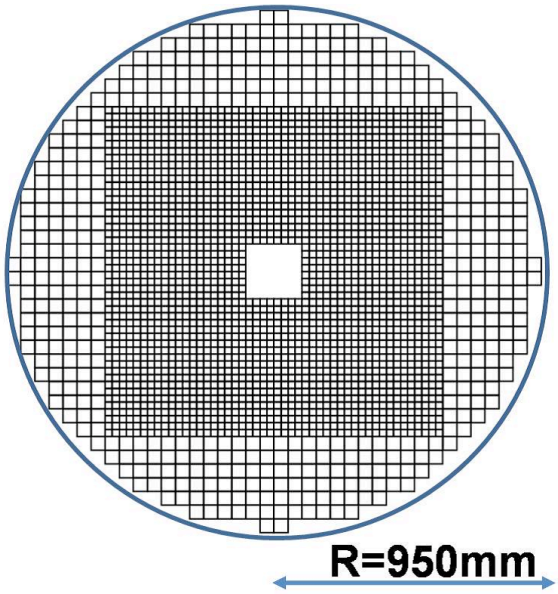

Figure 12.4: Front view of the upgraded CsI calorimeter in the K^{O}TO experiment.

Countermeasure against each background source

Based on the understandings of the background sources in the E391a experiment, the K^{O}TO experiment implements a number of improvements to reduce these background events.

CC02-π^0background To suppress the CC02-π^0 backgrounds, the K^{O}TO experiment implements following improvements;

- reduced halo neutron flux with well-collimated neutral beamline,
- improved photon energy resolution with the upgraded CsI,
- replacement of upstream collar-shaped counter.

In the E391a, we have understood that the CC02-π^0 background was caused by the inefficiency to low energy particles in the CC02. It was a sampling calorimeter and low energy particles could be lost in the lead converter. To improve this, CC02 is planned to be replaced with full-active counter. The new counter consists of pure CsI, fabricated from crystals used in the E391a, as the calorimeter. Its short radiation length, relative to the interaction length, naturally expect further detection efficiency for the particle produced in neutron interactions. The position of the counter is also optimized.

Combining the effects, the CC02-π^0 background will be suppressed by a factor of $\sim$8000 in total, compared to the E391a case, and the estimated number of CC02-π^0 background in the K^{O}TO experiment is 0.01 [58].

CV-π^0background To suppress the CV-π^0 backgrounds, the K^{O}TO experiment implements following improvements;

- reduced halo neutron flux with well-collimated neutral beamline,
- replacement of the CV.

In the E391a, the inner CV modules and their support structure were the sources of π^0 and η particles. To suppress the production of these particles, the CV is planned to be upgraded, as shown in Fig. 12.5. The inner modules are removed, the thickness of the CV is reduced to be 3 mm instead of 6 mm in E391a, and the position of the CV is optimized.

With above improvements, the CV-π^0 background will be suppressed by a factor of ∼5000 compared to the E391a case, and the estimated number of CC02-π^0 background in the K^{O}TO experiment is 0.08 [58].

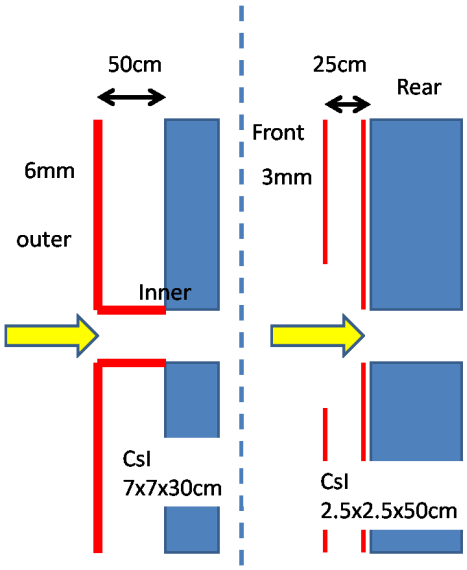

Figure 12.5: CV upgrade in the K^{O}TO experiment. Left figure shows the CV used in E391a, and right shows the improved design in the K^{O}TO experiment, taken from [58].

CV-η background The features to suppress the CV-η backgrounds is similar to the CV-π^0 case. To suppress the CV-η background, the K^{O}TO experiment implements following improvements;

- reduced halo neutron flux with well-collimated neutral beamline,
- replacement of the CV,
- reduced η production due to the softer halo neutron momentum,
- better discrimination in the CsI cluster using upgraded CsI.

A neural network selection on the CsI cluster shape is planned to be implemented, which is similar to the case in the present analysis. Thanks to the granularity in the K^{O}TO CsI calorimeter, the separation using the cluster shape is expected to work more effectively. With above improvements, the CV-η background will be suppressed by a factor of ∼1000 compared to the E391a case, and the estimated number of CV-η background in the K^{O}TO experiment is 0.3 [58].

$K_L^0 \to \pi^0\pi^0$ background In the E391a, the $K_L^0 \to \pi^0\pi^0$ background was estimated to be 0.024 events, where the remaining events in the simulation were caused by punch-through photons in the CsI and the detection inefficiency in the MB. In the KOTO experiment, the thickness of the CsI increases, and reduces the detection inefficiency due to punch-through photons. In addition, the thickness of MB is planned to increase from $14X_0$ to 18.5 X_0, which also reduces the photon inefficiency due to the punch-through in the MB. The BA is also planned to be replaced with a new detector, named beam hole photon veto (BHPV). The performance of the BHPV was checked in the Run-3 period of E391a by using the APC, which was a prototype module of the BHPV. With these improvements, the estimated number of $K_L^0 \to \pi^0\pi^0$ background in the KOTO experiment is 1.7, with the improvement factor of ∼20 from the E391a.

12.3 Other possible improvements in the $K_L^0 \to \pi^0\nu\bar{\nu}$ search

Toward further sensitivity beyond KOTO Step-1 in future, it is better to consider other possible improvements to obtain a better background suppression. Several ideas were proposed in the KOPIO experiment [59], which was a planned experiment to observe the $K_L^0 \to \pi^0\nu\bar{\nu}$ decay in Brookhaven National Laboratory (BNL) AGS accelerator, though it was not realized due to financial reason.

12.3.1 Angle measurement

By using the cluster shape information, the measurement of the incident angle of photons was carried out in E391a with neural network technique, as described in Sec. 7.4.3. The accuracy of the angle measurement was approximately 11 degrees in RMS. In the KOTO experiment, the angle resolution is expected to be improved by using fine segmented CsI calorimeter.

Another way to measure the incident angle of photons is to install the composition of photon converter and tracking detector. An example of this kind of device was suggested in the KOPIO experiment. A detector named “preradiator” was designed, consisting of eight layers of modules, with each module having a 0.1-mm-thick copper radiator and a drift chamber. In the preradiator, the incident angle of photons were measured by detecting the direction of electrons and positrons in the early stage of electromagnetic shower. The estimated angular resolution of preradiator was about 1.4 degrees. Since the total radiation length of the preradiator was 2.2, the probability of two photons to convert in the preradiator was about 50%. Even though the acceptance to the signal mode was lost by 50% from the angle measurement, the information on the incident angle of photons could offer the strong kinematic constraints to suppress background events.

12.3.2 K_L^0 momentum measurement

Another possibility to obtain kinematic informations is in the measurement of K_L^0 momentum using time-of-flight (TOF) method. KOPIO experiment suggested to utilize a beamline with unique time structure, called “microbunch” beam. The microbunch beam has the following timing structure; the beam in the narrow timing width of $\sigma \sim 200$ psec, were struck on the target in the repetition cycle of 25 MHz (or the corresponding interval was 40 nsec). By measuring the timing difference of primary beam hitting the target and K_L^0 decayed in the fiducial volume, the momentum of K_L^0 can be determined. This could offer additional kinematic constraints to the background rejection.

12.4 Prospects of the kaon physics

As discussed in the Chap. 1, the kaon rare decay modes, $K_L^0 \to \pi^0\nu\bar{\nu}$ and $K^+ \to \pi^+\nu\bar{\nu}$, take an important role to explore the world of new physics beyond the Standard Model. The E391a experiment was a milestone in the $K_L^0 \to \pi^0\nu\bar{\nu}$ search because it developed effective experimental methods and established analysis methods. These methods are the basis to design the KOTO experiment, a successor experiment of the E391a. The KOTO experiment is expected to reach the required sensitivity for the Standard Model prediction in 2014, and it will be followed by the experiment with further sensitivity (Step-2).

In the charged kaon decay, $K^+ \to \pi^+\nu\bar{\nu}$, the E787/E949 experiment reported the BR($K^+ \to \pi^+\nu\bar{\nu}$) mainly based on 3 observed candidate events. The next experiment to the $K^+ \to \pi^+\nu\bar{\nu}$ decay is planned as NA62 [60] at CERN SPS. The NA62 experiment is aiming to observe the $\mathcal{O}(100)$ events of $K^+ \to \pi^+\nu\bar{\nu}$ decay.

By combining the coming results in $K_L^0 \to \pi^0\nu\bar{\nu}$ and $K^+ \to \pi^+\nu\bar{\nu}$ decays, we hope to have strong indications in the world of new physics. Thus, we conclude that the kaon physics is promising in the particle physics.

Appendix A

CsI Calibration

Brief summary

Here, we introduce the method to calibrate the CsI calorimeter. We calibrated the CsI crystals in two steps: cosmic ray calibration and $K_L^0 \to \pi^0\pi^0\pi^0$ calibration. In the first step of the cosmic ray calibration, we used the cosmic ray penetrating the CsI crystals. In the second step of the $K_L^0 \to \pi^0\pi^0\pi^0$ calibration, we used the $K_L^0 \to \pi^0\pi^0\pi^0$ events. In the $K_L^0 \to \pi^0\pi^0\pi^0$ calibration, we calculated the energy-correction factors to the CsI crystals by using the kinematic constraints in the $K_L^0 \to \pi^0\pi^0\pi^0$ events. The process was carried out iteratively until the correction constants were converged.

A.1 Cosmic ray calibration

Cosmic-ray events were collected by the cosmic-ray calibration trigger, which was made by the penetrating hits in the MB modules. Figure 3.38 shows an example of the cosmic-ray track in the CsI. The cosmic-ray trajectory was reconstructed by fitting the CsI hit pattern by a straight line.

The path length across a single crystal was calculated by using the trajectory. The charge output of each crystal was normalized by the path length. Figure A.1 shows the distributions of raw charge output (top), the calculated path length (middle), and normalized charge output by the path length (bottom). The peak in the normalized charge output was fitted by a Landau function. The gain factor to convert the charge to the energy deposit was calculated by assuming the energy deposit in the CsI per a unit path length to be 5.63 MeV/cm [10]. Since the trajectory fitting was made in the 2-dimensional plane along the CsI surface, the path-length calculation had an ambiguity in the direction along the beamline.

A.2 $K_L^0 \to \pi^0\pi^0\pi^0$ calibration

In the cosmic calibration of the CsI, there remained the ambiguity in the path-length calculation due to its 2-dimensional-fit method. Also the method using the cosmic ray did not take into account the effect of scattering of muons in the CsI calorimeter. These features led into wider distributions in the charge normalized by the path length.

To improve the calibration, we developed a method using the $K_L^0 \to \pi^0\pi^0\pi^0$ decay [61]. In the $K_L^0 \to \pi^0\pi^0\pi^0$ calibration, we used the events having six-photon hits in the CsI. In order

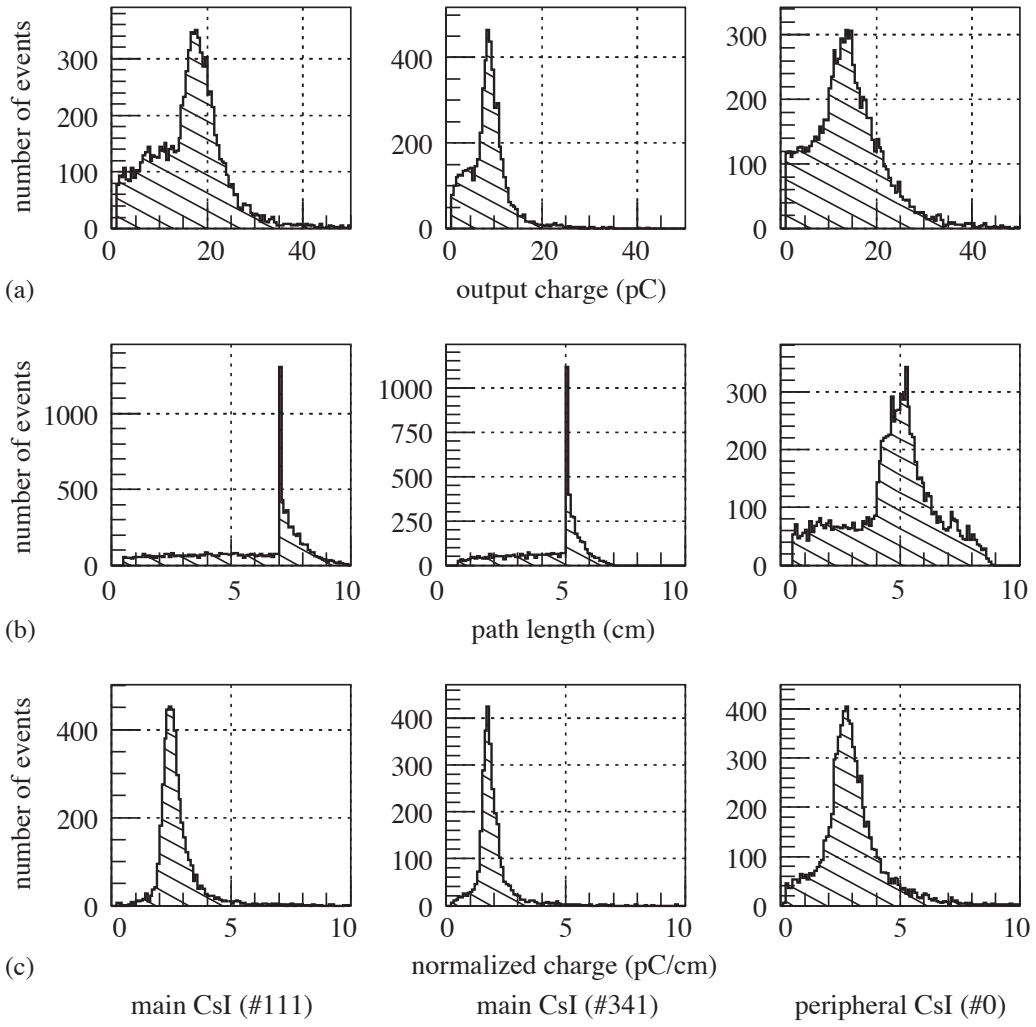

Figure A.1: Distribution of the raw charge (top), calculated path length (middle), and normalized charge (down) for each type of CsI crystal: Normal crystal (left), KTeV crystal (middle), and peripheral crystal (right), respectively.

to reduce the mis-combination in making the π^0 pairs, we required the best χ^2_Z to be smaller than 5 and the second best χ^2_Z to be greater than 8, where the definition of χ^2_Z can be found in Sec. 9.2.1.

In the $K^0_L \to \pi^0\pi^0\pi^0$ events, we measured the energy and position of six photons with their errors. Assuming (v_x, v_y, v_z) as the decay vertex of K^0_L, the $K^0_L \to \pi^0\pi^0\pi^0$ events have 6 kinematic constraints and they can be expressed as;

$$M(6\gamma) = M(K^0_L) \qquad (K^0_L \text{ mass constraint}) \tag{A.1}$$

$$M(2\gamma) = M(\pi^0) \qquad (\pi^0 \text{ mass constraint}) \times 3 \text{ combinations} \tag{A.2}$$

$$\sum_{i=1}^{6} x_i E_i = v_x \sum_{i=1}^{6} E_i \qquad \text{(center of energy)} \tag{A.3}$$

$$\sum_{i=1}^{6} y_i E_i = v_y \sum_{i=1}^{6} E_i \qquad \text{(center of energy) .} \tag{A.4}$$

Thus, we have 6 constraints with 3 unknown parameters. This system can be solved by least-square method with Lagrange multipliers at 3 degrees of freedom.

In the calibration process, we measured a correction factor from the gain value obtained by the cosmic calibration. The correction was applied only on the crystal with the largest energy deposit in a cluster. Then in the same event, the calibration procedures is applied to each photon cluster. After processing all the $K^0_L \to \pi^0\pi^0\pi^0$ event samples, the correction factor for each crystal was averaged and the resultant value was used as the initial value in the next iteration.

The performance of the calibration was checked by the $K^0_L \to \pi^0\pi^0\pi^0$ event. The events having even event number were used to performance check, though the events having odd event number were used to the calibration, which was to make an independent check of the calibration. The mass distributions before and after the calibration for the $K^0_L \to \pi^0\pi^0\pi^0$ events in the real data are shown in Fig. A.2. The width of K^0_L and π^0 mass were improved by 4.9% and 3.9%, respectively, where the number of remaining events after iteration was increased by 5% in the data and conserved in MC.

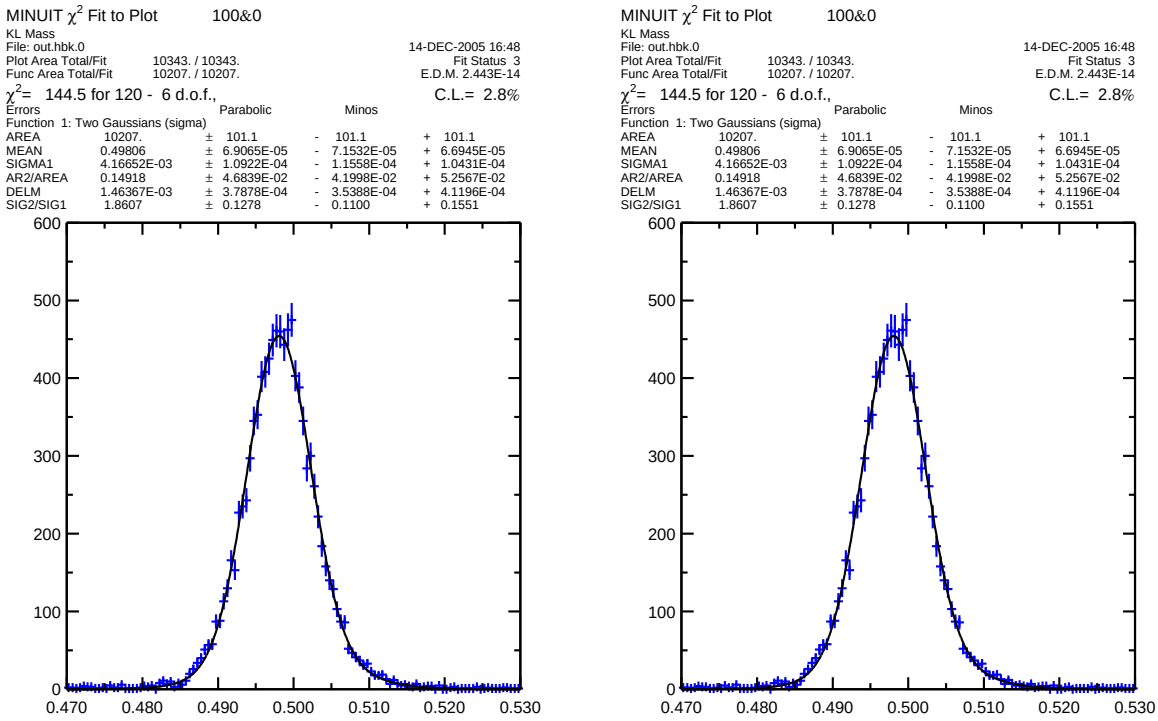

Figure A.2: Invariant mass distributions of the K_L^0 candidates from real data before (a) and after (b) the 5 iterations of the $K_L^0 \to \pi^0\pi^0\pi^0$ calibration.

Appendix B

Neural Network Selection

Brief summary

In this chapter, we present a detailed description on the kinematic selections which utilized neural network technique. An (artificial) neural network is a computer algorithm, which can extract information from multiple input parameters by simulating the structure and function of biological neural networks in a brain. The neural network is trained by sets of input parameters and given answers for them.

We first introduce the neural network algorithm, and second, we show a detailed description of kinematic selections that utilized neural network.

B.1 Introduction to neural network

A neural network (NN) is a computer algorithm used to model complex relationships between input and output parameters. The NN accepts multiple input parameters and can determine multiple output parameters by solving the relationship between input parameters. One of common applications of NN in particle physics is the discrimination of signal events from background events by using their signature.

The NN is a network consisted of several nodes (neurons) and connections between two nodes (synapse), as shown in Fig. B.1. Several neurons are grouped in layers, and synapses connect two neurons which belong adjacent layers. Input and output parameters are treated as neurons and grouped as input and output layers. Between the input and output layers, there are several hidden layers each of which contains multiple neurons. The network is trained by optimizing the strength of synapse by using sets of input parameters and given true output parameters (This process is called "supervised learning").

B.1.1 Number of hidden layers and neurons

When using the NN, we need to determine the number of hidden layers and the number of neurons in hidden layers. Hornik *et al.* showed that multilayer networks with as few as one hidden layer are capable of approximating any Borel measurable function, provided sufficient number of hidden units are available [62]. More complicated problems, such as discontinuous ones, can be solved with two hidden layer network [63]. It is difficult to determine the optimum number of neurons in hidden layers because it depends in a complex way on the number of input and output parameters, the number of training events, the complexity of the problem to

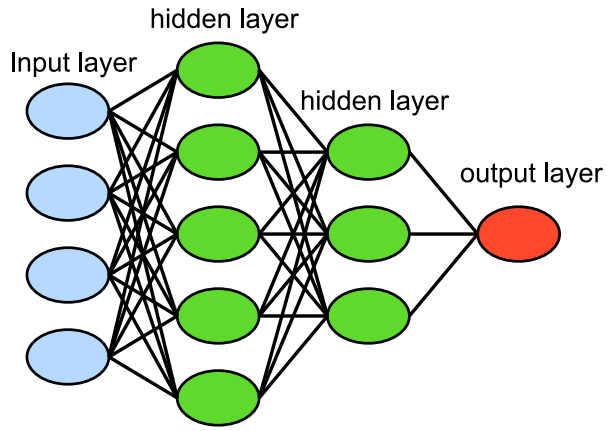

Figure B.1: Schematic drawing of neural network. The ovals represent the neurons and lines between them represent synapse connections.

be solved, *etc.* An empirical rule for the number of neurons in a hidden layer is to use twice as large as the size of input layer.

B.1.2 Functional models for synapses

Synapses are implemented by using several mathematical functions. Generally, any kinds of functions except for the constant or linear function can be used to represent synapses. There are several commonly used functions for synapses: Commonly used functions for synapses are step functions (includes Heaviside function) and a sigmoid function. The sigmoid function, which is the special case of the logistic function, has a S-shaped curve, as shown in Fig. B.2, and can be expressed as

$$\varsigma_a(x) = \frac{1}{1+e^{-ax}} \ , \tag{B.1}$$

where a is called "gain" of the function. One merit to use the sigmoid function is that its derivative can be expressed by using the sigmoid function itself, like

$$\dot{\varsigma}_a(x) = a\varsigma_a(x)[1-\varsigma_a(x)] \ . \tag{B.2}$$

Due to this feature, the sigmoid function is commonly used as a model function of synapses.

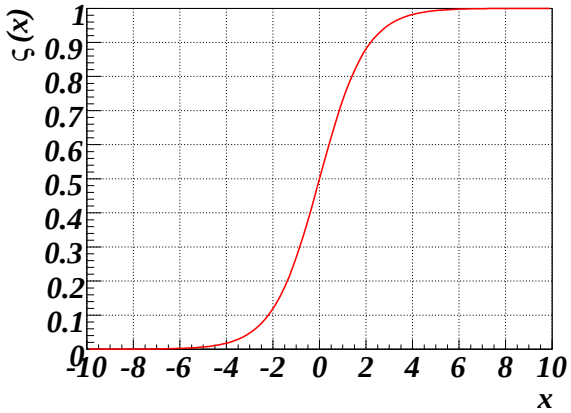

Figure B.2: Sigmoid function used as the model of synapse connections.

B.2 Selections with neural network technique

For an example of actual usage of neural network, we explain the case of the CV-η NN selection (See Sec. 7.4.1). In this case, the input parameters are relative positions and energy deposits of crystals in a photon cluster, and the output parameter is the type of that event, *i.e.* type = 1 for the signal events and type = 0 for the CV-η background events. We used the information of 11 crystals, and then the number of input parameters were 33, where each crystal contained 1 relative energy deposit and 2 position information. We used two hidden layer network, where the first hidden layer contained 60 neurons and the second one contained 15 neurons. Synapses are represented by the sigmoid function.

The training of the NN was carried out by using the MC events of $K_L^0 \to \pi^0\nu\bar{\nu}$ signal and CV-η background. In order to avoid over-optimizing to the particular events in the MC sample, we used odd-numbered samples for the training, and even-numbered samples for the monitoring. The number of iteration for the training was 50 times, which was determined by comparing the result of the training sample and the monitoring sample.

Since we had two discriminants from this NN from two photon clusters, we combined the two discriminants. The results of the combined discriminants are shown in Fig. 7.10.

Appendix C

Statistical Methods on the Upper Limit

Brief summary

In setting the upper limit to the BR($K_L^0 \to \pi^0\nu\bar{\nu}$), we adopted to use the Poisson statistics. In this chapter, we discuss other methods to derive the upper limits. First, we estimated the effect of uncertainties in the number of K_L^0 decay. Including the effect of the uncertainty, the upper limit varied by ∼1%, which was considered to be small enough.

We also tried another method, called Feldman-Cousins method, in which the expected number of background was taken into account. Using this method, the upper limit became better by 34%, though it was an overestimated value because the uncertainty in the background estimation is not considered. We carried out a numerical method to include the effect of uncertainty in the background estimation to the Feldman Cousins method, and the resultant upper limit became BR($K_L^0 \to \pi^0\nu\bar{\nu}$) $< 2.09 \times 10^{-8}$, which was 18% better compared to the Poisson statistics case.

We also report the "effective sensitivity" of the experiment, which was calculated by the single event sensitivity and the background level. We set the effective sensitivity of the present analysis to be 3.47×10^{-8}. The improvement in the effective sensitivity from the Analysis-2008 was 2.3.

C.1 Considering the uncertainty in the number of K_L^0 decay

C.1.1 Upper limit with the Poisson statistics

First, we review the method to set an upper limit by using the Poisson statistics. In the Poisson statistics, the probability to observe n events with the mean value of μ events can be represented as

$$P(n|\mu) = \frac{\mu^n \exp(-\mu)}{n!} \ . \tag{C.1}$$

In our case, μ is the expected number of signal events, *i.e.* $\mu = \mathrm{BR}(K_L^0 \to \pi^0\nu\bar{\nu})/\mathrm{S.E.S.}$.

The probability of μ to be less than a value μ_0 can be obtained by integrating the Eq. C.1 to be

$$Q(\mu < \mu_0) = \int_0^{\mu_0} P(n|\mu) d\mu \ . \tag{C.2}$$

Since we observed no events,

$$\begin{aligned} Q(\mu < \mu_0) &= \int_0^{\mu_0} P(0|\mu) d\mu \\ &= 1 - \exp(-\mu_0) \ . \end{aligned} \tag{C.3}$$

Here, the parameter μ_0 is called "interval" to set the upper limit.

In setting the upper limit, $Q(\mu < \mu_0)$ is called "Confidence Level" (C.L.), and the parameter μ_0 can be calculated by Eq. C.3:

$$\mu_0 = -\ln(1 - \text{C.L.}). \tag{C.4}$$

Taking the 90% confidence level, μ_0 becomes

$$\mu_0 = -\ln(1 - 0.9) \approx 2.30. \tag{C.5}$$

This means that

$$\mu < 2.30 \quad \text{at 90\% C.L.} \tag{C.6}$$

Reminding that $\mu = \text{BR}(K_L^0 \to \pi^0\nu\bar{\nu})/\text{S.E.S.}$ and S.E.S$= 1.11 \times 10^{-8}$, we set the upper limit to be

$$\text{BR}(K_L^0 \to \pi^0\nu\bar{\nu}) < 2.30 \times \text{S.E.S.} = 2.55 \times 10^{-8}. \tag{C.7}$$

C.1.2 Incorporating the errors in the number of K_L^0 decays

Since we had statistical and systematic uncertainties in the number of K_L^0 decays, *i.e.* in the S.E.S., the effect of these uncertainties on the upper limit was estimated.

The statistical treatment of uncertainties to set the upper limit is presented in Ref. [64]. Suppose we have an uncertainty $\sigma_{\text{S.E.S.}}$ in the S.E.S., the interval of 90% C.L. with zero event observation becomes

$$\mu_0' = 2.30(1 + 2.30\sigma_r^2/2), \tag{C.8}$$

where σ_r is the relative uncertainty of S.E.S. as $\sigma_r = \sigma_{\text{S.E.S.}}/\text{S.E.S.}$.

As presented in Eq. 10.5, we had S.E.S. $= (1.11 \pm 0.10) \times 10^{-8}$, and then we had $\mu_0' = 2.32$. The upper limit was altered to be

$$\text{BR}(K_L^0 \to \pi^0\nu\bar{\nu}) < 2.58 \times 10^{-8} \ \text{ at 90\% C.L..}, \tag{C.9}$$

though the difference was only $\sim$1%.

C.2 Feldman-Cousins method

C.2.1 Upper limit with Feldman-Cousins method

Feldman and Cousins introduced another method to set an upper limit, in which the number of estimated background was taken into account [65].

With the number of expected background events b, the probability to observe n events with the Poisson distribution is changed to be

$$P(n|\mu, b) = \frac{(\mu + b)^n \exp(-(\mu + b))}{n!} \ , \tag{C.10}$$

and thus, the upper-limit interval μ_0 is shifted. Since we estimated the number of background to be 0.87, the interval value became 1.69 by the Feldman-Cousins (FC) method from 2.30 by the Poisson statistics. The upper limit is altered to be

$$\begin{aligned} \mathrm{BR}(K_L^0 \to \pi^0 \nu\bar{\nu}) &< 1.69 \times \text{S.E.S.} \\ &= 1.87 \times 10^{-8} \text{ at 90\% C.L...} \end{aligned} \tag{C.11}$$

With the FC method, we had a 34% better upper limit value.

C.2.2 FC method with the effect of uncertainties

Since we had an uncertainty in the background estimation, the effect of the uncertainty should be considered to set the upper limit when the FC method was adopted.

To estimate this effect, we carried out a numerical approach. Given the expected number of background, we can derive a probability density function (PDF) of the number of observed events. In this numerical approach, we varied the expected number of background according to its uncertainty as shown in Fig. C.1. Then the obtained PDFs were stacked over the variation in the number of background, as shown in Fig. C.2. Then, we determined the 90% C.L. interval as the position below which the integrated probability of PDF became 90%.

Since the estimated number of background was 0.87 ± 0.41 in our experiment, we distributed the number of background with the standard deviation of 0.41. We tried two kinds of the distribution for the background: Gaussian and flat, as shown in Fig. C.1. In both cases, the estimated interval became 1.88 and the upper limit was altered to be

$$\mathrm{BR}(K_L^0 \to \pi^0 \nu\bar{\nu}) < 2.09 \times 10^{-8} \text{ at 90\% C.L..} \tag{C.12}$$

The difference was about 11% from the case without the uncertainties. The values obtained by various methods are summarized in Table C.1.

Table C.1: Upper limits calculated by different methods, where the difference is calculated by the relative difference from the value obtained by the Poisson statistics.

Method	Interval	Upper limit	Difference
Poisson	2.30	2.55×10^{-8}	—
Poisson with errors in $N(K_L^0)$	2.32	2.58×10^{-8}	1.2% worse
FC	1.69	1.87×10^{-8}	34% better
FC with errors in N_{bg}	1.88	2.09×10^{-8}	18% better

C.2.3 Effective sensitivity of the experiment

In the FC method, one may feel "strange" to the following thing: an ideal experiment, which expects no backgrounds and observes no events, is forced to set worse upper limit than another experiment, which expects finite backgrounds and eventually observes no events.

For this problem, Feldman and Cousins suggested to report an "effective sensitivity" of the experiment, where the effective sensitivity is defined as the average upper limit that would be obtained by an ensemble of experiments with the expected background and no true signal [65].

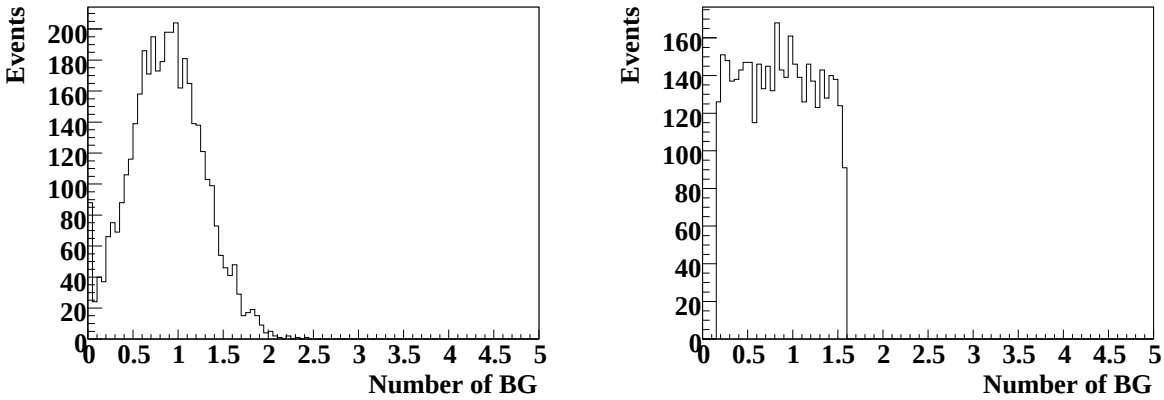

Figure C.1: Distributed number of background, where the $N_{bg} = 0.87$ and $\sigma_{N_{bg}} = 0.41$. Left figure shows the case of Gaussian distribution with a bound at the $N_{bg} = 0$, and right figure shows the case of flat distribution.

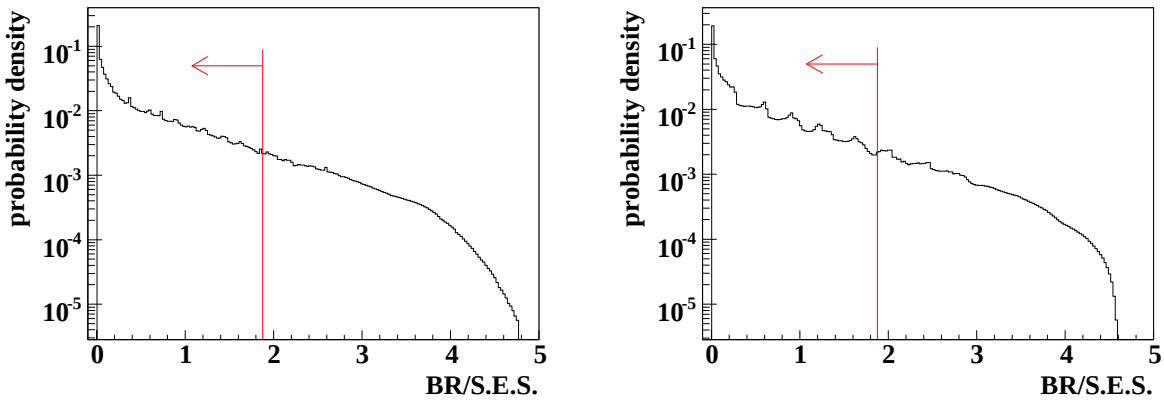

Figure C.2: Probability density function of the observed number of events calculated with the N_{bg} distribution shown in Fig. C.1. Left and Right shows the case with Gaussian and flat distribution in N_{bg}, respectively. Red lines show the 90% C.L. interval value.

In our case, the estimated number of background was 0.87 and the corresponding average interval became 3.13. Since we had S.E.S. of 1.11×10^{-8}, the effective sensitivity of the present measurement was 3.47×10^{-8}. This can be compared to the Analysis-2008 case: with 0.42 expected background events, we had interval value of 2.76 on average, and the effective sensitivity became 8.03×10^{-8}. Thus, in the viewpoint of the parameter effective sensitivity, the improvement of the present analysis from the Analysis-2008 was a factor of 2.31. The summaries of the effective sensitivity of the Analysis-2008 and the present Run-2+3 analysis is summarized in Table C.2.

Table C.2: Effective sensitivity of the Analysis-2008 and the present Run-2+3 analysis. N_{bg} is the expected number of background events.

	N_{bg}	Averaged interval	S.E.S.	Effective sensitivity
Analysis-2008	0.42	2.76	2.91×10^{-8}	8.03×10^{-8}
Present Run-2+3	0.87	3.13	1.11×10^{-8}	3.47×10^{-8}

Bibliography

[1] T. D. Lee and C.-N. Yang, Phys. Rev. **104**, 254 (1956).

[2] C. S. Wu, E. Ambler, R. W. Hayward, D. D. Hoppes, and R. P. Hudson, Phys. Rev. **105**, 1413 (1957).

[3] R. L. Garwin, L. M. Lederman, and M. Weinrich, Phys. Rev. **105**, 1415 (1957).

[4] J. I. Friedman and V. L. Telegdi, Phys. Rev. **105**, 1681 (1957).

[5] J. H. Christenson, J. W. Cronin, V. L. Fitch, and R. Turlay, Phys. Rev. Lett. **13**, 138 (1964).

[6] A. D. Sakharov, Pisma Zh. Eksp. Teor. Fiz. *5*, 32 (1967).

[7] G. D. Rochester and C. C. Butler, Nature **160**, 855 (1947).

[8] M. Gell-Mann and A. Pais, Phys. Rev. **97**, 1387 (1955).

[9] K. Lande, E. T. Booth, J. Empeduglia, L. M. Lederman, and R. Turlay, Phys.Rev. **103**, 1901 (1956).

[10] C. Amsler *et al.* (Particle Data Group), Phys. Lett. **B667**, 1 (2008).

[11] G. D. Barr, *et al.* (NA31 collaboration), Phys. Rev. Lett. **70**, 1203 (1993).

[12] R. Adler *et al.* (CPLEAR collaboration), Phys. Lett. **B363**, 243 (1995).

[13] A. Alavi-Harati *et al.*, Phys. Rev. D **67**, 012005 (2003).

[14] N. Cabibbo, Phys. Rev. Lett. **10**, 531 (1963);
M. Kobayashi and T. Maskawa, Prog. Theor. Phys. **49**, 652 (1973).

[15] L. Wolfenstein, Phys. Rev. Lett. **51**, 1945 (1983).

[16] C. Jarlskog, Phys. Rev. Lett. **55**, 1039 (1985).

[17] J. Charles *et al.* (CKMfitter Group), Eur. Phys. J. **C41**, 1 (2005), hep-ph/0406184.
Updated results are available at: http://ckmfitter.in2p3.fr/.

[18] A. J. Buras, F. Schwab, and S. Uhlig, (2004), hep-ph/0405132.

[19] Y. Grossman and Y. Nir, Phys. Lett. **B398**, 163 (1997), hep-ph/9701313.

[20] V. V. Anisimovsky *et al.* (E949), Phys. Rev. Lett. **93**, 031801 (2004), hep-ex/0403036.

[21] A. J. Buras, T. Ewerth, S. Jager, and J. Rosiek, Nucl. Phys. **B714**, 103 (2005), hep-ph/0408142.

[22] G. D'Ambrosio, G. F. Giudice, G. Isidori, and A. Strumia, Nucl. Phys. **B645**, 155 (2002), hep-ph/0207036.

[23] U. Haisch, A. Weiler, Phys. Rev. **D76**, 074027 (2007), hep-ph/07062054.

[24] M. Blanke, A. J. Buras, B. Duling, S. Recksiegel, and C. Tarantino, hep-ph/09065454.

[25] T. Goto, Y. Okada, and Y. Yamamoto, Phys. Lett. **B670** 378 (2009), hep-ph/08094753.

[26] C. Promberger, S. Schatt, and F. Schwab, Phys. Rev. **D75** 115007 (2007), hep-ph/0702169.

[27] W. S. Hou, M. Nagashima, and A. Soddu, Phys. Rev. **D72** 115007 (2005), hep-ph/0508237.

[28] F. Mescia and C. Smith, http://www.lnf.infn.it/wg/vus/content/Krare.html

[29] L. S. Littenberg, Phys. Rev. D **39**, 3322 (1989).

[30] J. Adams *et al.* (KTeV), Phys. Lett. **B447**, 240 (1999), hep-ex/9806007.

[31] A. Alavi-Harati *et al.* (E799-II/KTeV), Phys. Rev. **D61**, 072006 (2000), hep-ex/9907014.

[32] T. Inagaki *et al.*, *Proposal of an Experiment at the KEK 12-GeV Proton Synchrotron: Measurement of the* $K_L \to \pi^0\nu\bar{\nu}$, KEK Internal Report **96-13** (1996).

[33] J. K. Ahn *et al.*, Phys. Rev. **D74**, 051105 (2006), hep-ex/0607016.

[34] K. Sakashita, *Search for the decay* $K_L^0 \to \pi^0\nu\bar{\nu}$, Ph.D. thesis, Osaka University, 2006.

[35] J. K. Ahn *et al.*, Phys. Rev. Lett. **100**, 201802 (2008), hep-ex/07124164.

[36] G. N. Perdue, *Search for the rare decay* $K_L^0 \to \pi^0\nu\bar{\nu}$, Ph.D. thesis, University of Chicago, 2008;
T. Sumida, *Search for the decay* $K_L^0 \to \pi^0\nu\bar{\nu}$, Ph.D. thesis, Kyoto University, 2008.

[37] S. Ajimura *et al.*, Nucl. Instrum. Meth. Phys. Res. A **435**, 408 (1999);
S. Ajimura *et al.*, Nucl. Instrum. Meth. Phys. Res. A **552**, 263 (2005).

[38] H. Watanabe *et al.*, Nucl. Instrum. Meth. **A545**, 542 (2005).

[39] H. Watanabe, K_L^0 *beam line for the study of the* $K_L^0 \to \pi^0\nu\bar{\nu}$ *decay*, Ph.D. thesis, Saga University, 2002.

[40] M. Doroshenko *et al.*, Nucl. Instrum. Meth. **A545**, 278 (2005).

[41] M. Doroshenko, *A measurement of the branching ratio of the* $K_L^0 \to \pi^0\nu\bar{\nu}$ *decay*, Ph.D. thesis, Graduate University for Advanced Studies (SOKENDAI), 2005.

[42] T. Ikei, *Charged Veto Detector for the* $K_L \to \pi^0\nu\bar{\nu}$ *Experiment*, Master thesis, Osaka University, 2004.

[43] T. Inagaki *et al.*, High Energy News **23-1**, 13 (2004) (in Japanese).

[44] Y. Yoshimura *et al.*, *Extrusion scintillator made of MS resin* (to be published).
Y. Yoshimura *et al.*, Nucl. Instrum. Meth. **A406**, 435 (1998),
which is a report on injection molding of scintillator made of MS resin.

[45] M. Itaya *et al.*, Nucl. Instrum. Meth. **A522**, 477 (2004).

[46] Y. Tajima *et al.* (E391a), Nucl. Instrum. Meth. **A592**, 261 (2008).

[47] R. Ogata, *Study on the particle identification with fine-grained calorimeter.*, Master thesis, Saga University, 2007 (in Japanese).

[48] Y. Nakajima, *Development of the photon detector using aerogel, to be used in the neutral kaon rare decay experiment.*, Master thesis, Kyoto University, 2006 (in Japanese).

[49] T. K. Ohska *et al.*, KEK Report **85-10**, 1985;
IEEE Trans. Nucl. Sci. **33**, 98 (1986).

[50] MIDAS homepage, https://midas.psi.ch; https://daq-plone.triumf.ca/SR/MIDAS;
E391a-MIDAS,
http://www-ps.kek.jp/~e391/exp/daq/index.html.

[51] H. S. Lee, *Search for the rare decay $K_L^0 \to \pi^0\nu\bar{\nu}$ at E391a*, Ph.D. thesis, Pusan University, 2007.

[52] G. Battistoni *et al.*, *The FLUKA code: Description and benchmarking*,
Proceedings of the Hadronic Shower Simulation Workshop 2006, Fermilab 6–8
September 2006, M. Albrow, R. Raja eds., AIP Conference Proceeding 896, 31-49 (2007).

[53] CERN Program Library Long Writeup W5013, 1993.

[54] N. G. Deshpande and G. Eilam, Phys. Rev. Lett. **53**, 2289 (1984).

[55] T. Inagaki *et al.*, Nucl. Instrum. Meth. **A359**, 478 (1995).

[56] J. Comfort *et al.*, (J-PARC E14 Collaboration), *Proposal for $K_L^0 \to \pi^0\nu\bar{\nu}$ Experiment at J-Parc* (2006).

[57] http://j-parc.jp/ .

[58] H. Nanjo, (J-PARC E14 K$^{\mathrm{O}}$TO Collaboration),
J-PARC E14 K$^{\mathrm{O}}$TO *experiment for $K_L^0 \to \pi^0\nu\bar{\nu}$*,
in proceedings of the Kaon International Conference 2009 (KAON09), PoS(KAON09)047.

[59] I. H. Chiang, *et al.*, (KOPIO Collaboration),
KOPIO – a seach for $K_L^0 \to \pi^0\nu\bar{\nu}$, MRE Proposal, (1999).

[60] G. Anelli *et al.*, (NA62 Collaboration),
Proposal to measure the rare decay $K^+ \to \pi^+\nu\bar{\nu}$ at the CERN SPS,
CERN-SPSC-2005-013, SPSC-P-326 (2005).
G. Ruggiero, (NA62 Collaboration),
The NA62 experiment at CERN for $K^+ \to \pi^+\nu\bar{\nu}$,
in proceedings of the Kaon International Conference 2009 (KAON09), PoS(KAON09)043.

[61] K. F. J. Chen, *CsI Calibration Using* $K_L^0 \to \pi^0\pi^0\pi^0$ *Decays*, Internal Technote, 2005.

[62] K. Hornik, M. Stinchcombe, and H. White, Neural Newtorks **2**, 359 (1989).

[63] E. D. Sontag, IEEE Transactions on Neural Network **3**, 981 (1992).

[64] R. D. Cousins and V. L. Highland, Nucl. Instrum. Meth. **A320**, 331 (1992).

[65] G. J. Feldman and R. D. Cousins, Phys. Rev. **D57**, 3873 (1998), physics/9711021.